In-Vacuum Roll-to-Roll Patterning for Functional Devices



Thomas Cosnahan

St. Edmund Hall

University of Oxford

A thesis submitted for the degree of

Doctor of Philosophy

Trinity 2018

Abstract

This thesis investigates the viability and compatibility of an industrially-mature metal thin film patterning process, that uses flexography printing in vacuum environments, for application to functional organic devices.

The integral thermal mechanism of this process, called selective metallization, is modelled, showing its compatibility with functional organics (process temperature $< 60°C$, Al sheet resistance $< 1.59\Omega.\square^{-1}$). The first example of $sub - 10\mu m$ lateral patterning, using this technique, is presented. These results demonstrate that, for this process, the flexography ink transfer defines the pattern quality.

The pattern quality of the printed metal is optimised, using custom-built in-vacuum flexography equipment. The pattern quality metrics, quantified using specially developed image analysis code, vary parabolically with printing pressure and diminish with increased printing speeds. A hierarchical phenomenological model of ink transfer is developed, which fits the data well. Optimal printing parameters reduce line edge peak-to-peak roughness to $< 1/2$ nominal pattern gap, enough to remove electrical defects.

These optimised printed patterns are used as electrical contacts for organic thin film transistors (OTFTs), as a proof of concept. Device characterisation shows a change in transistor performance, compared to batch-processed Au contacts, resulting from a charge carrier injection layer, $MoO_x\,(x < 3)$, which is necessary for band matching of the organic semiconductor with the high work function Al. Overall, the changes with MoOx thickness and configuration demonstrate selective metallization is compatible with OTFTs, with a contact resistivity of $1\Omega.cm^{-2}$.

To conclude, exploratory results, of selective metallization applied to organic light emitting diodes, and in-vacuum printing of an organic dielectric material, demonstrate the potential wide applicability of in-vacuum flexography.

For Róisín

Acknowledgements

My first thanks go to my co-supervisors, who have been a patient a steady force, aiding me throughout my doctoral work. Working with Prof. Hazel Assender has been a joy and an invaluable experience of the impact that a great guide and mentor can have. Prof Andrew Watt's expertise and personable, hands-on approach has been a great help, for which I would like to thank him. I would like to thank them both for their guidance on the project, encouragement to keep going and wisdom to ask the critical questions about the research direction and value.

I am very thankful to whole wider group, including the various summer students and Part II's, for taking the time to help with current issues and share their work, which have broadened my understanding. In particular I would like to acknowledge: Dr. Vincent Tobin, Dr. Nanlin Zhang, Zhanet Zaharieva, Yujiro Tazawa, Wing Chung, Daniel Gregory, and Nina Klein for their friendship and help. My thanks go to Kai Zhang and Carmen Alonso-Herr and also now, Hui Luo, Xudong Tao and Bryan Stuart. You have each made my time here special and I wish you all the best with your research projects (and the equipment!). Thanks to Patrick Grant's groups, and others at Begbroke, for the never mundane but always unmissable lunches and chats.

Next, I would like to thank the hard work and generous expertise shared by Mr. Richard Turner, without whom my work would not have happened, and without half as much enjoyment. I would also like to thank Mr. Robin Vincent, Mr Greg Cook, and Dr. John Topping for their technical support. I'm also very grateful for the experience and support of Dr. Clara Barker, and Robert Gresham, at a moments notice, and throughout.

I would like to thank my collaborators at MIT, Dhanush Dura Mariappan for putting in so much time to send me sample and Dr. Sanha Kim for taking the time to meet me and being open to the work. I would also like to thank those who have provided me with encouragement and friendship

at conferences and meetings throughout the years, like: Pal Terek, those at the manufacturing group at Leeds University, members of WAFT, and my friends from the WCPC summer school.

I would like to thank my family and parents, who have been so thoughtful and kind, with phone calls and visits, interest and advice, which was, and will continue to be, a blessing I couldn't do without. Finally I would like to thank Roisin, for your love and emotional dedication. Your loving words, many dinners, and grounding humour have always been my rock, and always will be.

Statement Of Originality

This thesis is an account of work carried out by the author in the Department of Materials, the University of Oxford under the supervision of Professor Hazel Assender and Professor Andrew Watt. Any work of others that has been utilised, directly or indirectly, is duly acknowledged in the text, and a list of references is presented at the end of each chapter. No part of this thesis has been submitted towards the completion of another degree at the University of Oxford or elsewhere. Parts of the thesis have been submitted to or published in the following scientific journals or conference presentations:

Cosnahan, T., Watt, A. A. R. & Assender, H. E., Flexography Printing for Organic Thin Film Transistors. Materials Today: Proceedings 5:16051–7 (2018)

Cosnahan, T., Watt, A. A. R. & Assender, H. E., Modelling of a vacuum metallization patterning method for organic electronics. Surface and Coatings Technology 336, 128–132 (2018).

Cosnahan, T., Watt, A. A. R. & Assender, H. E., Depositing patterns of aluminium using a vacuum roll-to-roll flexography technique. Institute of Physics Postgraduate Student Conference: Printing for the future (January 2018) (Oral Presentation)

Cosnahan, T., Watt, A. A. R. & Assender, H. E., Flexography Printing for Organic Thin Film Transistors. International Symposium for Flexible Organic Electronics (July 2017) (Oral Presentation)

Cosnahan, T., Watt, A. A. R. & Assender, H. E., Sponsored Student: Flexographic Patterning in Vacuum of Sacrificial Oil for Aluminium Contacts of Organic Transistors. Society of Vacuum Coaters Annual Technical Conference (May 2017) (Oral Presentation)

Cosnahan, T., Watt, A. A. R. & Assender, H. E., Vacuum Flexographic Patterning of Sacrificial Oil for Organic Transistor Aluminium Contacts. Innovations in Large Area Electronics (January 2017) (Oral Presentation)

Cosnahan, T., Watt, A. A. R. & Assender, H. E., Direct Gravure Patterning in Roll-to-Roll Process. 2nd Plastic Electronics Conference (April 2015) (Oral Presentation)

Contents

1 Introduction **1**

1.1 Manufacturing for Functional Organics 1
1.2 Aims of thesis 3
1.3 Thesis Outline 5
1.4 References 7

2 Literature Review **8**

2.1 Flexible Technology Introduction 8
2.2 Fundamentals of Transistors and Material Requirements 10
2.2.1 Fundamentals of transistors 10
2.2.2 OTFT key parameters 13
2.3 Patterning for Flexible Devices 14
2.3.1 Outline 14
2.3.2 Roll-to-roll compatibility 15
2.3.3 Photolithography 18
2.3.4 Soft stamp printing 19
2.3.5 Gravure printing 22
2.3.6 Flexography Printing 23
2.3.7 Summary of patterning techniques 26
2.4 Flexography Printing 26
2.4.1 Foundations of flexography 28
2.4.1.1 New plate materials 29
2.4.1.2 New substrate materials 29
2.4.1.3 Improved ink metering methods 29
2.4.2 Modern flexography printing 30
2.4.3 Academic Research Focused on Industry 31
2.4.4 Modelling Liquid Bridges 36
2.5 Metal Patterning 44

2.5.1 Selective metallization 46
2.6 Conclusion 48
2.7 References 50

3 Experimental Materials and Methods 65
3.1 In Vacuum Flexography Letterpress 65
3.1.1 Design of printing system 65
3.1.2 Testing of the foam backing 67
3.1.3 Fabrication and design of print plate 67
3.1.4 Anilox inking pad selection 71
3.2 Patterning Tests and Analysis 73
3.2.1 Experimental method 74
3.2.2 Print Quality Image Analysis 75
3.2.2.1 Development of computer image analysis 75
3.2.2.2 Statistical Analysis 77
3.3 Fabrication and Characterisation of OTFTs 77
3.3.1 Experimental method 77
3.3.1.1 Fabrication Method and Materials 78
3.3.1.2 Characterisation of transistor behaviour 79
3.3.2 Characterisation of thin films 80
3.4 References 81

4 Selective Metallization Viability and Compatibility Modelling for Functional Organic Devices 83
4.1 Introduction 83
4.1.1 Selective Metallization 84
4.2 Method 87
4.2.1 Compatibility and Printing Analysis 87
4.2.2 Selective metallization printing 88
4.2.3 Heat Model 89
4.3 Results 89
4.3.1 Modelling results 89
4.3.2 Experimental Results 90
4.4 Discussion 91
4.4.1 Thermal Lift-Off 91
4.4.2 Patterned Metal Thin Films 94
4.5 Conclusion 95

4.6 References 97

5 Flexography printing analysis and optimisation 99

5.1 Introduction 99
5.1.1 Print quality trends and ink transfer 100
5.1.2 Flexography Analysis 101
5.2 Experimental Method 103
5.2.1 Contact width calculation 103
5.2.2 Plate design 106
5.2.3 Printing trials and analyses 106
5.3 Results 107
5.4 Discussion 109
5.4.1 Experimental Validity 109
5.4.2 Origin of errors and results analysis 114
5.4.3 Observed defects categories, static and dynamic 117
5.4.4 Effects of foam plate backing 120
5.4.5 Quality changes with pattern variation 121
5.4.6 Plate-substrate contact pressure effects 124
5.4.7 Printing speed effects on print quality 128
5.4.8 Optimisation of printing 131
5.5 Conclusion 139
5.6 References 142

6 Compatibility of Flexography Metallization for Organic Thin Film Transistors 145

6.1 Introduction 145
6.1.1 Compatibility of aluminium contact for OTFTs 146
6.2 Method 149
6.3 Results and Discussion 152
6.3.1 Control transistors with gold contacts 152
6.3.2 Aluminium contacts and effects of MoOx carrier injection layer 154
6.3.2.1 MoOx effects on output characteristics and mobility 155
6.3.2.2 MoOx effects on threshold voltage 156
6.3.2.3 MoOx effects on drain current, gate leakage & yield 158
6.3.2.4 Optimal compatibility of Al+MoOx OTFTs 160
6.3.3 In-line patterned contacts 161
6.4 Conclusion 166

6.5 References 168

7 Conclusion and Future Work **172**

7.1 Conclusion of thesis findings 172

7.2 Future Work 175

7.2.1 Selective Metallization 175

7.2.2 Flexography printing 176

7.2.3 Patterning for functional organic devices 178

7.3 References 181

List of Tables

1.1 Research questions, that are addressed in this doctoral thesis, of the viability and compatibility of selective metallization with functional organic devices. 4

2.1 Summary of the main patterning techniques found in the literature. Techniques are categorised as continuous (R2R) techniques or B for batch techniques patterning. 17
2.2 Table of equations defining the liquid bridge behaviour, used for modelling of extensional flow 38

3.1 Plate pattern nominal and actual (with 3% shrinkage) line dimensions, aspect and pattern ratios. 71

4.1 The values used for calculating the required liquid oil thickness to match the radiative energy as per thermal model. 90

5.1 Printing and impression roller specifications used for calculating the contact width. 106
5.2 Schema of experimental data presented in this chapter. 107
5.3 Table of the standard deviations of the data of three separate runs conducted across several months, with 30g dead weights and printing speed of $20m.min^{-1}$. 108
5.4 Definition of defects in the printed oil pattern (inverse of metallized pattern defects) as identified is Figure 5.11. 119
5.5 Linear gradients for P2P change with nominal line force, showing relative changes with speed which fits modelling predictions in the literature. 129
5.6 Table a. lists various values used for the P2P roughness model, Equation5.12, and shown in Figure 5.15. Table b. briefly describes the origin of the values used. 136

6.1 Average characteristics of in-line patterned OTFTs. 161

List of Figures

1.1 Schematic of a flexography printing set-up. 3

2.1 Examples of using flexible technology for new applications, from a) measuring the temperature of packaged fish to monitor food safety to b) and c) live monitoring of the cardiac rhythms of a zebra fish for drugs research. These two examples highlight the range of applications for conformable technology and how their are many more applications in the sea. 9

2.2 Schematic of a bottom gate top contact transistor. This image also highlights the key materials requirements for good transistor behaviour. 11

2.3 The thin film transistor parameters of a gravure printed top gate transistor. a) shows the output curves with the ohmic and accumulation regions highlighted. b) shows the transfer characteristics measured at -20V drain voltage. 14

2.4 The summary of printing process from the 2015 Road Map of the OE-A. The latest report continues to highlight the importance of patterning processes. 15

2.5 The principle of photolithography. 18

2.6 a. Gravure process schematic showing the key elements. b. change in print quality of conductive ink lines with cell spacing decreasing from (i) to (x) in 2.5\mu m steps from 42.5μm to 20μm, with 30μmcells having a 14pL volume. When cells spacing is too far apart isolated ink transfer occurs, too close and scalloped lines (to the point of discontinuity) occur, at the optimum spacing continuous lines are formed by ink spreading on the substrate. 21

2.7 Variation of printed line width with force applied to the contact region (nip) in gravure printing of silver conductive pastes of varying viscosities. 24

2.8 Flexography schematic, with a chambered doctor blade which prevents solvent evaporation under atmospheric conditions, and onto a plate and not another roller, though the principles are similar. 24
2.9 Spider diagram qualitatively comparing photolithography, inkjet, soft lithography, gravure and flexography with the theoretical ideal in the author's informed opinion. 27
2.10 A modern industrial printing press. 30
2.11 a. Transfer curve of oil based ink onto coated paper, showing how the fraction of ink transferred from the plate to the substrate changes with the amount of ink originally on the printing plate. b. Ink transfer splitting described can be described by the Walker-Fetsko equation. . 32
2.12 The line ruling interaction with the the anilox cell volume. 34
2.13 Schematic of asymmetric ink splitting between the plate and substrate. 37
2.14 Schematic of a cylindrical liquid bridge model undergoing plate separation 38
2.15 a. Transfer ratio changes with substrate contact angle variation. b. Simulation of equilibrium contact lines for a high aspect ratio ink bridge with smooth flat surfaces. 40
2.16 a. Schematic of 3D liquid bridge b. 2D freeze frame of a liquid bridge model with extension and rotation of the top plate. 42
2.17 a. and b. show optical microscopy images of a SelectMet® metallized pattern sample from Bobst who make selective metallization machines. c. schematic of the principles of the selective metallization in-vacuum production method 47

3.1 Schematic of the flexography-like set-up with the inking pad having passed through the contact region, to transfer ink to the printing plate, which subsequently patterns the substrate wrapped on the process drum. 66
3.2 Design of the custom-built letterpress flexography system to be operated within a vacuum chamber. 68
3.3 Free body force diagram of the principle behind controlling the printing line force, using a hanging dead weight. 69
3.4 Stress strain behaviour of the plate backing foam material. 70
3.5 Plate fabrication process describing the 3 steps for double casting of of PDMS to create the printing plate sleeve. 72

3.6 Change in oil volume on a $200\mu m$ wide plate feature with contact angle of the oil and the plate feature. 73
3.7 mages of a pattern created at $10m.min^{-1}$ with a nominal line force of $19.6N.m^{-1}$ at three stages of the image analysis, code shown in the appendix. 76
3.8 a. shows a schematic of the experimental range of the various types of contact, control and patterned with various molybdenum trioxide configurations labelled. b. photograph of a shadow mask patterned top contact bottom common gate transistors fabricated for this doctoral thesis. 79

4.1 Repeat unit of the Krytox® perfluoropolyether. 87
4.2 a. 5x optical micrograph of nominal linewidth 150\mu m line pattern printed with the selective metallization technique. b. 12x optical micrograph of the selective metallization pattern made with the CNT stamps. The nominal pattern is $10\mu m$ circle with $3\mu m$ spacing in a honeycomb grid arrangement. 92

5.1 Schematic of modelled contact, with various properties labelled. . . . 105
5.2 Image of wetting sessile drops, of approximately $10\mu L$ Krytox 1506 oil, on a. PDMS plate material and b. PET substrate, showing greater wetting on the latter. 108
5.3 Change in the P2P, and the standard error of 15 lines, with plate-substrate impression force for 1mm spaced lines from initial trail results with plate backing made of a. steel and b. foam. 109
5.4 Hertzian contact width change with increasing contact, calculated, Equation [eq:contact width], for a PDMS contact with steel backing (hard) and a foam supported PDMS plate (soft) contact with a steel impression cylinder. 110
5.5 a. - d. are common scale optical microscope images of $150\mu m$ lines at varying nominal line forces and $10m.min^{-1}$ printing speed,where the light grey is the PET substrate and the metal deposition is the dark grey regions. e. the entire metal pattern at 50g nominal line force. . 111
5.6 Graphs of the variation in P2P with force with varying pattern ratios of a. 2, b. 1.5, and c. 1 and d. 0.6 at $10m.min^{-1}$. 112

5.7 a-d. Change in P2P with force of impression for varying line widths, e. parabolic fit for the data showing the similar minimum at $42n.m^{-1}$ nominal line force. 113
5.8 Variation of RMS roughness with nominal line force at a print speed of $10m.min^{-1}$, showing a similar trend to that seen with P2P in Figure 5.7. 114
5.9 Change in line gain with plate-substrate impression force, for a. $1000\mu m$, b. $200\mu m$, c. $150\mu m$ and d. $100\mu m$. 115
5.10 Graphs of the variation in P2P with force with print speeds of a. $10m.min^{-1}$, b.$20m.min^{-1}$, and c. $35m.min^{-1}$ with $150\mu m$ nominal linewidths. 116
5.11 Microscopy image of the defining defects observed in a print ($65.4n.m^{-1}$ and $10m.min^{-1}$) of $200\mu m$ lines. 118
5.12 Stress strain curve for the foam plate backing material showing 3 distinct regions: elastic, hardening, and cell collapse. 122
5.13 a. schematic of PDMS plate feature deformation, giving definitions used in Equation 5.7. b. measure pressure profile through the contact of deformable coating rolls, with the negative pressure at the exit highlighted. 127
5.14 Schematic of the total P2P roughness as a function of the nominal line force which is the sum of the the observed trends seen in the plate backing ($B(F_L)$) , plate pattern feature deformation ($F(F_L)$) and ink distortion ($I(F_L)$), with the model summation shown in the continuous black line. 132
5.15 Fitting of the theoretical trends to the empirical data of the P2P line edge roughness variation with nominal line force (F_L). 137

6.1 a. Resistance experienced by a charge carrier as it moves from source to the drain through the channel of an OTFT. b. TLM analysis graph with the insets showing the output curve from which the total contact resistance is derived, and the device design of varying channel length. 146
6.2 Graph of equilibrium band energies for DNTT and DNTT interfaces with aluminium and MoOx with aluminium. 150
6.3 Schematic experimental design showing the OTFT structure and the various contact materials and fabrication methods. 151

6.4 Output and transfer characteristics of OTFTs with gold contacts. The transfer curve is obtained at $V_{DS} = -30V$. 152
6.5 Transfer results in from previous work showing similar characteristics of transistors made here. 154
6.6 Change in output and transfer characteristics with changing MoOx thickness for contact with aluminium contact deposited using a shadows mask. The transfer curves are obtained at $V_{DS} = -30V$. 155
6.7 Schematic showing a. the ideal sharp interface between a metal contact and organic semiconductor, b. rough metal organic interface with metal clusters penetrated into the organic and c. with the cluster creating a conductive bridge from the contact to the dielectric layer. . . 157
6.8 Output and transfer characteristics of transistors with both aluminium and 18nm MoOx deposited within a single pump down, transfer obtained at $V_{DS} = -30V$. 158
6.9 Characteristics of transistors with MoOx shadow mask patterned carrier injection layers of various thicknesses, with exposure to ambient before aluminium contact thermal evaporation, transfer obtained at $V_{DS} = -30V$ 160
6.10 Output characteristics of patterned transistors with 18nm MoOx coating varying source drain width created using in-line patterning, and the corresponding transfer curves, obtained at $V_{DS} = -30V$. 162
6.11 Greyscale optical microscopy image of the printed thin film transistors. 163
6.12 TLM analysis at $V_{DS} = -1V$ with patterned aluminium contacts and an 18nm MoOx coating, using in-line patterned aluminium contacts of varying spacings and nominal linewidth of $150\mu m$. 165

7.1 Schematic of the in-vacuum acrylate patterning process using flexography, followed by curing of the monomer liquid using an argon plasma.177
7.2 Optical micrographs of the printed TPGDA on silicon chips 1mm line patterns at a. 1× and b. 5× magnification. The darker regions are the unpatterned silicon surface. 179
7.3 a. Sample OLED from CDT, image from reference. b. Output characteristics of OLED with a cathode layer deposited using selective metallization. 180

List of Abbreviations

μCP Micro-contact printing

μTM Micro-transfer moulding

μTP Micro-transfer printing

CBP 4,4´-Bis(carbazol-9-yl)-biphenyl

CD Cross direction

CDT Cambride Display Technology Ltd.

CNT Carbon nanotube

DNTT Dinaphtho[2,3-b:20,30-f]thieno[3,2-b]thiophene

FE Finite element

FET Field effect transistor

FTA Flexographic Technical Association

HOMO Highest occupied molecular orbita

IOT Internet of Things

IPA Isopropanol

LUMO Lowest unoccupied molecular orbitals

MD Machine direction

MIMIC Micro-moulding in capillaries

OE-A Organic and Printed Electronics Association

OLED Organic light emitting diode

OPV Organic photovoltaic

OTFT Organic thin film transistor

P2P Peak-to-peak roughness

PDMS Poly-dimethyl siloxane

PDMS Poly-dimethyl siloxane

PE Polyethylene

PEN Polyethylene naphthalate

PET Polyethylene terephthalate

PS Polystyrene

PU Polyurethane

PVD physical vapour deposition

R2R Roll-to-roll

REM replica moulding

RIT Rochester Institute of Technology

RMS Root mean square roughness

STM Scanning tunnelling microscopy

TAPPI Technical Association of the Pulp and Paper Industry

TLM Transmission line analysis

TPGDA Tri-propyleneglycol diacrylate

UPS Ultra-violet photo-electron spectroscopy

UV Ultra-violet

VLSI Very large scale integration

WCPC Welsh Centre for Printing and Coating

Chapter 1

Introduction

Sections of this introduction chapter have been based on a published proceedings paper: Cosnahan, T., Watt, A. A. R. & Assender, H. E., Flexography Printing for Organic Thin Film Transistors. Materials Today: Proceedings 5:16051–7 (2018)

1.1 Manufacturing for Functional Organics

High throughput manufacturing is of key importance for flexible electronics based on functional organic thin films. One challenge in particular is patterning at high speeds and with sufficient resolution with roll-to-roll process (R2R). The applications of combining low cost manufacturing with a high value product, like organic thin film transistors (OTFTs), organic light emitting diodes (OLEDs), and conformal sensors, to name a few, are of great commercial value. The materials problems that need to be solved to do this would be of general scientific value. When assessing the feasibility and usability of a manufacturing process for any particular purpose, scientific investigation can yield answers about its viability and compatibility.

Viability experiments test the production process' capabilities in order to determine whether the process could be a method of production for the particular device. If a process is viable its mechanisms and physical properties will be understood sufficiently such that the required functional device can be fabricated. A non-viable production process could not create the required device due to the physical limitations of the process. Investigating viability first requires an understanding of the origins of the process, secondly the level of industrial know-how and skill required, and finally the physical mechanistic constraints.

Compatibility experiments test the effects of the production process on the materials involved to determine whether the process could create the required device

properties. A compatible process would create functional organic devices with material characteristics as similar to the ideal as possible. An incompatible production process cannot fabricate the device with materials characteristics good enough to function at the level required. Investigating the compatibility of a process first involves understanding of the device requirements and analysis, and then how these are affected by the material properties, and finally the ways the material properties are controlled by the fabrication process.

This thesis is concerned with the viability and compatibility of flexography patterning processes when applied to flexible electronics. Flexography dates back to turn of the 20th century when technological leaps of the industrial revolution, legislative pressure, and new man-made materials were improving the possibilities of industrial scale printing. Since then it has been developed and improved, particularly throughout the 2000s, so that it now holds a large market share of the graphics industry.[1] Its low contact pressure printing can be applied to a wide range of substrates from cardboards to plastics. Another part of its success within the graphics printing field lay in the broad range of usable ink viscosities and the anilox system, which readily controls the amount of ink transferred from inking system to plate and subsequently to the substrate, see Figure 1.1. The lateral printed dimensions that are achievable using standard graphic flexography (in the order of a few 10's microns) are similarly applicable with large area electronics, but may be limiting for devices which require higher resolution patterning. The deposited ink thickness is about 1μm, according to a key textbook of graphics printing.[2] It is evident from this industrial know-how that flexography could be successfully applied to some organic devices to create electrical contacts or functional thin film layers. However the limits of patterning resolution and the effects of plate to substrate ink transfer are still unclear. These limits need to be fully explored to asses the viability of flexography for functional organic devices.

Organic thin film transistors are multi layered devices which date back to the 1980s.[3] The multi layered thin film structure is typical of many organic functional devices, and OTFTs provide a good test bed for compatibility assessments. OTFTs have made strong strides in device performance, particularly in terms of mobilities and source drain gaps. [4] This is due to materials chemistry improvements and novel laboratory scale fabrication techniques. Even though the technology is behind the father and workhorse of modern computing: rigid silicon based devices, the opportunity for flexible and large area devices is not in performance but ubiquity. Research into these devices has blossomed since the turn of the millennium and continues to

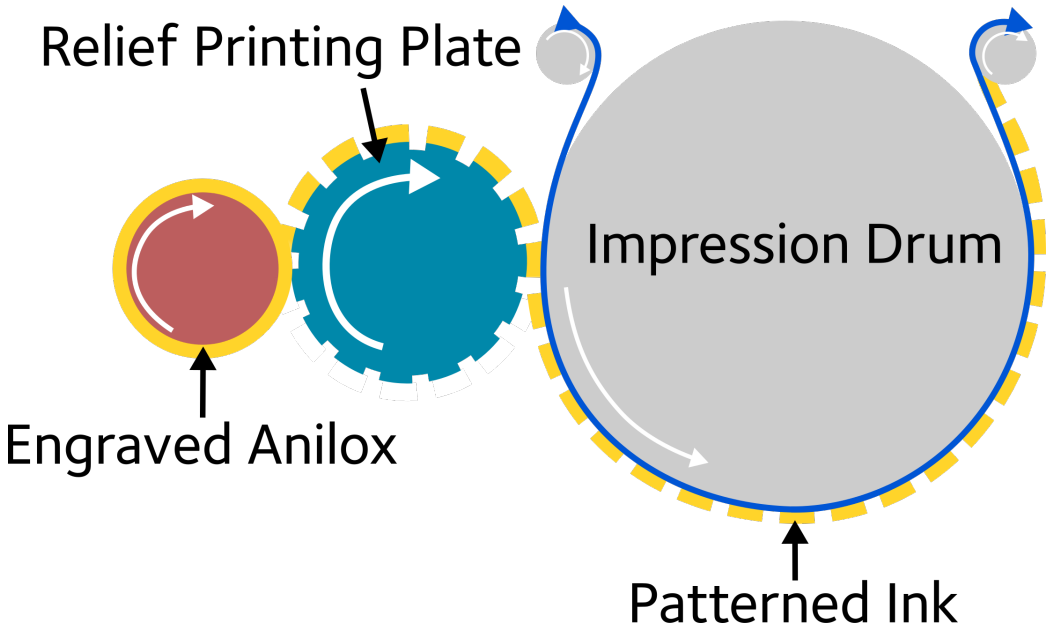


Figure 1.1: Schematic of a flexography printing set-up.

grow. However turning laboratory success into real world application is still a challenge. The sensitive chemistry of organics is also responsible for their wide processing windows and mechanical flexibility, opening up the possibility of the thin film devices to be made with roller based production methods. Patterning processes have been identified as a critical issue to overcome, for the commercial success of this field.[5] The problem of up-scaling sensitive lab processes and re-purposing existing industry techniques for these sensitive materials is a current interdisciplinary problem, with a need for a good understanding of materials compatibility.

1.2 Aims of thesis

This thesis aims to investigate the viability and compatibility for a metal patterning process, called selective metallisation, for printing of electrical source/drain contact on thin film transistors, as a proof of concept that the process can be used to create patterns for functional devices. The metallisation process involves printing an oil ink using flexography and this printing process is specifically considered, for its optimisation and viability limits. The metal patterning is used with aluminium, which is a new contact material for the OTFTs in question, and so the compatibility of this material is also investigated. Table 1.1 summarises the key viability and compatibility questions of this thesis.

Table 1.1: Research questions, that are addressed in this doctoral thesis, of the viability and compatibility of selective metallization with functional organic devices.

Viability	Compatibility
Could the process be used for patterning functional organic devices, and what process conditions make it viable?	Is the process compatible with functional organic devices and what considerations are specific to this process?
How does selective metallization compare to alternative techniques for creating conductive patterns, in terms of throughput, use of exotic and toxic chemicals, and the properties of the printed materials?	Does the process introduce damaging chemicals onto the functional organic or printing equipment? If so, what are the effects?
What are the limits on the the printing ability, in terms resolution and pattern defect concentration?	Is the functional organic exposed to damaging temperatures during the process?
Can the process be optimised, by changing the printing pressure and speed, to remove printing defects which would cause critical defects?	Can the patterned aluminium thin film achieve the necessary thickness, conductivity and surface roughness? How do these parameters interact with the processing conditions?
Has the process been scaled up? What were the compromises being made between careful experimental work and high volume industrial scale processes?	Can the pattered aluminium be used with existing OTFT organic semiconductor? What are the effects and optimal properties of a charge carrier injection layer?
Is in-vacuum flexography a viable way of patterning other materials?	Is the process compatible, more generally, with other organic functional devices?

1.3 Thesis Outline

This introduction has outlined the ways that this particular manufacturing process will be appraised and investigated scientifically, using the paradigm of viability and compatibility, to answer, by modelling, experiment, and data analysis, the questions outlined in Table 1.1. The next chapter addresses the current state of the art for functional organic fabrication processes and introduces the key requirements of viability of each process, and key compatibility considerations of functional organics, in particular OTFTs and conductive electrical contacts. This literature review moves on to a more focused review of approaches to understanding the mechanisms and factors of liquid transfer from one roller surface to another, and shows that there is still a lack of unified understanding joining together a large scale industrial empiricism to a more generalist modelling approach.

The subsequent Materials and Methods chapters, builds on this to present an experimental method which has been developed and necessary equipment that was custom built to address this knowledge void by mimicking flexography printing while faithfully recreating important factors in the modelling research.

After this the first discussion chapter introduces the selective metallization process in more detail and contrasts it with other metallization techniques. It goes on to show that the process is theoretically compatible with functional organic devices, in terms of processing temperature and chemical compatibility with the flexography printing tools. In doing so the material thermal mechanism, which is responsible for creating the metal pattern, is further described in terms of its thermal dependencies, adding to existing literature understanding. Using carbon nanotube stamps $sub - 10\mu m$ patterning is achieved, a first for this process. This, and other patterning results show that the printed liquid oil leads to the line edge roughness to the metal pattern, and that the metal pattern replicates the liquid oil pattern with high fidelity.

This finding is the basis of the following chapter, which looks to develop an understanding of the optimisation of the flexography printing process, in particular the optimum printing force and speed the create patterns with low edge roughness as the ink is transferred from the plate to the substrate. This central discussion chapter identifies the requirements for testing flexography printing and uses image analysis software that has been specially developed for analysis of the printed line patterns, as described in the Materials and Methods chapter. The parametric testing results show variation in the line edge roughness with printing force and changing behaviour with the printing speed and pattern dimensions. These are analysed, with a hierarchical

assessment of the various scale effects and time limitations to show agreement with other similar results in literature and are explained using the modelling trend results. In the end it shows that the print quality can be predicted with a model herein formularised. As the printing is performed at high print speeds and generally similar process variables to industrial flexography printing, the conclusions attempt to join together the practicable and theoretical understanding of flexography printing.

In the final discussion chapter the custom-built selective metallization process is applied to OTFTs and compared to control, batch shadow mask processed devices. The selective metallization process requires the electrical properties of aluminium, which has not been used before with these organic devices, to be shown to be compatible, and the introduction of this chapter explains the requirements of a charge carrier injection layer. The effects of this charge carrier injection layer are compared with control results, and the effects of varying its thickness and position are investigated and discussed. The successful creation of devices support the compatibility and the viability of the process. The differences in the characterised behaviours are explained and the patterning is used to extend the analysis into assessing the new aluminium contacts' contact resistance. Overall the process is shown the be compatible and viable with functional organics.

The chapter on further work that could be carried out highlights possible further investigations into the thermal modelling of the selective metallization process. Next, the optimisation of flexography printing could be further investigated, and the ways of doing this are described, to further support the theoretical description developed in this work. Alternate inks could also be used, and experimentation with functional organic inks is described briefly, showing the wide applicability of flexography printing. Other functional devices are put forward as candidates for beneficial employment of this selective metallization, and the wide applicability is further supported by present results of OLED devices that were fabricated in a collaborative exercise. The differences with control batch devices and the consideration needed to be made when using selective metallization are described.

Finally a conclusion summarises this doctoral thesis' findings, that have shown that selective metallization is a viable and compatible method of manufacturing functional organic devices.

1.4 References

[1] Inc. LPC. Benchmarking and Worldwide Market Trends for Flexographic Printing. Technical report, PRIMIR/NPES, 2010. http://www.npes.org/primirresearch/researchstudies/content.aspx?Topic=Benchmarking_and_Worldwide_Market_Trends_for_Flexographic_Printing.

[2] Helmut Kipphan, editor. *Handbook of print media: technologies and production methods*. Springer, Berlin ; New York, 2001.

[3] A. Tsumura, H. Koezuka, and T. Ando. Macromolecular electronic device: Field-effect transistor with a polythiophene thin film. *Appl. Phys. Lett.*, 49(18):1210–1212, November 1986.

[4] Hagen Klauk. Organic thin-film transistors. *Chemical Society Reviews*, 39(7):2643, 2010.

[5] OE-A. OE-A Roadmap for Organic and Printed Electronics Applications 2017. Roadmap, 2017.

Chapter 2

Literature Review

2.1 Flexible Technology Introduction

This literature review addresses literature on flexible technology and the patterning methods to make flexible devices. A wealth of research literature in this broad field has been motivated by functional applications, and the opportunity to capitalise on the low density, conformability and low-cost manufacturing possibilities of flexible electronics, compared to the existing rigid, silicon based, technologies. The possible functions can range from electronic logic circuits and sensors, to energy harvesting and light emitting devices. Flexible devices have applications that would have been impossible without direct contact with uneven or dynamic surfaces, two examples are displayed in Figure 2.1. The field for the applications also range widely from healthcare and vehicles, to wearables and internet of things (IOT). The expansion and improvement of possible applications of functional and flexible devices has introduced new reasons to solve material problems surrounding how they are made.

It is also a field that continues to grow and mature. The most recent IDTechEx market report estimates that the value of the flexible and organic electronics market will be worth $73bn by 2027.[1] The Organic and Printed Electronics Association (OE-A) predicts a 7% increase in sale revenue in 2018, with 87% of respondents expecting industry growth in a business climate survey.[2] Within scientific research, there has been significant investment from government and research agencies [3, 4, 5], as well as from competing private firms.[6, 7]. The number of scientific articles on flexible electronics has grown by over 450% in the last 20 years, with continued year-on-year growth according to Web of Science Clarivate Analytics. The possible economic impacts and consumer products have heralded popular interest as an exciting avenue of future technology.[8, 9]

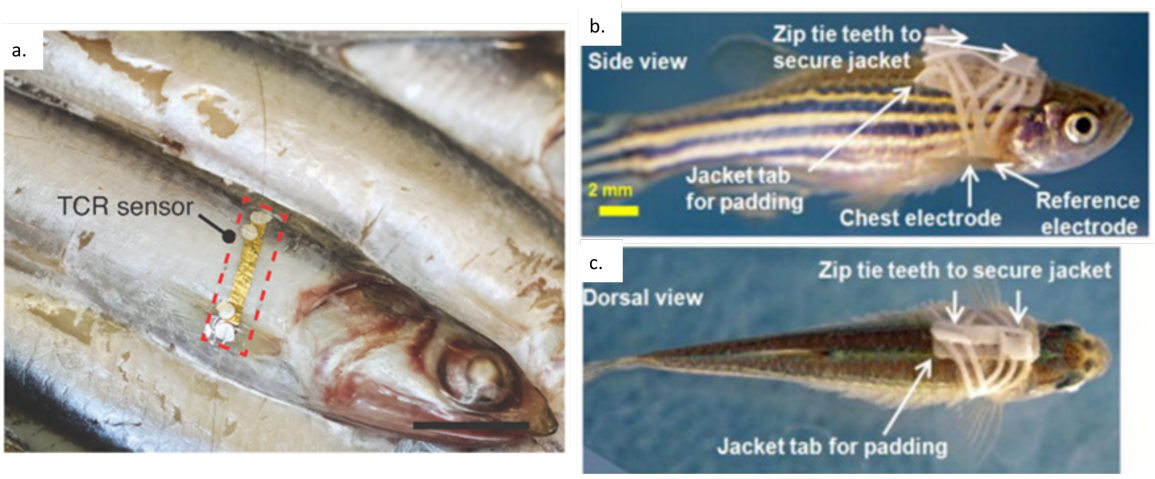


Figure 2.1: Examples of using flexible technology for new applications, from a) measuring the temperature of packaged fish to monitor food safety from reference [10] (creative commons license) to b) and c) live monitoring of the cardiac rhythms of a zebra fish for drugs research. Reprinted from reference [11] with permission © 2015 Elsevier. These two examples highlight the range of applications for conformable technology and how their are many more applications in the sea.

Although, this large, varied field can be depicted as grossly unfocussed and frailly dependent on some ever-on-the-horizon profitable product, the enthusiasm sparked for scientific investigation into material problems involved in both the functionality and the production of flexible electronics has developed a field with far-reaching generalisable findings. This review of the existing literature and state of the art presents some of these findings, as evidence that applied research can be advantageous beyond any final application.

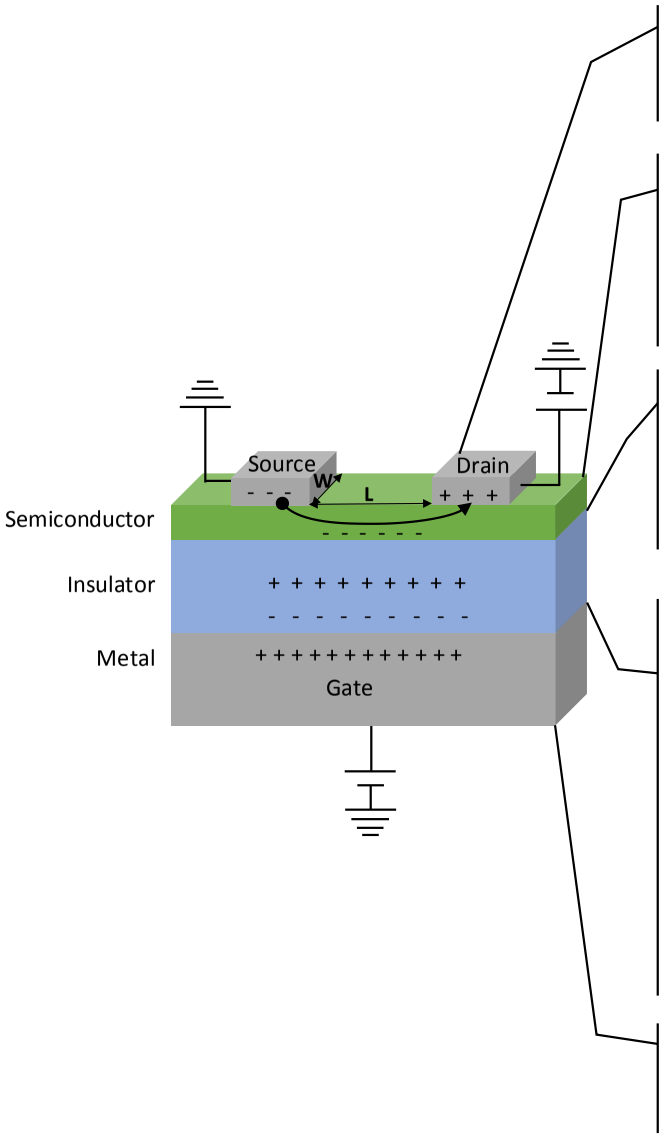
This review provides an introduction to the field of flexible electronics production, the recent advances and areas of interest in order to provide a context for this doctoral research. First, as an example organic functional device, organic transistor technology is introduced, demonstrating that device performance relies on viable high throughput production methods that are compatible with the material requirements. Hence, roll-to-roll (R2R) technology is described, which highlights the need for patterning systems that can build up the layered structures used in flexible technology. The main patterning technologies are then described, and compared based on their applicability to the high throughput manufacture of flexible electronics. This extends to more detailed reviews of low and high throughput techniques, as well as other non-conventional techniques. Subsequently, more in depth research relevant to flexography printing is discussed and the need for further is work addressed as a justification for the research endeavours presented in this doctoral thesis.

2.2 Fundamentals of Transistors and Material Requirements

A transistor is an on/off switch within a computer. It is an electrical current switch which is controlled by a second current and voltage. The switch both controls current flows and is initiated by a second current flow: a system of circular causation. By linking together the output current of the switches to the controlling input currents, transistors can be joined up to create logic circuits (AND, NOT, NOR, etc.). By combining many transistors (currently billions) together a computer can calculate quickly enough to be able to perform the functions which are required of technology today, such as graphical user interfaces, display back panes, and document processing. As a whole computer circuit can be compiled by adding transistors together in a particular manner, the transistor is the most basic building block of this computer logic and calculation system. Therefore, flexible transistor circuitry is only possible if you can create transistors that also work with a flexible substrate. Additionally, the multilayered thin film structure of transistors, and their electrical material requirements, are shared with other flexible device requirements. This make transistors good candidates for proof of concept device in the scientific investigations of fabricating and optimising flexible devices. This section goes into further detail on how flexible organic transistors are constructed, their material requirements, and how transistors are assessed for their computing efficiency.

2.2.1 Fundamentals of transistors

In a field effect transistor (FET) , see Figure 2.2, the movement of charge carriers, between two conductive contacts is controlled by a semiconducting material which will only conduct if it has enough majority carriers in mobile positions within the band structure. By applying a voltage across a gate electrode an electrical field is induced across a dielectric material. This electrical field promotes electrons, or holes, within the semiconductor into the lowest unoccupied molecular orbitals (LUMO), or the highest occupied molecular orbital (HOMO) bands, so the charge carrier becomes mobile. Thus, when there are sufficient charge carriers for current to move between a source electrode and a drain electrode, the transistor is 'on'. Reducing the voltage of the gate contact will revert the semiconductor to an insulating state, which will inhibit the movement of current from the source and drain i.e. the 'off state'. The physical phenomena of transistors, organic and inorganic, are covered in various text books.[12, 13, 14]



Source and Drain
Must be conductive with source drain gap as small as possible, ideally <1µm, for high switching speeds.
Need low contact resistances

Organic Semiconductors
High mobility
Polymer blends can improve process ability and interface mobility.
Typically semi-crystalline and close packing is beneficial. Need long conjugation length and correct growth modes.
Need high purity, low oxygen and water impurity concentration

Semiconductor/Dielectric Interface
Channel conductance depends on interface roughness, surface energy, and charges at the interface. Roughness (>10nm route mean square) disturbs pi-pi stacking of semiconductor and creates more grain boundaries. Can reduce trapped charges by annealing, otherwise can cause –ve drift in VT

Organic Dielectrics
Dielectric structure can determine semiconductor growth during deposition. Capacitance lowers voltage require for accumulation.
Can increase capacitance by increasing dielectric constant or making dielectric thinner. In rigid electronics silicon oxide is the typical dielectric material with a capacitance of 0.01uF and a dielectric constant of 3.9.
Organic dielectrics have comparable dielectric constants but 10^3 lower capacitance.
Organics have ionic and electronic polarization mechanisms, freq. $>10^{12}$Hz
Pinholes increase with decreasing thickness. Can use SAMs to get thinnest layers, ~100nm.
Thinner films can experience breakdown at lower voltages
Complete coverage of the gate to prevent leakage currents and pinholes.

Gate
Smooth interface for the other layers to be deposited onto and must be conductive.

Figure 2.2: Schematic of a bottom gate top contact transistor. This image also highlights the key materials requirements for good transistor behaviour.

The transferred effect of the dielectric's electric field on the semiconductor depends on: the semiconductor's work function (energy to remove a charge carrier from the fermi-level position): the band gap relative to the source and drain; and on the applied gate voltage potential, where the source electrode is taken as zero potential. Organic (low mobility semiconductor) thin film transistors (OTFT) operate under the accumulation/depletion regimes where mobile charge carriers are created at the semiconductor/dielectric interface due to the electric field's attraction/repulsion of electrons in the semiconductor. In the accumulation regime, the drain current, i.e. the resulting current out of the switch, is proportional to the gate voltage until the voltage of the drain is the similar to the gate voltage, known as 'pinch off'. After this point the transistor is operating in the saturation regime, where the current between the source and drain is most stable and is independent of the gate voltage.

The drain current (I_D) is fundamentally defined as:

$$I_D = \frac{Q.WL}{t} \tag{2.1}$$

where Q is the charge per unit area due to the depletion/accumulation of holes or electrons across the channel area, which has dimensions of W and L, see Figure 2.2; t is the time taken for the charge to move from source to drain. This basic definition can be expanded to include the mobility (μ):

$$\mu = \frac{v}{E} = \frac{vL}{V_D} = \frac{L^2}{tV_{SD}} \tag{2.2}$$

where $v = \frac{L}{t}$ is the charge carrier's constant speed at a perfect semiconductor/dielectric interface due to the electric field E induced in the dielectric by by the gate between the source and drain, and V_{SD} is the voltage difference between the source and drain. The areal charge, Q in Equation 2.1, can be described in terms of the capacitance of the dielectric, C, for a given gate voltage: V_G:

$$Q = C(V_G - V_T) \tag{2.3}$$

where V_T is the threshold voltage bias for flat band energy alignment. Combining these definitions of the current flow and assuming that there is a saturation of charge carriers , i.e. $V_G \approx V_D \gg V_T$, leads to:

$$I_D = \frac{W}{2L} C\mu(V_G - V_T)^2 \tag{2.4}$$

2.2.2 OTFT key parameters

Equation 2.4 dictates the parameters required for good transistors: having rapid switching from one state to the other while requiring little energy for maximum drain current. The mobility of an OTFT should be as high as possible, typically in the order of $0.1 - 10cm^2.V^{-1}.s^{-1}$ for a good semiconductor. The capacitance of the dielectric layer must be high which requires a high dielectric material that is also very thin. High mobility and dielectric capacitance will mean a lower gate voltage is required to create the charge carrier accumulation/depletion in the channel, providing conductance from the source to the drain, in the semiconducting layer. This gate voltage is the threshold voltage, V_T in Equation 2.4, and describes the energy required for the transistor to work. It is optimally a few volts. The threshold voltage can be extrapolated from the transfer characteristics of the transistor, see Figure 2.3.

Furthermore, the amount of energy required to switch the transistor from 'on' to 'off', or vice versa, is characterised by the sub-threshold swing, see Figure 2.3, and values less than $100mV.dec^{-1}$ are desirable. A final metric is the on/off ratio, which is the ratio of the drain current when the device is on to when the device is considered off. As the drain current is dependent on the applied voltages, Equation 2.4, these must also be quoted to qualify the on/off ratio, which is optimally $10^6 - 10^8$ meaning a large difference in signal strength for an on and and off current.

These parameters are discussed elsewhere in further detail.[12, 13, 14] Optimal transistors will have low contact resistances, allowing the charge to be extracted from the semiconductor into the contacts. The small molecule organic semiconductor and its interface with the dielectric layer will provide a good transport channel for the charge carriers, while ensuring there is no leakage current from the gate through the dielectric layer, see Figure 2.2. In addition to this, the performance can be improved by making the device small. Shrinking the distance the charges have to move at the semiconductor/dielectric interface has driven transistor advancement because it means the switching ability is improved (see Equation 2.2 to see the square increase in mobility). This highlights that the science of creating a transistor and of patterning the material layers, crucially relates directly to the transistor performance and efficiency.

Organic semiconductors also have challenges. Their electrical properties can be unstable when exposed to oxygen and moisture.[**?**] Another challenge for low conductivity organic semiconductors is the large contact resistance with associated with organic-metal junctions. [13] This scales inversely with voltage, so small turn on

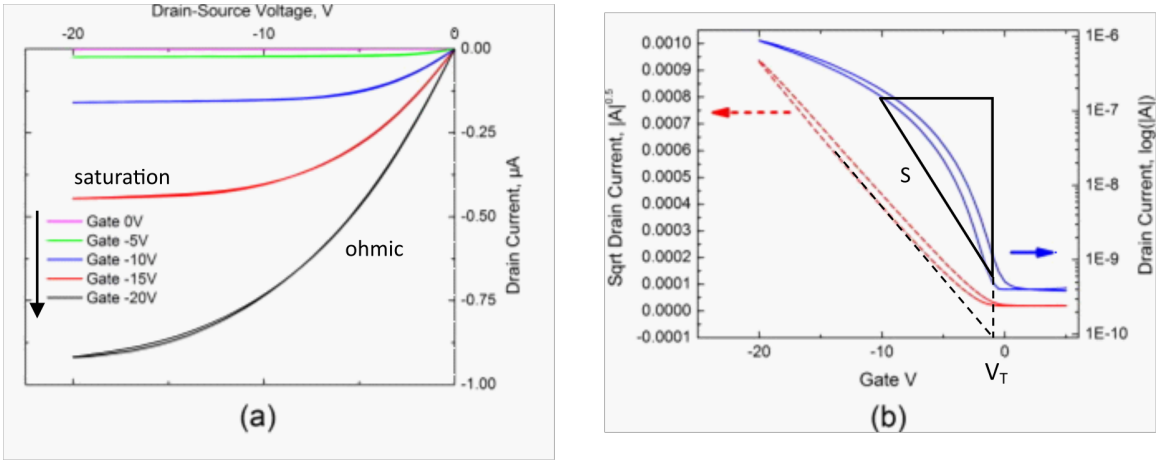


Figure 2.3: The thin film transistor parameters of a gravure printed top gate transistor. a) shows the output curves with the ohmic and accumulation regions highlighted. b) shows the transfer characteristics measured at -20V drain voltage. The threshold voltage (V_T) is extrapolated from the gradient of gate voltage against square root of source-drain current and at the gate voltage for which the drain current (on a log scale) ceases to be exponential. Furthermore the sub-threshold swing ($S = \frac{\partial \log I_d}{\partial V_G}$) is displayed to be calculated from the gradient of the log transfer curve above the threshold voltage and below the onset voltage, which is taken as 10V from the output curves. Edited from reference [15] with permission © 2015 Elsevier B.V.

voltages, which are energetically favourable, have the most losses due to contact resistance. These challenges are discussed, and also addressed with experimental results, in more detail in the final discussion chapter of this doctoral thesis, see Chapter 6. These challenges also limit the application of OTFTs to academic and a few novel applications such as sensors and back panes for commercial concept display technology (e.g. Flexenable - www.exenable.com/technology)

2.3 Patterning for Flexible Devices

2.3.1 Outline

In the latest OE-A report, processing and resolution are identified as a 'red brick wall' for the industry, for which 'major breakthroughs' are still needed.[16] In the previous report, flexography was highlighted as a viable process technology amongst the gamut available, see Figure 2.4. Lately, inkjet has risen on the wave of the research successes, with screen printing often holding the best device properties achievable, predominantly due to the thickness of the patterned material that can be deposited. These trends are focussed on solution-based functional inks. Throughout the OE-A

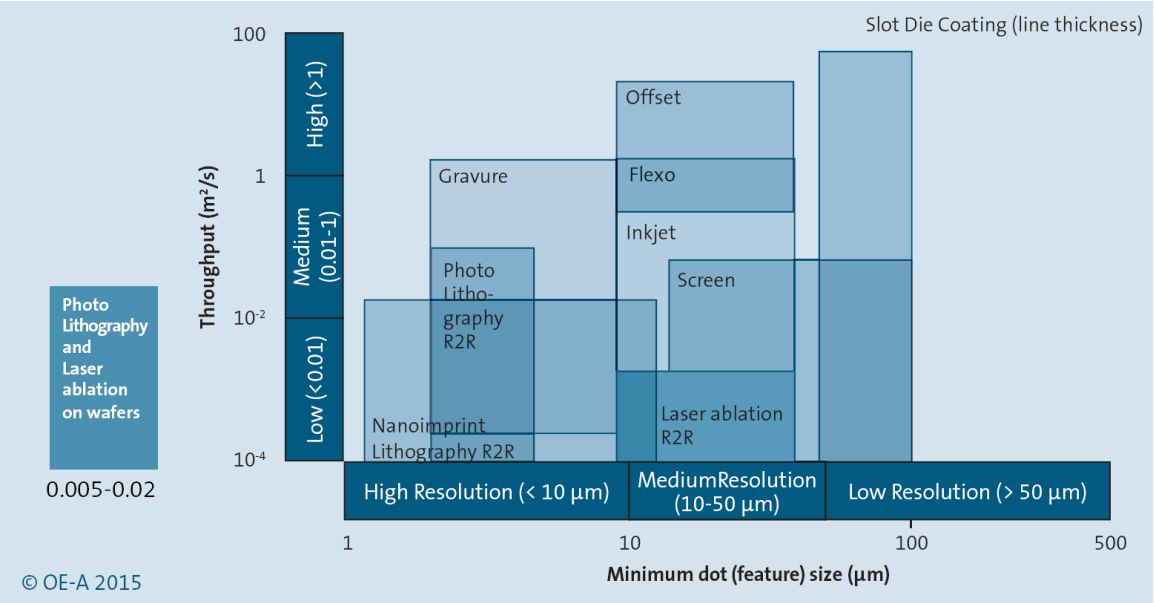


Figure 2.4: The summary of printing process from the 2015 Road Map of the OE-A. The latest report continues to highlight the importance of patterning processes.[18]

report, and the affiliate member profiles, there is a trend towards scalability (another red brick wall); that is to say there is a general desire for higher throughput manufacturing processes. Given the flexibility of the substrates and adoption of existing printing methods used with organic printed electronics, there is a natural reliance on R2R processing. However, other substrate handling methods, like roll-to-sheet, sheet-to-sheet and sheets-on-shuttle, can be preferential with particular substrate variety and registration requirement.[17] As the market matures the importance of creating reliable, cost-effective and sustainable processes continues to grow, particularly for continuous fabrication methods like R2R.

This section of the review begins by setting up the categorisation of patterning methods based on R2R compatibility. Then some of the key patterning methods, photolithography, soft stamp printing, gravure and flexography printing, are described in more detail, with relevant applications to flexible technology, including OTFTs and metal contacts, highlighted.

2.3.2 Roll-to-roll compatibility

As highlighted above R2R, production is highly advantageous for the mass production of electronics. To use R2R methods, the pattern depositing technique must be designed with the high throughput roller based system. Proven laboratory techniques leading to good material and device properties often cannot be transported across

to a R2R web coater. This review explains to show the trends within the various patterning techniques, their commonalities in mechanisms, and differences in applications and results. This will highlight the range of throughput, patterning control, and patterning ability, with a few techniques described in detail, finally suggesting possible developments that could be made in patterning of OTFTs and their metal contacts.

The research field of patterning electronics has been active almost as along as organic electronics have been chemically viable, although only in the last decade or so has the importance of matching chemical properties with patterning material requirements been the focus.[19, 20] Moreover, as many of the patterning techniques are borrowed from graphics and other fields, the wealth of literature is disparate and nomenclature often confused. Table 2.1 summarises the family of patterning techniques most widely covered. Many of these techniques are highly diversified. For example soft lithography has many variants with many different abbreviations, but Table 2.1 simply provides a summary of the key techniques.

A few trends are shown in Table 2.1. First, as the resolution increases fewer of the techniques are compatible with continuous R2R technology and extremely high resolution techniques are not scaleable. This trade-off is one that must be minimised if large area electronics are to become as cost-effective as possible. Moreover, in general, subtractive processes tend to have higher resolution, although some additive techniques are not ruled out of high resolution patterning, exemplified by photolithography in Table 2.1.

The review by Kahn, on this subject, was particularly pertinent as it organised the patterning techniques based on their physical deposition methods.[29] Work by Søndergaard, Hösel and Krebs, which gave an overview of some of the typical industrial film patterning techniques, has also been influential.[22] They highlighted that vacuum free R2R is the "final goal" for organic electronics based on solution processing. Environmental R2R would definitely be a great solution to the mass manufacture of large area electronics, and is quite possible in the case of photovoltaics, which these authors have mainly focused on [31, 40, 41].

However, the possibility of intricate patterning combined with the direct deposition of the material layers (leading to superior material qualities) would be an equally high goal for organic electronics. The research on ambient printing systems can be applied to vacuum processing, often with increased simplicity. The next sections give a description of some of the main patterning techniques and critiques their compatibility and viability with organic electronics, as seen in the literature. Finally, the

Table 2.1: Summary of the main patterning techniques found in the literature. Techniques are categorised as continuous (R2R) techniques or B for batch techniques patterning.

Patterning Technique	Throughput type	Lateral Resolution (µm)	Thickness Resolution (µm)	Throughput (m^2/sec)	Remarks
Intaglio letter press	B	>1000	-	-	
Slot & Die	R2R	>1000	>0.1 [21]	0.1-200 [22]	Coating technique, lateral resolution in the order of centimetres.
Gravure	R2R	5-50 [23, 24]	1-8 [25]	~100 [26]	Line spacings can be down to 2µm.[26]
Flexography	R2R	50-100 [27, 28]	0.1-5	10 [29]	<20µm lateral resolution can be achieved.[30]
Screen printing	B	10s [31]	100-500 [31]	-	Can be continuous with rotary screen printing.
Inkjet	B	1 [32]	>0.1 [33]	-	10's µm lateral resolution without ink spreading suppressed.[20]
Aerosol Jet/Spray Lithography	B	10 [34]	-	-	Can be used with many material liquids <5 Pa.s[29]
Offset Lithography	R2R	10-50 [29]	<2.5 [29]	20 [29]	Requires complex and high viscosities.
Organic Vapour Phase Jet (OVPJ)	B	1 [35]	-	-	Thickness depends on deposition rate (a few Å$cm^{-2}s^{-1}$). Low resolutions require a mask.
Soft lithography	B	0.1 [36]	Monolayer	-	Using SAM's. Potential sub micrometer.
Laser induced forward transfer (LIFT)	B	5 [37]	<1	0.0016	
Photolithography	B	0.01 [38]	<1	-	Can be R2R compatible.[39]

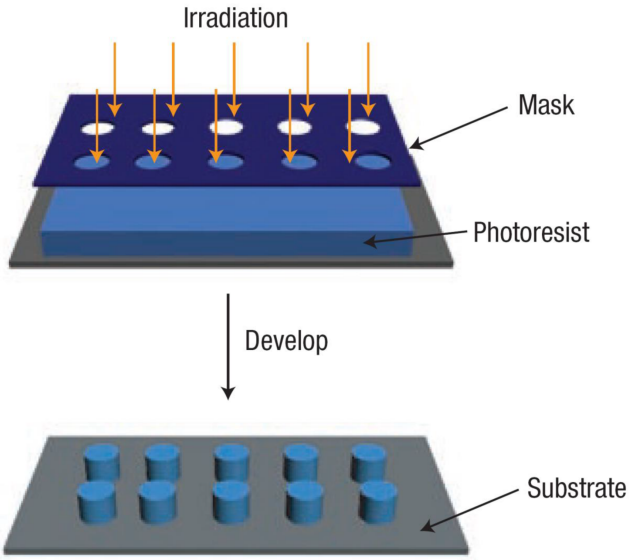


Figure 2.5: The principle of photolithography. Used with permission from reference 1. Nie Z, Kumacheva E. Patterning surfaces with functional polymers. Nat Mater. 2008 Apr;7(4):277–90. © 2008 Nature Publish Group.

patterning methods are compared according to the metrics of patterning ability, productivity and control. A more thorough review of flexography printing follows, which is the focus of this thesis.

2.3.3 Photolithography

Photolithography has been the predominant method of transistor production since the 1960s.[42] This top down technique uses electromagnetic rays to photo-cure or de-polymerise a resist material layer by using a mask to pattern the irradiated areas, see Figure 2.5. The unwanted material is then removed and, with conventional photolithography, etching or deposition forms the desired pattern on the substrate. Having been the standard production technique for rigid technology for so long it is now well developed and understood. Its longevity is owed to the patterning resolution (R) only being limited by the Rayleigh diffraction limit:

$$R = \frac{k\lambda}{n \sin \sigma} \tag{2.5}$$

where k is a system constant (a.k.a. Raleigh coefficient of resolution), $n \sin \sigma$ the numerical aperture and λ the irradiating wavelength. By reducing the wavelength,

using extreme UV, and using immersion techniques to optimise the system constant and the numerical aperture, the resolved patterns can have feature sizes down to the $10nm$ range with rigid silicon based transistors.[43] For flexible substrate electronics optical lithography has been focussed on larger lengths scales, typically micron or half micrometer.[44, 45] These flexible photolithography methods often use temporary rigid supports with varying flexible substrate materials and removal methods.[46] R2R photolithography is possible using stepper technology to move the web a controlled distance at a time. However, this means that the thin film coating, irradiating and development must be performed at separate, non-continuous stages.[39]

Photolithography's advantages in patterning resolution are met by the expensive requirements of clean rooms and low wavelength light sources. For patterning flexible substrates, this technique has too small a tolerance for non-planar surfaces, and given the many steps required to create a pattern, it is unlikely to be incorporated in continuous manufacturing systems, although it has seen success in the organic light emitting diodes (OLED) manufacturing which use fixed flexible display layers.[47]

2.3.4 Soft stamp printing

Using a soft stamp to create material structures on a substrate has many different forms, both additive and subtractive, but is usually referred to as soft lithography which, as shown in Table 2.1, can have very high resolutions approaching those of optical lithographic techniques. Though not digital, like inkjet printing, once the master mold has been made, the casting and curing of the poly-dimethyl siloxane (PDMS) stamp is a very quick process and the stamps can be used multiple times [48], although longer use degradation has been reported.[49] There are several guises in the literature: micro-contact printing (μCP), micro-transfer printing(μTP), replica moulding (REM), micro-transfer moulding (μTM), and micro-moulding in capillaries (MIMIC) each having associated variants and nano dimensional cousins. This section focusses on μCP to show how the mechanics of this low throughput technique can be applied to high throughput process.

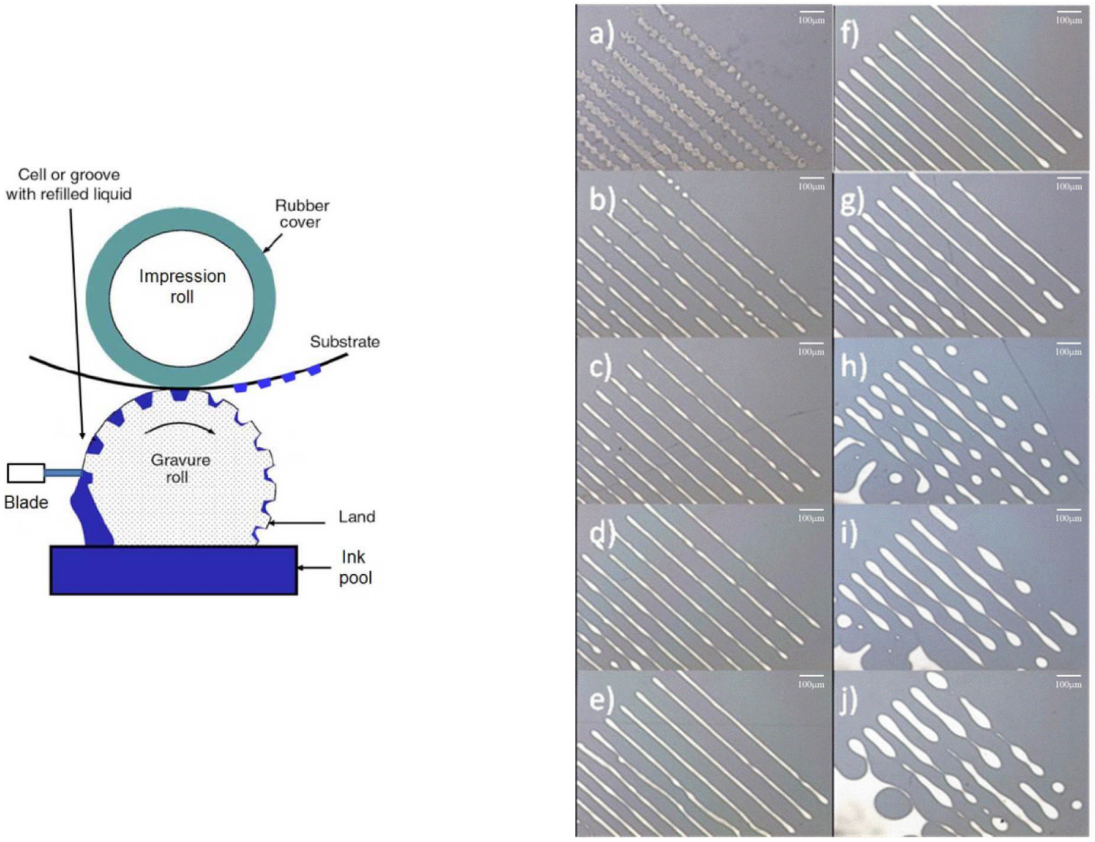
The mechanism for soft stamp printing is simple, relying on surface energies to create adhesion between a relief pattern on the stamp and the inking material. The patterned material is transferred to the substrate when the inked stamp comes into conformal contact with it, if the surface energies satisfy[50]:

$$E^{Ink/Stamp} < E^{Ink/Sub} \tag{2.6}$$

where E^x is the interfacial binding energy ($\mathrm{J}m^{-2}$) as defined by the Young-Dupré equation, and the indices (x) correspond to the ink, stamp, or substrate (Sub) interfaces. To aid this energetic requirement the PDMS stamp can be plasma treated [51] or self assembled monolayers (SAMs) with hydrophobic/phillic tendencies are used. SAMs have been well researched for application on TFTs and OLEDs [52], including, metal contacts.[53] SAMs are also used in multi-step deposition to alter the substrate's surface energy and wetting properties to pattern subsequent material deposition.[54] It is therefore notable that the high resolution of μCP is due to both the physical dimensions of the mask and the chemical potential of the deposited material.

Soft lithography is a developed technique, although it has little presence in the manufacture of commercial flexible devices, despite research with companies like IBM.[55] Silicone, specifically poly-dimethyl siloxane (PDMS), is almost always the elastomeric stamping material of choice due to its inertness, ease of casting and durability.[48] One crucial technical limitation is the relief pattern aspect ratio. It must not be less than 0.2 to prevent a sagging of the non-relief section and not above 2 if the relief pattern is to remain stable at the micrometer scale.[48, 56] This has been investigated further since, by Petrzelka and Hardt, who considered various modes of deformation for PDMS features.[57] Moreover, there is a shrinkage of 1% from the master as the PDMS cures.[48] As soft lithography is a transfer technique, the mask can not be changed or altered without changing the master, which often has to be created with expensive lithography techniques. This downside of analogue methods, and the elasticity inherent in the stamp, also means that registration is difficult to control.[48]

Finally, as a planar ink and stamp technique, it is not very high throughput, nor is it R2R compatible. However research has been conducted on using a roller based μCP with SAM's.[58] This lifting from the planar to cylindrical form means the patterning technique become easier to integrate into a R2R system. Similarly in the gravure field patterned rollers have been fabricated from planar silicon using a polymer cast to create the cylindrical metal print head.[26] The next sections investigate these roller, based patterning techniques that have higher throughput.



a. b.

Figure 2.6: a. Gravure process schematic showing the key elements. b. change in print quality of conductive ink lines with cell spacing decreasing from (i) to (x) in $2.5\mu m$ steps from $42.5\mu m$ to $20\mu m$, with $30\mu m$ cells having a $14pL$ volume. When cells spacing is too far apart isolated ink transfer occurs, too close and scalloped lines (to the point of discontinuity) occur, at the optimum spacing continuous lines are formed by ink spreading on the substrate. a. From [59] © 2010 IEEE. b. From [60] © 2009] IEEE

2.3.5 Gravure printing

In this intaglio-like process, a cylinder engraved with the desired pattern of micro cavities collects ink from a bath and the excess is removed using a blade, leaving the recessed cavities filled with ink. The cylinder is then pressed against the substrate which is supported by a cushioned drum to aid conformation at the nip of the gravure cylinder and the substrate, see Figure 2.6. The transfer process has two steps according to Sung, de la Fuente Vornbrock, and Subramanian: ink emptying and ink spreading.[61] Grau et al.'s review [62] highlights that each step of the gravure ink transfer process is highly dependent on the capillary number (Ca) of the fluid ink, which is the ratio of the viscous forces to surface tension forces:

$$Ca = \frac{\mu U}{\sigma} \tag{2.7}$$

where μ is the viscosity, U the printing speed, and σ the surface energy.[63]

Emptying a cavity (or 'cell') is driven by a reduction of surface energy and so is affected by the cavity's shape and dimensions; shallower, larger cavities have a lower surface area to volume ratio, so empty more readily than deep, small-based cells [64], although this depends on the shape and pattern of the cavities[65]. Furthermore, the relative surface energy of the substrate must be considered.[61]

The amount of ink that transfers from the cavity onto the substrate during contact also depends on:

- the print speed and ink viscosity [66];
- how completely each cavity is filled with ink;
- the conformal contact and pressure at the roller contact.[64]

As a result of these interplaying factors, low viscosity ($0.05 - 0.2Pa.s$) is typical for gravure printing) inks empty more completely than high viscosity, shear resistant materials. However, higher viscosity inks can control the substrate spreading process that is driven by the minimisation of inter-facial energy and due to the inertia of this high throughput process.[61]

All this depends on the ink material and substrate surface energies within the patterning environment as well as the intended pattern. For instance, to print continuous lines of a conductive ink, the distance between cavities is reduced so that each dot of printed material spreads into the contiguous dots, see Figure 2.6b.[67, 60] This leads to uniform printed lines if the cavities are correctly spaced for the volume of ink

transferred, as has already been explored with inkjet printing.[68, 69] This highlights how patterning techniques can share theoretical concepts of underlying mechanisms.

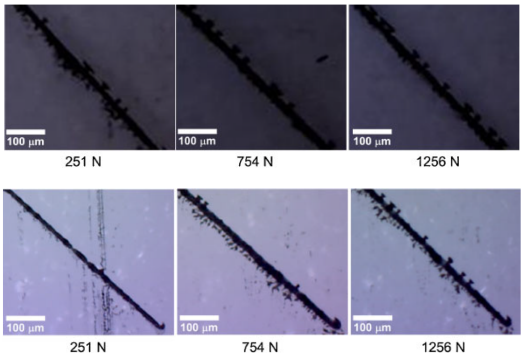
Gravure can achieve quite high resolutions, see Table 2.1. The prevalence of gravure in the high quality print media industry has yet to be mirrored in the flexible electronics world. This could be due to the large upfront costs of engraving the gravure cylinders. It is not a digital technique, as the gravure pattern is set in the metal, or ceramic, gravure roller. The hardness of these rollers also poses a risk of partial patterning if the surface is not smooth, or worse, of damaging the existing uneven micro-structure. The scaling of gravure depends on the amount of liquid dragged out of the cavity by the blade, which is a function of the blades wettability, not the capillary number. This poses a challenge for low volume cavities, where inevitable drag-out will impede scaling to smaller printed features.[67]

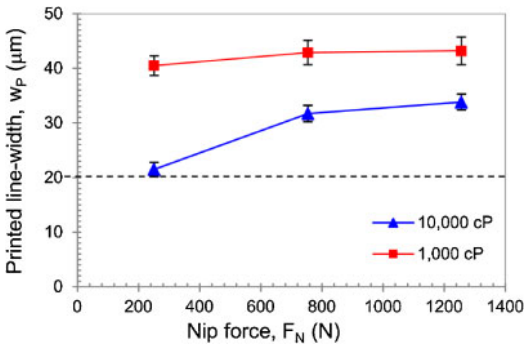
High printing pressure ($1.5 - 5MPa$) also poses a similar risk to the viability of gravure for printing on multilayered flexible electronics. Pressure on the contact region is typically set by the printing speed and ink viscosity. Nguyen et al. investigated the printing pressure further, modelling that printing pressure can lead to substrate deformation in the order of cell dimensions (microns).[70] The increase of the printed line width with pressure and ink viscosity, see Figure 2.7, was predicted using a fluid mechanical model, based on Navier-Stokes equation. The authors acknowledged the key assumption that ink spreading only occurred during contact, which is a concept developed later in the review. Although the work was highly analytical of substrate deformation, it did not deal with the resultant print quality effects on the functional properties of the printed conductive silver ink.

With respect to patterning OTFTs it has been noted that the semiconductor charge transport can be altered by changing the cavity size/density and the print direction (relative to the OTFT structure).[15] This is corroborated by research showing a seven-fold increase in mobility of an oriented polymer depending on the transfer roll direction and nearly a three-fold mobility increase on the spin coated control when a 30^{0} roll angle was used.[71] These are exciting observations as they show increased device performance and high throughput patterning can work in tandem, if the correct patterning and materials science is used.

2.3.6 Flexography Printing

Flexography is another roller based patterning system that is generally considered to have better consistency and edge smoothness than gravure deposited pattens.[73, 74, 27] It is not an intaglio printing technique but has its origins with the letter press,





a. b.

Figure 2.7: Variation of printed line width with force applied to the contact region (nip) in gravure printing of silver conductive pastes of varying viscosities. a. microscopy image of the printed patterns. b. graph of data obtained from images using 5 different samples. From [70] Copyright (2014) The Japan Society of Applied Physics.

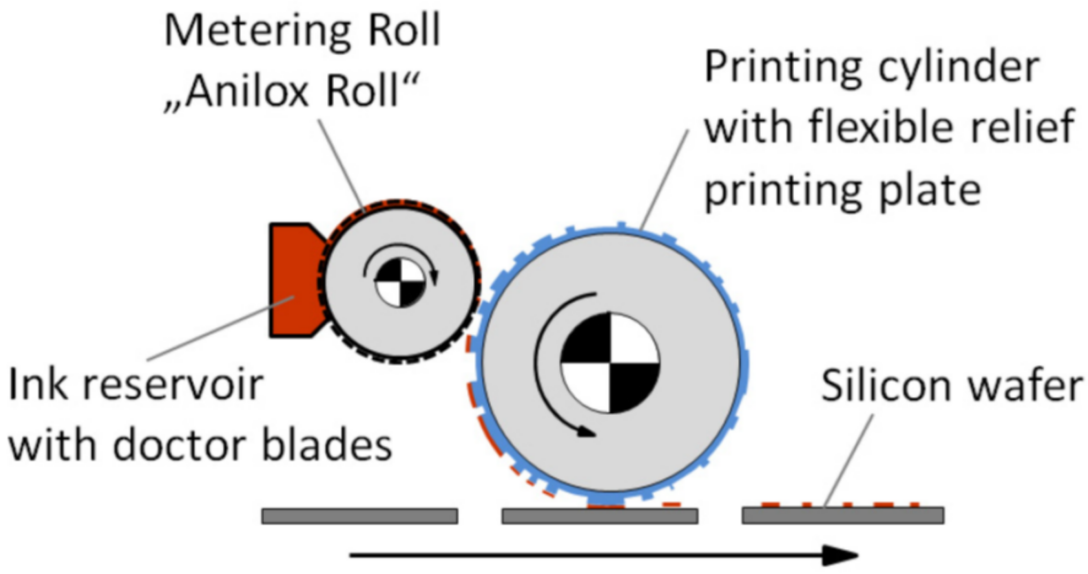


Figure 2.8: Flexography schematic, with a chambered doctor blade which prevents solvent evaporation under atmospheric conditions, and onto a plate and not another roller, though the principles are similar. From [72] reproduced under Creative Commons.

since the inking material sits on the raised relief pattern of the flexographic print roller.[75] The ink is transferred when it comes into contact with the substrate, see Figure 2.8. The similarities with soft stamp printing, section 2.3.4, are obvious, and the mechanical descriptions can be borrowed, although flexographic printing only uses liquid ink.

The inking of the flexographic printing plate is performed by the anilox roller. Akin to gravure, this roller has small densely packed cavities that are filled by an ink bath and then are emptied onto the raised flexographic relief pattern. The anilox system is important, as it can control the deposited thickness, without changing the patterning plate.[75] In industry patterning plates are easily interchanged and cheap, so although not digital, it does offer more pattern control and changeability than gravure.

It is not as fast as gravure printing but it is still has a high enough throughput to see growth in the graphics industry.[75] This is partly due to the use of the flexible and soft patterning plate, which allows the pattern to be deposited on uneven non-planar surfaces (such as cardboards), also an advantage with multi-layered flexible electronics. It is more commercially successful than other techniques described here, achieving some commercial success in the printed electronics industry.[76] There have been patents for transparent conductive grids that use flexographic printing.[77, 78] High volume flexographic printing has also been demonstrated with $100m$ long photovoltaics.[79]

Though used on the very first high throughput manufactured integrated circuits[80], flexography applied to OTFTs has been more sparse than other patterning techniques described. This might be due, in part, to the low film uniformity often associated with flexographic printing.[81] Thickness uniformity is less important for the source and drain with top contact transistors. Jo et al. tookFlexography schematic, with a chambered doctor blade which prevents solvent evaporation under atmospheric conditions, and onto a plate and not another roller, though the principles are similar advantage of this, achieving small source drain gaps (16μm) using flexography directly applied to flexible substrates.[82]

Flexography and gravure have been compared and contrasted in the literature. A paper published in Nature described the use of gravure and flexography used with an n-type semiconductor.[83] Although there was obvious film morphology from the printing plate, the top gate bottom contact device characteristics were acceptable, though not as good as gravure deposited devices. The OTFTs fabricated by Schmidt et al. used flexography to modify the substrate surface energy before a gravure system

deposited the electrodes, to achieve a 10μm source drain gap.[84] This was an excellent investigation showing that combined processes can lead to exemplary results.

Scientific research has shown that, like soft lithography, very low resolutions can be reached. Kwak et al. describe forming 20μm resolution by using a μCP or μTP technique to ink a PDMS mould. This work built on ideas from nano particle fabrication[85] to achieve de-wetting of the ink to the edges of the mould using 'mould confinement'.[30] This technique used a conductive ink with low viscosity and had to be repeated six times to increase the pattern thickness, which reduced the resistivity. Researchers from Massachusetts Institute of Technology have also reported nano porous flexography based on carbon nano tubes.[86] This work achieved $3\mu m$ linewidth honeycomb structures at a printing speed of $0.2m.s^{-1}$. This is slow compared with graphics printing (which can operate above $1.67m.s^{-1}$or $100m.min^{-1}$) but it is still a continuous process with very high printing resolution.

In general, it should be noted that flexography used the graphics industry has a low resolution, see Table 2.1, due to the soft plate which easily deforms under the printing pressure, as well as the liquid not being laterally contained, as in gravure printing. In this situation, printing speed and pressure, as well as the fluid behaviour of the ink with the contact region, become very important for achieving high patterning quality. This is discussed in the following sections, which focusses on flexography printing and its mechanisms in more detail.

2.3.7 Summary of patterning techniques

The preceding sections have described some key patterning techniques in detail and given examples of how the patterning techniques have been used to fabricate functional devices. A summary of the particular characteristics of the techniques is shown in Figure 2.9. Each has its strengths and weaknesses. This review has also shown that to create more ideal patterning techniques, the mechanisms from different patterning techniques must be combined and improved upon. Finally, the detail of the mechanisms involved in the patterning process are important for the final material properties of the fabricated thin films.

2.4 Flexography Printing

This section of the literature review focusses on literature relevant to the printing process of flexography. To set the context for this doctoral thesis, the historical origins and research into the physical mechanisms that control the printed quality are

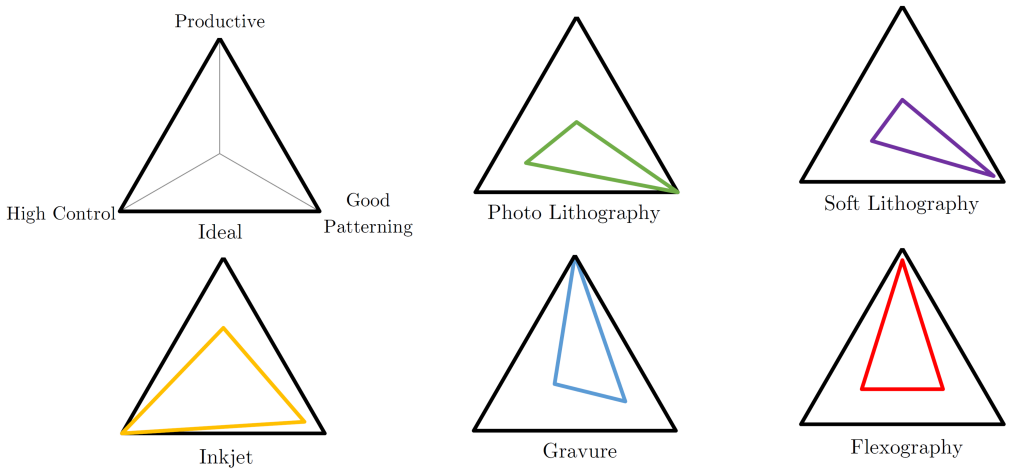


Figure 2.9: Spider diagram qualitatively comparing photolithography, inkjet, soft lithography, gravure and flexography with the theoretical ideal in the author's informed opinion. Productive patterning process have high throughput and yield, good patterning infers high resolution, uniformity and desired material properties, and control is a measure of how easily it is to create intricate patterns and alter the deposited pattern (i.e. is it digital or analogue). Designed as a literature trend guide it shows that combining elements of the techniques offers a way to get closer to the ideal. Also that achieving high control, for example with inkjet, can be at the cost of other parameters.

presented and critiqued. This is to build a case for the research presented and to highlight the relevance and requirement for this additional research into the field. First, the historical origins of the flexography printing press are presented. Subsequently modern scientific research on flexography printing is introduced. Attention is paid to research that has been applied to large scale and commercially oriented testing, as well as applied to functional devices and related problems. Following this, studies of the more abstract modelling and mathematical treatment of the ink transfer mechanisms, which create the printed pattern, are described and criticised for their applicability to real world printing systems. Together these applied and theoretical studies provide important insights into the nature of flexography printing. This section concludes with the need for complimentary scientific research to understand and improve flexography printing for functional devices further.

2.4.1 Foundations of flexography

The origin of flexography lies in the materials development of the rubber printing plate and quick drying inks, along with the development of the rotary printing press. This section describes some of the key technological advances that have contributed to the modern flexography printing press. Some developments were scientific, others were commercial or regulatory, but the commonality is the motivation to create a profitable printing process with ever better printing quality.

The rotary press has existed in Europe since the 18th century.[87] However, the first industrial steam-powered printing press was produced by Keonig and Bauer in 1814.[88] The vulcanisation of caoutchouc[89] (a.k.a. natural 'rubber' as coined by Joseph Priestly) by Charles Goodyear in 1844 introduced a new waterproof and durable material into the industrial revolution. The first patent to bring together the advances in rotary press and the new polymeric rubber materials was in 1853. [90] However it was not until 1890 that Bibby, Baron & Sons created the first known printing process with a rotary rubber stamp for their paper bag manufacturing process, although their water based inks were prone to smearing.[91]

Beyond this effort, there was more successful mechanical printing in Europe in the early 20th century using the rubber printing plates with aniline inks, which was based on improvements in the synthetic dye production methods, like the Béchamp reduction.[92] These inks created more brilliant colours, printed on a variety of substrates beyond flat paper, like corrugated board and paper bags. This printing method was also called gummidruck (German for 'rubber-print') and continued to grow in Europe and the United States in the graphical printing industry, particularly during

austere war years, as rubber plates were cheaper to fabricate and a quicker way to produce blocks of colour. Inventiveness with gummidruck, or aniline printing, only grew with this versatile, albeit unreliable, printing technique. Improvements were made in the drying processes, plate making and registration, as well as the following three key developments through the 20th century.

2.4.1.1 New plate materials

First, the vulcanized rubber plates were replaced by synthetic rubber, first developed in Russia, where a viable industrial process was invented to synthetically polymerise butadiene rubbers from ethanol derived from grains and potatoes instead of rubber trees.[93] The new material did not swell with oil based inks and became cheaper and more reliable than naturally derived alternatives.

2.4.1.2 New substrate materials

Next, non-absorbent and transparent substrates, like cellophane by DuPont, were introduced, challenging the ink makers create more opaque inks based on TiO_2 with alcohol as a solvent. The growth in food packaging and adhesive labels created a greater market for printing.

2.4.1.3 Improved ink metering methods

Lastly, in 1941, the Interchemical Corporation's International Printing Ink division filed for a patent describing the anilox roller that metered the amount of ink applied to the printing plate, but never completed the patent process, so the idea was publicly disclosed but remained protected. Based on the idea of gravure rollers (mechanically engraved metal cylinders), tiny pits across the entire surface held the miniscule amount of ink well enough to be transferred to the printing plate in the appropriate volume to avoid smearing and for opaque printing. All these changes removed the reliance on artisan skills for ensuring good prints with weather dependent substrates, ink behaviours and printing plate ageing.

The anilox inking system (from Interchemical Corporation's ink branding) introduced scientific analysis to producing the best prints. Kidder Press Company found that the size ratios of the rubber roll and anilox roll should be about 4-6:1 to prevent the ink drying and thickening before printing. There were many other vital developments made to improve the process and the standards of the industry, as its role in the printing of packaging grew, particularly for foods. After the Food and Drugs Administration in the United States ruled the aniline inks inappropriate for food



Figure 2.10: A modern industrial printing press. Used with permission Bobst Ltd.

packaging,the Mosstype Corporation's Newsletter released a reader's poll to choose a new name for 'aniline printing' that had no toxic connotations: 'flexography' was chosen.

2.4.2 Modern flexography printing

Since the end of the 20th century, the graphical printing industry's growth has slowed and in some cases, like magazine printing, receded. Flexography, however has remained prominent, often with year on year growth in market share.[75] Developments in pre-press computer aided graphic design revolutionised the industry.[94] Today, printing presses are highly automated and advanced manufacturing machines, see Figure 2.10. The research and development of the process still continues in industry, with many of the original companies still innovating today. Developments in the plate making process, particularly photolithography, and anilox engraving methods, such as laser etching, have only made flexography more competitive with other high throughput printing techniques like gravure. Relevant improvements, to this thesis, are discussed in sections 2.4.3 and 2.4.4.

As flexography printing moves beyond application to graphical printing, the understanding of the process must improve to meet the new challenges. The historical industrial setting of flexography and its development has meant that research into flexography within academic settings has only come about in the last 30 years or so. Part of the research endeavours has been systematising and categorising flexography printing, which is sometimes considered to be an art form based on experience and know-how, rather than a scientific process.[95] The next section discusses some of this

research, which has also investigated the link between flexography printing variables and printed quality, often relying on industrial concepts and terms such as those listed in the appendix.

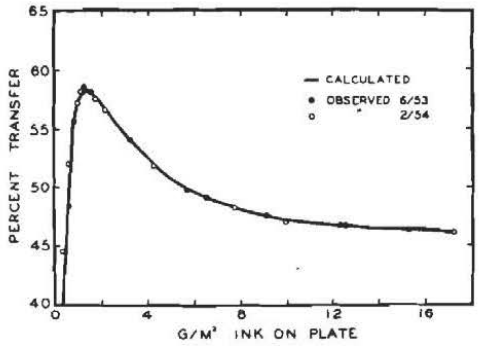
2.4.3 Academic Research Focused on Industry

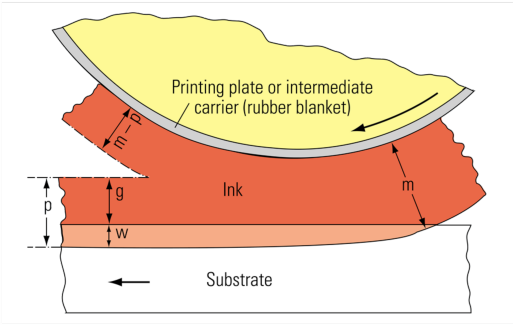
This section describes in more detail some of the scientific observational studies of flexography in the late 20th century to the present day, which were either based in the graphics printing industry or within research institutions using machines equivalent to those used in industry. The main ideas of flexography ink transfer recorded in the literature are summarised and critiqued to show that breaking down the flexography process into defined mechanisms is needed for a full understanding of the process.

A large amount of research has been conducted on paper substrates, and can be found through Technical Association of the Pulp and Paper Industry(TAPPI). Paper was a common substrate in the throughout the 1900s. Work conducted at Rochester Institute of Technology (RIT) as part of the Flexographic Technical Association (FTA) in the United States also brought more scientific research to the industry. Research was divided into three categories: ink research; ink transfer research; and substrate research. In view of the scope of this thesis only ink transfer research is taken further in this review.

Early academic researchers were interested in determining the amount of ink transferred from the printing plate to the substrate. The transfer of the ink from the printing roller to the substrate was described as a liquid film splitting between the two rollers, after passing through the contact region.[96] Therefore, the main factors of ink transfer are the amount of ink supplied, the applied force at the contact, the period of contact, ink rheological properties (which is affected by temperature) and the substrate surface properties. Focused on newsprint, with rough absorbent paper substrates, ink absorption into the substrate also had to be considered.

The seminal work by Walker and Fetsko at the National Printing Ink Research Institute, developed existing ideas to explain a peaked 'transfer curve', see figure 2.11, which plotted the relative fraction of ink transferred, during printing, as a function of the ink originally on the printing plate. As the ink thickness on the printing plate increased, initially an increasing amount of ink transferred to the substrate, because the plate-to-substrate contact was becoming more complete, and the paper's roughness was matched by the thicker ink film. The following plateau section results from the substrate absorbing only a finite amount of ink. The excess ink, also termed 'free ink', could split between the inked plate and ink saturated substrate, resulting in





a. b.

Figure 2.11: a. Transfer curve of oil based ink onto coated paper, showing how the fraction of ink transferred from the plate to the substrate changes with the amount of ink originally on the printing plate. [97] b. Ink transfer splitting described can be described by the Walker-Fetsko equation. Edited from reference [75] © Springer-Verlag Berlin Heidelberg 2001.

the observed asymptotic decrease towards a certain percentage of transfer. This final transferred percentage varied depending on the process conditions, so an empirical factor was required for fitting.

In this way, Walker and Fetsko described the amount of ink transferred per unit area (Y) as:

$$Y = b + f(x - b) \tag{2.8}$$

where b is the volume of ink that can be absorbed (termed 'immobilized'), x is the initial volume on the plate, and f is the splitting factor that can be derived from empirical graphs. This equation holds for small values of x, but a more general form, which takes into account non-symmetrical splitting of the free ink, is:

$$p = (1 - \exp{(am)}^x) \left[w_0 \left\{ 1 - \exp\left(\frac{-m}{w_0} \right) \right\} + \alpha \left\{ m - w_0 \left(1 - \exp\left(\frac{-m}{w_0} \right) \right) \right\} \right] \tag{2.9}$$

where the dimensions p, m and the absorption w_0 (gm^{-2}) are defined in Figure 2.11b, a is the print smoothness indicator (m^2g^{-1}), α is the ink splitting factor, and x is the dimensionless device factor which is found empirically. This is a complex equation that does not consider standard material concepts such as interfacial energies, as it has come from the graphics production industry, and requires an experimental understanding printing machines. That said it is widely adopted as a rudimental approach in literature and has been developed further.[98, 99, 100, 101]

Developments in flexoography in the late 20th and early 21st century were also advanced by the developments made in the inks industry, extending into functional inks, and also the plate development techniques, such that higher resolution patterns ($2400dpi$, $10s\,\mu m$) could be developed.[102] As a result the Welsh Centre for Printing and Coating (WCPC) undertook research in flexography. Their work mainly focused on anilox plate interactions, and to this end they clarified industrial terms such that they could scientifically model and accurately test the flexography process. Thorough experimental print trials with industrial scale machines (Timsons T-Flex 508) resulted in a number of findings, the most relevant for this thesis are discussed below.

Firstly, it was shown that the image transfer quality (solid density, tone gain and ink spreading) was predominantly affected by the anilox cell volume, relative to the pattern's line ruling see Figure 2.12.[103] With halftone images, where the image is made up of regularly spaced dots, the line ruling is the number of dots per unit length. As the anilox cells become larger, and each could hold a larger volume of ink, the printed dots appear to have a larger ink film thickness. It was is compared to other metallization methods. also shown that the engagement (displacement between plate and impression drum) has a similar but less pronounced affect. The maximum solid density is achieved before the uppermost variables that were tested, which is associated to an 'ink spreading limit'. In other words, with sufficient ink, the pattern solid density (thickness) does not depend on the patterns line ruling or plate to substrate engagement. It should be noted that there should be 6-10 anilox cells to each halftone dot, to prevent the dot feature penetrating a cell and being inked on the stem beyond the face, which leads to dot gain.[104]

This study was possible as UV curable ink was used which cured quickly and without solvent loss and also a single bespoke anilox with all the variant line rulings was laser engraved. This meant the various results were comparable having occurred within the same print run and the measured printed pattern was closely representative of the immediate effects of the nip variables. Although it does not answer some questions of the relationship of the plate ruling with the anilox ruling, it does present a good description of data which could easily have been lost in a complexity of industrial know-how and nomenclature.

In another paper modelling of the deformation of the printing plate feature was used to compare the dot gained observed in experimental print runs. The feature was displaced under normal engagement with a plate (as the impression roller is often much larger than the printing plate and its features) and the change in the size of the contact was calculated using a finite element (FE) analysis. It found that

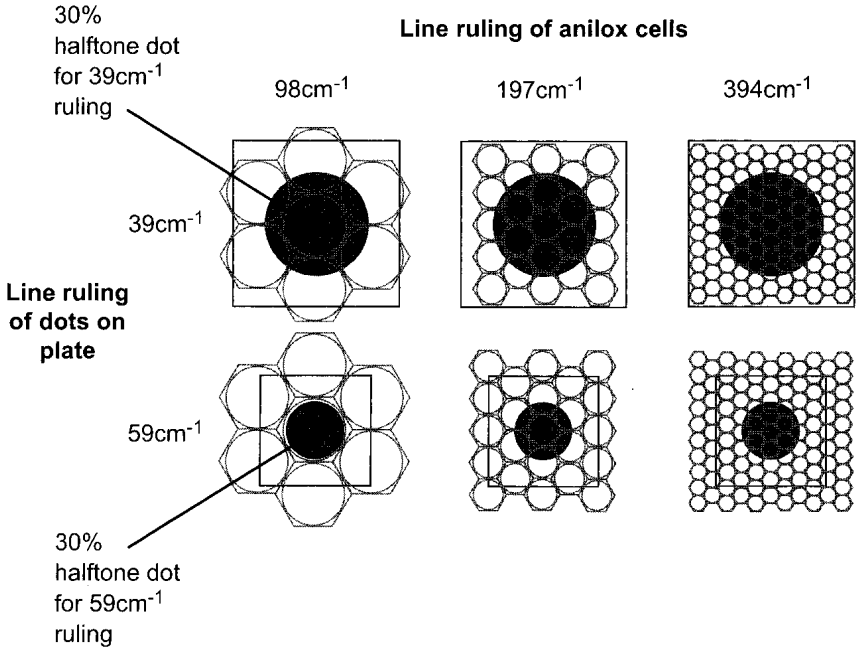


Figure 2.12: The line ruling interaction with the the anilox cell volume. From: [103]

there were two mechanisms of the dot expanding laterally under the contact pressure, termed expansion and barrelling, see Figure 2.12, which increased with pressure. This analysis is particularly important as it includes the a variation of half-tone dot sizes (coverages) and the plate backing material, which is a soft foam.

The findings indicate that the dot barrelling mechanism contributes most to the dot gain, see Figure 2.12 and that printing pressure has the largest effect on dot gain. Square dots have a decreasing rate of expansion as the engagement (printing pressure) increases, in contrast to round features. They suggest that the barrelling effects increase the yield stress for further deformation. The gain in printed dot size was most pronounced at low coverages with changes of impression pressure. The authors went on to show the relative contributions to printed feature gain is dominated by ink spreading effects over plate feature deformation, for higher tonal coverages above 5%. It is concluded that the dot gain is a function of the dot perimeter to dot area ratio.

This experimental investigation has probed the smaller scale effects involved in the mechanism of ink transfer. The investigation's conclusion is clear: the pressure used to transfer ink from the plate to substrate is a key parameter for controlling the print The line ruling interaction with the the anilox cell volume.quality. Although it only considered dry roller contacts (with no liquid ink modelled), the one phase system

avoided unrealistic stresses with a low coefficient of friction. The modelling did not includ is compared to other metallization methods. e shear or rotational effects on the plate deformation and was limited to half tone dot patterns, though this is a printing standard. The use of graphics printing terminology and quality measures, which are not based on material physics, does not provide a direct application of this research to printing for flexible devices. An example of this is optical dot gain, which considers the relative change of printed pattern dimensions to the nominal (plate) dimensions as a logarithm of the reflectance, which is itself a function of the fundamental material expansion due to transfer effects.

A flexography printing trial report which did focus on functional behaviour for flexible devices, printed circuit board conductive circuits from silver flake and nanoparticle inks.[104] The ink flakes ($7 - 10\mu m$ diameter) clogged higher line ruling anilox cells causing line gain, leading to the empirical rule of cell opening size being 3 times the largest particle size. With polyethylene terephthalate (PET) substrates $20.7 \pm 4.8\mu m$ line widths were achieved printing in the machine direction, with an anilox roll with $800 cells.in^{-1}$ and a cell volume of $3.3BCM$ (billion cubic microns); notably cross direction printing lead to larger line gains. However the printed patterns on the PET were not conductive, as the printed volume was too low, although coated paper substrates did produce conductive patterns with a minimum linewidth of $29.1 \pm 4.0\mu m$ (length $3.88mm$) albeit with a resistance of 75Ω. Working with harder plate backing foams (a hardness value was not given), reportedly produced more line gains, and fewer line discontinuities in the printed patterns, creating more conductive pattern on paper. High printing pressure was suggested as a cause of low print quality, although the printing pressure was not stated and the Harper flexo proofing system used a fixed spring, so it could not be varied. This said, this paper is a rare example of a scientific investigation into how the printing conditions affect the functional performance of the printed pattern, although its success was limited due to the fluid dynamics of the solvent based inks creating low thickness pattern, which diminished the conductivity..

One other example of research which also applies the printing quality assessment into functional applications is by Kahn et. al. [81] In this work an Omet Varyflex 530 flexography printer, which has a modular design, was used to print at $30.5m.min^{-1}$, to allow for a long enough dwell time need for drying the ink, although it can print up to $200m.min^{-1}$. The previous work was only conducted at roughly $6m.min^{-1}$ so this work is closer to industrial printing norm. Using aqueous nano particle silver inks various anilox volumes brands of plate materials and linewidths were compared

by the measured sheet resistance of the printed lines. Bulk resistances as low as 3 times silver ($1.6\mu\Omega.cm$) were achieved. The orientation of the printed lines was also shown to have an effect on the resistivity as machine direction lines were wider. In this printing trial report achieved, the minimum printed linewidth and the minimum gap between lines, that had no shorting defects but was conductive, was $40\mu m$, with the plate exposed to air during photo-polymerisation, creating a rounded tip that was smaller than the master form.

The literature in this section has been focussed on commercially applicable experiments, with industrial scale printing machines. Changing the printing variables, such as printing speed, pressure and varying the printing plate and anilox setting have all be found to have an influence on the printing quality. In turn, some research has extended the observational results to show that the printing parameters can affect the functional properties of conductive patterns which could be used in flexible devices. Although they are useful for improving existing working practise they do not fully test more general explanations for how the process variable affect the ink transfer and print quality. The next section is focussed literature which delves deeper into how the underlying printing variables change the mechanisms of ink transfer that control the final print quality.

2.4.4 Modelling Liquid Bridges

The previous section described research focussed on scientific investigations of the application of flexography, leading to empirical models and observed trends by parametric study. This section includes research which has been less application focussed, and instead taken an approach of reducing ink transfer into mechanisms of liquid flow which can be modelled to estimate the amount of liquid transferred from plate to substrate.[105]

An early example of this type of work was by De Grace and Mangin in the 1980s reported at the International Association of Research Institutes for the Graphic Arts Industry research conferences.[106] They proposed that asperities on the substrate (non-absorbent) lead to cavitation in the liquid contact, originating due to the pressure variation through the contact. This cavity growth was the mechanism of ink film splitting, which was not symmetrically distributed between the plate and substrate, see Figure 2.13. It was found that the fraction of ink transferred to the substrate decreases with higher printing speeds; explained by cavity expansion time available. Repeated printing passes onto the substrate indicated that surface asperities were not the only origin of cavitation, and air inclusion at the roller contact was suggested.

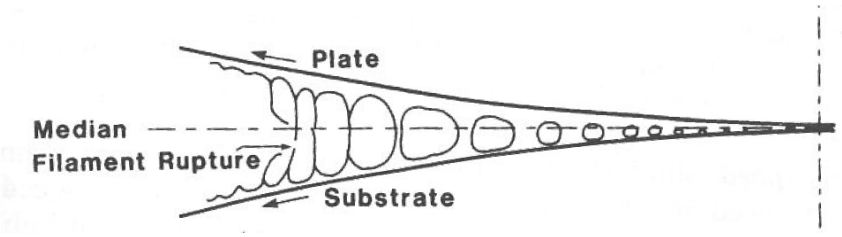


Figure 2.13: Schematic from [106] of asymmetric ink splitting between the plate and substrate.

This study took a mechanistic view of the ink transfer, which could be detected by the measurable film thickness transfer, and then varied the printing parameters to probe this mechanism of bridge formation through the measured outputs. It was highly applicable, and led to developed understanding of the means to improve the printing quality.

This mechanistic approach has been continued in more modern modelling approaches. In this body of work, a model is used to represent the movement of the liquid ink from the plate to the substrate, see Figure 2.14. The dimensions of the ink are assumed to be very small compared with the size of the rollers and so parallel plates can be used as a simplification.This liquid bridge model can be simulated and solved analytically in 1 or 2 dimensions using the Navier-Stokes equations of viscous fluid behaviour and characterised using other hydrodynamic and fluid flow terms, see Table 2.2. This more general definition of ink transfer has been empirically supported by, and applied to, a wide range of patterning methods and increased the understanding of the physical limits, as touched on in the gravure section above, § 2.3.5. However, as is now discussed in detail, the practical relevance to high volume and high throughput printing can be curtailed by this precise model's dynamic limits.

An investigation, in this vein, by researchers at Princeton University focussed on patterning fidelity in an offset process.[107] A silicon or glass plate was chemically patterned, using photolithography, with varying aspect ratios of hydrophilic regions. These patterned regions were inked (using dip coating [108]) and carefully brought into contact with the substrate using spacers to define the liquid bridge aspect ratio, then the plates were separated and the volume transferred was measured. This experimental approach supported their theoretical calculations, at quasi-static conditions of plate separation and controlled ink film thickness.

The modelling approach built on calculations from the 1980s, showing that the amount of ink transfer depended on the relative contact angles of the plates, see Figure 2.15.[109, 110] For this contact angle energy minimisation, they found there is

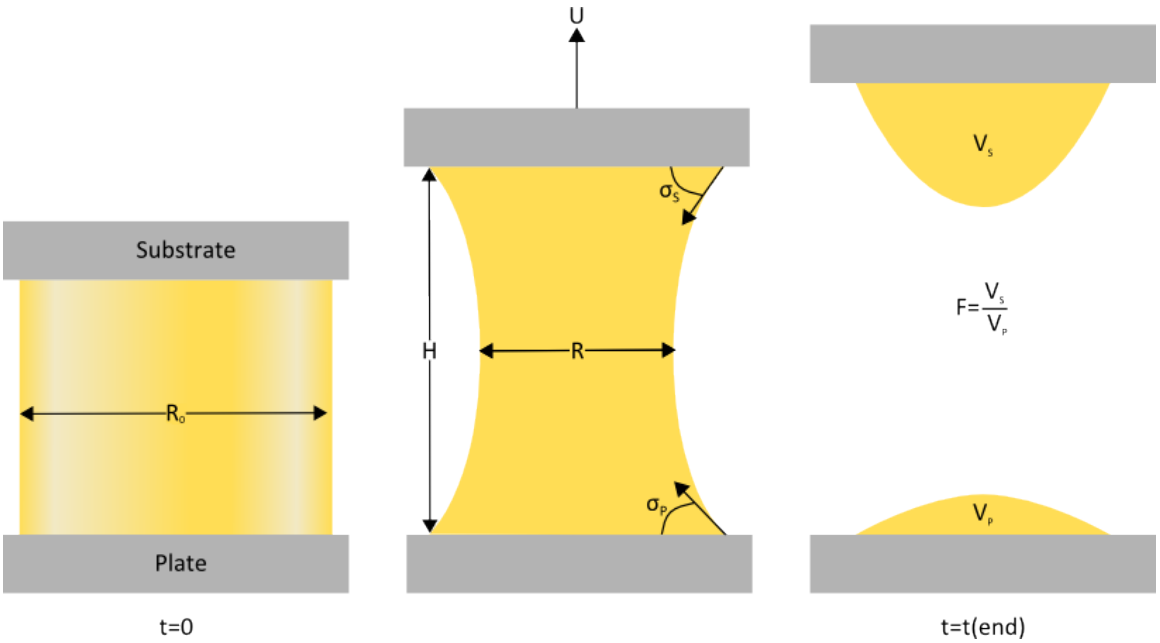


Figure 2.14: Schematic of a cylindrical liquid bridge model undergoing plate separation (left to right), with the following labelled: time (t) from 0 to end of separation ($t(end)$); bridge height (H); bridge radius (R) where the bridge aspect ratio is $\frac{H}{R}$; the contact angle (either static or dynamic) of the liquid-plate σ_P and liquid substrate σ_S interface; the volume fraction transferred after separation F, given the volume on the substrate (V_S) and plate (V_P).

Table 2.2: Table of equations defining the liquid bridge behaviour, used for modelling of extensional flow. Definitions for the terms can be found in Figure 2.14.

Equation	Physical meaning
$A = \frac{H}{R}$	Liquid bridge aspect ratio.
$Re = \rho\frac{UR}{\mu}$	Reynolds number: ratio of inertial to viscous forces.
$Ca = \frac{\mu U}{\sigma}$	Capillary number: ratio of viscous to inter-facial forces.
$St = \frac{\rho g R^2}{\mu U}$	Stokes number: ratio of gravitational to viscous forces.
$Bo = \frac{\rho g R^2}{\sigma}$	Bond number: ratio of gravitational to inter-facial forces.
$Oh = \frac{\mu}{\sqrt{\rho\sigma R}}$	Ohnesorge number: Capillary number at the capillary wave speed ($= \sqrt{\frac{\sigma}{\rho R}}$) giving the ratio of the viscous forces to the inertial and inter-facial forces.

a tendency for the ink to accumulate at acute pattern corners. These findings assume the speed of the plate movement is lower than the liquid's contact line speed. It was modelled that as the plates separate the ink recedes to the centre; the bridge aspect ratio increases. In contrast, at higher plate speeds, there is less ink redistribution, and the fraction transferred tends to be 50%, which is known from earlier research.[109, 110]

The features that were patterned in this investigation were on the order of micrometers so gravitational and inertial forces were neglected. This led to the surprising argument that, due to the intrinsic redistribution velocity being only a function of viscous and capillary forces, the pattern fidelity does not depend on the feature size but only on the liquid bridge aspect ratio. This suggests that liquid transfer patterning critical dimension size is not limited, only the deposited thickness is, if the contact angles can be minimised to ensure complete wetting and pattern fixation with curing processes.

However the process used to transfer the liquid was highly controlled. By testing various substrate materials, showing a variation of transfer ratio, indicates that the contact angle and its movement during extension (a.k.a. contact line slip) is important for pattern fidelity.[111] Using constant separation speeds which are slower than the contact line slip is a luxury not available in higher throughput process like flexography (where roll separation speeds are $> 0.1 m.s^{-1}$). Although the fluid mechanical treatment was insightful, it also showed that at these low speeds (i.e. low Reynolds and capillary numbers), the capillary forces dominate over the viscous forces, which is not representative of high volume printing. The plates were moved unrealistically slowly and parallel to one another without investigating the effects of contact line slip.

Another study, in this field of liquid bridge modelling, included the shear and rotational effects which are experienced by an ink bridge separated by a roller printing system. Dodds et. al. focussed on the FE modelling of liquid bridges with moving contact lines, based on development of 3D solutions to the Navier-Stokes problems and FE mesh improvements. Assuming constant volume, mass, and momentum with negligible ambient gas effects, the Navier-Stokes equations could be written as:

$$Re\frac{D\boldsymbol{v}}{Dt} = -\nabla P + \nabla^2 \boldsymbol{v} + St; \tag{2.10}$$

$$\nabla \cdot \boldsymbol{v} = 0, \tag{2.11}$$

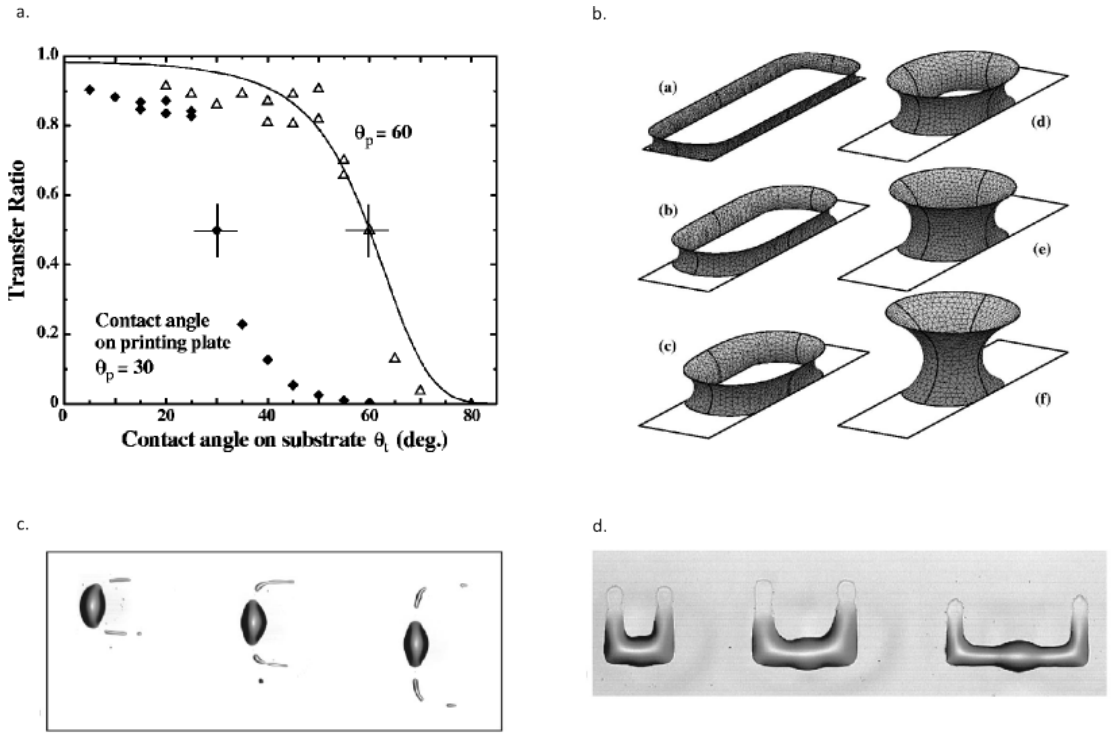


Figure 2.15: a. Transfer ratio changes with substrate contact angle variation, using glycerol ink between zinc plates (triangles), or zinc-polymer plates (diamonds) at low plate separation speeds. At even contact angles a 50% ink distribution is modelled (solid line), nearly complete transfer can also be achieved when the ink wets the substrate. The work also showed at low speeds more viscous glycerol formulations decreased the transfer ratios. From reference [109]. b. Simulation of equilibrium contact lines for a high aspect ratio ink bridge with smooth flat surfaces. The change with constant quasi-static plate separation, (a)-(d), demonstrates the contact energy minimisation effects of patterning fidelity. c. Photographs of transferred ink on a partially wetting substrate, with de-wetting filaments leading to satellite droplets, due to the low viscosity ink compared to d. which had 5 times the ink viscosity and a completely wetting substrate. b.-d. from reference [107] Reprinted from Darhuber AA, Troian SM, Wagner S. Physical mechanisms governing pattern fidelity in microscale offset printing. Journal of Applied Physics 2001;90:3602–9. doi:10.1063/1.1389080 with the permission of AIP Publishing.

where $\boldsymbol{v}$ is the velocity, P is the pressure, t is the time and other terms are defined in Table 2.2. The Stokes number is considered negligible for the range of typical values used. These are solved using boundary conditions of the liquid-solid interface and capillary stresses. Including the movement of the interface due to contact line slip was achieved by using a Navier slip:

$$\boldsymbol{t}_{cl} \cdot (\boldsymbol{n}_w \cdot \boldsymbol{T}) = \frac{1}{\beta} \boldsymbol{t}_{cl} \cdot (\boldsymbol{v} - \boldsymbol{v}_{surf}), \tag{2.12}$$

and the dynamic contact angle (Θ) was modified from the static contact angle (Θ_S) using:

$$cos(\Theta) = cos(\Theta_s) - \Gamma Ca.x \tag{2.13}$$

The vector terms are defined in Figure 2.16a and $\boldsymbol{T}$ is the total stress tensor in the liquid. β is the factor that controls the size of the slip region (typically around 100nm). A large value of β creates a smaller slip region, but one more affected by the bulk stresses, than a smaller β as was used in this work ($\beta = 10^{-2}$). Finally the dynamic contact angle is defined by the contact line friction, Γ, which is a property of the materials present at the bridge interface. This coefficient is larger for silicone oils on glass than for water on polyethylene (PE).[112, 113] From equation 2.13 it is evident that as the contact line friction increases, the term x must decrease so the left hand expression remains between -1 and 1. x is a simplified term which includes the contact line velocity, so as the contact line friction increases, the contact line must become pinned. Further details are available in reference [114].

In these modelling results shearing the liquid bridge, which was frame invariant and with low capillary number, was found to have no effect on the ink redistribution after separation, which contradicts empirical results.[115] Differently, rotational movement of one plate extended the time before bridge splitting as the axial velocity overcame the capillary force effects, Figure 2.16b and d. This rotational effect on the flow of liquid also resulted in a greater proportion of the ink remaining on the non-rotating plate. This effect is seen in real printing systems where one roller has a much smaller diameter than another to create a relative rotational movement, meaning that ink favours the larger roller.

Modelling of liquid bridges with moving contact lines also highlighted the importance of the contact line friction on the pinning and pattern fidelity. It was concluded that the most complete transfer is obtained when the contact line friction is small

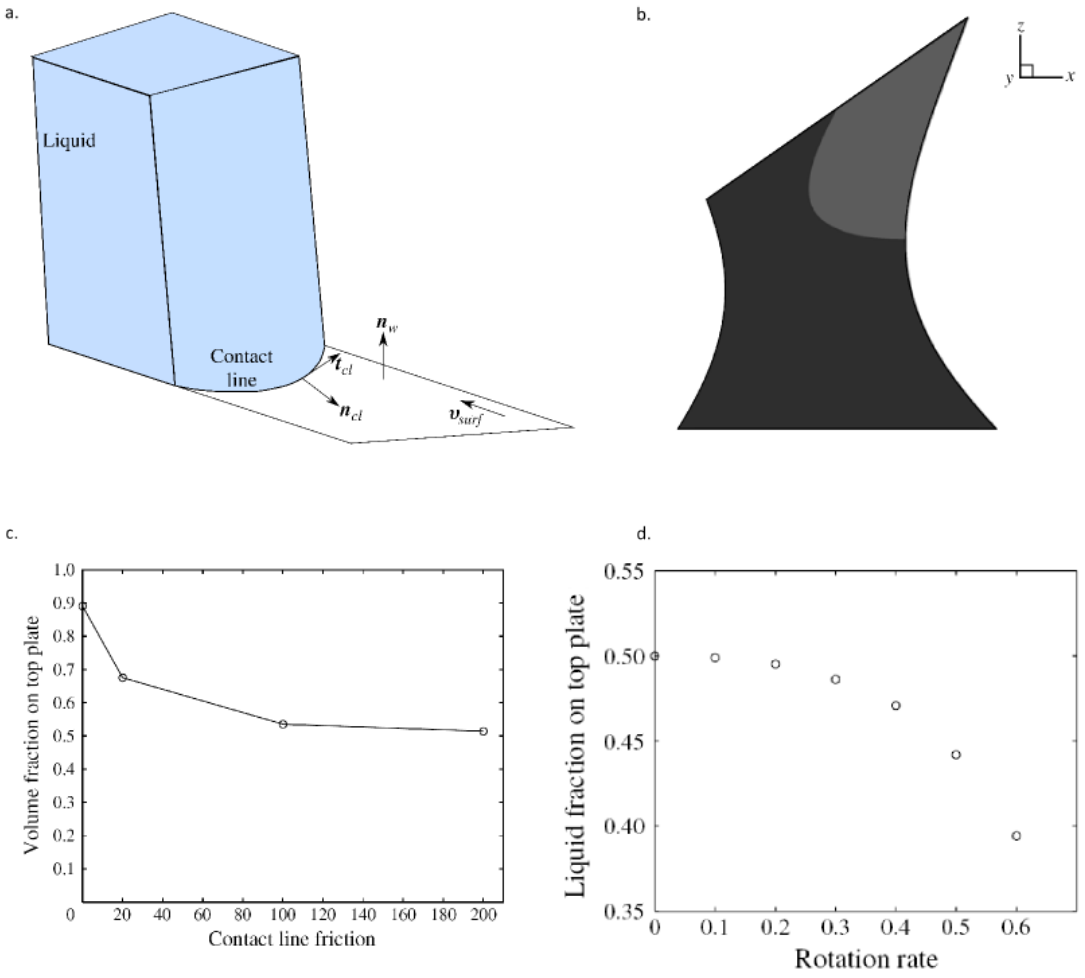


Figure 2.16: a. schematic of 3D liquid bridge with the various vectors labelled. b. 2D freeze frame of a liquid bridge model with extension and rotation of the top plate leading to a smaller region of ink having a velocity towards the rotating top plate (denoted by light grey shading) than ink experiencing a velocity towards to the non-rotating plate (dark grey). This leads to a reduced fraction of liquid on the top plate, which increases with rotation rate, as depicted in d. c. shows that with contact line friction modification, of the bottom plate, a greater than 50% fraction of ink can be moved to the top plate. Increasing the contact line friction diminishes this effect, as the liquid ink/plate interface is more pinned and conserves volume. All the data was collected with the following model parameters: $U = 1cm.s^{-1}$, Ca=0.1, $\Theta_s = 80°$and $60°$ for the bottom and top plate respectively, and the top plate $\Gamma = 100$. Edited from: Dodds S, Carvalho MS, Kumar S. The dynamics of three-dimensional liquid bridges with pinned and moving contact lines. Journal of Fluid Mechanics 2012;707:521–40, reproduced with permission. [114]

on the bottom (donor) plate, allowing the bridge interface to slip, while a large contact line friction of the top (acceptor) plate will pin the liquid bridge to the desired pattern form. Unlike capillary number, which is a bulk property, tuning the contact line friction, with processes like plasma treatment, can create a substrate favouring bridge splitting behaviour, Figure 2.16c.

This modelling work was focused on printing systems and used relevant figures of merit, so it is highly applicable to flexography printing, although the examples given in the paper focussed on gravure processes. The trends observed are insightful, although the modelling did not include the effects of the final thinning of the bridge, when the Re is low and small satellite droplets can form as the volumes are small.[116, 117, 118] However, even with small volumes, these satellite droplets can become critical defects when printing for conductive electronics. Finally, this 3D modelling process was not corroborated with experimental findings or linked to observed printing quality and defects.

An approach to apply the advantageous predictive power of modelling to flexography printing effects has been reported by Hans Sauer et al. In their 2015 paper the viscous flow of Newtonian liquid bridge between an rigid plate and elastic printing plate, with a relief printing feature, was analytically solved for, using Navier-Stokes equations, similar to previously described investigations. It was reduced to a 2D problem by introducing a lubrication theory approximation, namely that the geometry across the plate surfaces is much larger than the plate-to-substrate separation. This focusses the analyses on stress distribution across the liquid bridge height, incorporating the deformation of a visco-elastic top plate in a three-phase liquid bridge model, which is more representative of the use of a soft flexography printing plate.

The model considered a bridge with a cross-section of a rectangle with length to width ratio such that the change of pressure in the length of stripe is negligible, giving a pressure profile in terms of the bridge height and width, and time. This showed that the elongation flow rate was smaller than the shear rate, and that the shear forces lead to deformation of the visco-elastic plate. This inequality does not hold at the thin central region of the bridge, in other words if the bridge aspect ratio is < 1. This hydrostatic pressure shear effect shrinks as the plate separation increases. The work by Dodds, previously described, is therefore consistent for frame invariant shearing of liquid bridges with aspect ratios near unity. The following analysis included the effects of compressible plates, ink squeezing due to compression, and cylindrical geometry effects. Using an 'effective nip length' for the contact region, which depends on the relative roller ratios and the minimum distance of the two plates. This is a non-linear

relation, depending on the liquids hydrostatic pressure, so can not be directly solved but several scaling relations can be found. An example is the width of a defect termed a 'seam' which results from the rear edge of the printed feature and is therefore a representative of the contact length. The scaling of the seam width with speed was measured to be within 21% of the modelled value.

There are other questions of droplet formation, which can be modelled with diffuse interfaces such as reference [119]; empirical investigations still needed to corroborate theoretical findings; and the effect of non-Newtonian inks, which are often used in solution based ink printing.[120] However as a tool for isolating specific transfer mechanisms modelling of liquid bridges yields useful trends and certain principles for ink transfer as a whole. Although it is limited by thermodynamic equilibrium or generalities which ignore certain complexities of the full printing process, printing trials can be enhanced by being designed with the fundamental fluid action in mind. The results will then benefit from both practical applicability and theoretical insightfulness.

2.5 Metal Patterning

There are various methods for creating thin films of metal on polymer substrates with conductive properties and the required dimensions. As an introduction to the existing understanding surrounding conductive pattern formation methods, and there compatibility and viability with industrial scale manufacture of thin film flexible organic functional devices. Selective metallization is introduced and reviewed in more detail, as it is the focus of this thesis' experimental investigation. First, a few of the other methods are summarised

Wet etching of a foil coating is an effective and simple subtractive process with good industrial standing. In this process, the metal coating (or any other material which oxidises in acidic environments) is exposed to an acid (phosphoric, acetic, hydrochloric and hydrofluoric acids are common as well as hydrogen peroxide in combination with these) and the reacted salts are washed away by the liquid processing. The chemical reaction rate must be matched with the throughput, meaning that the processing speeds are low ($1 \times 10^{-2} m.min^{-1}$). Also, to be compatible, the substrate must not react with the chemicals involved. The patterning is achieved using resist masks with batch processes or vertical (in-line direction) patterning can be achieved with R2R processes.

Pulsed laser scribing is another subtractive process for metal thin film patterning without the need for environmentally harmful chemical and good resolution con-

trol. It has been established technology since the 1990s, then applied to silicon photovoltaics.[121] In recent years it has been commercially applied in the field of flexible photovoltaics (in-vacuum),[122] and other commercial businesses.[123] The critical dimension is limited by the laser beam's interaction with the ablated materials, but can achieve resolutions down to $10s\,\mu m$.[124] Large area processing is limited by the ablation rates and matching of the photon energy to the multi layered material structures, although the material properties are that of the bulk, with this subtractive process.

Mask techniques, where a coating technique is applied to a substrate with areas covered has been the workhorse of academic work, in particular in vacuum thermal evaporation of metal thin films. Other deposition techniques include sputtering and solution deposition. The mask can either be laser cut metal or polymer patterned sheet which is fixed to the substrate, or a photolithography patterned mask which is then removed with a chemical lift-off process. There can be issues with shadowing effects and material build up on the mask, with high volume processes. The mask must be fixed relative to the substrate so integration with R2R process is difficult, although moving belt masks have been used.[125] Generally though, mask processes are considered low throughput batch processing for this reason.

As described in the literature review, for ambient solution processing, graphics printing techniques can be re-purposed with conductive inks. In this solution processing field, some of the best results are obtained with inkjet and screen printing. Inkjet has good pattering control and resolution limits ($\mu m's$), but the thickness ($\sim 1\mu m$) of the deposited thin films and the fluid requirements, often requires several deposition layers for low resistance patterns to be formed.[126, 127] Screen printing creates much thicker patterned thin films ($10 - 500\mu m$), although it has higher resolution limits ($\sim 100\mu m$) and is not a digital technique.[128] The curing of solution based inks is critical to the thin film's conductivity. In this step the solvent is removed and the conductive portion of the ink is fused to create charge carrier pathways. Improper curing can lead to reduced conductivity or surface roughness, as well as requiring additional processing time. Sintering organometallic inks, can, at best, achieve resistances about half bulk resistivity, if the temperature can be withstood by the substrate (around $150°C$).[129]

A final novel technique, adhesion lithography [130], has recently been developed by researchers at Imperial college, who have achieved nano-gap separation between two dissimilar metals with self assembled molecules. Although they have demonstrated functional applications [131, 132], a commercial setting has still yet to be shown.

Each of the above processes are limited in some way by the viability or compatibility of the process with functional organics processing. Although each have certain levels of success reported in the literature reviewed, there is still a need for improved patterning techniques, one option is selective metallization, as described in the following section.

2.5.1 Selective metallization

Serendipity is reported to have played a role in the invention of this process, when contaminating diffusion pump oil left defects in metal coatings. This led to the deliberate introduction of an oil mask onto the substrate using a range of deposition methods, as discussed later, to pattern the metallization.[125] Nowadays, selective metallization is an industrially mature process being used to make decorative packaging and holograms.[133, 125] After its covering patent expired in 2001 [134], it has been employed by commercial businesses [135] as an efficient high throughput ($1000 m.min^{-1}$)[133] metal thin film patterning process. It is possible to create grey-scale images for the metal thin films, with half-tone dots as flexography printing is used to deposit oil mask. In general then the resolution is limits to $10s\,\mu m$ with a product sample from Bobst company showing discontinuous lines, in the machine direction, of $0.005mm$ width, and metal pattern spacings down to $0.01mm$, see Figure 2.17a and b.[135]

The principles of the selective metallization process are shown schematically in Figure 2.17. Relying on a high vacuum ($< 10^{-4} mbar$) environment, a substrate, supported by the rotating impression drum, is patterned with an oil thin film. The negative pattern can be applied using a range of techniques: fixed mask/apertures for an oil vapour, inkjet from a nozzle, or impression from a transfer technique like flexography, as used here. After this printing step, the oil-patterned substrate passes over the metallization boat (physical vapour deposition (PVD) source), at which point the metal vapour condenses and adheres to the non-patterned regions of the substrate. The oiled regions prevent metal deposition, which creates the positive pattern of metal thin film. In concert, the sacrificial thin film of oil is removed by the heat of the PVD, and pumped out the chamber. The reciprocal oil removal during the metal deposition is a simple and effective mechanism.

The role of the sacrificial patterned oil is similar to the mask of an additive photolithography process. Instead of chemical lift-off of the photoresist layer, selective metallization relies on the oil thin film being vaporized by the heat of the thermal evaporation source. This critical step is designated as a 'thermal lift-off' mechanism,

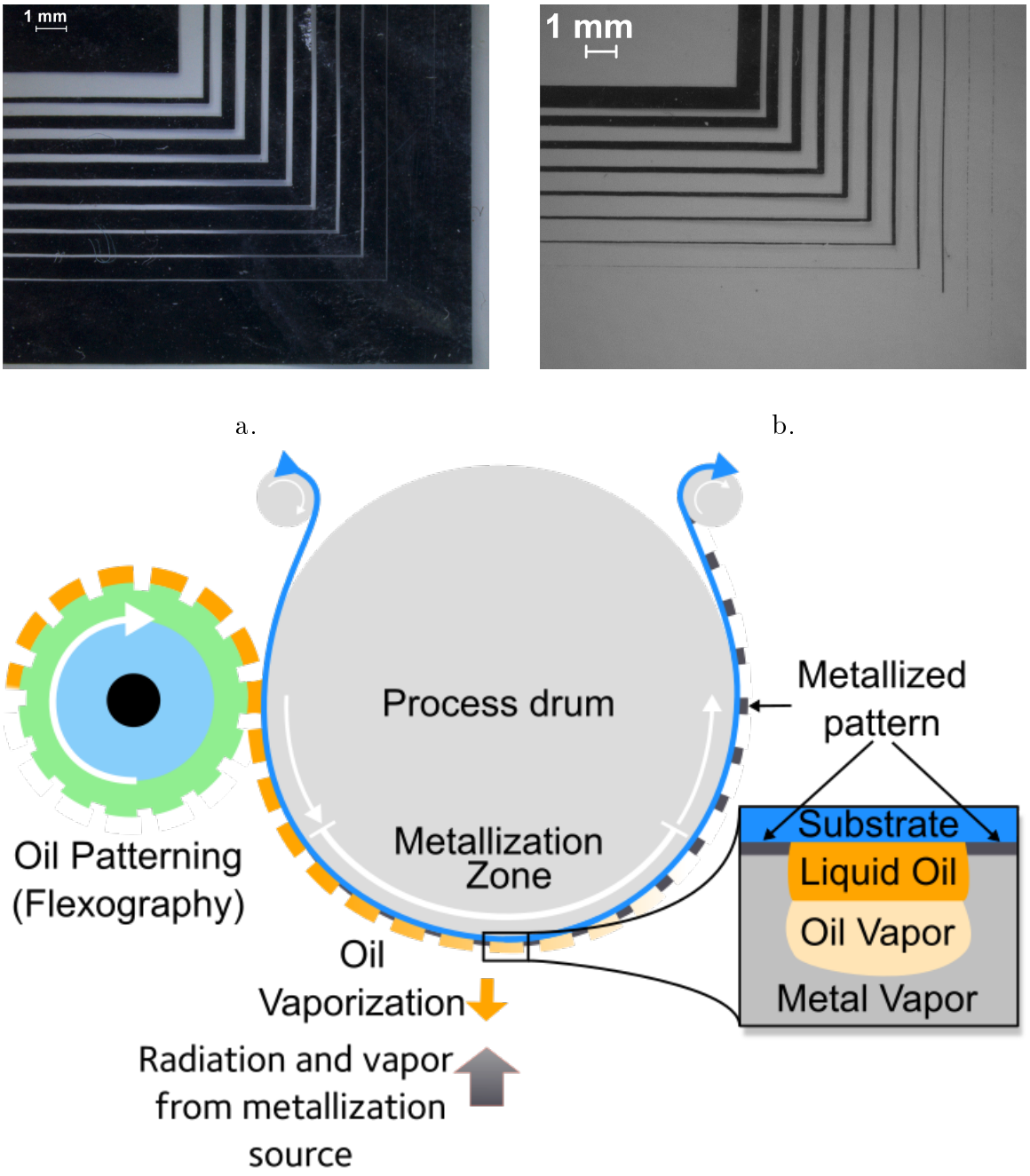


Figure 2.17: a. and b. show optical microscopy images of a SelectMet® product sample from Bobst who make selective metallization machines.[135] This shows the existing pattern resolution limits of 10μm of this industrially mature process. In these images the machine print direction is vertical. The darker regions are metallized and the light grey regions are the polymer substrate. c. schematic of the principles of the selective metallization in-vacuum production method, in which, flexography printing is used to create a pattern of sacrificial oil on a organic device (the substrate) which is moved over the PVD source to create a metal pattern on the substrate and vaporize the oil simultaneously. The inset is a magnified view of the phases present in the metallization zone. Further details on the actual process can be found in the Materials and Methods chapter.

and is due to the radiative heating of the PVD source and/or the latent heat of fusion of the metal vapour upon the oil thin film surface. The balance of matching both (i) the oil volume with the thermal energy of the PVD process, to prevent unintended over-metallization, with (ii) the efficient process requirement that the entire oil volume is removed with the metallization zone, Figure 2.17, requires careful consideration. These synchronous deposition/vaporization must occur within this single thermal lift-off step. Without this balance, in the thermal lift off process, the metal pattern could have blurred edges and pattern loss, or remnant excess oil will require further processing to be removed.

2.6 Conclusion

Patterning process are key to the success of flexible electronics which are to be produced by high throughput techniques. Unlike the graphics printing industry the final device and material characteristics are very important. The requirement for a successful printing is not determined by the human eye, as with graphics printing but by the passage of an electron or charge carrier. Lateral resolution and other concepts can be borrowed from the graphics industry, which proves the reliability and consistency of a particular technique, but this must be built on and improved upon, if the deposited material properties are to be appropriate for the application. Although there is an inverse trend for throughput and lateral resolution, in a few cases high throughput patterning techniques can aid the material properties and examples of this were given. The review presented scientific research into other aspects of printed materials which become more important, such as surface roughness and printed thickness.

All the manufacturing techniques described have been applied to transistor technology to some degree.[42, 66, 53, 84] The description of the various patterning techniques highlighted the mechanistic similarities between techniques. Planar concepts of one technique can be modified for roller based techniques, e.g. μCP and flexography. Additionally surface processes like controlled dot coalescence are common to inkjet and gravure. These similarities can be simultaneously investigated by reducing the problem to the fundamental mechanism and borrowing from other fields such as fluid dynamics. The success with device fabrication, particularly with inkjet, have shown that patterning methods can be optimised to balance patterning ability with throughput.

Other areas which have not been covered in this review but are fundamental to flexible electronics are the mechanics of stretchable patterns[136], registration [136, 59,

137, 138] and improving device stability through encapsulation.[139] Also developing solutions to recycling and sustainability of these organic based devices needs careful thought from the outset of designing fabrication methods.[140, 141]

This doctoral thesis is focussed on flexography and the final sections reported on this technique in particular. The commercially driven origins of this printing process showed that there have been many complimentary factors which led to its success, being legislative change, commercial market growth, and scientific advance. Today scientific research continues with a Janus-like focus. On one side the holistic rigorous testing of the printing systems, and how the print quality varies with printing parameters is valuable for finding practical solution to engineering problems. On the other side fundamental research into specifically defined models can yield general understanding the phenomenological problems. The need for this chiral and disjointed approach is because flexography printing has many inter-dependent processes which creates a hierarchical problem, involving interactions between solid and liquid phases often with non-uniform pattern variation and non-steady state dynamics. There is a need for experimental design which begins with considering the modelling limits and connecting that with realistic flexography printing.

All this has gone to show that the patterning science which informs the improvement of the printed pattern fidelity and quality will influence the flexible electronics functional performance. Examples of such studies have been given, but research connecting these observations with the fundamental ink transfer mechanisms is scarce. Given the body of work presented here, there is still a need for further investigation into controlling factors of the the print quality with flexography printing. Finally selective metallization, which is the focal method of this thesis has been introduced and contrasted with other metallization techniques. This has shown that it is a candidate to be a viable and compatible technique with organic electronics, but there are no reports that this has been done previously. This doctoral thesis presents research aimed at proving selective metallization is viable and compatible with exible devices, and has advantages over other patterning methods, that have been described in section 2.5.

2.7 References

[1] IDTechEx. Printed, Organic & Flexible Electronics Forecasts, Players & Opportunities 2017-2027. https://www.idtechex.com/research/reports/printed-organic-and-flexible-electronics-forecasts-players-and-opportunities-2017-2027-000510.asp, December 2016.

[2] OE-A. The Organic and Printed Electronics industry is expecting a 7 percent increase in sales revenue in 2018. http://www.oe-a.org/article/-/articleview/582126, 2018.

[3] defense.gov. DoD Announces Award of New Flexible Hybrid Electronics Manufacturing. https://www.defense.gov/News/News-Releases/News-Release-View/Article/615132/dod-announces-award-of-new-flexible-hybrid-electronics-manufacturing-innovation/, 2018.

[4] Engineering and Physics Research Council. Research to make UK manufacturing flexible and adaptable - EPSRC website. https://epsrc.ukri.org/newsevents/news/flexibile/, 2018.

[5] gov.uk. PragmatiC: business wins major investment for flexible circuits - Case study - GOV.UK. https://www.gov.uk/government/case-studies/pragmatic-business-wins-major-investment-for-flexible-circuits, 2018-04-04.

[6] reuters.com. LG Display to take on Samsung as it lifts OLED investment - reuters. https://uk.reuters.com/article/uk-lg-display-results-investment/lg-display-to-take-on-samsung-as-it-lifts-oled-investment-idUKKBN1AA0MX, 2018-04-04.

[7] Bryan Harris. Samsung expected to cut OLED investment- financial times. https://www.ft.com/content/b0ff4c7a-1dc2-11e8-aaca-4574d7dabfb6, March 2018.

[8] On a roll - printing with conventional rotary presses will create cheaper electronics. *The Economist*, July 2016. http://www.economist.com/news/science-and-technology/21702741-printing-conventional-rotary-presses-will-create-cheaper-electronics.

[9] Timothy Revell. Transistor stretchier than skin for ultra-flexible wearable tech - new scientist. https://www.newscientist.com/article/2117285-transistor-stretchier-than-skin-for-ultra-flexible-wearable-tech/, 2017.

[10] Michael Drack, Ingrid Graz, Tsuyoshi Sekitani, Takao Someya, Martin Kaltenbrunner, and Siegfried Bauer. An imperceptible plastic electronic wrap. *Advanced Materials (Deerfield Beach, Fla.)*, 27(1):1, January 2015.

[11] Xiaoxiao Zhang, Tyler Beebe, Nelson Jen, Chia-An Lee, Yuchong Tai, and Tzung K. Hsiai. Flexible and waterproof micro-sensors to uncover zebrafish circadian rhythms: The next generation of cardiac monitoring for drug screening. *Biosensors and Bioelectronics*, 71:150–157, September 2015.

[12] Mark Geoghegan. *Polymer electronics*. Oxford master series in condensed matter physics Y. Oxford University Press, Oxford, 2013.

[13] Zhenan Bao and Jason John Locklin. *Organic field-effect transistors*. Optical science and engineering (Boca Raton, Fla.) ; 128. Y. CRC Press, Boca Raton ; London, 2007.

[14] F. M. Li. *Organic thin film transistor integration : a hybrid approach*. Wiley-VCH, Weinheim, 2011.

[15] Marja Vilkman, Tomi Hassinen, Mikko Keränen, Roger Pretot, Paul van der Schaaf, Teemu Ruotsalainen, and Henrik G. O. Sandberg. Fully roll-to-roll processed organic top gate transistors using a printable etchant for bottom electrode patterning. *Organic Electronics*, 20:8–14, May 2015.

[16] OE-A. OE-A Roadmap for Organic and Printed Electronics Applications 2017. Roadmap, 2017.

[17] Jürgen Willmann, Daniel Stocker, and Edgar Dörsam. Characteristics and evaluation criteria of substrate-based manufacturing. Is roll-to-roll the best solution for printed electronics? *Organic Electronics*, 15(7):1631–1640, July 2014.

[18] OE-A. OE-A 2014 Flexible and Organic Electonics Road Map. Road Map, OE-A, 2015.

[19] Etienne Menard, Matthew A. Meitl, Yugang Sun, Jang-Ung Park, Daniel Jay-Lee Shir, Yun-Suk Nam, Seokwoo Jeon, and John A. Rogers. Micro- and Nanopatterning Techniques for Organic Electronic and Optoelectronic Systems. *Chemical Reviews*, 107(4):1117–1160, April 2007.

[20] Mang Mang Ling and Zhenan Bao. Thin Film Deposition, Patterning, and Printing in Organic Thin Film Transistors. *Chemistry of Materials*, 16(23):4824–4840, November 2004.

[21] Frederik C. Krebs. Polymer solar cell modules prepared using roll-to-roll methods: Knife-over-edge coating, slot-die coating and screen printing. *Solar Energy Materials and Solar Cells*, 93(4):465–475, April 2009.

[22] Roar R. Søndergaard, Markus Hösel, and Frederik C. Krebs. Roll-to-Roll fabrication of large area functional organic materials. *Journal of Polymer Science Part B: Polymer Physics*, 51(1):16–34, January 2013.

[23] H. Sirringhaus, T. Kawase, R. H. Friend, T. Shimoda, M. Inbasekaran, W. Wu, and E. P. Woo. High-Resolution Inkjet Printing of All-Polymer Transistor Circuits. *Science*, 290(5499):2123–2126, December 2000.

[24] Hongki Kang, Rungrot Kitsomboonloha, Kurt Ulmer, Lisa Stecker, Gerd Grau, Jaewon Jang, and Vivek Subramanian. Megahertz-class printed high mobility organic thin-film transistors and inverters on plastic using attoliter-scale high-speed gravure-printed sub-5μm gate electrodes. *Organic Electronics*, 12(15):3639–3647, 2014.

[25] Ashok Sridhar, Thomas Blaudeck, and Reinhard R. Baumann. Inkjet printing as a key enabling technology for printed electronics. *Material Matters*, 6(1):12–15, 2011.

[26] Gerd Grau, Rungrot Kitsomboonloha, and Vivek Subramanian. Fabrication of a high-resolution roll for gravure printing of 2μm features. volume 9568, pages 95680M–95680M–9, 2015.

[27] Pieter F. Moonen, Iryna Yakimets, and Jurriaan Huskens. Fabrication of Transistors on Flexible Substrates: from Mass-Printing to High-Resolution Alternative Lithography Strategies. *Advanced Materials*, 24(41):5526–5541, November 2012.

[28] Tapio Mäkelä, Tomi Haatainen, Päivi Majander, and Jouni Ahopelto. Continuous roll to roll nanoimprinting of inherently conducting polyaniline. *Microelectronic Engineering*, 84(5-8):877–879, May 2007.

[29] B.E. Kahn. Patterning Processes for Flexible Electronics. *Proceedings of the IEEE*, 103(4):497–517, April 2015.

[30] Moon Kyu Kwak, Kyu Ho Shin, Eung Yeoul Yoon, and Kahp Y. Suh. Fabrication of conductive metal lines by plate-to-roll pattern transfer utilizing edge dewetting and flexographic printing. *Journal of Colloid and Interface Science*, 343(1):301–305, March 2010.

[31] Roar Søndergaard, Markus Hösel, Dechan Angmo, Thue T. Larsen-Olsen, and Frederik C. Krebs. Roll-to-roll fabrication of polymer solar cells. *Materials Today*, 15(1-2):36–49, January 2012.

[32] Jang-Ung Park, Matt Hardy, Seong Jun Kang, Kira Barton, Kurt Adair, Deep kishore Mukhopadhyay, Chang Young Lee, Michael S. Strano, Andrew G. Alleyne, John G. Georgiadis, Placid M. Ferreira, and John A. Rogers. High-resolution electrohydrodynamic jet printing. *Nature Materials*, 6(10):782–789, October 2007.

[33] Anke Teichler, Jolke Perelaer, and Ulrich S. Schubert. Inkjet printing of organic electronics - comparison of deposition techniques and state-of-the-art developments. *Journal of Materials Chemistry C*, 1(10):1910–1925, February 2013.

[34] Volker Zöllmer, Matthias Müller, Mike Renn, Matthias Busse, Ingo Wirth, Dirk Godlinski, and Mike Kardos. Printing with aerosols. *European coatings journal*, 7(08):46, 2006.

[35] Max Shtein, Peter Peumans, Jay B. Benziger, and Stephen R. Forrest. Micropatterning of small molecular weight organic semiconductor thin films using organic vapor phase deposition. *Journal of Applied Physics*, 93(7):4005–4016, April 2003.

[36] Jae Won Jeong, Woon Ik Park, Lee-Mi Do, Jong-Hyun Park, Tae-Heon Kim, Geesung Chae, and Yeon Sik Jung. Nanotransfer Printing with sub-10 nm Resolution Realized using Directed Self-Assembly. *Advanced Materials*, 24(26):3526–3531, July 2012.

[37] James Shaw-Stewart, Thomas Mattle, Thomas Lippert, Matthias Nagel, Frank Nüesch, and Alexander Wokaun. The optimisation of the laser-induced forward transfer process for fabrication of polyfluorene-based organic light-emitting diode pixels. *Applied Surface Science*, 278:341–346, August 2013.

[38] Anuja De Silva and Christopher K. Ober. Patterning by Photolithography. In Wolfgang Knoll and Rigoberto C. Advincula, editors, *Functional Polymer Films*, pages 475–499. Wiley-VCH Verlag GmbH & Co. KGaA, 2011.

[39] Hao Zhang, M.D. Poliks, and B. Sammakia. A Roll-to-Roll Photolithography Process for Establishing Accurate Multilayer Registration on Large Area Flexible Films. *Journal of Display Technology*, 6(11):571–578, November 2010.

[40] Markus Hösel, Henrik F. Dam, and Frederik C. Krebs. Development of Lab-to-Fab Production Equipment Across Several Length Scales for Printed Energy Technologies, Including Solar Cells. *Energy Technology*, February 2015.

[41] Frederik C. Krebs, Jan Fyenbo, and Mikkel Jørgensen. Product integration of compact roll-to-roll processed polymer solar cell modules: methods and manufacture using flexographic printing, slot-die coating and rotary screen printing. 20(41):8994–9001, October 2010.

[42] Norman S. Allen. *Photochemistry and photophysics of polymer materials*. Wiley, Oxford, 2010.

[43] Daniel P. Sanders. Advances in Patterning Materials for 193 nm Immersion Lithography. *Chemical Reviews*, 110(1):321–360, January 2010.

[44] Mária Péter, François Furthner, Jochem Deen, Wim J. M. de Laat, and Erwin R. Meinders. Lithographic patterning of metals on flexible plastic foils. *Thin Solid Films*, 517(10):3081–3086, March 2009.

[45] Gerwin Gelinck, Paul Heremans, Kazumasa Nomoto, and Thomas D. Anthopoulos. Organic Transistors in Optical Displays and Microelectronic Applications. *Advanced Materials*, 22(34):3778–3798, September 2010.

[46] Janglin Chen, Jia-Chong Ho, Glory Chen, and Cheng-Chung Lee. Invited Paper: Reliability Improvement of Flexible AMOLED Based on Auxiliary Functional Film Technology. *SID Symposium Digest of Technical Papers*, 43(1):264–267, June 2012.

[47] J. Chen and C. T. Liu. Technology Advances in Flexible Displays and Substrates. *IEEE Access*, 1:150–158, 2013.

[48] Younan Xia and George M. Whitesides. Soft Lithography. *Annual Review of Materials Science*, 28(1):153–184, 1998.

[49] Marc J. Madou. *Fundamentals of Microfabrication: The Science of Miniaturization, Second Edition.* CRC Press, March 2002. Google-Books-ID: 9bk3gJeQKBYC.

[50] Boseok Kang, Wi Hyoung Lee, and Kilwon Cho. Recent advances in organic transistor printing processes. *ACS applied materials & interfaces*, 5(7):2302–15, April 2013.

[51] C. Donzel, M. Geissler, A. Bernard, H. Wolf, B. Michel, J. Hilborn, and E. Delamarche. Hydrophilic Poly(dimethylsiloxane) Stamps for Microcontact Printing. *Advanced Materials*, 13(15):1164–1167, August 2001.

[52] Dawen Li and L. Jay Guo. Organic thin film transistors and polymer light-emitting diodes patterned by polymer inking and stamping. *J. Phys. D: Appl. Phys.*, 41(10):105115, 2008.

[53] Yueh-Lin Loo, Robert L. Willett, Kirk W. Baldwin, and John A. Rogers. Additive, nanoscale patterning of metal films with a stamp and a surface chemistry mediated transfer process: Applications in plastic electronics. *Appl. Phys. Lett.*, 81(3):562–564, July 2002.

[54] T. L. Breen C. R. Kagan. Patterning Organic-Inorganic Thin-Film Transistors Using Microcontact Printed Templates. *Applied Physics Letters*, 79(21):3536–3538, 2001.

[55] B. Michel, A. Bernard, A. Bietsch, E. Delamarche, M. Geissler, D. Juncker, H. Kind, J. P. Renault, H. Rothuizen, H. Schmid, P. Schmidt-Winkel, R. Stutz, and H. Wolf. Printing meets lithography: Soft approaches to high-resolution patterning. *IBM Journal of Research and Development*, 45(5):697–719, September 2001.

[56] Emmanuel Delamarche, Heinz Schmid, Bruno Michel, and Hans Biebuyck. Stability of molded polydimethylsiloxane microstructures. *Advanced Materials*, 9(9):741–746, January 1997.

[57] Joseph E. Petrzelka and David E. Hardt. Static load-displacement behavior of PDMS microfeatures for soft lithography. *J. Micromech. Microeng.*, 22(7):075015, 2012.

[58] Younan Xia, Dong Qin, and George M. Whitesides. Microcontact printing with a cylindrical rolling stamp: A practical step toward automatic manufacturing of patterns with submicrometer-sized features. *Advanced Materials*, 8(12):1015–1017, December 1996.

[59] Jinsoo Noh, Dongsun Yeom, Chaemin Lim, Hwajin Cha, Jukyung Han, Junseok Kim, Yongsu Park, Vivek Subramanian, and Gyoujin Cho. Scalability of Roll-to-Roll Gravure-Printed Electrodes on Plastic Foils. *IEEE Transactions on Electronics Packaging Manufacturing*, 33(4):275–283, October 2010.

[60] A. de la Fuente Vornbrock, J. M. Ding, D. Sung, Huai-Yuan Tseng, and V. Subramanian. Printing and scaling of metallic traces and capacitors using a laboratory-scale rotogravure press. In *2009 Flexible Electronics Displays Conference and Exhibition*, pages 1–7, February 2009.

[61] D. Sung, A. de la Fuente Vornbrock, and Vivek Subramanian. Scaling and Optimization of Gravure-Printed Silver Nanoparticle Lines for Printed Electronics. *IEEE Transactions on Components and Packaging Technologies*, 33(1):105–114, March 2010.

[62] Gerd Grau, Jialiang Cen, Hongki Kang, Rungrot Kitsomboonloha, William J. Scheideler, and Vivek Subramanian. Gravure-printed electronics: recent progress in tooling development, understanding of printing physics, and realization of printed devices. *Flexible and Printed Electronics*, 1(2):023002, 2016.

[63] Rungrot Kitsomboonloha, S. J. S. Morris, Xiaoying Rong, and Vivek Subramanian. Femtoliter-Scale Patterning by High-Speed, Highly Scaled Inverse Gravure Printing. *Langmuir*, 28(48):16711–16723, December 2012.

[64] Xiuyan Yin and Satish Kumar. Flow visualization of the liquid emptying process in scaled-up gravure grooves and cells. *Chemical Engineering Science*, 61(4):1146–1156, February 2006.

[65] Leonard W. Schwartz. Numerical modeling of liquid withdrawal from gravure cavities in coating operations; the effect of cell pattern. *Journal of Engineering Mathematics*, 42(3-4):243–253, April 2002.

[66] Hongki Kang, Rungrot Kitsomboonloha, Jaewon Jang, and Vivek Subramanian. High-Performance Printed Transistors Realized Using Femtoliter Gravure-Printed Sub-10 μm Metallic Nanoparticle Patterns and Highly Uniform Polymer Dielectric and Semiconductor Layers. *Advanced Materials*, 24(22):3065–3069, June 2012.

[67] Rungrot Kitsomboonloha, S. J. S. Morris, Xiaoying Rong, and Vivek Subramanian. Femtoliter-Scale Patterning by High-Speed, Highly Scaled Inverse Gravure Printing. *Langmuir*, 28(48):16711–16723, December 2012.

[68] P. C. Duineveld. The stability of ink-jet printed lines of liquid with zero receding contact angle on a homogeneous substrate. *Journal of Fluid Mechanics*, 477:175–200, February 2003.

[69] Dan Soltman and Vivek Subramanian. Inkjet-Printed Line Morphologies and Temperature Control of the Coffee Ring Effect. *Langmuir*, 24(5):2224–2231, March 2008.

[70] Ho Anh Duc Nguyen, Kee-Hyun Shin, and Dongjin Lee. Effect of process parameters on fidelity of printed line width in high resolution roll-to-roll gravure printing. *Jpn. J. Appl. Phys.*, 53(5S3):05HC04, May 2014.

[71] Takashi Kushida, Takashi Nagase, and Hiroyoshi Naito. Angular distribution of field-effect mobility in oriented poly[5,5-bis(3-dodecyl-2-thienyl)-2,2-bithiophene] fabricated by roll-transfer printing. *Applied Physics Letters*, 104(9):093304, March 2014.

[72] A. Lorenz, A. Senne, J. Rohde, S. Kroh, M. Wittenberg, K. Krüger, F. Clement, and D. Biro. Evaluation of Flexographic Printing Technology for Multi-busbar Solar Cells. *Energy Procedia*, 67:126–137, April 2015.

[73] Cheng-Yao Lo, O.-H. Huttunen, J. Hiitola-Keinanen, J. Petaja, H. Fujita, and H. Toshiyoshi. MEMS-Controlled Paper-Like Transmissive Flexible Display. *Journal of Microelectromechanical Systems*, 19(2):410–418, April 2010.

[74] Cheng-Yao Lo, Johanna Hiitola-Keinänen, Olli-Heikki Huttunen, Jarno Petäjä, Jukka Hast, Arto Maaninen, Harri Kopola, Hiroyuki Fujita, and Hiroshi Toshiyoshi. Novel Roll-to-roll Lift-off Patterned Active-matrix Display on Flexible Polymer Substrate. *Microelectron. Eng.*, 86(4-6):979–983, April 2009.

[75] Helmut Kipphan, editor. *Handbook of print media: technologies and production methods*. Springer, Berlin ; New York, 2001.

[76] XTouch Sensors. `http://www.unipixel.com/home/products/xtouch-sensors/`Acessed: 18/09/2015.

[77] Robert Petcavich and Reed Killion. Low-visibility antennas based flexographic printing, October 2013.

[78] Robert J. Petcavich. Polarizer resistive touch screen, February 2014.

[79] Frederik C. Krebs, Nieves Espinosa, Markus Hösel, Roar R. Søndergaard, and Mikkel Jørgensen. 25th Anniversary Article: Rise to Power - OPV-Based Solar Parks. *Advanced Materials*, 26(1):29–39, January 2014.

[80] A. C. Huebler, F. Doetz, H. Kempa, H. E. Katz, M. Bartzsch, N. Brandt, I. Hennig, U. Fuegmann, S. Vaidyanathan, J. Granstrom, S. Liu, A. Sydorenko, T. Zillger, G. Schmidt, K. Preissler, E. Reichmanis, P. Eckerle, F. Richter, T. Fischer, and U. Hahn. Ring oscillator fabricated completely by means of mass-printing technologies. *Organic Electronics*, 8(5):480–486, October 2007.

[81] Bruce E. Kahn, Liam H. O'Hara, Chip Tonkin, Howard E. Nelson, William J. Ray, Chris Wargo, and Michael Mastropietro. The Impact of Plate Imaging Techniques on Flexographic Printed Conductive Traces. *Journal of Imaging Science and Technology*, 56(4):1–8, December 2012.

[82] Jeongdai Jo, Jong-Su Yu, Taik-Min Lee, and Dong-Soo Kim. Fabrication of Printed Organic Thin-Film Transistors Using Roll Printing. *Japanese Journal of Applied Physics*, 48(4):04C181, April 2009.

[83] He Yan, Zhihua Chen, Yan Zheng, Christopher Newman, Jordan R. Quinn, Florian Dötz, Marcel Kastler, and Antonio Facchetti. A high-mobility electron-transporting polymer for printed transistors. *Nature*, 457(7230):679–686, February 2009.

[84] G. C. Schmidt, M. Bellmann, B. Meier, M. Hambsch, K. Reuter, H. Kempa, and A. C. Hübler. Modified mass printing technique for the realization of source/drain electrodes with high resolution. *Organic Electronics*, 11(10):1683–1687, October 2010.

[85] Wenlong Cheng, Nokyoung Park, M. Todd Walter, Mark R. Hartman, and Dan Luo. Nanopatterning self-assembled nanoparticle superlattices by moulding microdroplets. *Nature Nanotechnology*, 3(11):682–690, November 2008.

[86] Sanha Kim, Hossein Sojoudi, Hangbo Zhao, Dhanushkodi Mariappan, Gareth H. McKinley, Karen K. Gleason, and A. John Hart. Ultrathin high-resolution flexographic printing using nanoporous stamps. *Science Advances*, 2(12):e1601660, December 2016.

[87] Zina Weygand. *The Blind in French Society from the Middle Ages to the Century of Louis Braille*. Stanford University Press, August 2009.

[88] Koenig and Bauer. History | Koenig and Bauer | we're on it. `https://www.koenig-bauer.com/en/holding/history/`.

[89] Charles Goodyear. Improvements in India-Rubber Fabrics, June 1844. Patent US3633 A.

[90] John L. Kingsley. Improvement in compounds for stereotype-plates, January 1853. Cooperative Classification C08L9/00, C07C327/00.

[91] Flexographic Technical Association. *Flexography: principles and practices 6.0.* 2013. OCLC: 863440545.

[92] Antoine Béchamp. De l'action des protosels de fer sur la nitronaphtaline et la nitrobenzine. nouvelle méthode de formation des bases organiques artificielles de Zinin. *Annales de chimie et de physique.*, 42:186–196, 1854.

[93] Serge V Lebedev. Verfahren zur Darstellung von Diolefinen, June 1933. IPC:DE577630A.

[94] J. Page Crouch and Page J. Crouch. *Flexography Primer*. Printing Industries Pr, 2 edition edition, June 1998.

[95] Joseph Rach. Flexography: Art or Science? *Paperboard Packaging*, 91(1):26–27, January 2006.

[96] Jacqueline M. Fetsko and William C. Walker. Measurements of ink transfer in the printing of coated papers. *American Ink Maker*, 11(33):38, 1995.

[97] William C. Walker and J.M. Fetsko. A Concept of Ink Transfer in Printing. *American Ink Maker*, 33(12), 1995.

[98] Yong-Hua Xang. A new approach for modelling ink transfer. *Tappi Journal*, 76(7):97–103, July 1993.

[99] Jacqueline M. Fetsko and William C. Walker. Measurements of ink transfer in the printing of coated papers. *American Ink Maker*, 11(33):38, 1995.

[100] Samya el sherbiny and S Elsayad. *A Review of Printing Ink Transfer Equations.* January 2002.

[101] Dein Wang. *An investigation of the applicability of Walker and Fetsko ink transfer equation on and the influence of ink viscosity on heat set ink used on the web offset process.* PhD thesis, Rochester Institute of Technology, 1986.

[102] Kodak. FlexcelNX_systemfamily_brochure - kodak. `https://www.kodak.com/uploadedFiles/Graphics/Products/Flexographic/FLEXCEL_NX_Digital_Flexographic_System/Resources/FlexcelNX_SystemFamily_Brochure.pdf`.

[103] D C Bould, S M Hamblyn, D T Gethin, and T C Claypole. Effect of impression pressure and anilox specification on solid and halftone density. *Proceedings of the Institution of Mechanical Engineers, Part B: Journal of Engineering Manufacture*, 225(5):699–709, May 2011.

[104] Michael James Joyce, Dr Paul D. Fleming Iii, Sai G. R. Avuthu, Sepehr Emamian, Ali Eshkeiti, Dr Massood Atashbar, and Tony Donato. Contribution of Flexo Process Variables to Fine Line Ag Electrode Performance. *International Journal of Engineering Research and Technology*, Vol. 3 - Issue 8 (August - 2014), September 2014.

[105] Satish Kumar. Liquid Transfer in Printing Processes: Liquid Bridges with Moving Contact Lines. *Annual Review of Fluid Mechanics*, 47(1):67–94, 2015.

[106] J. H De Grâce, Patrice J Mangin, International Association of Research Institutes for the Graphic Arts Industry, and Research Conference. *A mechanistic approach to ink transfer. Part II.* Pulp and Paper Research Institute of Canada, Pointe Claire, Québec, 1987.

[107] Anton A. Darhuber, Sandra M. Troian, and Sigurd Wagner. Physical mechanisms governing pattern fidelity in microscale offset printing. *Journal of Applied Physics*, 90(7):3602–3609, October 2001.

[108] Anton A. Darhuber, Sandra M. Troian, Jeffrey M. Davis, Scott M. Miller, and Sigurd Wagner. Selective dip-coating of chemically micropatterned surfaces. *Journal of Applied Physics*, 88(9):5119, 2000.

[109] A. V. Chadov and E. D. Yakhnin. *Investigation of the transfer of a liquid from one solid-surface to another. 1. slow transfer-method of approximate calculation*, volume 41. PLENUM PUBL CORP CONSULTANTS BUREAU, 233 SPRING ST, NEW YORK, NY 10013, 1979.

[110] E. D. Yakhnin and A. V. Chadov. Investigation of the transfer of a liquid from one solid-surface to another. 2. Dynamic transfer. *COLLOID JOURNAL OF THE USSR*, 45(6):1034–1039, 1983.

[111] Bian Qian and Kenneth S. Breuer. The motion, stability and breakup of a stretching liquid bridge with a receding contact line. *Journal of Fluid Mechanics*, 666:554–572, January 2011.

[112] Srinivas R. Ranabothu, Cassandra Karnezis, and Lenore L. Dai. Dynamic wetting: Hydrodynamic or molecular-kinetic? *Journal of Colloid and Interface Science*, 288(1):213–221, August 2005.

[113] Terence D. Blake. The physics of moving wetting lines. *Journal of Colloid and Interface Science*, 299(1):1–13, July 2006.

[114] Shawn Dodds, Marcio S. Carvalho, and Satish Kumar. The dynamics of three-dimensional liquid bridges with pinned and moving contact lines. *Journal of Fluid Mechanics*, 707:521–540, September 2012.

[115] Liming Wang and Thomas J. McCarthy. Shear Distortion and Failure of Capillary Bridges. Wetting Information Beyond Contact Angle Analysis. *Langmuir*, 29(25):7776–7781, June 2013.

[116] Wei-Xi Huang, Seung-Hyun Lee, Hyung Jin Sung, Taik-Min Lee, and Dong-Soo Kim. Simulation of liquid transfer between separating walls for modeling micro-gravure-offset printing. *International Journal of Heat and Fluid Flow*, 29(5):1436–1446, October 2008.

[117] Xiaoguang Zhang. Dynamics of drop formation in viscous flows. *Chemical Engineering Science*, 54(12):1759–1774, June 1999.

[118] Hyun Wook Kang, Hyung Jin Sung, Taik-Min Lee, Dong-Soo Kim, and Chang-Jin Kim. Liquid transfer between two separating plates for micro-gravure-offset printing. *Journal of Micromechanics and Microengineering*, 19(1):015025, January 2009.

[119] D. Deganello, A. J. Williams, T. N. Croft, A. S. Lubansky, D. T. Gethin, and T. C. Claypole. Level-set method for the modelling of liquid bridge formation and break-up. *Computers & Fluids*, 40(1):42–51, January 2011.

[120] Jyun-Ting Wu, Marcio S. Carvalho, and Satish Kumar. Transfer of rate-thinning and rate-thickening liquids between separating plates and cavities. *Journal of Non-Newtonian Fluid Mechanics*, 255:57–69, May 2018.

[121] Malcolm C. Gower. Industrial applications of laser micromachining. *Opt. Express, OE*, 7(2):56–67, July 2000.

[122] Heliatek – The future is light. `http://www.heliatek.com/en/`.

[123] M-Solv Laser Micromachining systems for Photovoltaic and Micro-electronics manufacture Large Area Electronics Micromachining Micro deposition Spray Laser Inkjet Hybrid Micromachining Hybrid Technology Advanced Laser processing System multiplexing Intercon. http://www.m-solv.com/.

[124] Aart Schoonderbeek. Laser Processing of Thin Films for Photovoltaic Applications. *Journal of Laser Micro/Nanoengineering*, 5(3):248–255, December 2010.

[125] Charles A. Bishop. *Vacuum deposition onto webs, films, and foils.* William Andrew/Elsevier, Amsterdam ; London, 2nd ed. edition, 2011.

[126] V. Pynttari, R. Makinen, J. Lilja, V. Pekkanen, P. Mansikkamaki, and M. Kivikoski. Significance of Conductivity and Thickness of Thin Inkjet Printed Microstrip Lines. In *2008 12th IEEE Workshop on Signal Propagation on Interconnects*, pages 1–4, May 2008.

[127] Brian Derby. Inkjet Printing of Functional and Structural Materials: Fluid Property Requirements, Feature Stability, and Resolution. *Annual Review of Materials Research*, 40(1):395–414, 2010.

[128] Roar Søndergaard, Markus Hösel, Dechan Angmo, Thue T. Larsen-Olsen, and Frederik C. Krebs. Roll-to-roll fabrication of polymer solar cells. *Materials Today*, 15(1-2):36–49, January 2012.

[129] Gerard Cummins and Marc P.Y. Desmulliez. Inkjet printing of conductive materials: a review. *Circuit World*, 38(4):193–213, November 2012.

[130] David J. Beesley, James Semple, Lethy Krishnan Jagadamma, Aram Amassian, Martyn A. McLachlan, Thomas D. Anthopoulos, and John C. deMello. Sub-15-nm patterning of asymmetric metal electrodes and devices by adhesion lithography. *Nature Communications*, 5:3933, May 2014.

[131] James Semple, Stephan Rossbauer, Claire H. Burgess, Kui Zhao, Lethy Krishnan Jagadamma, Aram Amassian, Martyn A. McLachlan, and Thomas D. Anthopoulos. Radio Frequency Coplanar ZnO Schottky Nanodiodes Processed from Solution on Plastic Substrates. *Small*, 12(15):1993–2000, April 2016.

[132] J. Semple, G. Wyatt-Moon, D. G. Georgiadou, M. A. McLachlan, and T. D. Anthopoulos. Semiconductor-Free Nonvolatile Resistive Switching Memory Devices Based on Metal Nanogaps Fabricated on Flexible Substrates via Adhesion Lithography. *IEEE Transactions on Electron Devices*, 64(5):1973–1980, May 2017.

[133] N J Copeland, A Jack, and L Harland. In-Register In-Vacuum Pattern Printing - From Wish to Reality. In *52nd Annual Technical Conference Proceedings*, page 712, Santa Clara, CA, May 2009. Society of Vacuum Coaters.

[134] Kyosuke Nagatomi, Teruki Kajiwara, Hisashi Ookuma, and Ryo Tachibana. Process for producing metallized plastic film, May 1989.

[135] Bobst. SelectMet - Overview. `http://www.bobst.com/usen/products/equipments/overview/machine/selectmet/#.V7q64vkrKHs`, 2016.

[136] J. Song. Mechanics of stretchable electronics. *Current Opinion in Solid State and Materials Science*, 2015.

[137] Jongsu Lee, Jinwoo Seong, Janghoon Park, Sungsik Park, Dongjin Lee, and Kee-Hyun Shin. Register control algorithm for high resolution multilayer printing in the roll-to-roll process. *Mechanical Systems and Signal Processing*.

[138] ER Patchett, Aled Williams, and Ziqian Ding. A high-yield vacuum-evaporation-based R2r-compatible fabrication route for organic electronic circuits. *Organic Electronics*, 2014.

[139] J.S. Lewis and M.S. Weaver. Thin-Film Permeation-Barrier Technology for Flexible Organic Light-Emitting Devices. *IEEE Journal of Selected Topics in Quantum Electronics*, 10(1):45–57, January 2004.

[140] Stephan Kirchmeyer. The OE-A roadmap for organic and printed electronics: creating a guidepost to complex interlinked technologies, applications and markets. *Transl. Mater. Res.*, 3(1):010301, 2016.

[141] Jenna R. Jambeck, Roland Geyer, Chris Wilcox, Theodore R. Siegler, Miriam Perryman, Anthony Andrady, Ramani Narayan, and Kara Lavender Law. Plastic waste inputs from land into the ocean. *Science*, 347(6223):768–771, February 2015.

Chapter 3

Experimental Materials and Methods

3.1 In Vacuum Flexography Letterpress

The introduction and literature review have highlighted the main features of a flexography printing press. In this research, the printing press is required to create patterns which can be used in electronics fabrication and representative of the ink transfer from plate to substrate to provide reliable and accurate results when the key variables of printing speed and pressure are varied. To this end, a suitable flexography letter press system was designed, developed, and fabricated to fit within the Edwards 306A vacuum chamber and create flexography pattern with a single rotation of the impression drum. This section describes the material and design choices and demonstrates that the system is a valid means of testing flexography printing.

3.1.1 Design of printing system

The printing system was designed to be held above the evaporation source. The printing system was custom designed and built to fit the existing equipment and fulfil the necessary variation of printing pressure and speed for the experiments. Unlike common industrial systems the plate and impression drum were pressure controlled, not engagement distance. This allows the particular pressure experiments to be conducted, and is discussed more in Chapter 5. The main components were a central impression drum which was held above the evaporation source and driven by motor and the printing head held against the impression drum, which is described more below. Using this rudimentary but effective system, the printing head could be inked using the central impression drum loaded with an inking pad (as described in section 3.1.4), and then the inked printing head could pattern the substrate held on the impression drum, which would subsequently pass over the evaporation source, to create

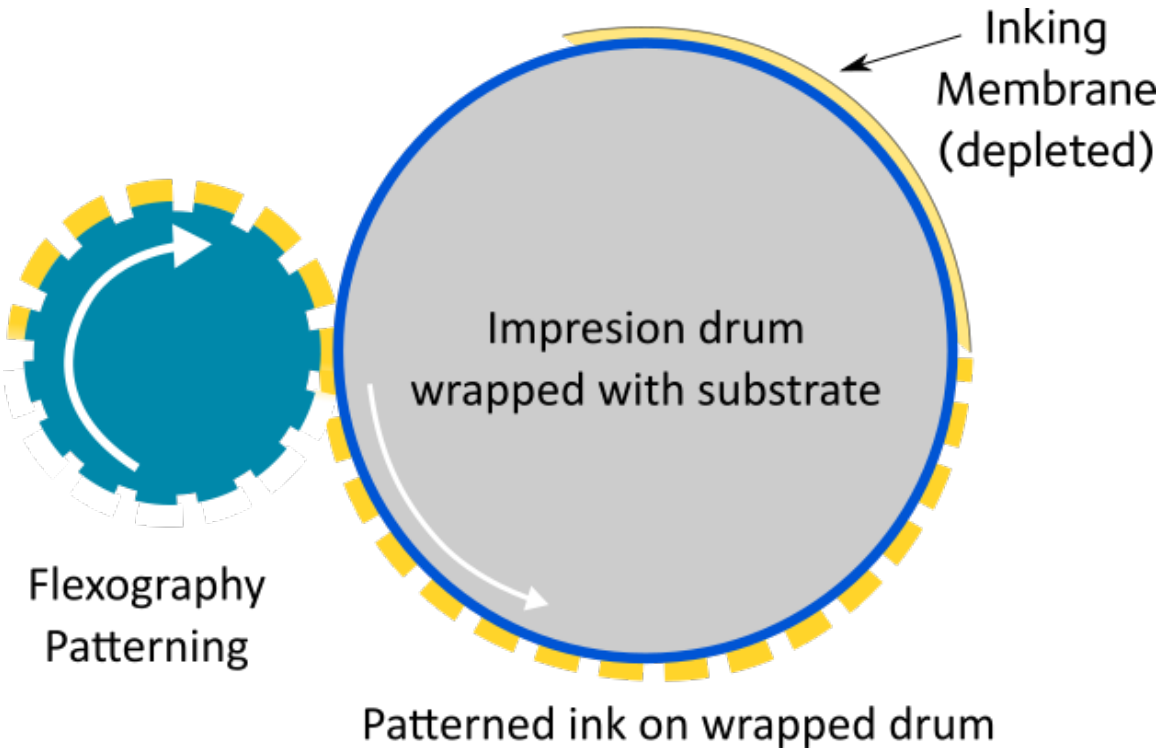


Figure 3.1: Schematic of the flexography-like set-up with the inking pad having passed through the contact region, to transfer ink to the printing plate, which subsequently patterns the substrate wrapped on the process drum.

the selective metallised patterns. All theses steps were performed in a single rotation as schematised in Figure 3.1, with each printed pattern being collected for analysis after a single rotation of the impression drum, and the system reset. Each step and component is described in the following sections.

The custom built design is illustrated in Figure 3.2 and the supporting principle is shown in the free body force diagram Figure 3.3. It shows that the driven impression drum and the printing roller are held next to each other with axes parallel and are then brought into line contact by the gravitational force of hanging dead weight from the respective axes. The design provides for an electronic motor which can vary the speed, and the dead weights can vary the nominal line force (F_L) by:

$$F_L = \frac{2W \times g}{C_l} \tag{3.1}$$

Where W is the mass of each dead weight (in Kg), for which there is one suspended on each side of the contact length (C_l) (drum width) and the acceleration due to gravity (g) is taken to be constant: $9.81 m.s^{-1}$.

The drive of the print head was achieved by introducing circular cross-section polyurethane (PU) drive belts with grooved cogs of appropriate ratios and brass

journal bearings. PU was chosen as it is a commonly used rubber for vacuum systems, as it does not out-gas. Journal bearings were used so the system was simple and reliable with brass construction for the contact points and load bearing parts. The tensioning wires were made from nylon which has a high stiffness. The drive system was designed so it did not impose any radial force to the rollers' contact. A full design of the custom built system is shown in the appendix.

3.1.2 Testing of the foam backing

The stress strain behaviour of the foam is particularly important and so was characterised. The foam's stress strain behaviour was found by loading the foam. A sample (5x5x1cm) was placed on digital weighing scales, under a rigid plate of known mass with dead weights, similar to the loading in situ. The results are shown in Figure 3.4. The compression strain was measured with a micrometer, with three repeat measurements. The stress uncertainty was due to the mass which has largest relative strain error of $\frac{0.005g}{20g} = 0.025\%$. This foam was chosen for its low stiffness which is favourable for probing a a greater range of printing effects within the possible experimental limits.

3.1.3 Fabrication and design of print plate

The print plate was fabricated from poly-dimethyl siloxane (PDMS). PDMS was chosen for its high resolution feature reproduction in casting and its chemical inertness. Also its visco-elastic properties are similar to standard commercial printing plates. This material choice seen in other work, looking to extend the printing resolution limit of flexography processes, by borrowing from successes in μCP field of research. [1, 2]

The pattern to be printed was created by cutting grooves into a silicon wafer, casting PDMS onto this to create a flat master plate. This was then held in a cylindrical forme to create the printing sleeve plate, see Figure 3.5.

In detail, the fabrication process begun with a single side polished $500\mu m$ thick silicon wafer (procured from UniversityWafer.com) and cut to relevant size. Grooves were cut into this silicon wafer's polished surface, using a diamond saw (Loadpoint, MicroAce), see inset A in the plate fabrication process schematic in Figure 3.5. These grooves were cut to a range of widths, spacings and depths, see Table 3.1 in sets of 10.

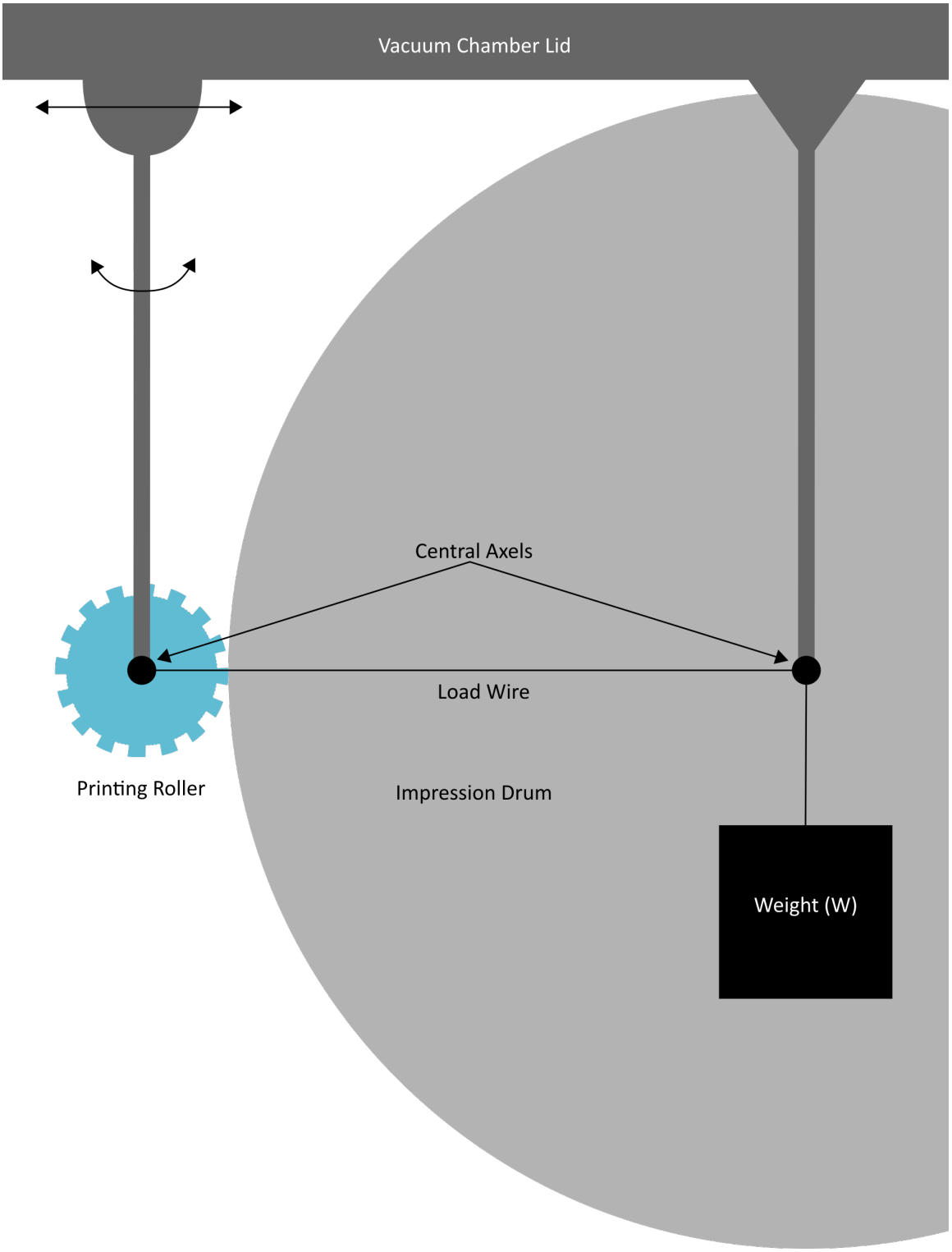


Figure 3.2: Design of the custom-built letterpress flexography system to be operated within a vacuum chamber. The printing roller and impression drum are have a consistent scale.

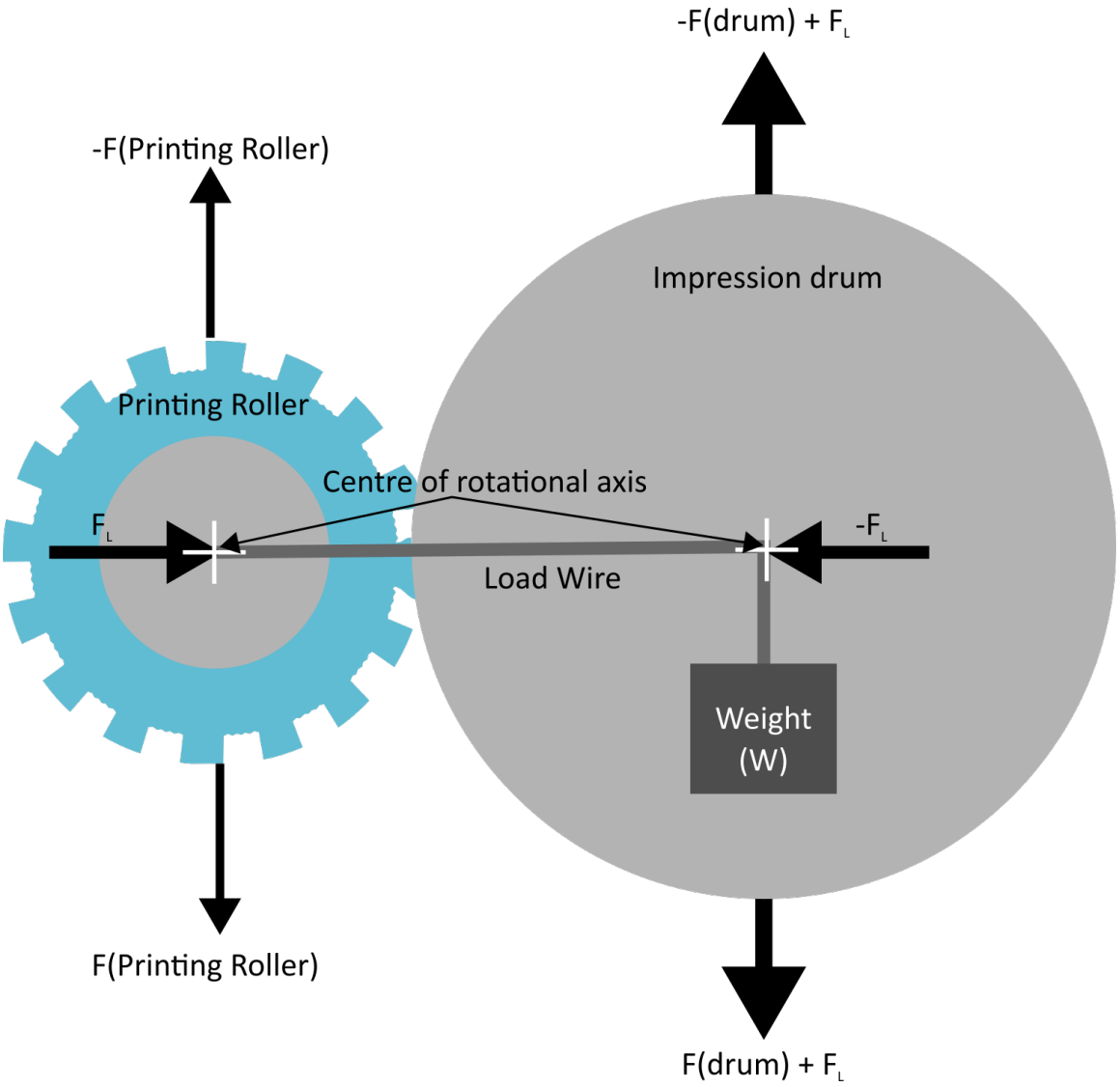
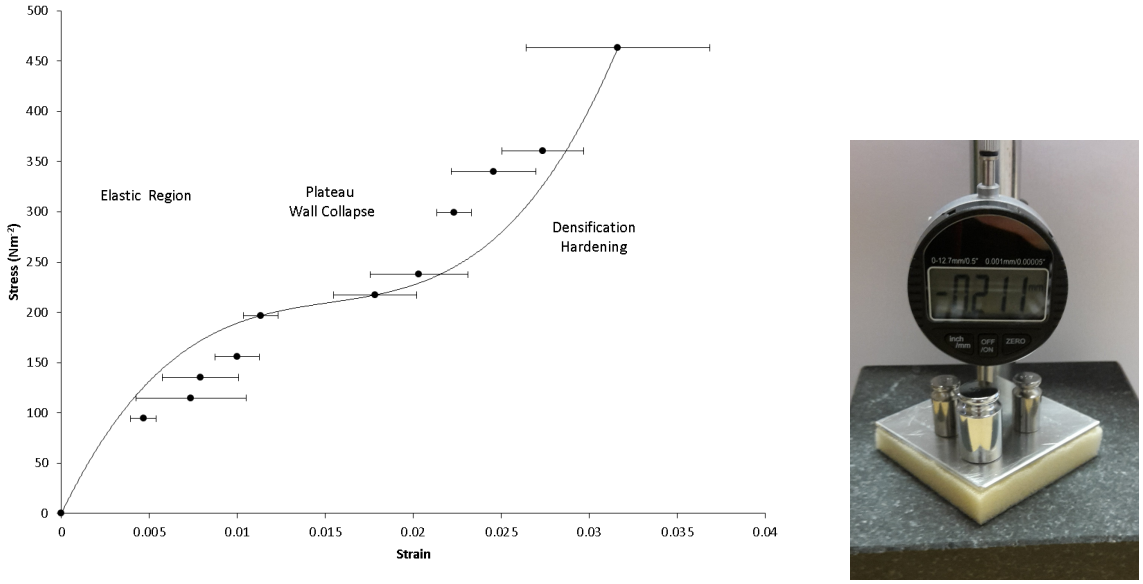


Figure 3.3: Free body force diagram of the principle behind controlling the printing line force, using a hanging dead weight.



a. b.

Figure 3.4: a. Stress strain behaviour of the plate backing foam material. b. Example of the foam being loaded in the experimental set up as described in section 3.1.2 . The 3 mechanisms of strain are labelled over there representative regions and a polynomial fit has been added to further show the non linear stress strain behaviour.

Next, PDMS (procured from Dow Corning) with a base to curing agent ratio of 10:1, was cast onto the cut silicon, within a 3mm deep forme which was 110x30mm long and wide. This flat rigid printing plate was cured at $100°C$ for 20 minutes and removed. Then it was placed within a metal collar, which had a closed base and an open end, and with an inner circumference equal to the PDMS master plate's length. A rod, positioned axially parallel in the centre of the collar, had a diameter equal to the printing roller, such that the space between central shaft and cured PDMS master could be filled with 10:1 ratio liquid PDMS mixture, which was subsequently cured at $100°C$ for at least 20 minutes. A release agent was used between the cut silicon and PDMS, and also between the PDMS layers, consisting of isopropanal (IPA) mixed with 5% volume consumer branded washing up liquid. This release layer ensured complete, non-damaging but high fidelity separation of the cylindrical printing plate from the flat PDMS printing plate master as used in reference [3]. This double casting method, Figure 3.5, meant that the crystalline smooth surface of the silicon master was replicated as the printing plate relief's face, rather than the cutting grooves.

The diamond saw blade had a profile of $20\mu m$ and so the actual plate recessed feature dimensions were slightly reduced. Also there is a theoretical shrinkage of the PDMS (3%) with each casting which reduced the actual plate relief feature di-

mensions, see Table 3.1. The edge roughness of the silicon grooves was measured, using the same method as the printed lines which is described later, and found to be $0.048 \pm 0.036mm$ and $0.0083 \pm 0.0015mm$ for the peak-to-peak and root mean square line edge roughness respectively.

Table 3.1: Plate pattern nominal and line dimensions in micrometers, aspect and pattern ratios. Each set was cut in the silicon master 10 times, producing 9 lines on the final printing plate.

Width	Spacing	Actual Width	Depth	Aspect Ratio	Pattern Ratio
20	50	19	20	1.00	2.50
40	50	38	40	1.00	1.25
50	50	47	50	1.00	1.00
100	100	94	100	1.00	1.00
150	150	141	150	1.00	1.00
200	200	188	200	1.00	1.00
20	300	19	250	12.50	15.00
40	300	38	250	6.25	7.50
50	300	47	250	5.00	6.00
100	300	94	250	2.50	3.00
150	300	141	250	1.67	2.00
200	300	188	250	1.25	1.50
500	300	475	250	0.50	0.60
500	50	475	250	0.50	0.10

3.1.4 Anilox inking pad selection

To achieve consistent and reliable inking of the printing plate in vacuum, a system was devised to fit within the vacuum chamber. Instead of a standard anilox system, an inked surface was passed through the contact region, immediately after the impression drum begun to rotate. This was performed by placing an ink saturated membrane onto the impression drum, which had the same length as the printing plates circumference. A variety of membrane materials were trialled, by the most consistent and the one with no observable transfer of texture effects on the printed pattern was a paper tape. It adhered well to the impression drum, held sufficient ink to achieve patterning, but did not transfer excessive amounts to the plate, which would have been seen as remnant oil.

This inking membrane was bar coated with 1ml of oil (ink) (Krytox 1506 procured from Sigma Aldrich) over an area of $11.0 \times 4.5cm$, which was soaked for 5 minutes, before the excess was removed. The final mass of oil used was $0.25 \pm 0.05g$, on the

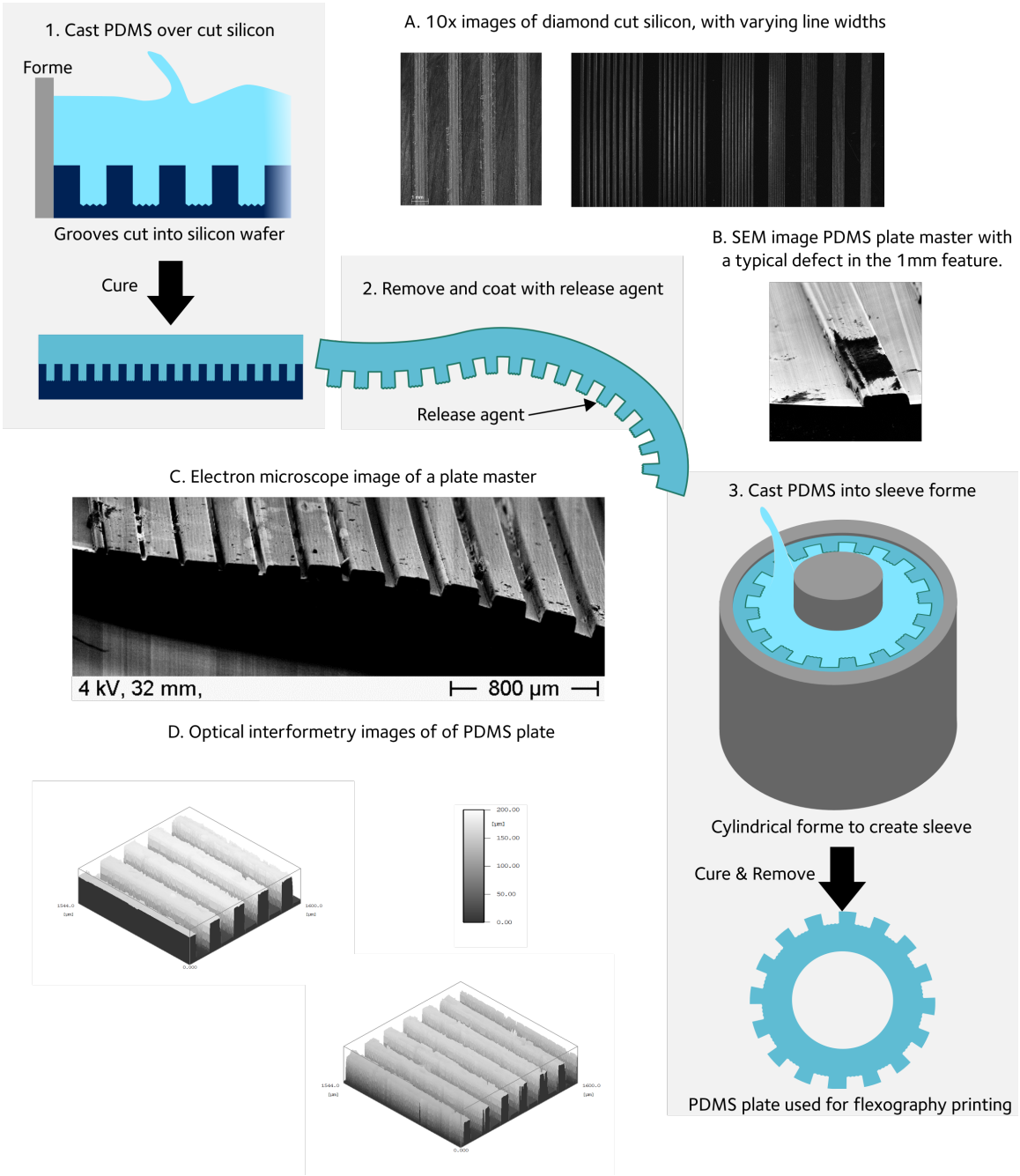


Figure 3.5: Plate fabrication process describing the 3 steps for double casting of of PDMS to create the printing plate sleeve. Example inserts show: A. optical microscopy images of the grooves that were cut into the silicon chips using a diamond blade saw, with the groves being formed by multiple contiguous cuts leading to rough groove floors, hence the double casting; B. an electron microscopy image of typical defect caused by improper handling, silicon debris from cutting or incomplete removal of the cured PDMS from the silicon master (accelerating voltage and working distance are the same as shown in C); C an electron microscopy image of a PDMS plate showing other foreign defects and the diamond cutting roughness on the relief of the pattern; D optical interferometry images of two sets of linewidths, 200μm and 150μm, displaying the floor roughness similar to that seen in the cut silicon.

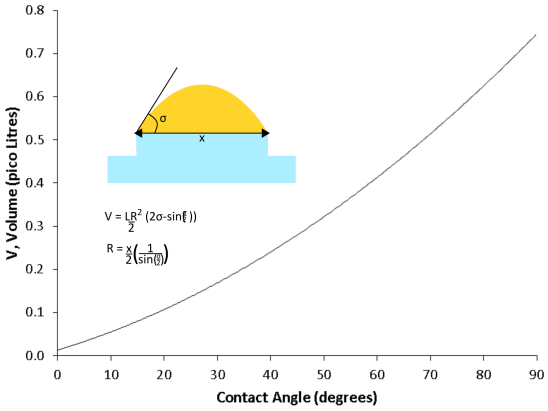


Figure 3.6: Change in oil volume on a $200\mu m$ wide plate feature with contact angle of the oil and the plate feature.

inking membrane. This means the maximum oil thickness across the membrane (i.e. with no absorption) was $30.2 \pm 6.1\mu m$ (however the pad had a thickness of $20\mu m$). In the literature review it was shown that the non absorbed ink splitting tends towards 50% transfer ratio, with higher speeds, as used in this work. Therefore the theoretical maximum thickness of oil transferred from the membrane to the substrate, via the patterned plate, would be $7.5 \pm 1.5\mu m$ which is one quarter (2 even ink splitting steps) of the volume held on the ink membrane, by weight. This value is the maximum physically available ink to be transferred, and it is likely to be an over-estimate of the actual volume of ink transferred, as this assumes all oil in the ink membrane can be split evenly with the plate, however the plate will be limited by the maximum volume possible on the plate features. Figure 3.6 shows that the volume of oil held on the relief features is much less than the available oil in the inking membrane, for a range on contact angles. Given that the inking membrane has an excess of oil, the transfer to the printing plate is not limited, as it is with anilox systems by cell volume and dimensions in standard flexography printing. Hence the amount transferred to the plate will always be the maximum possible, which for the printing force and speed ranges used here can be assumed to be of constant maximum volume given the contact angle.

3.2 Patterning Tests and Analysis

The patterning tests evaluated the effect of pressure and speed on the patterning print in terms of printed line edge quality and deviation from the nominal linewidth, as represented on the printing plate. This section describes the experimental plan to

cover the range of operational setting seen in industry, available with the equipment and necessary to test scientific theories of ink transfer as well as the methods for quantitative analysing the printed pattern.

3.2.1 Experimental method

Initial tests conducted with a plate with 1mm lines, in the cross direction, showed an obvious, to the eye, variation in print quality and so the following experiments were designed to further examine this variation, and achieve smaller higher pattern resolution. First a range of linewidths were tested, see Table 3.1.The nominal line force, Equation 3.1, was varied from 2x20g counter weights ($F_L = 13.1N.m^{-1}$) to 2x200g (nominal line force $F_L = 98.1N.m^{-1}$) and the speed varied from $10m.min^{-1}$ (the defining minimum 'high thoughput' speed) to $35m.min^{-1}$ which was limited by the equipment but still representative of high quality printing run in industry. The plate backing was steel for initial 1mm patterning, with which a foam backing material, as descibed in section 3.1.2, was also tested and proved to yield better print results so subsequent smaller patterns were printed using this foam plate backing.

The experiments were performed at a vacuum of $1 \times 10^{-4}mbar$ with the custom printing flexography apparatus, as previously described. The printing plate was wiped clean with IPA gently between each run, and as stated above a re-charged inking pad was used after each pattern as collected from a single rotation of the impression drum. The impression drum was wrapped in the PET substrate, with polyimide tape securing the ends. 10g of aluminium chips were evaporated from a tungsten boat, or 20g from a tungsten coil (both from Kurt J Lesker) with higher print speeds ($> 30m.min^{-1}$), during the print rotation of the impression drum. Evaporation was controlled by altering the current so that a steady rate of deposition, averaging $10nm.s^{-1}$, as measured by a quartz crystal monitor placed below the print head, was maintained. A shutter controlled the exposure of the drum. First, the impression rotated the inking pad through the contact region immediately before the shutter was opened. The printing plate created the oil pattern on the substrate which passed over the evaporation source. The motor to the central impression drum was switched off once the inking pad returned, around, to the printing head, simultaneously the shutter was closed and the power to the evaporation boated removed. The chamber was vented and the substrate carefully removed from the impression drum, with the first printed pattern removed for image analysis.

The entire print pattern was scanned into a computer using Cannon 24400XF scanner, with 4800dpi resolution in monochrome, and analysed using the image analyses described above. Initial 1mm line patterns were imaged partially using Leica M165C microscope and analysed using the ImageJ plugin, Analyze_Stripes.[4]

3.2.2 Print Quality Image Analysis

3.2.2.1 Development of computer image analysis

The code developed in this work first began as an ImageJ plugin called analyze_stripes.[4, 5, 6] During the initial trials it was found that this could only measure one stripe per analysis and so the original source MATLAB code, from which the plug-in had been converted to ImageJ was found.[7] This code's basic programming routine was developed into a new MATLAB code which extended the functionality to analyse an image with multiple stripes simultaneously and multiple images within a batch process. Once the particular set of lines for a pattern were cropped and oriented vertically, they could be analysed to find the average actual linewidth of the oiled regions and line edge roughness of the pattern set. Figure 3.7 shows an example of the image processing involved to make the measurements. The full code, with comments, can be found in the appendix. From the pixel positions the following line edge measurements were made of oiled (non metallized) regions:

- Linewidth: distance between two adjacent lines, each with a horizontal pixel positions (L_x, L_y) which define the oiled region, i.e. $x = 1, 3, 5..17$ and $y = 2, 4, 6..18$, so for each given oil line pattern (i):

$$L_i = average(L_y) - average(L_x),\ 1 < i < 9; \tag{3.2}$$

- Peak-to-peak roughness (P2P): maximum horizontal peak to valley height of both lines,

$$P2P_i = Max\left[max(L_x) - min(L_x),\ max(L_y) - min(L_y)\right]; \tag{3.3}$$

- Root mean square roughness (RMS) of the lines defining an oil pattern, given the number of pixels in each line (n):

$$RMS = \sqrt{\frac{\sum L_{xp} - \bar{L_x}}{n_x} + \frac{\sum L_{yp} - \bar{L_y}}{n_y}}. \tag{3.4}$$

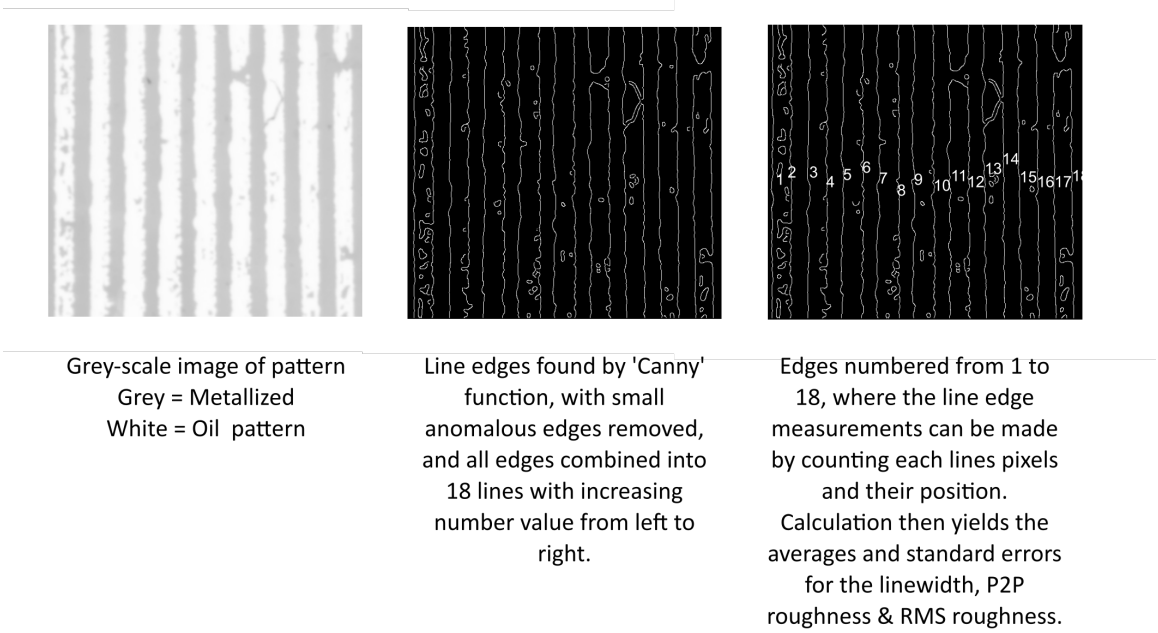


Figure 3.7: Images of a pattern created at $10m.min^{-1}$ with a nominal line force of $19.6N.m^{-1}$ at three stages of the image analysis, code shown in the appendix. The first image is the scanned pattern section (nominal linewidth $200\mu m$), where the dark grey regions are the areas of metal deposition and the light (white) areas are where the oil was patterned onto the substrate (for scale the image height is 4mm). The following image is taken part way through the image analysis code, showing the line edges identified with the built in 'Canny' function. It can sometimes identify anomalous small defects which are removed, and the detected edges are combined into the continuous line edges of the pattern. The final image shows the lines labelled, so they can be measured and the pixels' positions used to calculate the average and standard error of the linewidth, P2P roughness and RMS roughness of the printed line edges, see Equations 3.2, 3.3, and 3.4 above.

3.2.2.2 Statistical Analysis

Given the statistical nature of function device failure due to critical defects (only need one critical defect in the area used by the functional device for failure), only functionally relevant portions of the prints were analysed. This gave data which was representative of the printing process to a degree which is relevant to the application of functional devices. Hence the image portions were chosen to have a line height of 4mm, which is the width of the source/drain contacts (with a width scaling with the pattern size). The standard error of the mean of a pattern set's 9 lines, based on the sample standard deviation, was used to show how far the 9 lines deviated from the population mean. Further error analysis and testing validity is discussed in the following chapters.

3.3 Fabrication and Characterisation of OTFTs

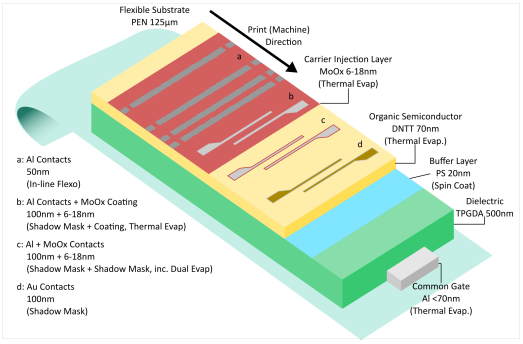
3.3.1 Experimental method

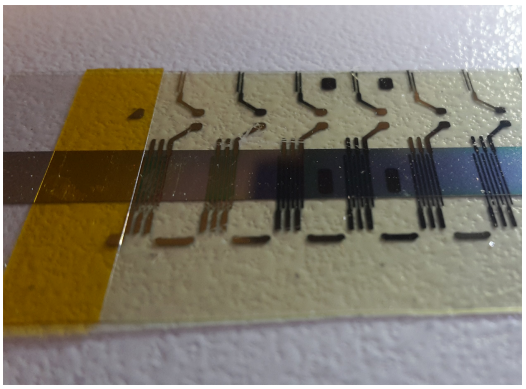
To test the effect of printing on the OTFT behaviour, OTFTs were fabricated in large batches, so that any slight variation within thin film deposition processes would not affect the reliability of the results.The common gate OTFTs were fabricated, as described below, up to the organic semiconductor layer as a single batch. After this the various contact material and deposition processes are separated out, while not being processed the devices were stored in a dark box with controlled humidity. Selective metallization printing had the same pattern as used for the patterning tests and analysis. However, the contacts had a regular width ($150\mu m$) with varying spacing (150, 200, $500\mu m$). Registration was an issue that was overcome by arranging the partially fabricated devices in-line with the pattern. The OTFTs had long common gates, the long dimension was placed in the direction of printing, with the common gate length being made longer than the printing plate circumference. This meant that the cross direction lines were guaranteed to be printed at some point along the common gate. The cross direction lines were also wider than the common gated OTFT structure, so lateral registration could be achieved by position the partially fabricated OTFT on the impression drum width by eye. The continuous metallized edges were removed by scouring the pattern after printing.

3.3.1.1 Fabrication Method and Materials

The transistors were fabricated as per previous group research.[8, 9, 10, 11] First, aluminium common gates were thermally evaporated ($1-5nm.sec^{-1}$) through shadow masks, in an Edwards 306 desktop vacuum system as was used in all the subsequent vacuum stages unless specified, onto $125\mu m$ polyethylene naphthalate (PEN) (DuPont Teijin Films) substrates, with a gate width of $4mm$, on a $25 \times 50mm$ wide substrate. The aluminium pellets ($10g$) were evaporated for tungsten boats (Kurt J Lesker). The following steps were performed with the gate contact area ($5 \times 4mm$) masked. Within a 300mm wide industrial vacuum webcoater, tri-propyleneglycol diacrylate (TPGDA) (Sigma-Aldrich) monomer was flash evaporated across the entire substrate, and cured with Argon plasma ($current = 5.9A$, $voltage = 270V$). To achieve this the samples were taped to the PET wrapped drum, which rotated at $25m.min^{-1}$.The flash evaporated monomer condensed onto the substrate and was cured into a polymer thin film using and Argon plasma ($current = 5.9A$, $voltage = 270V$). Details of this process, its arrangement and optimization, are found in the above references. Next a $0.6wt\%$ polystyrene (PS) toluene solution was spin coated onto the devices at $3000rpm$ for 1 minute, followed by 10 minutes held at $100°C$ leading to $\sim 15nm$ smoothing layer covering the acrylate dielectric layer. The environmentally stable DNTT (synthesised at Manchester as per reference [12]) was then thermally evaporated at an average rate of $0.3nm.min^{-1}$ in high vacuum ($< 1 \times 10^{-4}mbar$) using the aforementioned evaporator, with the device exposed to ambient during handling. A MoO_3 carrier injection layer was produced by thermal evaporation, in high vacuum, at a rate of $2nm.min^{-1}$obtaining the experimental range of thicknesses ($6-18nm$) required. For control devices, using shadow masks the aluminium contacts were deposited (thermal evaporation as with the gate layer) onto this layer. Gold contact devices were also fabricated without the MoO_3 carrier injection layer, as a comparison to previous work. Gold was thermally evaporated, similarly to aluminium but with a rate of $< 1nm.sec^{-1}$.

Aluminium contacts were patterned using a custom built in-vacuum flexography selective metallisation set up. Optimal printing pressure and speed were used to minimise pattern edge roughness. To achieve in-line patterning, the partially fabricated transistors were taped onto the drum and the gate contact masked prior to the patterning process. Control samples with shadow masks were also created on the same rotating drum rig and runs as the patterned samples, to ensure that the control and patterned sample saw the same degree of metallization. A schematic of the transistor





a. b.

Figure 3.8: a shows a schematic of the experimental range of the various types of contact, control and patterned with various molybdenum trioxide configurations labelled. b. photograph of a shadow mask patterned top contact bottom common gate transistors fabricated for this doctoral thesis. The top contacts (gold) are in sets of 6 with $150\mu m$ gaps, and are across the 4mm width of the aluminium common gate. The design and results of the various transistor structure are discussed further in Chapter 6.

design, with the experimental range represented is shown in Figure 3.8a and a photo graph of a patterned contacts common gate transistor is shown in Figure 3.8b.

3.3.1.2 Characterisation of transistor behaviour

Characterisation of the transistors was conducted in a clean room in the dark, in otherwise ambient conditions. Output and transfer characteristics were obtained using two Keithley 2400 source meters. Device metrics were obtained from these curves, as per IEEE Standard Test Methods for the Characterization of Organic Transistors and Materials.[13] The on/off ratio was determined from a graph of log scale drain current against the gate voltage at a source-drain voltage of 30V. The threshold voltage was determined from extrapolating the linear region of the curve on the $\sqrt{I_D}$ vs gate voltage (V_G) transfer graph and the gradient used to find the saturation mobility as per:[14]

$$\mu = \left(\frac{dI_D}{dV_G}\right)^2 . \frac{2L}{W} . \frac{1}{C} \tag{3.5}$$

Where C is the dielectric capacitance, with the value from previous trials[9] used: $13nF$, L is the length and W is the width of the transistor channel, as introduced in the Literature Review.

3.3.2 Characterisation of thin films

Thin film thickness was characterized by measure step heights with a Dektak stylus profilometer. Averages and standard errors, were calculated from 5 measurements moving both up or down the step for 2 or 3 of the measurements, to ensure the step height was correctly measured. Step heights were measure from reference glass slides, which were placed alongside the samples within the evaporation chamber during the respective thermal evaporation. The tape which held the slide to the sample stage was used to mask an area, and was removed to create the thin film step.

Light interferometers, MicroXam and NanoFocus, were used to obtain the various surface profiles and roughness measurements, as are describe in the relevant chapters. Surface roughness measurements were obtained from reference samples of the thin film, as done with step heights, although on single side polished silicon chips (UniversityWafers.com). Each measurement was repeated 5 times to obtain averages. Silicon ships were chosen as the surface was oriented across the crystal plane and could be cut to appropriate sizes that could be taped to the relatively large circumference of the impression drum. In this way the silicon chips could be deposited onto within the same patterning process of the aluminium patterning, providing representative results.

Sheet resistance was measured with a four-point probe method, where the sheet resistance was calculated from the measured resistance (R_m): $R_s(\Omega\square^{-1}) = R_m \times 4.53$.[15] As above the aluminium deposited during the patterning onto a silicon chip provided a reference sample without the probe penetrating the substrate. 5 resistance measurements were made across 5 voltage decades to obtain the average and standard error of the resistivity.

3.4 References

[1] M.I. Maksud, M.S. Yusof, and M. Mahadi Abdul Jamil. An Investigation onto Polydimethylsiloxane (PDMS) Printing Plate of Multiple Functional Solid Line by Flexographic. *Advanced Materials Research*, 844:158–161, November 2013.

[2] Muhamad Nor Nodin and M.S. Yusof. A Preliminary Study of PDMS Stamp towards Flexography Printing Technique: An Overview. *Advanced Materials Research*, 844:201–204, November 2013.

[3] Jiaxing Wang, Mingxin Zheng, Wei Wang, and Zhihong Li. Optimal protocol for moulding PDMS with a PDMS master, June 2010. Originally published at www.rsc.org.

[4] R Bickford. Analyze_stripes ImageJ Plugin, 2013.

[5] Curtis T. Rueden, Johannes Schindelin, Mark C. Hiner, Barry E. DeZonia, Alison E. Walter, Ellen T. Arena, and Kevin W. Eliceiri. ImageJ2: ImageJ for the next generation of scientific image data. *BMC Bioinformatics*, 18:529, November 2017.

[6] Johannes Schindelin, Ignacio Arganda-Carreras, Erwin Frise, Verena Kaynig, Mark Longair, Tobias Pietzsch, Stephan Preibisch, Curtis Rueden, Stephan Saalfeld, Benjamin Schmid, Jean-Yves Tinevez, Daniel James White, Volker Hartenstein, Kevin Eliceiri, Pavel Tomancak, and Albert Cardona. Fiji: an open-source platform for biological-image analysis. *Nature Methods*, 9(7):676–682, July 2012.

[7] Justin R. Bickford. Automatic Stripe Analysis Tool. Technical report, Army research lab Adelphi MD sensors and electron devices directorate, 2013.

[8] Gamal a. Abbas, Ziqian Ding, Hazel E. Assender, John J. Morrison, Stephen G. Yeates, Eifion R. Patchett, and D. Martin Taylor. A high-yielding evaporation-based process for organic transistors based on the semiconductor DNTT. *Organic Electronics*, 15(9):1998–2006, September 2014.

[9] Ziqian Ding, Gamal Abbas, Hazel E Assender, John J Morrison, Stephen G Yeates, Eifion R Patchett, and D Martin Taylor. Effect of Oxygen, Moisture and Illumination on the Stability and Reliability of Dinaphtho[2,3-b:2',3'-f]thieno[3,2-b]thiophene (DNTT) OTFTs during Operation and Storage. *ACS applied materials & interfaces*, 6(17):15224–31, September 2014.

[10] D. Martin Taylor, Eifion R. Patchett, Aled Williams, Ziqian Ding, Hazel E. Assender, John J. Morrison, and Stephen G. Yeates. Fabrication and simulation of organic transistors and functional circuits. *Chemical Physics*, 456:85–92, July 2015.

[11] Gamal Abbas, Hazel Assender, Mervat Ibrahim, and D. Martin Taylor. Organic thin-film transistors with electron-beam cured and flash vacuum deposited polymeric gate dielectric. *Journal of Vacuum Science & Technology B*, 29(5):052401, September 2011.

[12] Tatsuya Yamamoto and Kazuo Takimiya. Facile Synthesis of Highly π-Extended Heteroarenes, Dinaphtho[2,3-b:2‘,3‘-f]chalcogenopheno[3,2-b]chalcogenophenes, and Their Application to Field-Effect Transistors. *Journal of the American Chemical Society*, 129(8):2224–2225, February 2007.

[13] IEEE Standard for Test Methods for the Characterization of Organic Transistors and Materials - Redline. *IEEE Std 1620-2008 (Revision of IEEE Std 1620-2004) - Redline*, pages 1–27, December 2008.

[14] Zhenan Bao and Jason Locklin. *Organic Field-Effect Transistors*. CRC Press, May 2007.

[15] Dieter K. Schroder. *Semiconductor Material and Device Characterization*. John Wiley & Sons, 2006.

Chapter 4

Selective Metallization Viability and Compatibility Modelling for Functional Organic Devices

This chapter is based on the article published in Elsevier Surface and Coatings for the proceedings of the SVC 2017 Annual Technical Conference. The carbon nanotube stamps were designed and fabricated by: Dhanush Durai Mariappan, Prof. John Hart, Dr. Sanha Kim, Dr. Junjie Zhao and Prof. Karen Gleason Of Massachusetts Institute of Technology who designed and fabricated the stamps.

4.1 Introduction

This chapter outlines the process that is the focus for this doctorate thesis: selective metallization. This is an industrial thin film metallizing technique, based on flexography printing, which will be shown to be theoretically viable and compatible with organic electronics. The following chapters will test this experimentally, by optimising the printing and applying the process to organic thin film transistors. In the literature review a comparison was presented of selective metallization and other techniques for creating patterned metal thin films, highlighting the existing understanding of the challenges and advantages of thermal evaporation. Here, the thermal lift-off process will be further described, adding to existing literature understanding of the fundamental thermal principles involved. The thermal lift-off mechanism will be described in terms of thermal energy to demonstrate that it would not cross key processing limits of organics, as used in organic thin film transistors. It is important to note that the substrate in this work is considered to be a partially fabricated organic device, and so these process defects could lead to erroneous and defective functioning.

The discussion presents the limits of this analysis and assesses the compatibility of the properties of the metal thin films. Furthermore, the wide applicability range of this process is supported by the favourable patterned metal properties, such as conductivity and roughness, showing the advantages of this technique over other metal patterning techniques for organic electronics, as described above. This theoretical compatibility study is supported by experimental results, of metallized patterns.

4.1.1 Selective Metallization

Given that the volume of oil used in the thermal lift-off step and patterning of selective metallization is small, and that the PVD process operates well above room temperature, it is henceforward assumed that the radiative heat, of the physical vapour deposition, is solely responsible for the oil vaporization removal, and the latent heat of fusion due to deposition of the metal vapour is ignored. This assumption is revisited in the discussion to confirm its validity. With this in mind, the thermal lift-off step can be optimised, by varying the PVD conditions and system geometry to alter the amount of thermal radiation exposure of the oil, which also has a tunable volume and vaporization behaviour.

The flexography printing step defines the masking oil's pattern, and the volume deposited. The volume should be of uniform thickness (thermal depth) and so can be generalised as a thickness of a unit area. The deposition method must be compatible with the selected oil, and as discussed in the literature review, flexography is a versatile printing technique with a wide viscosity range of $0.05 - 0.5 Pa.s$.[1]

The oil must also be chemically inert and compatible with the vacuum environment. It is also necessary for the sacrificial masking oil to have the physical properties to impede metallization of the substrate while allowing the complementary oil evaporation from the substrate, in the lift-off step of the selective metallization process. There has been little academic research into these selection criteria.

The main contributor to this research speciality, is Pagani et al. [2] who investigated the efficiency of different types of sacrificial oils used for the selective metallization process. By creating a model mechanism wherein the vaporised oil forms a cloud that acts to 'shield' the substrate from the metal vapour, the ideal vapour pressures of the oil could be equilibrated with the metal vapour. This led to an expression for the dimensions of shielding vapour cloud, namely thickness per unit area, and the physical properties of the oil that determines this dimension. The authors suggested that with a thinner vapour cloud thickness, a more 'precise' print pattern can be created (taken to mean reduced loss of fidelity due to shadowing effects) and also

reduce the materials consumption. The radiation heated oil vapour's partial pressure exceeds the metal vapour's partial pressure, and inhibits metal deposition. Their modelling approach showed that the oil's vapour pressure is inversely proportional to the vapour thickness.

Building on this model of the thermal lift-off mechanism it is insightful to use the Clausius-Clapeyron equation to describe the phase change, of the oil from the patterned liquid into the masking vapour, due of the radiative heating. Specifically, the temperature change ($dT_{Radiative}$) leading the oil vapour pressure change (dP_{Oil}) can be described in terms of the thermal-lift off process temperature ($T_{Process}$), the oil's specific volume (v_{Oil}) and latent heat (H_{Oil}):

$$\frac{dP_{Oil}}{dT_{Radiative}} = \frac{H_{Oil}}{T_{Process}.v_{Oil}}. \tag{4.1}$$

This implies, to protect the organic device from damaging temperatures to which this process is being applied to, the term $T_{Process}.v_{Oil}$ must be minimised. A small oil volume will reduce any possible shadowing effect of the oil vapour and oil consumption. Maximizing the the pressure-temperature gradient of coexistence curve of the liquid and vapour phases, will create a low energy cost for for vaporization, as the additional radiative heat required will be small. This steep phase boundary will also create a higher vapour pressure in the oil, for a given radiative heating amount, which will better match the metal vapour's pressure, creating an efficient masking mechanism. In summation to achieve a high pressure change for little radiative heating of the oil, while keeping the volume and temperature seen by the sensitive functional substrate small, requires maximizing the latent heat of the oil, according to equation 4.1.

The latent heat can be optimised by choosing the correct chemistry and physical properties, like polymer molecular weight of the oil. The chemistry will act to increase the internal pressure if there are forces of attraction between the vaporised molecules. While the molecular weight will act to contain the vapour cloud close to the liquid oil pattern, by increasing the mean free path of the molecule and increasing the number of possible attractive intermolecular bonds.

As is standard in industry, and described in the Materials and Methods chapter, Krytox® oil [3] was used here and is a high molecular weight perfluoropolyether, see Figure 4.1. The high electron affinity fluorinated chemistry has instantaneous dipole-induced intermolecular forces along the length of each molecule. The intermolecular bonds are individually weak, but in greater numbers attractive enough to create a positive internal pressure. In previous thermal lift-off modelling work [2], ideal gas

behaviour of the vaporized oil was assumed. A fuller description can achieved by considering the oil vapour pressure (P_{oil}) as per the Van der Waal equation:

$$P_{oil} = \frac{nRT}{V - nb} - \frac{an^2}{V^2} \tag{4.2}$$

where n, R, T and V is pressure, molar amount, Boltzmann constant ($8.31446 m^3.Pa.K^{-1}.mol^{-1}$) absolute temperature and volume respectively. The constant b is another constant taking account the molecule's volume. The term a is the Van der Waal constant, related to the internal pressure (π_T) by the definition:

$$\pi_T = \frac{an^2}{V^2}. \tag{4.3}$$

The constant a can be found to be $2.25 Pa.m^6.mol^{-1}$.[4] Assuming that at the critical points the change and rate of change of pressure with temperature is zero, i.e. $\left(\frac{\partial P}{\partial T}\right)_{T_C}, \left(\frac{\partial^2 P}{\partial T^2}\right)_{T_C} = 0$, the constants a and b are [5]:

$$a = \frac{27}{64}\frac{R^2 T_c^2}{P_C}, \tag{4.4}$$

$$b = \frac{RT_c}{P_c}. \tag{4.5}$$

Given that the critical constants are $T_c = 437.70K$, and $P_c = 2.481 MPa$ [4] (originally from [6]), for the perfluoropropyl methyl ether repeat unit ($C_4H_3F_7O$) of the particular oil in question, the constants are found to be: $a = 2.25 MPa.m^6.mol^{-2}$ and $b = 0.001466 m^3.mol^{-1}$.

The large constant a is similar to toluene, which is known for low vapour concentrations required for flash ignition in laboratory safety procedures.[4] The value of b is small so will have little repulsive effect on the oil vapour cloud. These constants suggest that the ideal vapour modelling did not consider the attractive intermolecular forces of the oil's chemistry, which lead to a negative vapour pressure. Assuming nb is comparatively small, the difference in ideal oil vapour pressure ($= \frac{nRT}{V}$) to the real vapour pressure, is the internal pressure term of Equation 4.2 This will act to localise the oil vapour to the liquid oil, leading to a more constrained oil vapour cloud. In summary the latent heat of vaporisation of the oil, which relates to the oil's chemistry, is larger and increases the $\frac{dP_{Oil}}{dT_{Radiative}}$ term in Equation 4.1.

This brief analysis has shown the suitability of the selected patterning oil to the thermal lift-off process. Its compatibility with other aspects of the selective metallization process are discussed in the Method section below. Following this the radiative

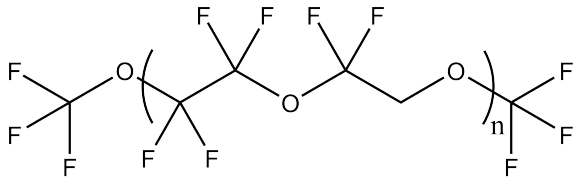


Figure 4.1: Repeat unit of the Krytox® perfluoropolyether.

heating of the oil as it passes over the metallizing source is used to calculate the optimal volume of liquid oil, that is required to prevent metallization but also be completely evaporated. This modelling continues to assume that the oil vapour acts as a mask above the liquid oil so that no aluminium vapour condenses onto the liquid oil, but only the radiative energy of the evaporation source contributes towards the thermal lift off process, see Figure 2.17. This assumption is discussed in the following sections along with printing results.

4.2 Method

4.2.1 Compatibility and Printing Analysis

The chemical structure is well suited to vacuum systems (high vapour pressure), it is inert and has a viscosity suitable for flexography printing, $0.12 Pa.s$.[3] Absorption of the oil inking material into the polydimethyl siloxane (PDMS) would cause swelling and degraded patterning features of the PDMS mould. Swelling is the measure of solubility for cross linked polymers. Dissolution and swelling is greatest when minimal energy is required for breaking down the material's cohesive bonding structure. It occurs when there is a similarity in chemical bonding properties between the solvent and solution, or more commonly 'like dissolves like'.

This thermodynamic minimum is quantified for a given temperature by the cohesive energy density ($cal.mol^{-1}$), c, defined as the molar internal energy per unit volume.[7, 8] This definition of the enthalpy of a material's bonding can be used to compare material 'likeness', in which case the Hilderbrand or solubility parameter is used: $\delta = \sqrt{c}$.[9] Materials with similar solubility parameters will tend cause swelling. PDMS has a solubility parameter of $7.3 cal^{1/2}.mol^{3/2}$, so solvents such as hexanes cause significant swelling.[10]

Using the Fedors[11] additive function method the solubility parameter can be estimated. In this process each constituent functional group of the repeat unit of the polymer has an empirical energy contribution to the vaporization energy and to

the molar volume. The sums for the repeat unit are divided and rooted to give the solubility parameter, with corrections for the end groups with high molecular weight polymers. Fedors claims a 10% accuracy when compared with experimental values, at 25^{o}C, which is appropriate for this investigation. The reported method has a good range of values and only requires knowledge of the structural formula. To further ensure compatibility of the oil with the PDMS plate, 24 hour swell tests, as per Lee et. al.'s method were performed. [10]

4.2.2 Selective metallization printing

Printing was performed as per the Materials and Methods Chapter with a printing force of $42N.m^{-1}$ and speed of $10m.min^{-1}$. The printed pattern contained 10 metal lines with a nominal (plate) linewidth of 150μm (141μm actual), and equal spacing, of which the nine oil masked regions were analysed and the line width and edge roughness data averaged. Electrical characterization was performed with a four point probe and optical microscopy images (Leica M165 C) were obtained to asses the print quality. Thickness measurements, from surface profiles, were made with MicroXam optical profiler (50x magnification), with five repetitions averaged to give the reported values. Slight deviations in data are expected to be due to print pressure variance due to equipment imperfections and operational error with analysis equipment.

Additionally, and separately, high resolution patterning was performed using printing stamps which were fabricated by Dhanush and co-workers at Massachusetts Institute of Technology, as per published results.[12] These carbon nanotube (CNT) stamps were formed using a chemical vapour deposition process which created vertically aligned 'forests' of CNTs with fine features defined by a photolithography process. A full description of the fabrication methods, analysis, and ultra-high resolution flexography printing of solvent based inks using these stamps can be found in reference [12]. The CNT stamps were spin coated with $1ml$ of the sacrificial oil at $1500rpm$ for 3 minutes, then mounted onto the impression drum of the flexography letterpress set-up. At first rotation, the CNT stamp was impressed onto a smooth (unpatterned) PDMS plate, and then on the subsequent print head rotation, this oiled printing roller deposited onto the polyethylene naphthalate (PEN) wrapped drum. A nominal line force, across the plate width, of $39.2N.m^{-1}$was used and the printing speed was $10m.min^{-1}$. The fine feature oil pattern was then exposed to the PVD as per the described selective metallization process. The nominal pattern was a hexagonal grid of $10\mu m$ diameter circles with $3\mu m$ spacings.

4.2.3 Heat Model

The volume of liquid oil required for effective masking was modelled by calculating irradiation heat (Q) which is the radiative energy per unit square:

$$Q(Wm^{-2}) = A\varepsilon_{source}\varepsilon_{oil}\sigma(T_{Al}^4 - T_{Oil}^4) \tag{4.6}$$

where A is the geometric view factor of the oil on the process drum as it passes over the evaporation boat, ε_x is the emissivity of x, σ the Stefan-Boltzmann constant, T_{Al} the temperature of the aluminium thermal evaporation source, and T_{oil} the temperature of the oil as it enters the metallization zone.

The thermal radiation energy (E) seen by oil as it passes the source is then:

$$E(Jm^{-2}) = Q.\frac{metalization\ zone\ length}{web\ speed}. \tag{4.7}$$

This energy will be converted into thermal energy to heat the liquid oil and account for the energy cost of vaporisation phase change, both of which will depend on the oil density (ρ). This density can be related to the oil thickness (t) that is required to match this thermal energy per unit area. This calculated by dividing the thermal radiation seen, by the specific (C_P) and vaporization heats (C_V):

$$t = \frac{E}{\rho(C_p.\Delta T_{oil} + C_V)}. \tag{4.8}$$

Here ΔT_{oil} the change in temperature of the oil from ambient liquid state to the vaporization temperature. This temperature change will give the $T_{Process}$, which needs to be below $100°C$, to prevent possible thermal damage to functional organics.

4.3 Results

4.3.1 Modelling results

Equation 4.6 shows the importance of controlling the source temperature accurately, as the radiative energy scales to the fourth power. Maximizing the source temperature will ensure the oil is completely removed, but, as with all thermal evaporation processes damage to the substrate limits the safe operating temperature, which for functional organics is less than 100°C as a general rule, but could be even lower.

The view factor can be assumed to be infinitely long strip of finite width W (thermal evaporation boat source) to a cylinder, impression drum of radius R [13]:

Table 4.1: The values used for calculating the required liquid oil thickness to match the radiative energy as per Equations 4.6 - 4.8. These values are calculated from the system geometry or DuPont Krytox® sales literature unless otherwise referenced.

Parameter	Value
View Factor	0.49
Emissivity of the source	0.04[14]
Emissivity of the oil	0.03[15]
Stefan-Boltzmann Constant ($W.m^{-2}.K^{-4}$)	5.67×10^{-8}
Temp Source (K)	1250[16]
Temp Oil (K)	293
Irradiation ($W.m^{-2}$)	1.45×10^{3}
Web speed ($m.s^{-1}$)	0.04
Process zone length (m)	0.31
Radiation seen by oil ($J.m^{-2}$)	3.81×10^{2}
Oil Density ($Kg.m^{-3}$) at $62.5°C$	1799
Oil Vaporization enthalpy ($KJ.Kg^{-1}$)	37.78
Oil Specific heat ($J.Kg^{-1}.K^{-1}$)	1046 [4, 17]
Oil Temperature Change (K)	42.5

$$A = \frac{R}{W} \arctan\left(\frac{W}{H}\right), \tag{4.9}$$

where there is a distance H from there centres. Given the system described in the Materials and Methods chapter, $R = 100mm$, $W = 5mm$ and $H = 200mm$.

Given the typical values, shown in Table 5.6, the thickness of the liquid oil required is $1.63 \pm 0.31 \mu m$ to match the radiative energy. This is the same order of magnitude of the even splitting maximum ink transfer of this system which would lead to $7.6 \pm 1.5 \mu m$ deposited ink thickness on the substrate. This required liquid oil thickness is specific to the system, and would change proportionally with other view factors.

4.3.2 Experimental Results

Using the Fedors [11] additive function method, the sacrificial oil's solubility parameter was found to be $11.12 cal^{1/2}.mol^{3/2}$ which is significantly different from that of PDMS ($7.3 cal^{1/2}.mol^{3/2}$). This suggests that swelling of the stamping mould by the

ink should be negligible. The swelling trials supported this and showed no swelling of the PDMS due to the oil, so no plate pattern distortion is expected.

Figure 4.2 shows an example of the cross direction aluminium thin film stripes, patterned onto PEN at $2.4m.min^{-1}$ with nip line pressure of $50Nm^{-1}$. The pattern line edge roughness between the stripes, could translate into critical, shorting, defects for source/drain contacts of a transistor. The stripe edge's root mean square (RMS) roughness for this print was found to be $9.0 \pm 1.3\mu m$ and the peak-to-peak height (P2P) was $64.0 \pm 24.0\mu m$. The spacing between stripes was $165.1 \pm 2.7\mu m$, 10% larger than the nominal plate stripe width. The aluminium thin films were measured to be between 30 and $50nm$ thick with $4.5 \pm 0.7nm$ RMS surface roughness over a $3.24 \times 10^{-8}m^2$ and a sheet resistance of$1.59\Omega.\square^{-1}$. Figure 4.2b shows the CNT patterning.

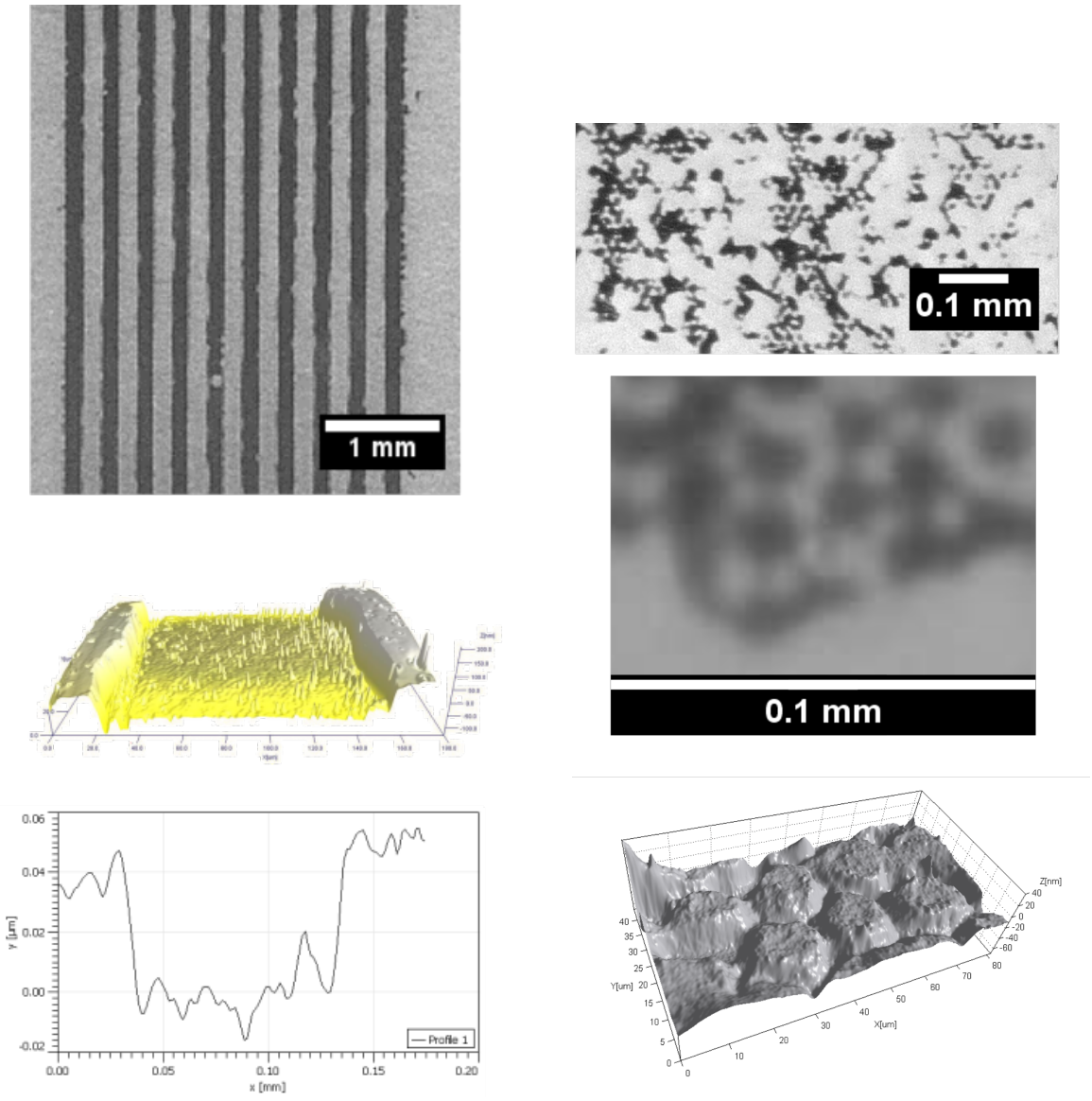
4.4 Discussion

4.4.1 Thermal Lift-Off

The predominant source of error in the modelled liquid oil thickness value is the determination of the particular oil's physical properties, which can be limited in sales literature. The emissivity estimate can also vary with oil thickness. It should be noted that the volume of oil required is small and so vacuum system contamination is minimal. The oil temperature change is only $42.5K$ which is suitable for organic materials as the $T_{Process}$, if vaporising from ambient, is only $62.5°C$.

The oil thickness found by the thermal model is in the order of thickness that is deposited using flexography printing. The same is true for inkjet printing, but screen printing would have to operate at its low operational limit, or use an oil which a lower latent heat of vaporisation. In this way any oil deposition technique would need to match the deposited thickness with the thermal energy deposited. This said, the evaporation view factor and web speed can also be manipulated to ensure the correct balance of oil volume and radiative heating.[18]

The optical image of the metal pattern shows this technique has adequate resolution capabilities to be used in functional devices, albeit with some edge roughness. As discussed in the next chapter, optimisation of the flexography printing process can reduce the metal pattern edge roughness to below half critical dimension meaning critical defects would be avoided if used in functional devices, such as transistors. The pattern resolution used here is near at the limit of this technique, which can



a. b.

Figure 4.2: a. 5x optical micrograph of nominal linewidth $150\mu m$ line pattern printed with the selective metallization technique. The dark areas are the metallized regions and the light grey is the substrate. Other micrographs of selective metallization prints are found in chapter 2, see Figure 5.5. Below the microscopy image is a 3D surface plot showing the sharp metal thin film edges, and thin film edge roughness with observable line edge roughness. At the bottom is a typical profile showing the sharp clearly defined edges of the metallized/non-metallized regions. b. 12x optical micrograph of the selective metallization pattern made with the CNT stamps. The nominal pattern is $10\mu m$ circle with $3\mu m$ spacing in a honeycomb grid arrangement, and this is distinguishable in the digitally enlarged image (middle). Below this is a a surface map of the printed pattern showing an observable gradient to the pattern edges ($30\mu m$ vertical change over $< 5\mu m$).

achieve 10's of microns with even less rough line edges, see Figure 4.2b. However the challenge is engineering a high throughput process on large scale with such precision.

Evidently the edge roughness is a result of the liquid oil on the substrate not a masking oil vapour, which would lead to a blurring and thinning of the deposition at the pattern's edges where the vapour cloud dissipates. This could imply that the latent heat of fusion, of aluminium deposition directly onto the liquid surface, is driving the thermal lift-off process, which is contradictory to the assumption made earlier, namely importance of radiative heating in this role. However the latent heat of fusion is roughly order of magnitude greater that the radiative heating[14], so the oil thickness to match would have to be on the order of $10's\mu m$. This printed thickness is not achievable with this printing set-up. Instead it is proposed that the oil vapour, which is constrained tightly by its internal pressure, as introduced earlier, acts to mask the substrate. However as the metal deposition occurs on the substrate surface, it is the liquid oil boundaries which define the region of metallization. Additionally, the oil volume estimated to be transferred to the substrate, which is greater than the thermally modelled amount, does not preclude some condensation of the Al vapour onto the liquid oil. Further testing could be done to measure the remnant oil after the selective metallization, but this is difficult due to the miniscule volumes used. Generally directly probing the oil's behaviour is difficult with enclosed vacuum systems. Ultimately, this model and results have shown that only the liquid oil that is transferred to the substrate affects the pattern quality, in terms of line edge roughness and fidelity, and not the liquid oil vapour effects.

The assumptions of this thermal lift-off model are now addressed. Firstly, it is assumed that the process is adiabatic, except for the thermal radiation and vaporization of the oil. This is valid as the oil is within a vacuum with no conduction and negligible radiative pathways to lose thermal energy. The interfacial thermal conductivity of the oil and the substrate could be considered, but the thermal conductivities would be minimal given the predominance of the surface effects of radiation and also difficult to accurately ascertain. Secondly, the oil's physical properties are assumed constant throughout. The oil viscosity could decrease as it is heated, although the oil temperature change is only $42.5K$ which would not lead to large changes in viscosity. Some pattern distortion, due to spreading, could be seen in initial experiments at ambient temperatures. There is time for spreading within the metallization zone ($1.8s$ at $10m.min^{-1}$) but importantly the time between oil pattern deposition and metallization is nearly instantaneous, with this view factor and set-up, so the liquid oil pattern will be pinned as soon as it is transferred. This only leaves impression

spreading effects which will be investigated in the subsequent Chapter. If these can be compensated for, then the limits of the smallest feature achievable with selective metallization, could be vary small which makes it favourably viable for creating functional devices.

4.4.2 Patterned Metal Thin Films

Although these results presented are in early development, this doctoral work has reported for the first time sub-10μm metal thin film patterning with the selective metallization process, see Figure 4.2b. The 3μm gaps achieved show the potential for this industrially mature process to create conductive metal thin films with dimensions appropriate for high performance functional organic devices. The results present here, using the CNT stamps, is a preliminary trial and so the overall patterning quality was low and reproducibility was also low, of 12 printing trials only one achieved a distinguishable pattern. The hexagonal arrangement of the metallized dots represent successful image transfer of the printing plate design (honeycomb CNT forest). The overall low quality is associated with shearing forces in the flexography printing process damaging the vertically aligned CNTs stamps during printing and excess ink removal. This has proven a difficulty with these stamps, as described by co-workers in reference [12]. Additionally there was a significant time for spreading with this printing process (as the oil moved from impression drum to plate to substrate) which can be seen in the print results as a coalescence of the liquid honeycomb form (light grey areas in Figure 4.2b). This coalescence led bridging of the printed dots at some points, which can be thought of as an electrical short, although ignoring these, the pattern edge roughness was high enough to create distinct dots. In earlier trials, when the stamps were impressed onto glass slides in ambient and then waited for $\sim 10mins$ before metal evaporation, due to chamber pump down, the pattern exhibited more coalescence. Importantly this result confirms that the pattern formation depends on the oil printing process, and the shape of the oil, as transferred to the substrate, with define the metal pattern shape.

This is also seen in the larger scale patterning, with the standard flexography printing of the oil, Figure 4.2a. Here the linewidths are consistent and the printing quality appears reliable and sufficient that devices could be made using this patterning; printing quality is addressed thoroughly in the following chapter. For the larger patterns there is a vertical line edge roughness, see surface maps in Figure 4.2, and an edge gradient of $< 6/5$ with the 10μm dot CNT stamp patterning. This supports the

modelling of a constricted masking oil vapour, and demonstrates the high contrast patterning achievable with selective metallization.

The excellent surface roughness and electrical characteristics of the patterned aluminium is equivalent to aluminium thin film coatings.[19] The direct bulk material deposition, with standard PVD process, makes the selective metallization technique attractive, compared with some ambient solution based printing methods, such as silver inks, do not achieve this conductivity with the same thickness and the printed solute can be quite rough.[20, 21] Furthermore these processes can require more chemical control, for solvent orthogonality, and use costly materials. The simple concurrent steps of deposition and mask removal with the thermal lift-off mechanism gives this process an edge in terms of viability of production method, as higher processing speeds can be used and without toxic chemicals as seen with de-metallization processes. All this supports the compatibility and viability of selective metallization with organic functional devices.

4.5 Conclusion

This chapter has introduced the selective metallization technique in detail, showing that it is a versatile technique for creating high quality metal patterns at process temperatures, modelled to be $62.5°C$, which are generally compatible with functional materials. The sheet resistance and roughness, $1.59\Omega.\square^{-1}$ and $4.5\pm0.7nm$ respectively, particularly set this high-throughput process apart as a promising technique for creating cost effective flexible electronics and organic devices.

A thermal model for calculating the thickness of oil on the substrate for effective masking of the oil was described and critiqued. The model suggests that printed oil a few microns thick would be adequate, although were some of the latent heat of fusion of the metal vapour condensing directly onto the liquid oil contributing to vaporization, the thickness would need to be greater. The estimated value of $1.63 \pm 0.31\mu m$ is based on the specific system geometry and view factors, and in a real world processing environment the patterning process should provide a thicker oil layer as complete masking is more vital than complete oil removal, which can be performed in post processing or remain with negligible effects. [22] It is assumed that the oil vapour has the largest masking effect but as the thermal lift off and metal deposition processes are simultaneous the metal pattern edges reflect the liquid oil's bounds. Hence the engineering challenge of reducing the linewidths is limited most by controlling the liquid deposition process. The results showed for the first time

that the selective metallization can achieve sub-10μm gaps and good quality larger scale patterns. The optimization of the flexography printing is discussed in the follow chapter, before this process is applied to OTFTs.

4.6 References

[1] Helmut Kipphan, editor. *Handbook of print media: technologies and production methods*. Springer, Berlin ; New York, 2001.

[2] A. Pagani, P. Raugei, and F. Rimediotti. Patterned Metallized Films: State-of-the-art and Growth Opportunities. In *50th Annual Technical Conference Proceedings*, pages 757–761. Society of Vacuum Coaters, 2007.

[3] Krytox® Lubricants - By DuPont. http://www.krytox-lubricants.com/.

[4] David R. Lide. *CRC Handbook of Chemistry and Physics, 84th Edition*. CRC Press, June 2003. Google-Books-ID: kTnxSi2B2FcC.

[5] Robert C. Reid. *The properties of gases and liquids*. McGraw-Hill chemical engineering series. McGraw-Hill, New York ; London, 4th ed. edition, 1987.

[6] Takeshi Sako, Masahito Sato, Noriaki Nakazawa, Masaru Oowa, Masahiko Yasumoto, Haruaki Ito, and Shiro Yamashita. Critical Properties of Fluorinated Ethers. *J. Chem. Eng. Data*, 41(4):802–805, January 1996.

[7] James E. Mark. Physical properties of polymers handbook [computer file], 1996.

[8] D. W. van Krevelen and Klaas te Nijenhuis. *Properties of Polymers: Their Correlation with Chemical Structure; their Numerical Estimation and Prediction from Additive Group Contributions*. Elsevier, February 2009.

[9] Joel H. Hildebrand. *Solubility of non-electrolytes*. Monograph series (American Chemical Society) ; 17. Reinhold Publishing, New York, 2nd ed edition, 1936.

[10] Jessamine Ng Lee, Cheolmin Park, and George M. Whitesides. Solvent Compatibility of Poly(dimethylsiloxane)-Based Microfluidic Devices. *Analytical Chemistry*, 75(23):6544–6554, December 2003.

[11] Robert F. Fedors. A method for estimating both the solubility parameters and molar volumes of liquids. *Polym Eng Sci*, 14(2):147–154, February 1974.

[12] Sanha Kim, Hossein Sojoudi, Hangbo Zhao, Dhanushkodi Mariappan, Gareth H. McKinley, Karen K. Gleason, and A. John Hart. Ultrathin high-resolution flexographic printing using nanoporous stamps. *Science Advances*, 2(12):e1601660, December 2016.

[13] Robert Siegel. *Thermal radiation heat transfer*. Hemisphere, Washington ; London, 3rd ed edition, 1992.

[14] Charles A. Bishop. *Roll-to-Roll Vacuum Deposition of Barrier Coatings*. John Wiley & Sons, August 2015.

[15] Emissivity Table. http://www.optotherm.com/emiss-table.htm, 2016.

[16] Richard Edward Honig and Dean A. Kramer. *Vapor Pressure Data for the Solid and Liquid Elements*. RCA Laboratories, David Sarnoff Research Center, 1969.

[17] E. Richard Booser. *CRC Handbook of Lubrication and Tribology, Volume III: Monitoring, Materials, Synthetic Lubricants, and Applications*. CRC Press, December 1993. Google-Books-ID: gnOJoug5R8IC.

[18] G. Comini, S. Savino, N. Magriotis, and S. Muratori. Thermal modeling of vacuum web coating. *Applied Thermal Engineering*, 27(2–3):611–618, February 2007.

[19] P. Quintana, A. I. Oliva, O. Ceh, J. E. Corona, and M. Aguilar. Thickness effects on aluminum thin films. *Superficies y vacío*, 9:280–282, 1999.

[20] R. Venkata Krishna Rao, K. Venkata Abhinav, P. S. Karthik, and Surya Prakash Singh. Conductive silver inks and their applications in printed and flexible electronics. *RSC Adv.*, 5(95):77760–77790, 2015.

[21] David J. Finn, Mustafa Lotya, and Jonathan N. Coleman. Inkjet printing of silver nanowire networks. *ACS Appl Mater Interfaces*, 7(17):9254–9261, May 2015.

[22] F. Rimediotti. Process & Equipment for Specialty Web Products. AIMCAL, 2005.

Chapter 5

Flexography printing analysis and optimisation

5.1 Introduction

This chapter will examine flexography printing quality and explain its optimisation by analysis of the influencing process controls. The previous chapter has shown, in theory, that selective metallisation is a suitable process for producing patterned metal thin films on organic functional devices. However, for this process to be a viable production method the quality of the printed pattern must be sufficient to create defect-free devices. The modelling in Chapter 4 supported the idea that the condensed metal thin film mimics the outline shape of the printed liquid thin film. This oil thin film is printed using flexography, and so consequently, optimisation of the flexography printing will optimise the metal thin film patterning.

The literature review highlighted some of the main research conducted in academia and within industry, into the flexography printing process. This research has focussed on absorbent substrates and anilox specification effects, as well as modelling of liquid bridges. Some of this work will be built upon in this chapter and further critiqued, to show that there is still some lack of understanding of the mechanism of transfer of the liquid ink from the plate relief pattern onto the substrate. By using a carefully designed and simplified flexography print system, the fundamental parameters, namely printing pressure and speed, will be varied to give observable effects, which are also relevant to the application. These quantified results are then discussed to show that there are commonalities with pilot trial results, and a link between the print quality trends and theoretical modelling of liquid bridges.

Based on the findings, the optimal print quality will be identified, which is then used to create defect-free organic devices in subsequent chapters. This chapter high-

lights the need for understanding of the basic physical mechanism involved in a printing process for the successful re-purposing of the process from the graphics printing to functional devices printing.

5.1.1 Print quality trends and ink transfer

The literature review highlighted that the existing understanding of flexography printing can be divided into two approaches. On the one hand, the industrially focussed research considers the effects of flexography printing parameters. While on the other hand, the fluid mechanics modelling and experiments consider the behaviour of liquid bridges which are representative of the conditions experienced by the ink in the printing contact. In both cases it is clear that the printed patterns are representative of the ink transfer mechanism from the plate to the substrate, assuming anilox inking effects and substrate and ink properties are equal.

Within the contact region the liquid thin film of ink is localised on the plate relief pattern and impressed onto the substrate, as the counter rotating rolls move concurrently and synchronously, both the plate, the plate features and the ink can be deformed differently by the:

- Magnitude of the printing pressure felt by the liquid ink, which is controlled by: the contact force; the plate thickness and material's properties (as well as the properties of the supporting layers); the area of contact (given the particular relief pattern at the contact region);
- Passage through the contact region within a certain period of time, which also relates to the contact impression width and printing speed.

These interdependent factors, which lead to ink transfer, are hierarchical, as the literature review concluded, and occur over several length scales. At the largest length scale there is deformation of the printing roller and at the smallest is the viscous, inertial, and interfacial energy effects on the liquid ink shape. In order, then, to fully characterise the ink transfer a parametric analysis is needed of the printing pressure and speed, to make the research relevant to real world applications. However the experiment must also be designed so that the results can be understood in terms of fluid dynamic behaviour, so that general trends can be derived from physical models.

5.1.2 Flexography Analysis

The outcomes of research in flexography ink transfer have been expounded in the literature review and so will not be re-examined. Instead, in this section, the methods of analysis, how the print process was assessed, are further described and experimental techniques highlighted. The main criterion of a good printing analysis is that the printed pattern must be representative of the ink form immediately after it is transferred. From this literature discussion an experimental method is developed which will produce reliable, accurate, and insightful results.

The work conducted at the Welsh Centre for Printing and Coating (WCPC) [1, 2] investigated print quality of half tone dots with varying anilox and plate to substrate parameters. The experiments, like other investigations [3], made use of a ultraviolet (UV) curable inks with negligible transferred volume loss due to evaporation of solvents. The web speed was $122 m.min^{-1}$, and so presumably the ink spreading time, between deposition and curing, was small enough to be typical of a normal industrial printing press. This ensured that the printed patterns that were analysed, within the graphic printing criteria they were investigating, was 'representative of the ink thin film transferred during the printing process'.[1] Stable conditions were ensured by running for 244m of web before taking samples after a parameter was changed, similarly temperature was maintained within $\pm 1°C$, in other print trials a controlled humidity was also specified.[4, 5] Finally, cyan ink colour was chosen for highest contrast in optical measurements.

Non-absorbent substrates have a direct application to industry, and also serve two purposes for the scientific method. Firstly, absorbance introduces another non-linear variable, as different porous materials accept varying amounts of ink, as has been the subject of investigation previously.[6, 7, 8] Secondly it has been shown that the non absorbed (a.k.a. non-immobilized) ink splitting dominates the volume of ink transferred, and so likely has the greatest effect on the print quality as observed with ink gain in reference [7].

Darhuber et al.'s theoretical investigations also highlighted that the ink redistribution on substrates depends only on the printed feature's aspect ratio, not absolute size, albeit at quasi-static plate separation. To this end, and to be comparable across length scales, features must have consistent aspect ratios, and changes in the pattern ratio will mean that the printing results should vary.[3]

The modelling of liquid bridges, and the experimental verifications, often neglected gravitational effects and so the printed patterns must be small enough that viscous and contact energetic forces dominate. Also the work highlighted the importance of

contact line slip, which leads to pinning of the contact lines at normal printing speeds, and so to be representative of the types of ink hydrodynamics expected, the testing must be performed at typical printing speeds (webspeed$> 10m.min^{-1}$).

The liquid ink bridge research also highlighted there are shear, rotational and extensional forces involved in patterned roller printing. Unlike coating which has uniform axial plate coverage, the relief patterned plates have an ink split that is created and ended over the distance of the relief pattern through the contact area. The problem is three dimensional, but isolating parallel (machine direction) and perpendicular (cross direction) effects are possible by creating the respective cross product analogue plate patterns, where the pattern feature has a large aspect ratio, such that a two dimensional problem can be reasonably constructed. This is to say that idealistically, machine direction lines only reflect the lateral variations of ink transfer, plates with angled relief patterns are affected by lateral and vertical variations, and finally, cross direction pattern lines are solely affected by vertical variations. The literature review implied that two dimensional modelling in this way, is valid for certain trends[3, 9, 10, 11], although three dimensional modelling has improved understanding further.[12] Experimentally it has been reported in various articles that the cross direction patterns have a lower print quality, more line gain and shearing effects, compared with machine direction patterns, see references [13] and [14] and also for gravure printing: [15]. All this supports the idea that to test flexography ink transfer from plate to substrate, in a way that is relevant to the model theories and probes a single but common cause of defects relevant to practical print quality problems, the plate pattern should be reducible to two dimensions and in the cross direction. Furthermore this striped line pattern is appropriate for electrical contact structures in functional devices.

To summarise, to accurately and reliably measure the spatial-temporal fidelity of a liquid thin film as it is divided within a flexography-like roller system, the following experimental features must be present:

- Analysable printed pattern, which is closely representative of the form of ink immediately after it is transferred from the plate to the substrate;
- Stable conditions of printing, in terms of length of run as well as ambient control;
- Non absorbent substrate, with a surface energy larger than the ink so that ink wetting is possible;

- Industrially similar materials and process settings like speed should be used for the most representative results;
- A pattern of cross direction lines, with known aspect ratios, which are consistent of the range of dimensions investigated, and the dimensions must be sufficiently small so gravitational force effects do not dominate;
- Negligible ambient atmospheric effects.

This introduction has outlined the key requirements of a probing flexography testing method. The next section describes how the experiments in this doctoral research performed, to show they met these criteria. The following discussion of the results will show that the experiments yield useful results, and suggest further ways the experimental method can be improved to shed more light on the flexography ink transfer mechanisms. Specifically, after a discussion of the validity and reliability of the results, the discussion is structured in the following way. First, the static contact pressure magnitude is investigated, to show that the nominal line force has quantifiable, understandable, and sometimes deleterious effects on print quality, for which defects are defined by their causing ink transfer mechanisms. The effects of this pressure on the pattern quality is inspected further at different geometric scales, starting with impression roller and printing plate scale effects, relating the results to the plate backing properties. Then the plate pattern scale is probed, by varying the plate pattern ratio. Following this, pattern feature deformation and then fluid ink effects are suggested from the supporting experimental results. These small scale pressure effects include dynamic mechanisms, relating to previous modelling in literature. Finally the period of time for passage through the contact is varied, by changing the printing speed, and observed printing quality change is again compared with theoretical models of liquid ink transfer. This complete understanding of the hierarchical mechanisms, which contribute to the total printing quality variation is then used to suggest a mathematical model for this variation with nominal line force, from which optimal flexography printing variables are explained, given the observed trends and mechanisms of ink transfer.

5.2 Experimental Method

5.2.1 Contact width calculation

The contact width is required to better understand the effect of impression on the ink transfer. For this investigation it is adequate to consider the contact width at

the scale of the impression drum and printing roller, in other words pattern feature deformation under the applied printing pressure is not directly probed. However because plate pattern is uniform axially across the plate, the axial area of contact will also be constant. At this scale then, the printing roller can be considered as a smooth frictionless roller with a static Hertzian contact.[16] However, to include the effects of the foam backing, the printing roller is assumed to have composite stiffness, and uniform poison ratio. Given the transverse orientation of the applied force and material layers, the printing roller is treated with the slab model (a.k.a. Reuss model), as seen with composite mechanics [17], see Figure 5.1.

The size of the contact width (w) for the axially parallel cylinders was calculated, as per Chapter 4 in reference [16] :

$$\frac{w}{2} = \sqrt{\frac{4.P.R}{\pi E_T^*}}. \tag{5.1}$$

Where P is the nominal contact pressure over the width of the drum ($\frac{weights \times acceleration(gravity)}{drumwidth}$), and the total radius of curvature (R) is:

$$\frac{1}{R} = \frac{1}{R_1} + \frac{1}{R_2}, \tag{5.2}$$

and the total modulus E_T^* is:

$$\frac{1}{E_T^*} = \frac{(1-\upsilon_1)^2}{E_1} + \frac{(1-\upsilon_2)^2}{E_2}, \tag{5.3}$$

where the subscripts 1 and 2 refer to the impression drum and printing roller, respectively, and E the is the elastic modulus and υ is the poisson ratio with the printing roller's elastic modulus estimated to be:

$$\frac{1}{E_2} = \frac{f_P}{E_P} + \frac{f_F}{E_F} \tag{5.4}$$

given the subscripts P and F correspond to the plate and foam backing, respectively, which each having thickness (or specifically volume) fraction f, given $1 = \frac{1}{f_P} + \frac{1}{f_F}$.

The contact pressure is proportional to the nominal line force, as is given by:

$$P_{contact} = \frac{P}{\pi w} \tag{5.5}$$

This modelling of the contact width and pressure has several assumptions, such as $w \ll R_{1,}R_2$ and the rollers behaving linear elastically, which is not true of the silicone

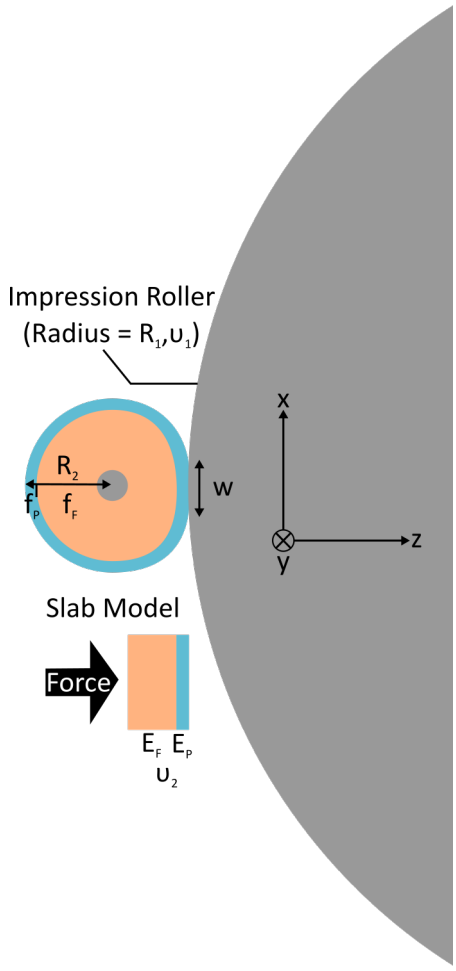


Figure 5.1: Schematic of modelled contact, with various properties labelled, see Table 5.1. Not to scale, axis of cross section displayed on the impression roller portion. The slab model shows the treatment of the layered printing roller, as a composite structure.

Table 5.1: Printing and impression roller specifications used for calculating the contact width.

Property	Symbol	Value	Unit
Radius of impression drum	R_1	0.1	m
Radius of printing roller	R_2	0.0015	m
Young's modulus of impression drum	E_1	200	GPa
Poisson's ratio of impression drum	υ_1	0.3	
Young's modulus of PDMS plate	E_P	1.50	MPa
Young's modulus of foam backing material	E_F	18.3	KPa
Poisson's ratio of printing roller	υ_1	0.3	
Thickness fraction of PDMS plate	f_P	0.2	
Thickness fraction of foam backing material	f_F	0.8	

plate or foam backing. These limits to the model are explored in the discussion. Also, given the assumption of infinite length (cross direction/ axial dimension), the model fails to consider a concentration of contact stress at the end of the roller, as addressed in Chapter 5 of reference [16]. However in this work the patterning does not occur close to the roller edges, and no deviations were noticed in the printing results. Given these assumptions, the contact width was calculated over the relevant contact forces, 0 to 4N with the roller materials specifications as shown in Table 5.1.

5.2.2 Plate design

The plate was fabricated as per the Materials and Methods chapter. The range of cross direction line created on a single plate allowed for a range of pattern ratios and aspect ratios to be printed within a single rotation of the printing roller, see Materials and Methods. This range covered various line widths with a pattern ratio (PR) of 1 and pattern ratios varying from 0.6 to 2.5. This range was chosen to give results which are typical of printed electrodes but also because it gave a large variation to be tested.

5.2.3 Printing trials and analyses

Initial tests with the custom-built letter press printing set-up, as described in the previous chapter, were conducted as part of the iterative improvements to the system. Once a mechanically reliable system was completed and consistent printing results

	Line force vs.		
Parameters	Peak-to-Peak Line edge roughness	RMS line edge roughness	Printed Linewidth
Backing Material	Steel, foam (Fig. 5.3)		
Pattern Ratio	0.6, 1, 1.5 and 2 (Fig. 5.6)		
Nominal Linewidth	1000, 200, 150, 100μm (Fig. 5.7)	200, 150μm (Fig. 5.8)	1000, 200, 150, 100μm (Fig. 5.9)
Speed	10, 20 35$m.min^{-1}$ (Fig. 5.10)		

Table 5.2: Schema of experimental data presented in this chapter, defining all the dependent variables (column titles) which are each plotted against the nominal line force in the relevant Figures, and the parameters at which the data that is presented was collected.

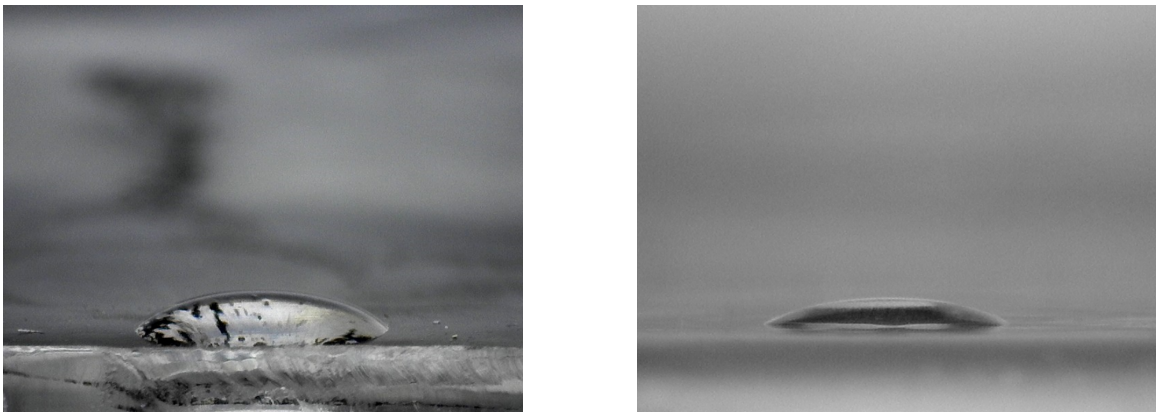
were achieved, parametric testing began. During these the initial trials a steel backing was used for the cylindrical plate, but later a foam backing support layer was placed between the printing plate and the brass printing roller. The difference in printing results was investigated.

Subsequently, using the foam backing, the impression force was varied, by using dead weights, as per the Materials and Methods Chapter: two 20g, 30g, 50g, 100g and 150g calibration weights. The drive system speed varied from 10$m.min^{-1}$ to the maximum achievable with the equipment: 35$m.min^{-1}$.

The initial trials with 1mm nominal line width patterning was imaged using a Leica M165C microscope and analysed using the ImageJ plugin, Analysis_Stripes.[18] The latter smaller printed pattern was imaged in its entirety using a Cannon 24400XF scanner, with 4800dpi resolution in monochrome. From the image analysis code, described in the Materials and Methods chapter, the oiled region's linewidth, root mean square (RMS) roughness, and peak-to-peak (P2P) roughness were calculated and tabulated for analysis, as presented in the following section.

5.3 Results

Initial experiments showed that the Krytox 1506 oil wetted both the PDMS plate and substrate, see Figure 5.2 and so initial trials were conducted with a steel plate



a. b.

Figure 5.2: Image of wetting sessile drops, of approximately $10\mu L$ Krytox 1506 oil, on a. PDMS plate material and b. PET substrate, showing greater wetting on the latter.

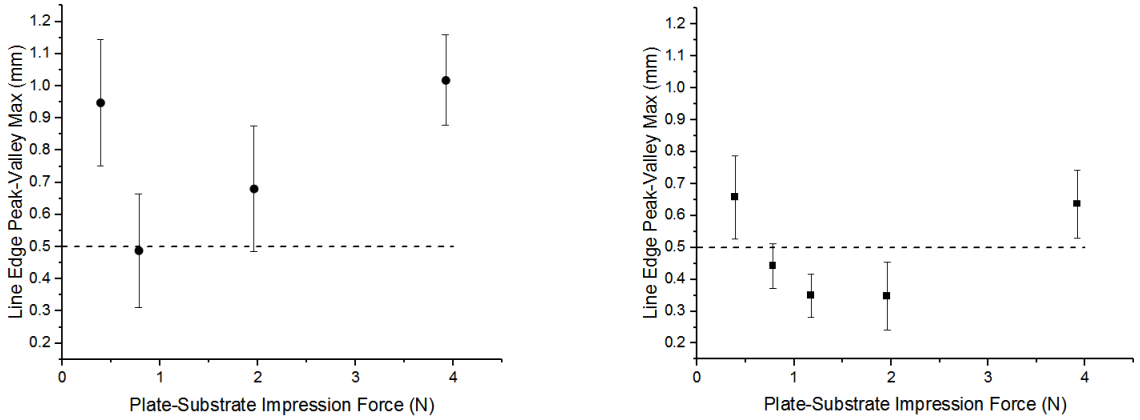
Table 5.3: Table of the standard deviations of the data of three separate runs conducted across several months, with 30g dead weights and printing speed of $20m.min^{-1}$. The standard deviation of the measured width and P2P between runs is less than the average standard deviation of the same within each print run of 9 measured lines, unlike the results for the RMS roughness.

	Width	P2P	RMS
Inter-run standard deviation of averages	0.00491	0.00735	0.00605
Average of intra-run standard deviation	0.01165	0.01537	0.00391

backing, which was then compared to the later results with 1mm pattern plate with a foam backing, see Figure 5.3. The foam backing material was also characterised mechanically, with the stress-strain curve shown in Figure 5.12 and the Hertzian contact width and pressure calculated for both plate backing materials is shown in Figure 5.9.

To test the validity of the experimental trials the error between three runs was calculated and found to be lower than the error within a single print's pattern of 9 lines, the data is shown in Table 5.3.

The results of the width varying printing force and line widths are shown in Figure 5.7 where the width and P2P each follow common trends between all the linewidths, see Figures 5.9 and 5.7. The RMS line edge roughness varied with nominal line force in the same way as P2P as shown in Figure 5.8, although the values of the mean RMS roughness varied more between runs than within the standard deviation measured within the 9 lines printed in one run, see Figure 5.8. However the similar trends, as seen in Figure 5.7, suggest the data is reliable. Representative images, which were



a. Steel plate backing

b. Soft foam plate backing

Figure 5.3: Change in the P2P, and the standard error of 15 lines, with plate-substrate impression force for 1mm spaced lines from initial trail results with plate backing made of a. steel and b. foam. The graphs display an initial decrease to a minimum before the trend changes with increasing P2P with force. Above a P2P of 0.5mm, highlighted by the dashed lines, shorting defects, due to the line edge roughness, are possible.

used for calculating the values of $150\mu m$ nominal line quality, are shown in Figure 5.5, along with a stitched together microscopy images of the entire metallized pattern.

5.4 Discussion

5.4.1 Experimental Validity

The selective metallization process is well suited for testing flexography, meeting most of the testing criteria introduced at the beginning of this chapter. This section lays out the validity of the experimental methods, with respect to these testing criteria, which were identified for reliable and accurate testing of print quality variation with printing speed and force due to ink transfer mechanisms.

With this selective metallization process, the deposited metal adheres to the non-print areas and so the observable thin film's lateral form is the same as the patterned ink (the sacrificial oil). Oil based inks are a valid candidate for flexography tests, as they are often used in flexography printing. Furthermore this oil has a viscosity ($0.116Pa.s$) within the range of normal printing inks ($0.05 - 0.5Pa.s$ according to reference [19]) and wets both the plate and substrate, see Figure 5.2. The substrate, PET, was chosen to be non-absorbent.

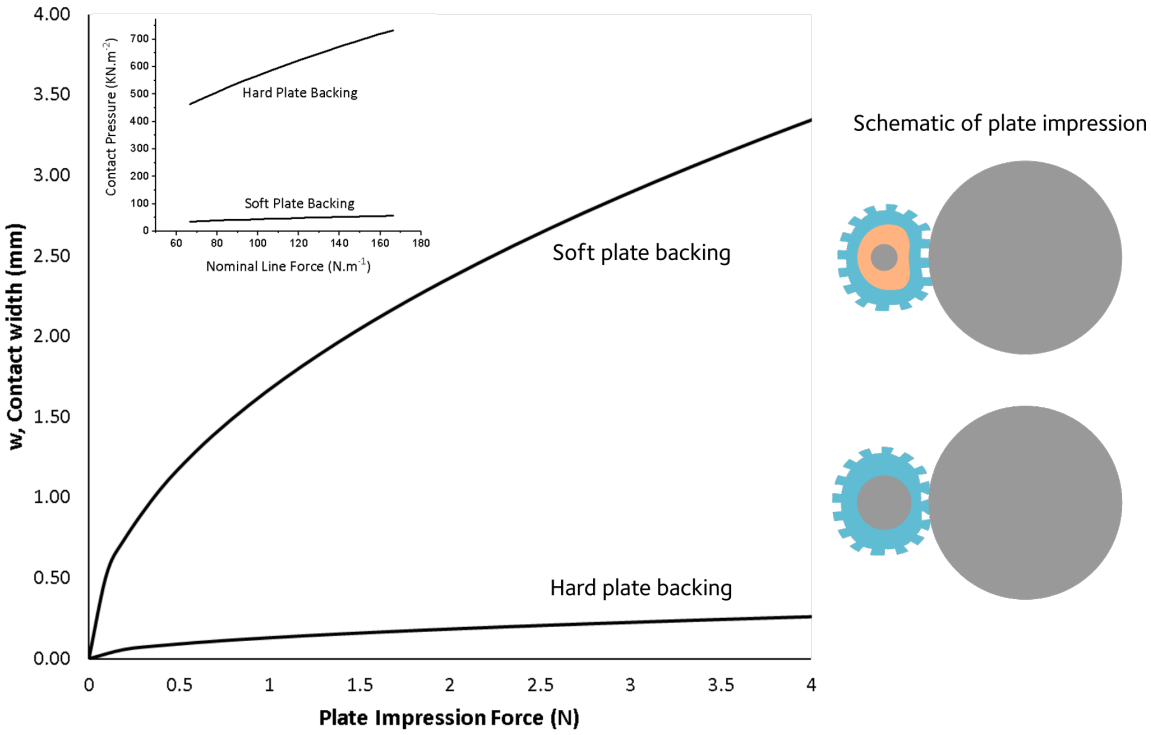
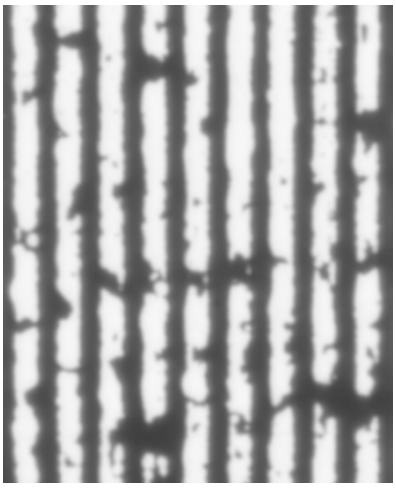


Figure 5.4: Hertzian contact width change with increasing contact, calculated, Equation 5.1, for a PDMS contact with steel backing (hard) and a foam supported PDMS plate (soft) contact with a steel impression cylinder. This shows the large difference of contact width for an elastic half plane with a change in material stiffness as shown in the schematics on the right hand side of the figure illustrating the difference in deformation. The inset shows the change in modelled contact pressure, from Equation 5.5, with nominal line force, for the hard and soft backing, showing that the hard plate backing leads to much higher contact pressures. The linear gradient is also larger for the hard plate backing ($2.632m^{-1}$), compared with the soft plate backing pressure gradient ($0.208m^{-1}$).



a. Nominal line force: $13.1 Nm^{-1}$



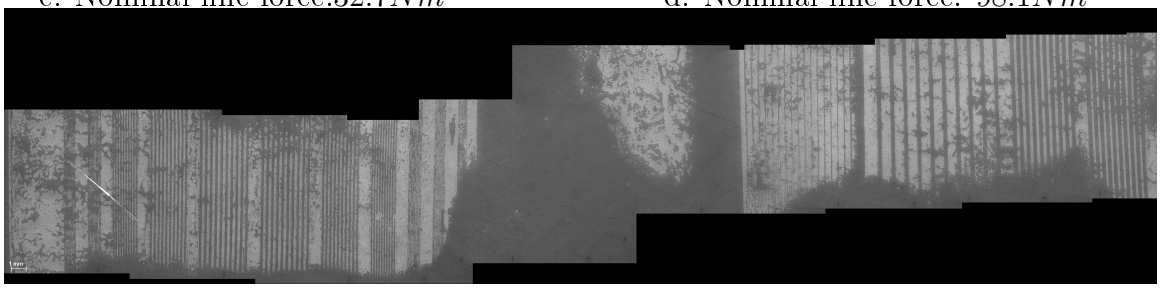
b. Nominal line force: $19.6 Nm^{-1}$



c. Nominal line force:$32.7 Nm^{-1}$

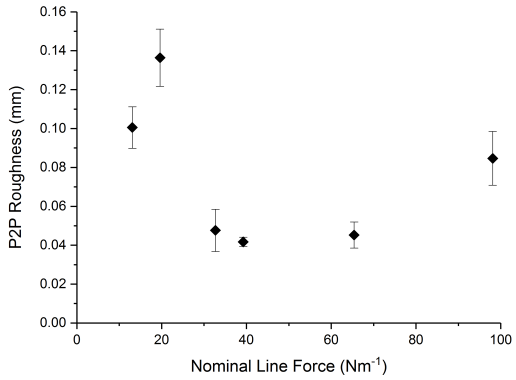


d. Nominal line force: $98.1 Nm^{-1}$

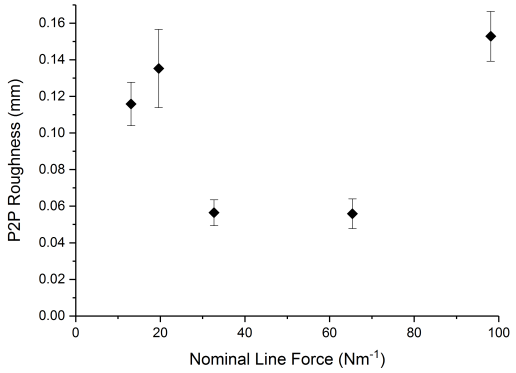


e. Stitched microscopy images showing the entire metal pattern.

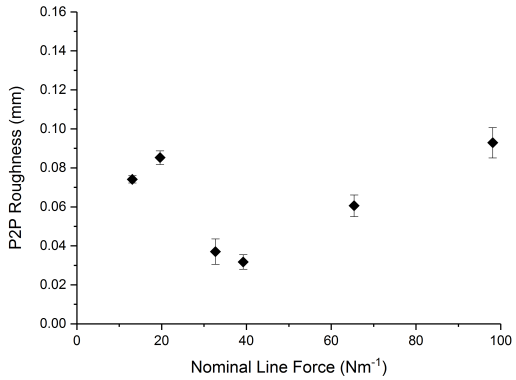
Figure 5.5: a. - d. are common scale optical microscope images of $150 \mu m$ lines at varying nominal line forces and $10 m.min^{-1}$ printing speed,where the light grey is the PET substrate and the metal deposition is the dark grey regions. e. the entire metal pattern at 50g nominal line force.



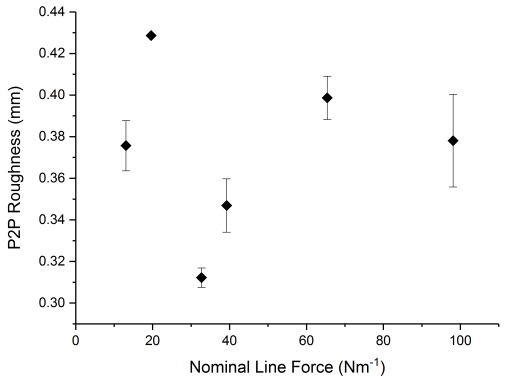
a. PR = 2 $\left(= \frac{150}{300}\mu m\right)$



b. PR = 1.5 $\left(= \frac{200}{300}\mu m\right)$

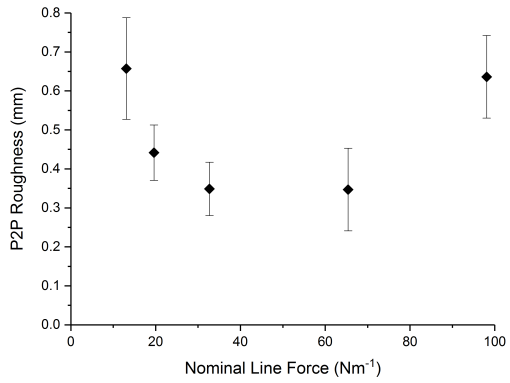


c. PR = 1$\left(= \frac{150}{150}\mu m\right)$

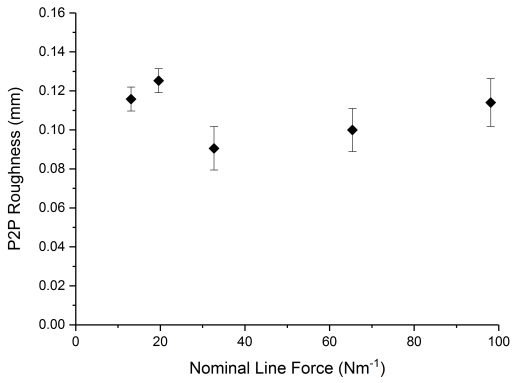


d. PR = 0.6 $\left(= \frac{500}{300}\mu m\right)$

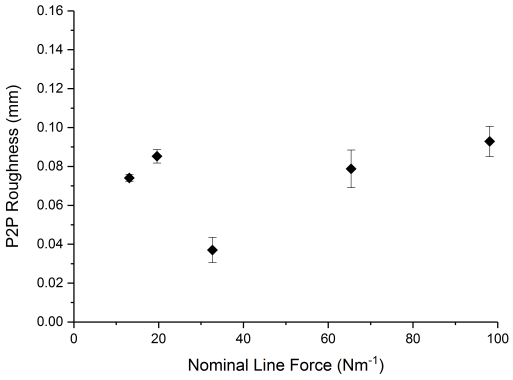
Figure 5.6: Graphs of the variation in P2P with force with varying pattern ratios of a. 2, b. 1.5, and c. 1 and d. 0.6 at $10m.min^{-1}$. All the data shows a trend of initial decrease in average P2P as nominal line force increases, followed by a subsequent increase, excluding the anomalous first data points and last data point in the 0.6 PR data. Figures a., c. and d. include data from a printing trial with a nominal line force of $39N.m^{-1}$which was performed several months after the other data was collected, supporting this trend.



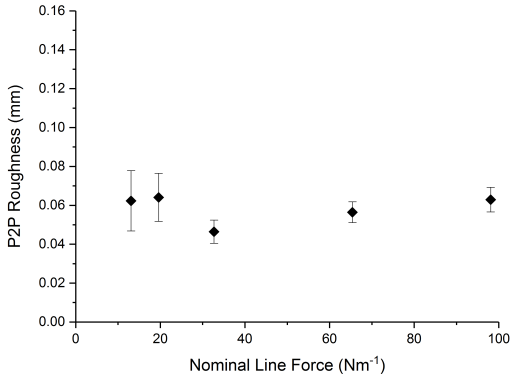
a. $1000\mu m$



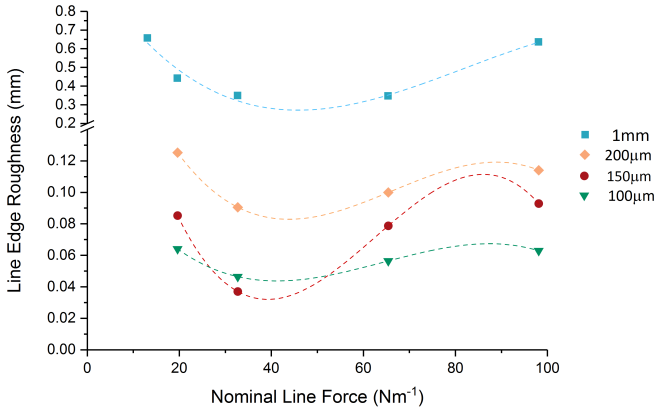
b.$200\mu m$



c. $150\mu m$



d. $100\mu m$



d. Parabolic fit

Figure 5.7: a-d. Change in P2P with force of impression for varying line widths, e. parabolic fit for the data showing the similar minimum at $42n.m^{-1}$ nominal line force.



a. $200\mu m$ b. $150\mu m$

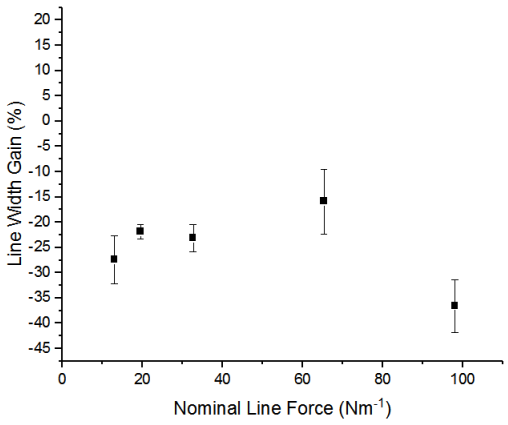
Figure 5.8: Variation of RMS roughness with nominal line force at a print speed of $10m.min^{-1}$, showing a similar trend to that seen with P2P in Figure 5.7.

The observable metal thin film patterns created can be used to probe the ink transfer that causes of the liquid ink shape on the substrate. The metal condensation onto the substrate begins immediately after ink transfer, given the view factor of the physical vapour source used in this set-up, and so the ink pattern is pinned immediately after flexography printing (the pattern of the transferred liquid ink is 'frozen in' by the metal deposition).

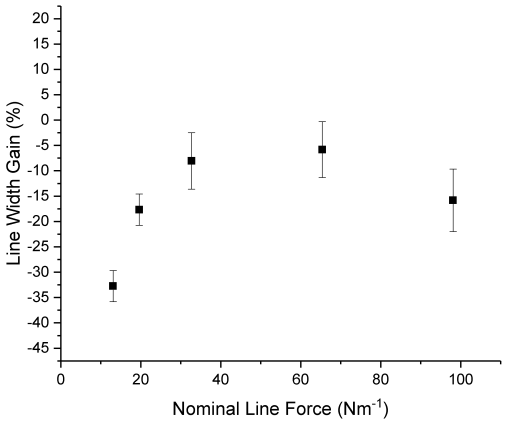
The process is performed in a stable vacuum, without ambient gas inclusions, and is directly applicable to industrial practices as is shown in Chapter 4. The printing parameters used in these experiments are similar to industrial printing speeds, albeit slightly slower in some cases but still fast enough to observe the effect of high speeds (above $10m.min^{-1}$). The materials used, the substrate and rollers, are also standard for commercial processes, although the foam plate backing was chosen to be less stiff here as a wider range of contact widths could be investigated, giving further insights into the effects of printing pressure. In this trial the plate backing had a stiffness of $18.3KPa$ compared with an industry brand hardness of $2.4MPa$ (converting from 65 Shore A).[20] The cross direction orientation and variation of pattern dimensions, means that liquid transfer effects, resulting from lateral transfer mechanisms, have been tested over a range of dimensions relevant for printed functional devices. The nominal patterns were precisely fabricated on a single printing plate, hence the various linewidths were printed within a single rotation. This improves the reliability of the measured printing effects, which is discussed in the next section.

5.4.2 Origin of errors and results analysis

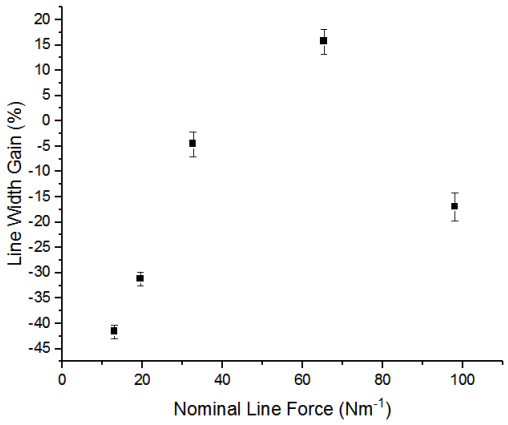
This section deals with the errors within the collected and calculated data presented in the above Results section. This discussion concludes that the data is accurate



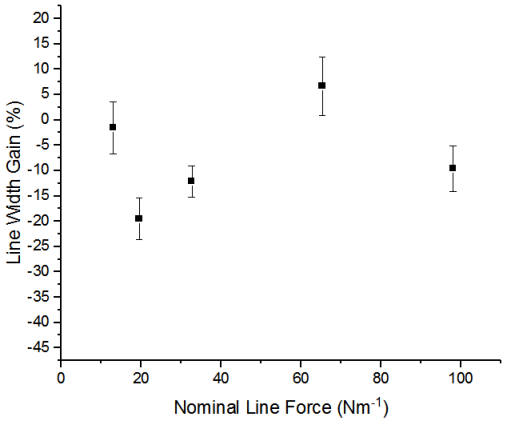
a. $1000\mu m$



b.$200\mu m$

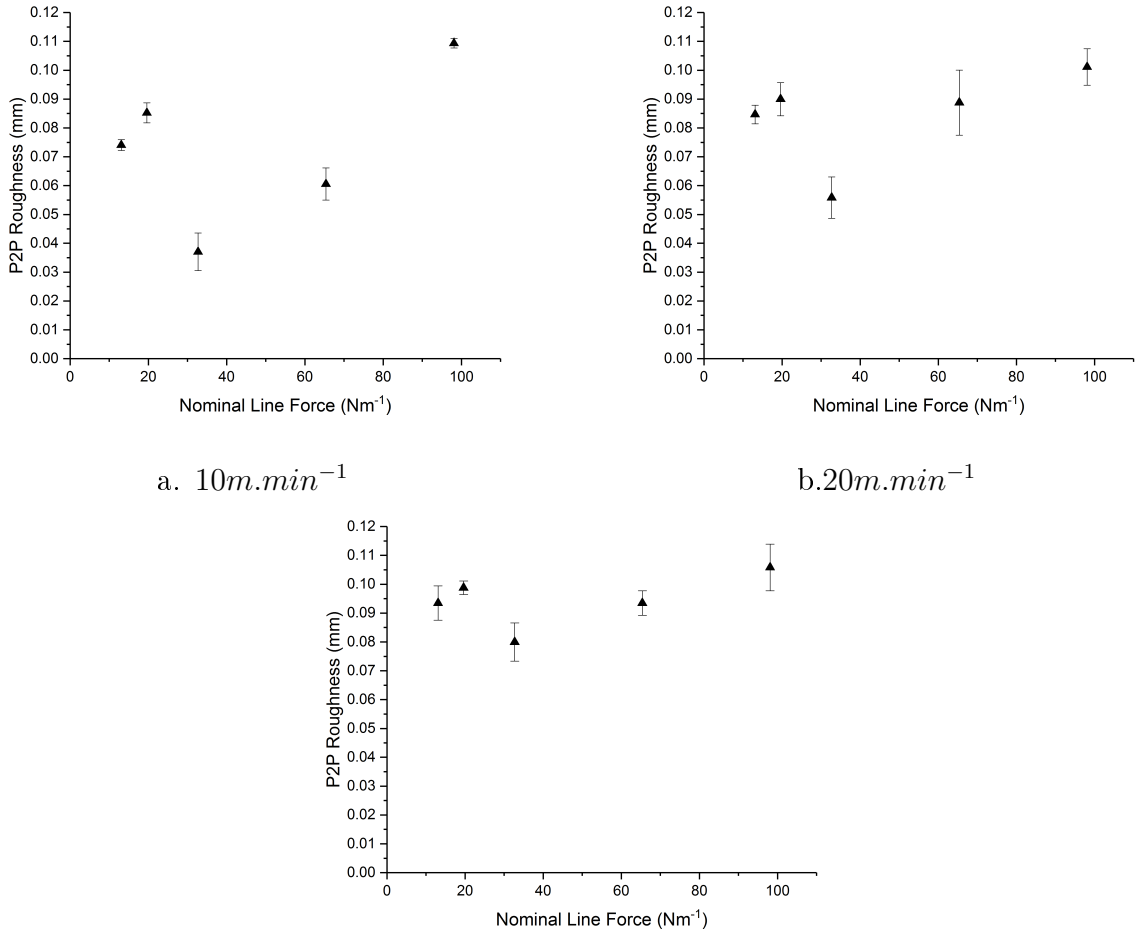


c. $150\mu m$



d. $100\mu m$

Figure 5.9: Change in line gain with plate-substrate impression force, for a. $1000\mu m$, b. $200\mu m$, c. $150\mu m$ and d. $100\mu m$, showing that initially line gain increases with impression force up to a common maximum between line widths and speeds, after which there is a decrease in line gain. Initially the lines are not as wide as the printing plate but can increase to be the wider than the printing plate.



a. $10m.min^{-1}$

b.$20m.min^{-1}$

c. $35m.min^{-1}$

Figure 5.10: Graphs of the variation in P2P with force with print speeds of a. $10m.min^{-1}$, b.$20m.min^{-1}$, and c. $35m.min^{-1}$ with $150\mu m$ nominal linewidths.

to a degree from which trends and causing physical mechanisms can be reliably and accurately deduced.

First, to establish certainty from the computer image analysis data, the intrinsic variability must be shown to greater than the inaccuracies in the measurement (which is the image processing and choice of measurements: linewidth, P2P and RMS roughness). Table 5.3 shows that the deviation from the average was smaller between three separate runs, made during a period of several months, than the average deviation of a single pattern set (9 lines). Table 5.3 shows that the average values obtained, for linewidth and P2P, are reliable from a single printing run, and would not vary beyond the standard deviation of each measurement if repeated. However, Table 5.3 also shows the RMS roughness was not as reliable, with significant deviation of the mean between runs. This said, Figure 5.8 shows that RMS and P2P roughness trends with force are the same, and so the RMS data can be relied upon as supportive indicators of the flexography machine mechanical properties and fluid behaviour, and similarly considered when discussing the observed variation with line force and speed.

Second, the standard errors seen in the print results graphs show the variation within one print run. This precision error can be associated with plate imperfections and lack of bearer bars as well as machine anomalies such as non constant rotational velocity, or impression drum wobble. Also the substrate has some degree of surface roughness and also tensioning effects, which have been neglected for simplicity without, evidently, negating the results. In practice, it is assumed that any flexography machine would include some engineering tolerances or imperfections, and the results highlight the importance of optimizing machine settings to the specific machine material properties.

Finally, it was seen that the P2P and RMS roughness measure values for a nominal line force of $13N.m^{-1}$ were inaccurately low. From the images in Figure 5.5 it can be seen that the incomplete contact lead to such a poor quality of print that the image analysis data can be disregarded as anomalous.

5.4.3 Observed defects categories, static and dynamic

The defects seen within the printed lines are labelled and categorised below in Figure 5.11 and Table 5.4 These definitions are based on definitions from the semiconductor very large scale integration (VLSI) industry [21], which conjoins the printing analysis and the use of the optimised printed lines as transistor contacts in subsequent work. When considering silicon technology transistors a 'killer' or critical defect would be any defect, in the pattern or due to foreign particles, which has dimensions which

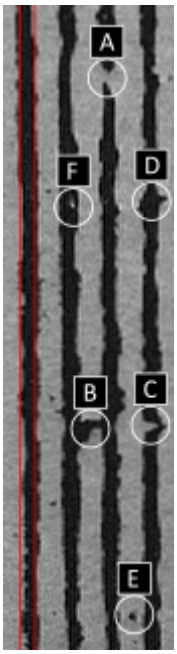


Figure 5.11: Optical greyscale microscopy image of the defining defects observed in a print ($65.4n.m^{-1}$ and $10m.min^{-1}$) of $200\mu m$ lines (nominal line edges shown in red), where the light grey is the PET substrate and the metal deposition is the dark grey regions. Label A is a bridge, B an interruption, C is an intrusion, D a protrusion, E is a pinhole and F a pin spot example defect of the oil pattern, shown by a lack of metal deposition.

in the order of magnitude of the source drain width, and could cause shorting or open circuits. This statistical criterion, typically stated as a number per unit area, ensures that the devices are patterned and cleaned to standards which ensure high yields. Within this R2R printing paradigm a parallel is to state that critical defects can occur when the P2P edge roughness is greater than half the line width. The printed area to be used for the functional device is taken as the area of measurement, as described in the Experimental Methods section.

Identifying the causing mechanisms of the defects is important for understanding which printing factors affect them. It is suggested that the defects, given the probable causing mechanisms listed in Table 5.4, can be categorised into defects with static causing mechanisms, and ones with dynamic causing mechanisms. The pin hole/spot defect arises from dynamic effects, which has been modelled for fluids with given Reynolds number (the ratio of inertial and viscous forces), as commented on in the Literature Review chapter.[22] Ink protrusions and intrusions can be thought of as defects caused by both, or either, static (time-independent) and dynamic effects; the causing mechanism can depend on the printing speed and/or pressure. For such a

Table 5.4: Definition of defects in the printed oil pattern (inverse of metallized pattern defects) as identified is Figure 5.11.

Defect	Inverse Equivalent	Possible Causing Mechanisms
Pin Hole	Pin Spot	Satellite droplet from breaking bridge (misting), or extreme protrusion extension in lateral direction, incomplete transfer of oil, non wetting of ink, onset halo effect and plate defect.
Protrusion	Intrusion	Contact width pressure instabilities leading to local shear in print direction, plate expansion and plate defect.
Bridge	Interruption	One or two protrusion or intrusion defects extending beyond half linewidth locally.

static-only type defect, the physical origin is linked to static pressure on the printing plate and on the ink thin film within the contact region. The pressure (p) on the plate and ink, which are assumed to be incompressible ($\nabla^2 p = 0$), has been modelled in previous work between parallel plates, which are perpendicular to the z axis, the axis of applied force and of compression/separation.[23] It was shown that with a viscoelastic plate, the pressure is harmonic:

$$\frac{\partial^2 p}{\partial z^2} = \frac{\partial^2 p}{\partial x^2} + \frac{\partial^2 p}{\partial y^2}. \tag{5.6}$$

With a plate pattern having cross direction lines, i.e. with the longer dimension in the y axis, shorter dimension travelling through the contact region in the x axis, the flows and pressure gradients in the y direction can be assumed to small compared to the x direction. This pressure relation implies that the applied pressure (in the z direction) should be proportional to any pressure effects observed in the x direction. This hydrostatic pressure profile naturally results in the ink movement leading to intrusions and protrusion in the transferred ink pattern which are generally found to be symmetric in the print direction (y axis), as observed in this investigation given the plate pattern orientation used. This said, dynamic effects could also lead to an observed P2P roughness, but the precise dynamic mechanism for this is not as clear, although some possible mechanism are suggested in Table 5.4.

5.4.4 Effects of foam plate backing

The previous section has defined the defects and discussed the possible causing mechanisms, and which printing variables might impact them. This section discusses P2P data change with the plate backing material mechanical properties, and relates it to the static pressure over the plate-impression drum contact. The data presented in Figure 5.3 showed the critical defect criterion as a dotted line, the data recorded above this has a P2P greater than half the linewidth for a set impression force. With a greater than critical P2P, the liquid oil transferred, due to the impression force applied, can lead to a metal pattern with interconnected lines, which would cause shorting, or conversely interrupted lines, creating to open circuits. However, for particular impression forces and plate backing, the P2P is reduced below this critical defect criterion, and so this operational parametric area of printing patterns will not cause device failure due to print defects.

As well as optimal impression force, the printing plate support material is seen to reduce the P2P, Figure 5.3. Initial trials used an earlier model of the custom-built flexography rig with a steel backing roller supporting the PDMS printing plate, and the resulting printed patterns had very rough edges. Subsequently, with a more compliant foam backing, where the foam had a lower stiffness than the printing plate, the contact length (dimension across the drum) between the plate and substrate became more conformal and the contact width increased, see Figure 5.4. The printing-plate-scale roughness was accommodated for, as the lower modulus foam backing was strained more than the printing plate under the applied load. As a result, the average P2P reduced for all printing impression forces.

This difference in elastic modulus of the plate backing is further characterised in Figure 5.4. The difference in the contact area when using steel and foam plate backing is shown by a large difference in the calculated Hertzian contact widths. In the case of the steel backing the impression force is distributed over a small contact area ($\pi w \times line\, length$). So the pressure applied, Equation 5.5, to the printing plate and liquid ink thin film is much larger, compared to the larger contact area with the foam backed printing plate, Figure 5.4 inset. The difference in the change of pressure magnitude with backing stiffness, results in greater plate feature deformation, pressure variation, and the viscous stresses seen by the liquid as they pass through the printing contact, see Table 5.4. This is supported by the nearly identical ratio of the rate of change in P2P data and the contact pressure gradient for hard and soft plate backings ($2.94 \times 10^{-7} N.m^{-1}$, and $2.95 \times 10^{-7} N.m^{-1}$ respectively), at nominal line forces above $60 N.m^{-1}$(the reason for only including data above this line force is explained in section

5.4.5). The correlation in the modelled pressure and the resulting print quality data supports the idea that they are physically connected by the hydrostatic pressure, Equation 5.6, as discussed in the previous section.

The use of foam tape to hold the plate onto the printing roller is standard within flexography printing. These results support this practice and quantified print quality assessment has provided additional insight into the physical mechanisms behind this practice, namely the effect of contact pressure on P2P. Importantly, the data has provided means of using quantified printing characterisation to predict device failure and yield. The following sections build on this understanding to find out what the optimal printing parameters are, given the foam backing properties, and the selection criteria for the foam materials properties. In the following section, the effect the plate pattern ratio has on print quality is addressed as the next step down in the hierarchical scales of flexography printing and to further explore the printing pressure effects.

5.4.5 Quality changes with pattern variation

The variations in the printing quality have similar trends across different patterning ratios, see Figure 5.6 and also linewidth dimensions with constant patterning ratio, Figures 5.7, and 5.8 (which were all performed with a foam plate backing). The shared line edge roughness trend with increasing nominal line force is: there is an initial decrease until approximately $40N.m^{-1}$, subsequently there is an increase, at a lower rate of change of the line edge roughness. The data from varying linewidths is plotted on one graph with parabolic fits, showing there is a common minimum at $42N.m^{-1}$, Figure 5.7e. The commonality of this trend with varying plate patterns implies the physical origin of the trend is related to printing system (larger) scale effects. In this way, the shared data minimum can be thought of as the common force, at which the line roughness due to the machining defects (drum wobble, plate-scale roughness) is overcome by the roughness of the ink transfer mechanisms due to the printing speed and pressure. This line force must depend on the mechanical properties of the flexography printing system. Exceptions to this otherwise unilateral trend, is data for the lowest line force ($13N.m^{-1}$), which was excluded from the parabolic fits, but this can be considered anomalous as discussed above. Also the data for PR 0.6 seems too variable for this trend to be clearly seen, Figure 5.6e. This section explores this system-scale mechanical dependence, to relate the optimal printing variables to the material choices of the printing foam backing.

The nominal line force of $42N.m^{-1}$ is associated with the calculated Hertzian contact pressure of $1.8MPa$ which is applied to the entire Hertzian contact area of

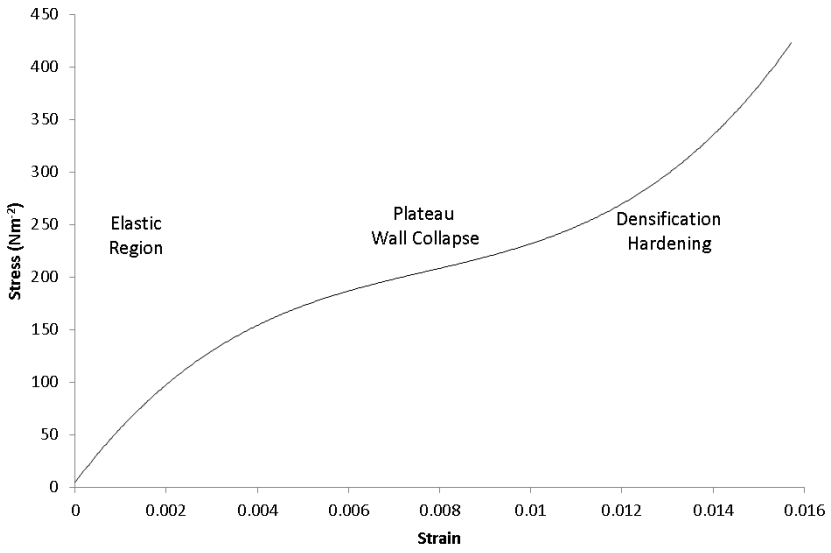


Figure 5.12: Stress strain curve for the foam plate backing material showing 3 distinct regions: elastic, hardening, and cell collapse.

the plate and impression drum. This is equivalent to a stress applied laterally onto the plate with foam backing, which were modelled using the common stress independent strain Reuss composites model, as explained in the above Experimental Methods, section 5.2.1. Considering the foam plate backing stress strain curve, shown in Figure 5.12, this stress corresponds to the end of the foam's elastic regime, and the beginning of the plateau regime, as the foam cells' walls collapse. As the foam is compressed the cell deformation leads to the force being applied the cell walls which bend elastically and then buckle and yield under the applied printing pressure (stress). Hence it can be assumed that after this nominal line force the pressure is carried proportionally more by the plate and ink thin film. It should be noted that even before this, in the elastic region, the printing pressure is carried proportionally by the printing plate, according to Equation 5.4, but accordingly it experiences 2 orders of magnitude less strain than the foam in this region, see also Table 5.1.

There is also an observed change in the P2P average of the printed line edges as the pattern ratio changes. Figure 5.6a. - c. show for PR ≥ 1 there is a shared trend, as described above. Compared to PR 1 data, there is an overall increased P2P before the minima associated with the plate backing, however the linewidths are also wider, which increases the P2P, as seen in Figure 5.7. Notably the P2P minimums for Figure 5.6a-c, have similar values, whereas below a PR of 1 the P2P minimum is much larger, Figure 5.6d, and never below the critical P2P size.

With a nominal line force above the global minimum P2P at $42N.m^{-1}$ there is a changing rate of increase in P2P as the PR changes. The gradient of the data increases with PR in this region, where the P2P is understood to be due to plate and ink deformation mechanisms. That is to say, the gradient of the PR 1 data is double the PR 2 ($1.05 \times 10^{-6} N.m^2$and $4.74 \times 10^{-7} N.m^2$ respectively). Furthermore for the PR of 0.6 data the gradient ($1.9 \times 10^{-6} N.m^2$) is close to $\frac{1}{0.6}$ times of PR 1's gradient, ignoring the final data point. As the relief area within contact region changes, that is the relief pattern ratio changes, the variation in printing quality correlates to the pattern ratio. This correlation supports the argument that the pressure experienced by each pattern feature leads to deformation and loss of fidelity of the transferred ink. To summarise, as the applied pressure increases, the deformation increases at a rate relative to the proportion of the plate relief pattern in contact (the pattern ratio).

It is now possible to disentangle the two opposing trends seen in the P2P variation with force. First, there is a consistent variation of the P2P decreasing because the plate backing foam creates a more conformal contact with the applied printing pressure. Due to its non-linear stress strain behaviour there is nominal force associated with a sudden decrease to zero P2P as the foam modulus plateaus. With optimal plate backing material selection then, any plate-scale roughness or machine defects, like drum wobble, should be accommodated for and the printing P2P fall to near zero. This P2P can be thought to be varying with the inverse of the foam's strain, where the plateau leads to an idealised effective infinite strain, and the strain is in the inverse (perpendicular) direction for the P2P roughness (z-direction instead of x-direction, see Figure 5.1).

However, there is a second competing P2P trend associated with ink and plate deformation, which varies with nominal line force. The rate of increase in this P2P trend is associated printing pressure acting over the pattern features, or more specifically the proportion of the plate relief within the total contact width. At some nominal line force this second trend will dominate over the first. For this system a PR >1 has a gradient such that the P2P roughness of the plate backing trend is always greater than the ink transfer trend and so the minimum is always the same within error for Figure 5.6a-c. This was further confirmed by the performing another experiment with the near optimal line force of $39N.m^{-1}$ after these trends had been first seen, as is shown in Figure 5.6, and the measured P2P fits the trend. However below a ratio of 1, the plate and ink deformation dominates over the plate backing P2P trend, before this sudden decrease drop, which can be distinguished from Figure 5.6.

The next sections build on the data gathered from this development of the custom-built flexography rig to probe this second trend which relates to ink and plate feature deformation, each with distinguishable trends. The following discussion considers smaller-scale effects that the printing force has on ink transfer.

5.4.6 Plate-substrate contact pressure effects

In the previous sections, the print quality variation due to large scale effects of pressure on the plate backing material and pattern ratio were discussed, and shown to be crucial to removing critical defects. In this section, the various effects of the plate to substrate impression force are considered and linked to the smaller scale physical mechanisms of the plate relief features and ink. At these smaller scales the variation of pressure through the contact region is used to explain the observed results, with further discussion of the dynamic effects discussed in the following section.

Firstly, Figure 5.7 shows the non-linear trend, as discussed in the previous section, for P2P change with impression force, spanning an order of magnitude difference, and this is supportingly seen with RMS roughness variation, Figure 5.8. In both measurements, there is an initial decrease of the line edge roughness as the impression force increases, as discussed in detail in the previous section. The subsequent increase in edge roughness, see Figure 5.7 and 5.8, can only result from an over pressure causing plate deformation and the liquid ink to move out perpendicular to the applied force, as per Equation 5.6. The rate of change of the edge roughness with pressure was evaluated in the previous section, here the possible smaller scale mechanisms of the plate features and ink within the contact that lead to the observed P2P increase with nominal line force are discussed.

The second effect which is thought to also be due to plate and ink deformation mechanisms is the line gain, which is the percentage difference of the printed oil width to the plate's nominal feature width. Within flexography printing parlance this would be referred to as physical line gain, see definitions in Appendix, but here it is not reported as the percentage point difference from the intended solid density (which is nominally 50% in these results as the PR is 1), which is the graphics industry standard.[19] In this sense the results are not directly applicable to flexography printers but this terminology and heuristic is more general and more directly relevant to the formation of the printed patterns.

Figure 5.9 shows that the linewidth initially increases with applied load and then there is a slight decrease after a line force of around $70 N m^{-1}$, with all the different nominal linewidths. The initial increase is assumed to be associated with the plate

expansion and ink spreading. This trend is similar to results published in reference [15]'s Figure 9. This similarly focussed on line patterns but with gravure printing. Now the plate feature deformation is described in terms of the pressure profile through the contact, after which the effects on the ink transfer fidelity are discussed.

Flexography plate feature expansion was previously discussed in the literature review, highlighting the work by Bould et. al, in which the deformation of the dot features was modelled and found to be highly dependent on the impression pressure. The mechanism of feature (half-tone dots) deformation was 'barrelling' (i.e. the feature walls bulging under compression), which dominates over the alternative dot face expansion mechanism, for low poisson ratio plate materials as used here.[2] Building on this, if the features are much smaller than the total contact size, which is true for Hertzian contacts with these plate features (i.e. $> mm$ contact width with $< 200\mu m$ feature size), then the pressure experienced by the plate features as they pass through the contact can assumed to be similar to static loading, like micro contact printing (μCP). In the μCP field, PDMS micro-feature deformation also exhibits barrelling mechanisms when the pattern ratio and aspect ratio are 1, although it is termed side wall collapse in reference [24], Figure 5.13. In this research paper the authors go on to define the side wall collapse onset, when the stiffness (S_c) of the micro features is equal to the bulk stiffness such that:

$$S_c \propto \frac{d\sigma}{dv_\infty} \sim \frac{dP_{contact}}{dD_{plate}}. \tag{5.7}$$

Figure 5.13 gives the definitions for the μCP far field stress (σ) and displacement (v_∞). Above the aforementioned plate backing P2P minimum, when the printing pressure is experienced by the plate and ink, these μCP variables are equivalent to a flexography printing system contact pressure ($P_{contact}$) and plate compression (D_{plate}) respectively. This is similar to treating the system as a lubricated hydrodynamical contact, like reference [23], from which the notation is borrowed. Note that $P_{contact}$ here is no longer given by the Hertzian Equation 5.5, as the plate and backing are no longer operating in the linear elastic regime.

Accordingly, this onset stiffness for micro feature deformation can now be understood in terms of the printing pressure and plate feature compression, as it passes through the contact region. Additionally, as the plate moves through the contact region the pressure and compression will vary with time. Rewriting this critical onset proportionality in terms of time (t):

$$\frac{dP_{contact}}{dD_{plate}} = \frac{dP_{contact}}{dt} \cdot \frac{dt}{dD_{plate}}, \tag{5.8}$$

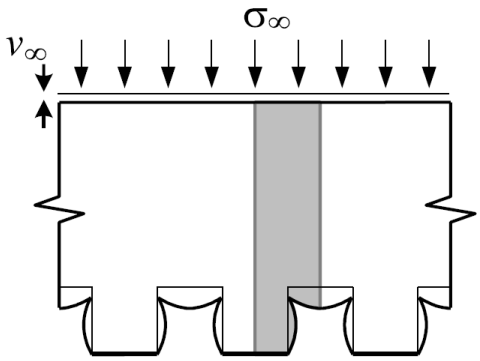
it is evident that the critical stiffness for plate deformation, Equation 5.7, changes dynamically through the contact width; the feature deformation onset pressure and deformation varies with time (printing speed). This is no longer a static pressure problem as discussed in previous sections with larger scale effects.

As the plate feature enters the contact region there is a positive pressure change and the onset stiffness for deformation will be overcome if the pressure is large enough. In the aforementioned flexography modelling, typical impression pressures (given as engagement distances) showed there was physical gain of the plate, for low poisson ratio plate materials.[2] Increasing the engagement increased the amount of plate deformation. This trend is similarly seen in the μCP field.

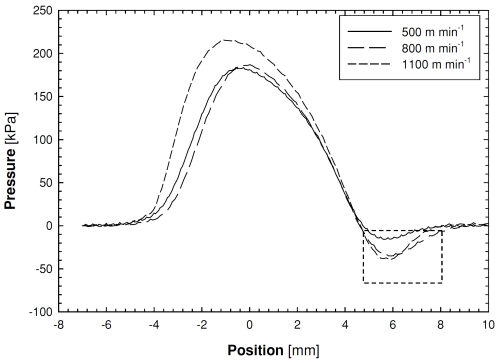
It can be stated that the pressure profile in the contact scales with the nominal line force, as seen with coating roller contacts, which is analogous to the situation here at the scale of the cross directional features.[25] With increasing line force the onset of barrelling will occur earlier within the contact region, and the scale of the feature barrelling will be larger. This is represented in the these findings by the overall increase in P2P with force, once the printing roller scale effects are overcome.

Figure 5.7 shows the P2P increases, after the minimum at $42N.m^{-1}$, which is in part due to the side wall collapse of the features, and any edge roughness extenuation associated with this. When the PR$<$1 and the relief pattern contact area within the contact is reduced, i.e. with low coverages, the rate of change of pressure variation within the nip will increase faster than when the feature contact area, as a proportion if the total contact area, is larger. Hence the onset for deformation will be reduced and the rate of feature expansion will increase. In other words, as the pressure profile through the contact is distributed over a smaller area, the rate of change of the pressure profile with increasing line force, increases. This is seen in these results as an increasing gradient in P2P with force for aspect ratios $>$1 (most pronounced with PR=2, and most linearly with PR=1) and for a PR=0.6 there is a decreasing P2P change with force (albeit larger). This follows tonal printing grain results.[2] The nominal line force required for barrelling of the features within the contact, which is reduced for lower aspect ratios, as can be distinguished in the shape of the P2P data, which widens as the pattern ratio is decreased.

The increasing line force, and resulting increasing positive pressure variation in the contact, will increase the amount of bulging of the plate features. This is observed in the line gain results, which show a steady increase in line gain as the plate features



a. Plate feature side wall collapse (barrelling)



b. Measure pressure profile against contact position

Figure 5.13: Two separate phenomena. a. schematic of PDMS plate feature deformation, giving definitions used in Equation 5.7. b. measured pressure profile through the contact of deformable coating rolls, with the negative pressure at the exit highlighted. Printing speeds are shown other printing parameters can be found in the source. a. from [24] b. from [26] 5.6

contact area increases. The end of this trend at $\sim 70N.m^{-1}$ is then associated with the maximum side wall deflection possible, before the critical stress for rupture.

Also, it has been reported that the ink spreading dominates over plate deformation, for tonal gain with halftone printing plates.[2] It was found that the physical gain due to the plate was up to 10 times less than gain due to ink, although ink gain increased less as a function of engagement (impression pressure). The viscous stress experienced by the liquid ink, due to the pressure variation within the contact region, will likely be focussed at the microscopic plate defects, which will be extenuated as liquid ink mimics the shape of the plate. The mechanism of ink splitting, at the speeds where viscous and inertial forces dominate over capillary action, is best considered from the work on liquid bridges. This body of research predicts an even distribution of ink after separation for the printing speeds used; and that with high dynamic viscosities there will be longer liquid bridges before bridge break up.[12] This follows the trends seen here, as increasing printing pressure will increase the effective viscosity of the ink in the contact. At higher printing forces string-like defects and pin defects become more prevalent, see Figure 5.5.

Finally it should be noted that the ink deformation does not have a critical onset stiffness (applied pressure), like feature deformation. In other words as soon as there is any contact between the ink and substrate, there will be some contact line roughness associated with the plate roughness and dependent on the wettability of the substrate,

leading to an internal pressure of the ink. This is exploited for some patterning work which uses highly (chemically) controlled pattern transfer with quasi-static speeds. For typical flexography operating conditions the ink will always have some line edge roughness due to plate feature edge roughness, which will decrease with the printing pressure, as volume conservation of the the spreading ink tends towards a minimal edge to volume ratio.[3] This is supported by the trend of line gain, which shows the ink volume distribution increasing from the lowest pressure used. Even below the printing roller scale roughness being accommodated for, there is an increase in the line gain, which if not plate deformation (when effectively only the foam backing is being stressed), consequently must be liquid ink pattern spreading during transfer, even at these low pressures. The plateauing of the line gain can also be associated with the limit of ink spreading due to volume conservation. The slight decrease at higher nominal line forces could be due to halo or seam effects , where the ink is squeezed from the centre of the plate feature. Or this negative shift could be a result of increases interruptions, due to increased P2P. These interruptions will be averaged within the code analysis to reduce the linewidth.

This section has shown that the pressure variation through the contact region deforms the plate features and ink pattern. In general the the ink deformation dominates at low contact pressures, originating from plate feature edge roughness. However this plateaus and is then superseded by plate deformation effects. Plate feature deformation accounts for the high printing force defect highlighted increase, after a critical onset pressure. In the next section the effects of printing speed on these mechanisms and the resulting printing quality are discussed.

5.4.7 Printing speed effects on print quality

The previous sections have highlighted the importance of matching the printing force to the materials properties of the printing system to achieve to the lowest line edge roughness. This section discusses the results obtained by varying the printing speed, which ideally would be maximised for high throughput manufacturing of organic devices.

The results in Figure 5.10 show that as the speed increases the amount of variation, in roughness with printing force, decreases, and also that the average roughness increases at all impression forces. This change can be understood in terms of the behaviour of the liquid ink with time, as it passes through the contact region and the levelling effects on the substrate.

Table 5.5: Linear gradients for P2P change with nominal line force, showing relative changes with speed which fits modelling predictions in reference [23]. The linear gradients are obtained with data above $42N.m^{-1}$ and show good agreement with the theoretical predictions.

Printing Speed	$10m.min^{-1}$	$20m.min^{-1}$	$35m.min^{-1}$
Gradient ($m^2.N^{-1}$)	12.0×10^{-7}	6.86×10^{-7}	3.97×10^{-7}
% change	-	42.8%	66.9%
Modelled % change	-	32%	65%

First, it is notable that gradient of the increasing in P2P roughness (for contact pressures above the plate backing elastic limit) shows a scaling with speed. For these linear gradients, when doubling the printing speed there is a 43% decrease in the gradient, and also a 67% decrease when increasing the speed 3.5 times, see Table 5.5

This is in good agreement by lubrication modelling work by Sauer et al. who predicted the change in pressure in the contact region was proportional to speed with an exponent of +0.4 (which would give 32% and 65% changes for the respective speed increases).[23] In this work the displacement of ink due to 'squeeze flow' with excessive printing pressure(W) is proportional to the average nip height (D) and the time (Δt), and inversely proportional to the nip width (pressure corrected) (λ_{nip}):

$$W = \frac{D^2}{12\mu}.\frac{\Delta P}{\lambda_{nip}}\Delta t \tag{5.9}$$

This is derived from the pressure variation (ΔP) with the limit that the pressure beyond the contact region (that is beyond the edges of the un-squeezed nominal liquid bridge pattern) has an atmospheric pressure, devoid of any pressure gradients as the ink expands into the ambient beyond the plate feature (leading to the halo effect) as seen with atmospheric solvent based inks. In the experimental results presented here, with an imposed extremely low pressure (i.e. in vacuum environment) the zero pressure assumption of Sauer et al. is more realistic, and perhaps why their model fits this experimental data well. This surprisingly good fit with a theoretical model further supports the idea that this P2P increase holds the answer to how pressure effects print quality.

The modelling work by Sauer et al. and Darhuber et al., amongst others, also shows that at high printing speeds there is less time for this squeezing of the ink.[23, 3] The shorter time scales of the liquid experiencing the pressure variation within the nip, and the smaller amount of time before leaving the the metallization zone,

when the ink is completely removed (in theory), leads to the explanation that higher speeds mean a shorter liquid levelling time.[27] This levelling time at slower speeds is used to redistribute the liquid ink into a form with a smaller oil-substrate contact (minimise the surface energy), as the oil favourably wets the substrate. This time varies proportionally most with the pattern feature dimensions (Λ) and ink height (h)[27]:

$$t_{level} = \frac{3}{16\pi^4}\frac{\mu}{\gamma}\frac{\Lambda^4}{h^3}. \tag{5.10}$$

Occasionally, it is seen in the results that larger features, and patterns with larger coverages (high pattern ratios) have increased rates of change of P2P with nominal line force (Figure 5.6 displays >1 pattern ratios, with plate feature width=300μm, had larger P2P variation than PR=1 where the feature dimension was 150μm). Smaller features, with lower pattern ratios tend to have smaller P2P variation, Figure 5.6e. However, this is not always present in other results, Figure 5.7, as the oil form is almost immediately pinned after patterning, as discuss in Chapter 4 . Also there is nominally no variation with the transferred ink height at these high printing speeds. In summary, ink levelling time is not a major factor in the effects seen in this work as the pattern fixation and printing speed is much faster than the ink spreading.

The liquid bridge behaviour has been shown to split evenly at higher speeds, although increasing rotation rates lead to a favouring of the larger substrate impression drum.[12] Also increasing the speed increases the Reynolds number, meaning that the inertial forces become more dominant in the liquid ink splitting behaviour:

$$Re = \frac{\rho U L}{\mu}. \tag{5.11}$$

With a large Reynolds number longer liquid bridges have been modelled, even to the extent of satellite drop formation.[22] As with ink spreading effects under increasing applied load discussed above, increasing the printing speed will make string-like interruption more prevalent. An equivalent explanation is to say that larger capillary numbers ($Ca = \frac{\mu U}{\sigma}$) lead to larger timescales as the extension speed is much faster than the contact line speed, which lead to longer bridges before splitting. In the Literature Review the concept on ink contact line speed was introduced and the modelling in literature showed that the contact line speed reduces with faster plate separation speeds. That is to say, the ink contact line is more pinned at higher printing speeds, which will mean that the transferred ink volume will redistribute less due to surface energy effect. Instead, it will more closely represent the plate feature edge

roughness (higher fidelity of plate feature edge roughness). The increased transfer to the substrate, the longer liquid bridges before break-up and reduced contact line slip length all contribute towards the increased average P2P seen in these results.

Although minimal line edge roughness is desirable in this research, the reliability of the higher print speeds, with lower line force variation, may be more attractive in an industrial setting. The next section summarises the findings of the variation of printing quality with force and printing speed to develop an optimised parameter set for this work and in general, so that the printing quality is high enough for functional devices.

5.4.8 Optimisation of printing

The previous sections have shown that the printing speed and force can vary the quality of the printed pattern. For use in functional devices, where the patterned aluminium is used as conductive contacts, this patterning quality needs to be high enough to avoid critical shorting defects. The discussion above can be summarised by considering the mechanisms that contribute to line edge roughness and reduced pattern quality, in terms of the scale of this hierarchical problem of ink transfer. These relationships can be used to minimise the printing defects.

There were three main trends associated with the increasing nominal line force: large scale effects and plate backing ($P(F_L)$); the effect of pressure on the printing plate and the pattern feature deformation ($F(F_L)$); and the ink distortion due to the applied pressure and dynamic effects due to the printing speed ($I(F_L)$). Here the nominal line force is assumed to be proportional to the printing pressure, which is true of Hertzian contacts and lubrication modelling, see Equation 5.5 and reference [25]. Hence the total P2P line edge roughness ($P2P$), which limits the viability of flexography for functional devices, can be described as a function of the nominal line force:

$$P2P(F_L) = B(F_L) + F(F_L) + I(F_L). \tag{5.12}$$

The possible form of this equation, given the observed trends described above, is shown in Figure 5.12.

The function $B(F_L)$ varies due to the non-linear stiffness of the foam backing, given its thickness and the inherent defects like drum wobble and plate scale roughness. This function has the largest scale and variation, with force, at low line forces, so is key to removing critical defects. Given the incompressibility of the ink and the

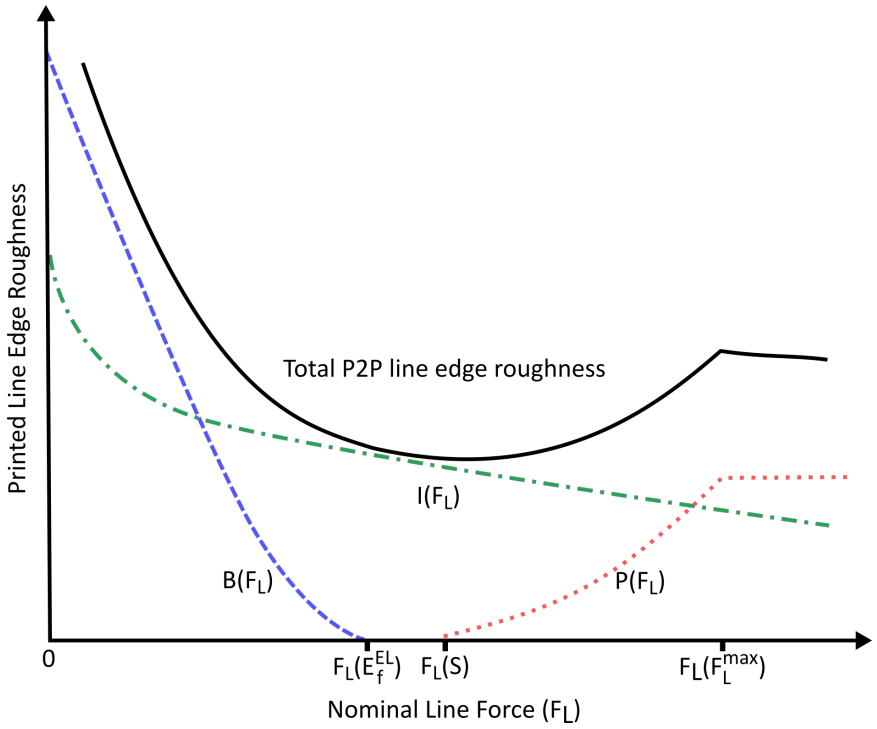


Figure 5.14: Schematic of the total P2P roughness as a function of the nominal line force which is the sum of the the observed trends seen in the plate backing ($B(F_L)$) (blue dash), plate pattern feature deformation ($F(F_L)$) (green dot-dash) and ink distortion ($I(F_L)$) (red dot), with the model summation shown in the continuous black line. The plate feature line edge roughness is also displayed as the grey dash roughness constant. The intercepts are defined as: $F(E_f^{EL})$ is the nominal line force at the backing material's elastic limit; $F_L(S)$ is the nominal line force for the critical onset stiffness of the plate feature deformation and F_L^{max} is the nominal line force at the maximum feature deformation possible that lead to the line edge roughness.

pressure's harmonic behaviour, Equation 5.6, the P2P can be considered as a measure of distortion orthogonal to the applied force in the z direction. Hence, with a plate backing of much lower stiffness than the printing plate, the roughness decreases relative to the foam stiffness. As seen here the stiffness plateaus, after an elastic limit (at $F(E_f^{EL})$) , so there is a sudden decrease in P2P, Figure 5.14. In theory all the plate scale roughness will be accommodated if the stiffness plateaus to zero, although in reality it will remain at a very small value. Therefore the initial gradient is proportional to the foam backing stiffness, and the negative gradient will increase (become more positive, horizontal) with stiffer plate backing materials, as a larger applied pressure is required to reduce the large scale defect less.

This function, $B(F_L)$, can be expressed by including the proportionality to the stiffness of the plate backing (E_f):

$$B(F_L) = \frac{a.E_f}{F_L - F(E_f^{EL})} \tag{5.13}$$

where E_f^{EL} is the backing material's elastic limit and a is a fitting parameter which incorporates scaling effects. Given the dependence on the contact width it can be asserted that this fitting parameter will vary according to Equation 5.1. So will increase with the total radius (R) and decrease with the total modulus (E_T^*), each to the power of 0.5, $a \propto \sqrt{\frac{R}{E_T^*}}$

A thinner plate backing corresponds to a smaller fraction of the composite stiffness, in the slab composite model of Hertzian contact. Hence a thinner plate backing will decrease the onset nominal line force of the plateau region, at which point the lowest roughness can be achieved. The limit of this is when the plate backing becomes so thin that there is little or no conformation of the plate scale roughness. To minimise $B(F_L)$'s value, a minimum contact width, which still fully removes the effects for pressure variation due engineering inaccuracies, with low nominal line force is preferred. This corroborates mathematical work in reference [28], where it was also added that poisson ratio variation has little effect, at maximum 10% change in contact length. Hence the plate backing material properties and relative thickness to the plate should be matched to the system inaccuracies. All this said, with increased engineering control this whole trend will decrease in P2P value.

The nominal line force at which the applied pressure is the elastic limit of the foam backing was found in this work to be $42N.m^{-1}$. Above this plate feature deformation $F(F_L)$ and ink spreading $I(F_L)$ dominate. In general $F(F_L) < I(F_L)$, as ink spreading dominates over feature deformation, except at high pressures.

Plate feature deformation ($F(F_L)$) occurs after a critical nominal line force ($F_L(S)$). $F_L(S)$ is the function of the nominal line force for the critical onset of feature side wall collapse (although in theory it could be any feature deformation mechanism). It is proportional to the printing force as per Equation 5.8. The plate feature deformation and onset vary inversely with the pattern ratio (coverage area) and have a rate of change of gradient proportional to the pattern ratio (coverage), so can be written as:

$$F(F_L < F_L^{max}) = \frac{b}{PR}(F_L - F_L(S))^{PR}, \tag{5.14}$$

given PR is the pattern ratio and the constant b includes effects of the pressure profile of the contact region, which is proportional to the ink viscosity, printing speed, deformable layer thickness and inversely proportional to the stiffness and the inverse square of the total radius. Finally P2P roughness due to plate feature deformation reaches a maximum (F_L^{max}), which for this work was found from the line gain data to be above $70N.m^{-1}$, see Figure 5.9. This maximum is associated with feature bulging being limited by the smaller of either the pattern spacing or conservation of possion ratio which would limit the feature gain to 2 before rupture. After this maximum the roughness due to plate deformation is constant.

Ink spreading will dominate over plate feature deformation, particularly at lower printing pressures. The line edge roughness for liquid ink occurs from first contact of the liquid ink and impression drum, resulting from the feature line edge roughness ($P2P_{feature}$), and decreases with line force up towards a minimum value due to substrate contact line movement and conservation of volume. As the printing speed increases, this initial rate of decrease is reduced, as the liquid ink splits more evenly and the contact lines become more pinned. The agreement of the experimental data presented above with the modelling work by Sauer et al. supported the assertion that the roughness changed with the nominal line force proportional to the speed with an exponent of 0.4. The printing force varies with the printing direction at the contact to the power of 0.5 (P2P direction, or the x direction in Figure 5.1). Given the force of ink distortion is perpendicular to the applied nominal line force, see Equation 5.6, the inverse of the applied force creates the P2P roughness. These effects combined to give the total P2P ink distortion contribution:

$$I(F_L) = \frac{c.U^{0.4}}{\sqrt{(F_L + P2P_{feature})}}, \tag{5.15}$$

where the constant c is dependent on the ink scaling (the feature size ideally). The fitting constant c must include the pattern feature size and ink thickness by

considering the spreading time, Equation 5.10, although this effect will be small as with these high speed process conditions, ink spreading has a negligible effects.

This theory is all schematised in Figure 5.14. The variation with nominal line force can then be fitted to the data, Figure 5.15 with Table 5.6 showing the values used to create the model. Extremes of the printing and pattern variables that were tested are chosen here to assess the agreement of this phenomenological model with the data.

The fitting shown in Figure 5.15 is encouraging because with a simplistic phenomenological model a meaningful fit with experimental data has been achieved with only the dependent variables altered. There are some disparities with the data, poor fitting with low pattern ratios, and, critically, there is still a lack of understanding of the fitting parameter values, so this can not be treated a general theory of flexography ink transfer. However using this model some important optimisation trends can be described, which will reduce line edge roughness and defects in functional devices.

With all the various printing settings, below $F_L \simeq 20N.m^{-1}$ the plate scale effects dominate the P2P line edge roughness. $B(F_L)$ has a steep variation with the nominal line force and dominates the downward trend up to the elastic yield point. The gradient is proportional to the foam's elastic stiffness, Equation 5.13, so a high stiffness of the plate backing is desirable. However, high stiffness foam materials generally have a higher elastic limit, which the backing roughness is inversely proportional to. This will make the plate backing fall to zero (ideal) at a higher nominal line force. Therefore the backing material must be chosen to have the maximum elastic modulus, with a low elastic limit. The assumption of zero stiffness in the plate backing after yield is unrealistic, but exemplifies the intended plate backing effect. In reality, there would be a small decreasing P2P, likely negligible up to the nominal line force for the foam cell densification, where the P2P would decrease at an even slower rate.

As an aside, if the backing and plate were completely rigid, with no deformation achievable at the forces used, then all the contact force would be felt by the liquid thin film. In this case high quality, high resolution patterning would also be achievable, as is seen with gravure printing that uses a metallic patterned roller. This technique uses micro pits to pin the liquid pattern. In these techniques then, without backing and feature deformation effects, only the ink distortion effects on the pattern edge roughness will limit the achievable quality. This has led to extremely low pattern edge roughness be reported, down to $2\mu m$ (RMS roughness) with gravure printing, although this also relies on a spreading and coalescence mechanism of ink after transfer from the femtoliter micro pits.[29]

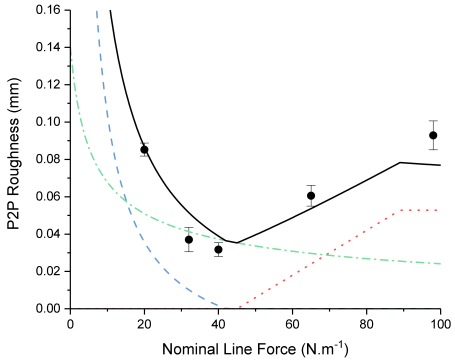
Table 5.6: Table a. lists various values used for the P2P roughness model, Equation 5.12, and shown in Figure 5.15. Note $P2P_f = P2P_{feature}$. Table b. briefly describes the origin of the values used, mm units were used where necessary. The details of the Figure 5.15 references are: a. $PR = 1\left(=\frac{150}{150}\mu m\right)$, $U = 10m.min^{-1}$; b. $PR = 1\left(=\frac{200}{200}\mu m\right)$, $U = 10m.min^{-1}$; c. $PR = 1\left(=\frac{150}{150}\mu m\right)$, $U = 35m.min^{-1}$; d. $PR = 2\left(=\frac{150}{300}\mu m\right)$, $U = 35m.min^{-1}$; e. $PR = 1.5\left(=\frac{200}{300}\mu m\right)$, $U = 10m.min^{-1}$; and f. $PR = 0.6\left(=\frac{500}{300}\mu m\right)$, $U = 10m.min^{-1}$.

a.

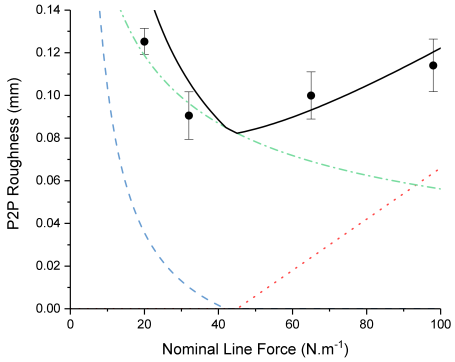
	$B(F_L)=\frac{a.E_2}{F_L-E_f^{EL}}$		$F(F_L<F_L^{max})=\frac{b}{PR}(F_L-S(F_L))^{PR}$			$I(F_L)=\frac{c.U^{0.4}}{\sqrt{(F_L+P2P_f)}}$		
Fig. 5.15	a	b	PR	$S(F_L)$	F_L^{max}	c	U	$P2P_f$
a.	7.45×10^{-5}	1.2×10^{-6}	1	45	89	1	166.7	0.14
b.	7.45×10^{-5}	1.2×10^{-6}	1	45	100	2.33	166.7	0.14
c.	7.45×10^{-5}	1.2×10^{-6}	1	40	100	1	588.3	0.14
d.	7.45×10^{-5}	1.2×10^{-9}	2	60	73	1	166.7	0.14
e.	7.45×10^{-5}	$1.2\times10^{-7.5}$	1.5	55	80	1	166.7	0.14
f.	7.45×10^{-5}	$1.2\times10^{-4.8}$	0.6	25	100	1	166.7	0.14

b.

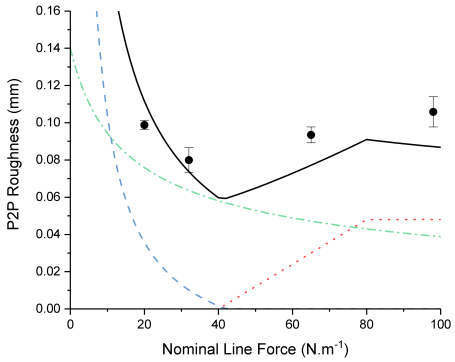
Term	Remarks
a	This value is $R_T^{0.5}\times E_T^{-0.5}$,as per Equation 5.1, with a P2P unit scaling factor of 10^2.
E_f	See table 5.1 for plate backing stiffness, value used:$18300Pa$.
E_2^{EL}	Extracted from parabolic fits in Figure 5.7e to be $42N.m^{-1}$, see also section 5.4.5.
b	Found fitting parameter (1.2×10^{-3}) from fitting to data ($PR = 1$, $U = 10m.min^{-1}$). The changing exponents are derived from the unit scaling with pattern ratio effects, given for $PR =$ 1the scaling was 1×10^{-3}.
PR	Pattern feature $\frac{spacing}{width}$, used without scaling factor.
$S(F_L)$	Assumptions based on fitting and change of onset stiffness with area coverage. These are the nominal values, which were adjusted to account for the gradient constants in the actual formulae.
F_L^{max}	Values for when $F(F_L)$ is equal to the maximum feature deformation possible.
c	Found from fitting, the value for b. was the additional percentage difference $\left(\frac{200}{150}\right)$from the variation in pattern size.
U	Speed in $mm.s^{-1}$.
$P2P_{feature}$	See Experimental Materials and Methods Chapter where the plate feature edge P2P due to the silicon master fabrication sawing was found to be $0.14mm$. This was adjusted in the formulae to account for the constants.



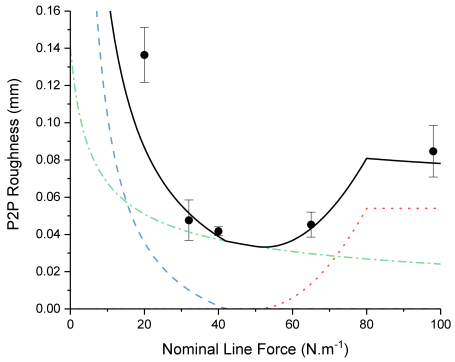
a. PR=1$\left(=\frac{150}{150}\mu m\right), U$=10$m.min^{-1}$



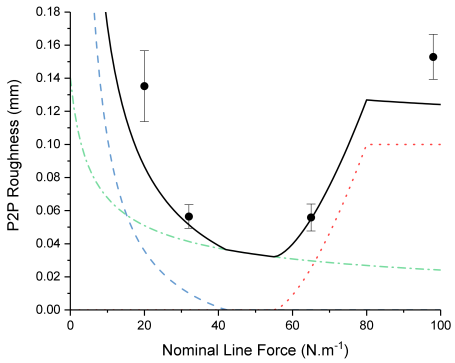
b. PR=1$\left(=\frac{200}{200}\mu m\right), U$=10$m.min^{-1}$



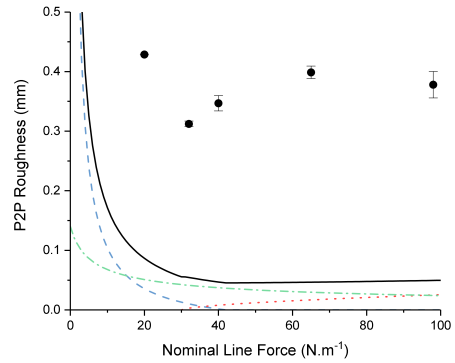
c. PR=1$\left(=\frac{150}{150}\mu m\right), U$=35$m.min^{-1}$



d. PR=2$\left(=\frac{150}{300}\mu m\right), U$=35$m.min^{-1}$



e. PR=1.5$\left(=\frac{200}{300}\mu m\right), U$=10$m.min^{-1}$



f. PR=0.6$\left(=\frac{500}{300}\mu m\right), U$=10$m.min^{-1}$

Figure 5.15: Fitting of the theoretical trends to the empirical data of the P2P line edge roughness variation with nominal line force (F_L). The mean and standard error of the data is shown by the circle with error bars, and the total theoretical P2P is shown by the solid black line, which is the sum of the other contributing mechanisms (broken lines) as per Equation 5.12. The dashed blue line is the contribution from the plate backing P2P function with nominal line force ($B(F_L)$), Equation 5.13. The contribution from the plate feature deformation ($F(F_L)$), Equation 5.14. The ink distortion contribution to the P2P ($I(F_L)$) is graphed with the dot dash green line, Equation 5.15. Table 5.6 give the values used to create the model, as per Equations 5.13 - 5.15. Only the feature scaling constant c changed for increased feature size (a and b), the printing speed, (a and c), and the critical feature deformation onset force and pattern ratio (a and c and d-f) are altered, to show the predictive consistency of the model with the experimental data.

The ink distortion in this model varied inversely with the square root of the nominal line force, Equation 5.15. It has a large effect at most line forces, and is limiting above $20N.m^{-1}$, and before plate distortion effects at very high printing pressures. An exception is the larger scale pattern, Figure 5.15b, as the fitting parameter has been increased by the relative change in the pattern size, so the ink contribution dominates at almost all nominal line forces. This fitting parameter change seems to have too large an effect as the model over-predicts below E_L^{EL}. However this implies that larger patterns need more control when being printed than smaller patterns, where viscous forces dominate over inertial. The exact influence of pattern scale on the fitting parameter remains elusive, except that it must have a positive effect. As it was difficult to ascertain an appropriate effect on the scaling parameter, no change was made for the model with speed and pattern ratio variations, which meant these model effects could be tested independently.

As the ink distortion is, at particular nominal line forces the minimum achievable P2P, it is the key to understanding how to reduce possible defects. $I(F_L)$ can be generally reduced by reducing the pattern feature roughness, $P2P_{feature}$. Indeed, the advancement in recent decades in commercial flexography printing resolution, has been driven by improved plate making techniques. In this work, the diamond saw cut silicon introduced significant edge roughness and alternate master forming methods could have been used such as laser engraving. For even smaller pattern high resolution techniques, such as ion beam milling, could be feasible as PDMS can replicate nano scale features. It should be noted that as the ink distortion tends to zero at high pressures, other mechanisms will become apparent as the impression forces exceed the liquid cohesive forces, which can lead to pin holes and filamentation, as the capillary number of the fluid is reduced.

In the case of increased speed, the modelled ratio ($U^{0.4}$) works sufficiently with the data, for the ink contribution to P2P. This is shown in Figure 5.15c, although it slightly under predicts above E_L^{EL}. The speed must be having a larger effect than included in this model, and must act to create a more positively scaled parabolic variation. Therefore minimising the printing speed is a key variable to achieve higher pattern resolution, which is not favourable for industrial high throughput printing. However, increasing the speed creates a small variation in the P2P with nominal line force, so for reliable results, where some nominal line force variance may occur, higher speeds are more reliable, as shown by the data. Furthermore, reducing the speed has a quality trade off with spreading effects, if the timescales become similar. Choosing a fluid with a non-linear viscosity change with time could be a material selections

strategy, to create a lower more level ink distortion variation. A shear thickening fluid would change the nominal line force exponent for -0.5 to a more positive number. It is common practise to use shear thickening fluids in graphics flexography printing.[30] At low speeds with a nominally Newtonian viscous ink, using the carbon nanotube stamps in Chapter 1, a group at MIT has been able to achieve a line edge roughness (RMS) of $0.2\mu m$, with ambient printing. This was possible due to negligible large scale roughness effects and controlled feature deformation, so only ink distortion, which was small at the μm scale feature size used, led to the low pattern edge roughness.

The pattern feature deformation effects varied with the pattern ratio and the proportionally with the nominal line force, Equation 5.14. This model formula fits the printing variable trends for $PR > 1$, although at high pressure the model underestimates the edge roughness, see Figure 5.15d-f. This variation highlights the importance of matching higher printing pressures to the particular pattern. With high pattern ratios this feature deformation dominates the P2P at high pressures. However it is possible this effect is exaggerated in this model, and the gradient ($\frac{b}{PR}$) decreases more with increased PR. For $PR < 1$ the model severely under predicts the edge roughness, although the trend of the variation is correct. In this low coverage case, the effect of deformation due to feature bulging will not be dominant, and other feature deformation mechanisms, such as roof collapse (feature spacing bowing) will dominate, according to static PDMS feature loading research.[31]. Also the aspect ratio was not kept constant for the changing PR. This could mean alternate mechanisms are contributing to the feature deformation. These could have different deformation maximums (F_L^{max}), which could account for the under prediction at high nominal line force. This said, these effects only dominate at higher force. The optimal force, as supported by the data, is around $42N.m^{-1}$.

5.5 Conclusion

This chapter has investigated the effects of printing force and speed on quantified printing quality. The selective metallization process is a good method for testing the printed liquid shape of the flexography ink (oil). Carefully designed patterns, cross direction stripes, with in-vacuum processing, has shown good fit with the existing models. This flexography printing process avoids internal inking defects, like viscous fingering and halo/seam effects, and so resolution is not limited by these. Instead the result of the liquid splitting effects are 'frozen-in' by the metallization process. The printing results lead to definitions of the printing defects observed, borrowing from

VSLI terminology: pin spots; protrusions; bridges and their inverses. The pattern edge P2P roughness should not exceed half the printed line spacing if critical defects are to be avoided.

The print quality image analysis data showed a U-shaped trend with nominal line force, where the minimum was at a nominal line force of $42N.m^{-1}$. Using a soft foam plate backing reduced the line edge roughness, compared with a steel backing roller. The gradient, and rate of change of gradient, above the minimum value changed with PR and printing speed but, with constant PR and printing speed, the trend was constant over an order of magnitude pattern sizes. This implied several separate variables were creating the pattern edge roughness.

From the observed trends in the data a phenomenological model was constructed comprising of three functions of the printing force, that total to yield to the total printed line edge roughness. They included contributions from the plate and machine scale defects, which are reduced by the plate backing compression, which has a non-linear plateau in its stiffness leading to an ideal zero contribution to edge roughness at a pressure corresponding to a nominal line force of$42N.m^{-1}$. The ability to accommodate for engineering machine inaccuracies (like drum wobble) and substrate roughness, as the backing has a lower stiffness than the printing plate and a low elastic stress limit, make flexography a favourable technique for reaching low resolution in a high volume production setting.

The smaller scale plate features also showed static pressure effects are important, but dynamic effects also play a role. Research results in literature from static loading and coating research led to a function of nominal line force which depended on the PR, (which determine the area pattern in contact with the drum), impressing the importance of matching the printing settings to the pattern design.

The final function of ink distortion was found by changing the printing speed, as dynamic effects in this regime are important. Good matching with theoretical modelling of the change in pattern quality with speed, to the exponent of 0.4, highlighted the success of the experimental design and advantage of in-vacuum experiments which remove ambient atmospheric affects. Increasing the speed then, increased the edge roughness, but also created smaller line edge roughness variation with changing nominal line force, so the print quality was more reliable.

This hierarchical model showed reasonable fitting with the experimental data, given simplistic fitting parameters were used, except with low pattern ratios where the feature deformation mechanism is likely changed and not accounted for. The interaction of these functions has not been explored but the simple additive nature

lead to meaningful fits and supports this hierarchical analysis. However it should be noted that this model is specific to this particular printing system, which has some differences from standard flexography set-up such as the foam stiffness being much lower than commercially available foams, as was discussed.

This model suggests, for this printing system, the minimum line edge roughness for larger pattern ratios (>1) will be at printing pressure greater than the pressure related to the decreased modulus of the foam plate backing and before (or as close to) the onset stress of the feature deformation. At this minimum only the ink distortion contributes to pattern edge roughness. If the optimum line edge roughness is to be used to create devices, than the force at this minimum should be used. Consequently, to further reduce the achievable minimum line edge roughness, the material properties of the flexography equipment must be optimised so that the machine defects are reduced to as near as possible to the ink distortion function. This in turn can be minimised by optimising the fluid properties, printed scale of the ink and importantly the plate feature edge roughness, as this defines the maximum P2P due to the ink effects.

From these parametric tests, the optimal print settings in terms of line gain and line edges roughness are found to be a low speed of $10m.min^{-1}$ with a nominal line force of $42N.m^{-1}$. These parameters must also be balanced with other aspects of device's fabrication. These could include the the registration requirement, the speed of pre- and post-processes, and the reliability and cost of operating the machine at theses conditions. Further discussion on this is presented in the following Chapter where these optimal printing settings are used to fabricate functional organic transistors.

5.6 References

[1] D C Bould, S M Hamblyn, D T Gethin, and T C Claypole. Effect of impression pressure and anilox specification on solid and halftone density. *Proceedings of the Institution of Mechanical Engineers, Part B: Journal of Engineering Manufacture*, 225(5):699–709, May 2011.

[2] D C Bould, T C Claypole, and M F J Bohan. An investigation into plate deformation in flexographic printing. *Proceedings of the Institution of Mechanical Engineers, Part B: Journal of Engineering Manufacture*, 218(11):1499–1511, November 2004.

[3] Anton A. Darhuber, Sandra M. Troian, and Sigurd Wagner. Physical mechanisms governing pattern fidelity in microscale offset printing. *Journal of Applied Physics*, 90(7):3602–3609, October 2001.

[4] D. Deganello, J. A. Cherry, D. T. Gethin, and T. C. Claypole. Patterning of micro-scale conductive networks using reel-to-reel flexographic printing. *Thin Solid Films*, 518(21):6113–6116, August 2010.

[5] D. Deganello, J. A. Cherry, D. T. Gethin, and T. C. Claypole. Impact of metered ink volume on reel-to-reel flexographic printed conductive networks for enhanced thin film conductivity. *Thin Solid Films*, 520(6):2233–2237, January 2012.

[6] William C. Walker and J.M. Fetsko. A Concept of Ink Transfer in Printing. *American Ink Maker*, 33(12), 1995.

[7] M. M. H. Megat Ahmed, D. T. Gethin, T. C. Claypole, and B. J. Roylance. A model for ink impression into a porous substrate. *J. Phys. D: Appl. Phys.*, 30(16):2276, 1997.

[8] Martin Dubé, François Drolet, Claude Daneault, and Patrice Mangin. Hydrodynamics of Ink Transfer. *Journal of Pulp and Paper Science*, 34, January 2008.

[9] A. V. Chadov and E. D. Yakhnin. Investigation Of The Transfer Of A Liquid From One Solid-Surface To Another. 1. Slow Transfer-Method Of Approximate Calculation. *Kolloid. Zh.*, 41:700–703, 1979.

[10] E. D. Yakhnin and A. V. Chadov. Investigation of the transfer of a liquid from one solid-surface to another. 2. Dynamic transfer. *Kolloid. Zh.*, 45(6):1034–1039, 1983.

[11] Bian Qian and Kenneth S. Breuer. The motion, stability and breakup of a stretching liquid bridge with a receding contact line. *Journal of Fluid Mechanics*, 666:554–572, January 2011.

[12] Shawn Dodds, Marcio S. Carvalho, and Satish Kumar. The dynamics of three-dimensional liquid bridges with pinned and moving contact lines. *Journal of Fluid Mechanics*, 707:521–540, September 2012.

[13] Michael James Joyce, Dr Paul D. Fleming Iii, Sai G. R. Avuthu, Sepehr Emamian, Ali Eshkeiti, Dr Massood Atashbar, and Tony Donato. Contribution of Flexo Process Variables to Fine Line Ag Electrode Performance. *International Journal of Engineering Research and Technology*, Vol. 3 - Issue 8 (August - 2014), September 2014.

[14] Bruce E. Kahn, Liam H. O'Hara, Chip Tonkin, Howard E. Nelson, William J. Ray, Chris Wargo, and Michael Mastropietro. The Impact of Plate Imaging Techniques on Flexographic Printed Conductive Traces. *Journal of Imaging Science and Technology*, 56(4):1–8, December 2012.

[15] Ho Anh Duc Nguyen, Kee-Hyun Shin, and Dongjin Lee. Effect of process parameters on fidelity of printed line width in high resolution roll-to-roll gravure printing. *Jpn. J. Appl. Phys.*, 53(5S3):05HC04, May 2014.

[16] K. L. Johnson. *Contact mechanics*. Cambridge University Press, Cambridge, 1985.

[17] Derek Hull. *An introduction to composite materials*. Cambridge solid state science series. Cambridge University Press, Cambridge, 2nd ed. edition, 1996.

[18] R Bickford. Analyze_stripes ImageJ Plugin, 2013.

[19] Helmut Kipphan, editor. *Handbook of print media: technologies and production methods*. Springer, Berlin ; New York, 2001.

[20] 3m Cushion-Mounting (TM) Plus Plate Mounting Tapes Technical Data. Product Specifications, 3M, June.

[21] Sami Franssila. *Introduction to Microfabrication*. John Wiley & Sons, October 2010.

[22] Shawn Dodds, Marcio Carvalho, and Satish Kumar. Stretching liquid bridges with moving contact lines: The role of inertia. *Physics of Fluids*, 23(9):092101, September 2011.

[23] Hans Sauer, Dominik Daume, and Edgar Dörsam. Lubrication theory of ink hydrodynamics in the flexographic printing nip. *Journal of Print Media Research & Technology*, J. Print Media Res. Technol.:163–172, September 2015.

[24] Joseph E. Petrzelka and David E. Hardt. Static load-displacement behavior of PDMS microfeatures for soft lithography. *J. Micromech. Microeng.*, 22(7):075015, 2012.

[25] D. J. Coyle. Forward roll coating with deformable rolls: A simple one-dimensional elastohydrodynamic model. *Chemical Engineering Science*, 43(10):2673–2684, January 1988.

[26] G Ascanio and G Ruiz. Measurement of pressure distribution in a deformable nip of counter-rotating rolls. *Measurement Science and Technology*, 17(9):2430–2436, September 2006.

[27] S. E. Orchard. The flow of paint coatings: a hydrodynamic analysis. *Progress in Organic Coatings*, 23(4):341–350, May 1994.

[28] Margaret Hannah. Contact stress and deformation in a thin elastic layer. *The Quarterly Journal of Mechanics and Applied Mathematics*, 4(1):94–105, 1951.

[29] Hongki Kang, Rungrot Kitsomboonloha, Jaewon Jang, and Vivek Subramanian. High-Performance Printed Transistors Realized Using Femtoliter Gravure-Printed Sub-10 μm Metallic Nanoparticle Patterns and Highly Uniform Polymer Dielectric and Semiconductor Layers. *Advanced Materials*, 24(22):3065–3069, June 2012.

[30] Helmut Kipphan, editor. *Handbook of print media: technologies and production methods*. Springer, Berlin ; New York, 2001.

[31] Joseph E. Petrzelka and David E. Hardt. Static load-displacement behavior of PDMS microfeatures for soft lithography. *Journal of Micromechanics and Microengineering*, 22(7):075015, 2012.

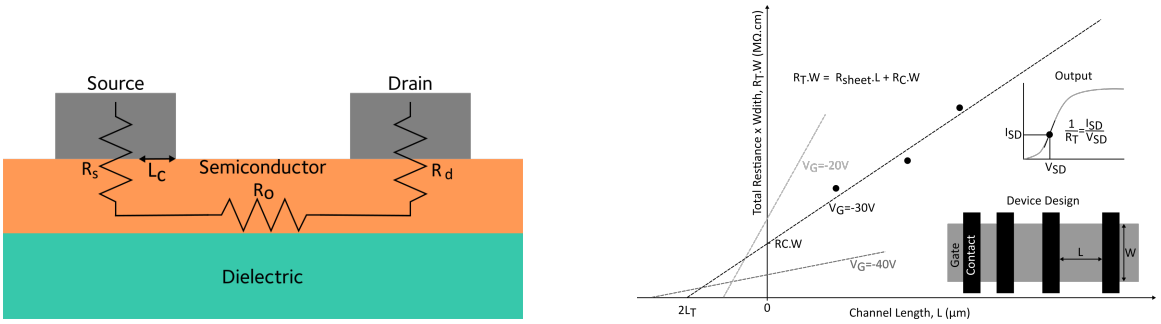
Chapter 6

Compatibility of Flexography Metallization for Organic Thin Film Transistors

Characterisation of thermally evaporated molybdenum trioxide on silicon chips using the kelvin probe method was performed by Yujiro Tazawa, Oxford University, Department of Materials.

6.1 Introduction

This chapter shows that selective metallization patterning of aluminium, is compatible with the fabrication of functioning of organic devices, namely organic thin film transistors (OTFTs). Firstly, this chapter introduces the material considerations of replacing gold with aluminium contacts. The existing processing [1] for OTFTs uses expensive gold source and drain contacts, which are vacuum evaporated through a shadow mask to create the desired pattern. Batch processed OTFTs, with gold contacts, are compared with previous results, as a control, with the differences to previous results, published by the research group, discussed. As a cost reduction and feasibility effort, it is shown that aluminium metal contacts are compatible with the organic device. It has already been shown in Chapter 4 that the patterned metal thin films have low sheet resistance, as pure aluminium is created with this direct deposition patterning method. Leading on from this, in this chapter, the resistance of aluminium contacts with the organic semiconductor (the contact resistance), is also discussed to show this is a compatible process for achieving charge extraction in organic devices. It is already known that aluminium's contact resistance, with the organic semiconductor, necessitates a carrier injection layer: molybedenum trioxide



a. b.

Figure 6.1: a. Resistance experienced by a charge carrier as it moves from source to the drain through the channel of an OTFT, see Equation 6.1. Only the layers above the dielectric are shown, with the contact length (L_T) labelled. b. shows TLM analysis graph with the insets showing the output curve from which the total contact resistance is derived, and the device design of varying channel length. The parameters that can be derived from the intercepts are labelled.

(MoO_3). Results from shadow mask devices with aluminium contacts are presented, exhibiting the expected contact resistance, which changes with carrier injection layer thickness, and the thin film position and coverage. Given these results, the optimum device fabrication route is chosen, in terms of device compatibility and viability, for use with in-line patterning of aluminium, as presented in previous chapters. The results show the compatibility and viability of the materials and process, although there is an optimisation trade-off between device performance and yield to be made.

6.1.1 Compatibility of aluminium contact for OTFTs

The selective metallization process provides a method of creating metal thin films for contacts, the source and drain, of OTFTs. Within an OTFT a charge carrier will experience a resistance as it passes from the metal source into the semiconductor (R_S), then resistance to the flow of this charge through the organic semiconductor channel (R_{OSC}) and finally resistance through the semiconductor drain interface (R_D), see Figure 6.1. The total resistance (R_T) can be written as the sum of these series resistances:

$$R_T = R_S + R_{OSC} + R_D. \tag{6.1}$$

The contact resistance (R_C) is the sum of the source and drain to/from the organic resistances: $R_C = R_S + R_D$, in the linear regime (when $V_{GD} \ll V_{SD}$). Ideally,

with ohmic contacts, the contact resistance should not impede the device's output performance, $R_{OSC} \gg R_C$.

From this resistance model several conclusions can be drawn, as found in common text books such as reference [2, 3]. Firstly, the channel resistance will proportionally scale with the channel length, meaning smaller OTFTs will be affected most by contact resistance. Secondly, the channel resistance will decrease with increasing gate voltage, so contact resistance will be most significant at low gate voltages.

The material mechanisms behind the term R_C are now discussed and include the:

- specific interfacial resistance, due to charge carrier transfer from one material to another;
- material properties slightly above and below the metal/organic interface;
- resistance of the contacts themselves, which is often negligible with metal-organic interfaces and;
- current crowding effects within the semiconductor at the contact edges.

The specific interfacial resistance is a measure of the efficiency of charge transport from the contact to the organic semiconductor. This relies on the alignment of electronic energy band structure of the two materials when brought into contact. Figure 6.2, which shows the band energy alignment for dinaphtho[2,3-b:20 ,30 -f]thieno[3,2-b]thiophene (DNTT) with aluminium. It illustrates the Fermi energy alignment at the material interface leading to a shift in the donor and acceptor energies, and band bending near the interface, which is discussed further later. The potential difference a charge carrier must overcome to cross the interface is given by the difference in the Fermi energy and the organic ionisation potential IP_O, which known as a valence band offset (VB_{offset}):

$$VB_{offset} = WF_M - IP_O \pm \Delta$$

where the bulk work function of the metal (WF_M) defines the the new fermi energy and there is an additional interfacial potential (Δ) which, in effect, shifts the vacuum level due to dipoles at the interface. Even with a slight positive VB_{offset} hole injection from the metal to the organic (charge transfer) is possible by: (i) thermionic emission, (ii) quantum tunnelling or (iii) defect state hopping. These mechanisms though cannot overcome the large valence band offset with aluminium contacts ($\sim 2.4eV$).

For material compatibility, when using an aluminium contact, an intermediate material which can accommodate the large difference in valence band energies must be used. This is referred to as a charge carrier injection layer and is often an insulating metal oxide, in this case MoO_3 or the non-stoichiometric air exposed MoOx (x<3). These materials have partially filled d-orbitals, as part of their elemental character leading to large work functions. This broad electron-energy structure has led to many being used as p, and some n, injectors/acceptor for a variety of organic devices beyond OTFTs, such organic light emitting diodes (OLEDs)[4] and organic photovoltaics (OPV)[5, 6, 7, 8]. The oxygen vacancies in MoOx lead to defect states which provide a conduction pathway, see Figure 6.2.

The next mechanism is related to the material above and below the interface. When materials are brought into contact it is often assumed that the vacuum levels equilibrate and the valence and conduction bands are shifted to accommodate a new shared common Fermi energy at the interface, which is the bases of most silicon semiconductor technology. However with organic molecules, as has been shown [9], a Fermi-energy pinning effect exists whereby the the energy alignment is controlled by the oxide's electron chemical potential with the organic's ionization potential. In other words there is significant band bending at the interface, leading to the valence/conduction bands acting as charge movement pathways, but the thermodynamic stability of a charged organic molecule depends on the oxide's Fermi energy being greater (more negative) than the ionization energy of the organic molecule. The thermodynamic change in energy due to this charge transfer can be thought of as a chemical potential. Therefore the selection and tuning of charge injection materials is a question of charge species defects, like oxygen vacancies in oxides, which alter the chemical potential. This is discussed more later in this chapter.

Resistance from the contacts themselves is often neglected as with metal-organic interfaces the difference in resistance is at least $10^6\Omega$. However when considering carrier injection layers the resistance can become important, particularly as the carrier injection layer thickness increases, and the resistivity increases, approaching that of the organic channel. For instance MoOx has a minimum resistivity of $10m\Omega.cm^2$ at a thickness of $10nm$ with p-type silicon, used for OPV.[10] With thinner MoOx layers, the resistivity increases as there is an incomplete thin film, due to island growth of the film thin. Thicker thin films ($> 20nm$), in this case increase at a rate of $2 \times 10^{-5} S.cm^{-1}$.

The final mechanism of contact resistance is current crowding effects. The path a charge carrier travels to a contact is often assumed to be directly vertical from

the organic semiconductor channel to the contact-organic interface. However due to the lateral voltage change within the accumulation layer beneath the contact, it has been shown [11, 12, 13], that the charge carrier current in the vertical direction is balanced by a lateral current near the edges of the contact interface. This leads to a 'crowding' of the current near the edges of the contact as this is a limiting geometrical interface. This current density over the potential drop leads to a resistance, which is proportional to the distance laterally of the contacts that the majority of charge carriers are collected from. This distance over which the majority are attracted to the contact is referred to as the transfer length, or in other words the contact has an effective length from which 63% charge carriers are collected, due to the organic semiconductor biasing.[3] 'Access resistance' is a dominant mechanism leading to total contact resistance, for top contact OTFTs.[2]

The transfer length (L_T), labelled in the schematic shown in Figure 6.1, can be ascertained by performing transmission line measurements (TLM).[3] This analysis technique measures the resistance over varying source/drain distances to ascertain the change in resistance over the channel width, as the channel length is varied. It can be derived, that the sub-zero x-intercept of this graph is the magnitude of double the contact length, and the y-axis intercept is the combined resistance from both contacts.[3] The contact length increases with larger gate source voltage (V_{GS}), however the total contact resistance will decrease as the channel resistance is lower, this exemplifies the interaction of this mechanism with the others involved in transistor performance.[13] Contact resistance will vary with temperature and granular structure of the organic.[11] Importantly reducing the contact length will mean that smaller scale devices can be achieved, as the size of the contacts are reduced. Besides processing limitations, contact resistance is a crucial issue to solve for the future scalability of OTFTs.

6.2 Method

To test the compatibility of the aluminium with MoOx contacts compared to gold contacts, OTFTs were created with varying contact materials and configurations, see Figure 6.3. All the OTFTs were tested from the same batch to remove any uncontrolled variation in the processing, leading to inaccuracies in the results. A full description of the device fabrication can be found in the Experimental Materials and Methods Chapter. The experimental design was to test batch processed material and configuration variations first, and assess the effects on contact resistance. Then

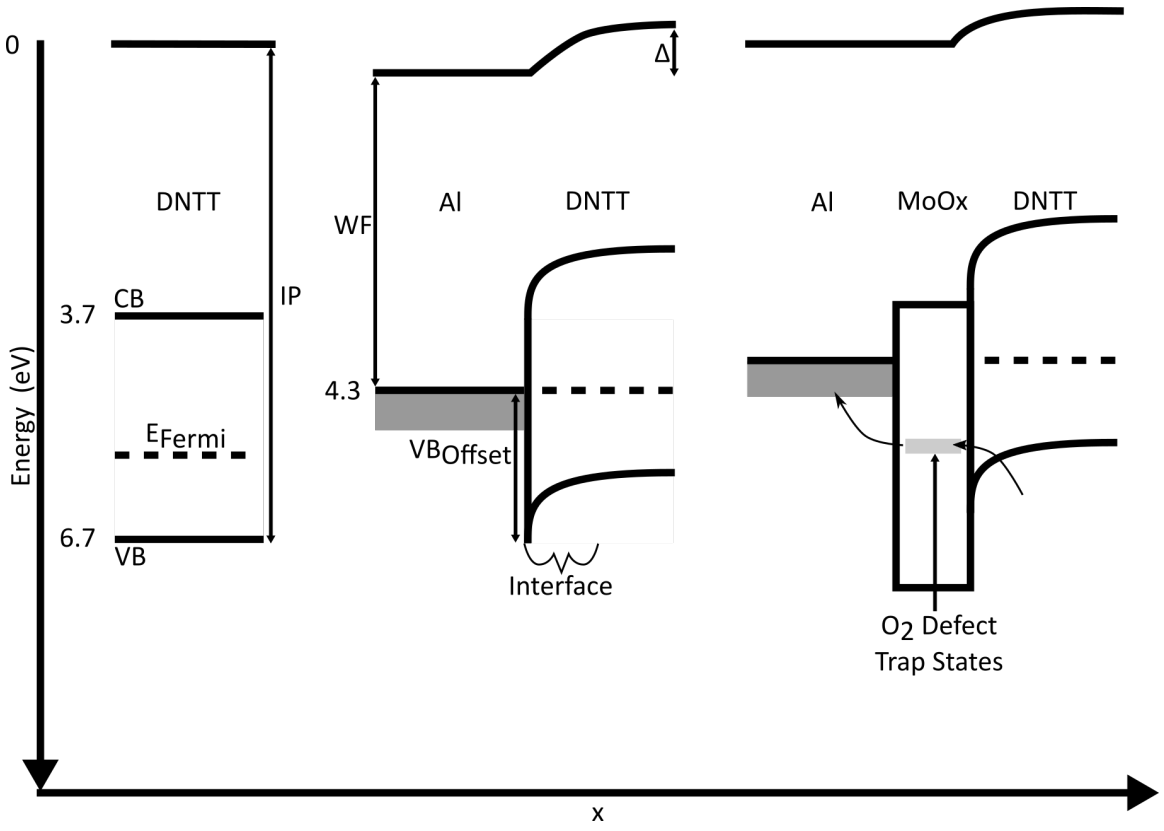


Figure 6.2: Graph of equilibrium band energies for DNTT and DNTT interfaces with aluminium and MoOx with aluminium. The DNTT valence band (VB) (HOMO) and conduction band (CB) (LUMO) energies were based on theoretical modelling in reference [14], and was supported by the work of Yujiro Tazawa, who found the work function of DNTT to be $6.57 \pm 0.28eV$ with kelvin probe tests. Work by the original synthesiser found the band gap to be 3.00eV using UV-Vis spectral analysis, but the HOMO was estimated to be 5.44eV cyclic voltammetry.[15] Gold is estimated to have a work function of $4.7eV$.[16] Aluminium's work function was set to $4.28eV$ as is standard for polycrystalline aluminium since the 1970s. [17] The band energies of MoOx are obtained from reference [18], with the oxygen vacancy defects states measured in reference:[19] with UPS.

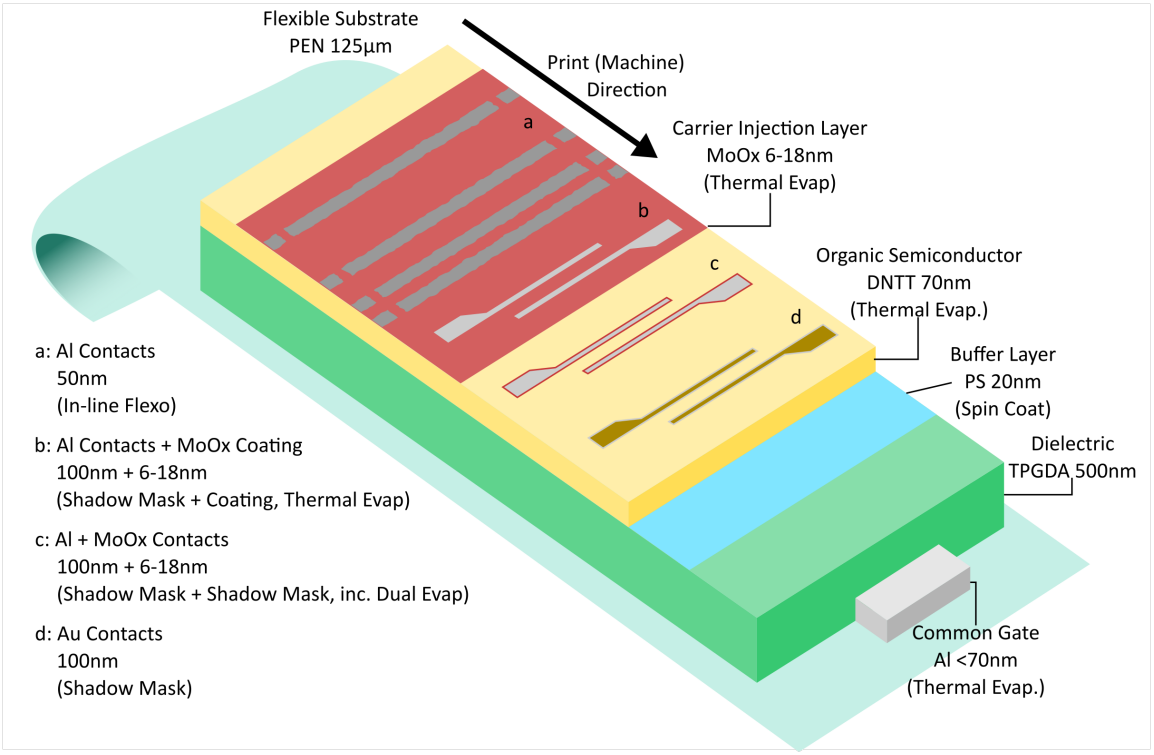
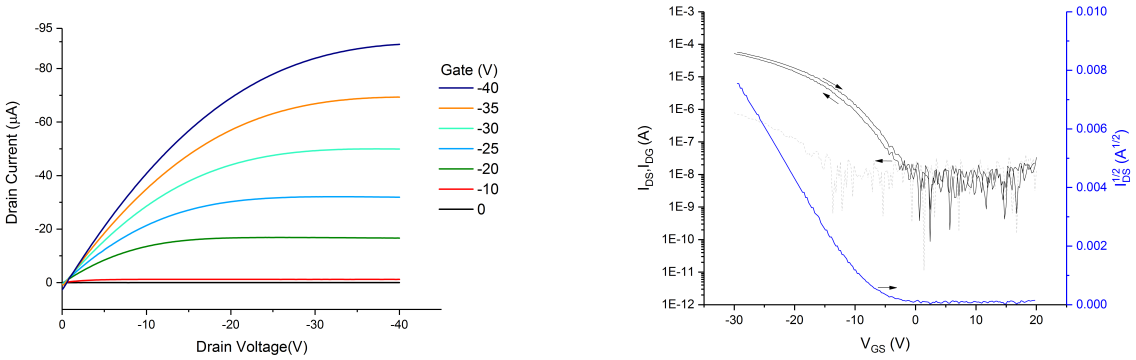


Figure 6.3: Schematic experimental design showing the OTFT structure and the various contact materials and fabrication methods.

using the optimum findings, in-line patterning with selective metallization, was used to fabricate the final devices, and assess the contact resistance further.

The batch processing was achieved by thermally evaporating gold and aluminium through shadow masks for the metal contacts. The MoOx layer was thermally evaporated either as a coating or through shadow masks. When depositing through shadow masks the mask was not moved between MoOx and Al depositions to ensure registration. To test the effects of contact resistance, the MoOx thickness was tuned from 6 to 18nm on separate devices. Additionally, for the patterned MoOx layer, aluminium was deposited without breaking the vacuum (dual evaporation) and compared with devices where the MoOx had been exposed to ambient atmosphere before the aluminium deposition. The MoOx thickness was measured using a quartz crystal monitor, calibrated with thickness verification methods using a Dektak stylus probe.

Finally in-line patterned devices were fabricated within the same batch, see print direction shown in Figure 6.3. The long common gate was aligned in the machine direction, with the device's PEN substrate fixed with double sided to tape to the existing polyethylene terephthalate (PET) impression drum wrap. This positioning meaning lateral registration, precise positioning in machine direction, was not re-



a. Output characteristics

b. Transfer characteristics

Figure 6.4: Output and transfer characteristics of OTFTs with gold contacts. The transfer curve is obtained at $V_{DS} = -30V$.

quired, as the common gate length could be made greater than the printing plate length. The printed metal lines were wider than the OTFT width, so horizontal registration, across the impression drum face, was minimal. The pattern edge was scoured to create the separate source and drain thin film lines, which had varying spacing (150, 200, 500μm) but constant nominal linewidth (150μm). Output curves and transfer characteristics were collected as per previous research and as described in the Materials and Methods chapter. Testing of the OTFTs was performed over a period of 2 weeks to assess the device stability.

6.3 Results and Discussion

6.3.1 Control transistors with gold contacts

The first devices characterised were the gold contact devices, made with shadow masks, as in previous work by the group.[1, 20, 21] These transistors showed similar behaviour, see Figure 6.4, with yields up to 100% and low variability in characterised metrics. The output graph, as shown in Figure 6.4a, exhibits the linear region of accumulation as the output current varies proportionally with the gate voltage, associated with the increased biasing at the semiconductor/dielectric interface leading to a greater number of charge carriers (in this case holes with p-type DNTT). Then after the pinch-off there is a stable saturation regime, as introduced in the Literature Review chapter. From this saturation regime the mobility of these devices was found to be $0.33 \pm 0.01 cm^2.V^{-1}.s^{-1}$, using the data shown in Figure 6.4b, as per the method laid out in the Materials and Methods chapter. Similarly the threshold

voltage was measured to be $-7.18 \pm 1.09V$ and the threshold swing, $9.61V.dec^{-1}$. The devices showed little hysteresis and little delineation at low voltages of the output curve, which is associated with the negligible contact resistance, as introduced above. Though these devices could be reliably reproduced and characterised it is worth comparing them with previous work before they are used as the controls in this experimental work.

This work developed on an existing set of thin film vacuum coating processes which made high yield, hysteresis-free bottom gate top contact OTFTs with large on/off ratios ($\sim 10^6$) and mobilities around $1cm^2V^{-1}s^{-1}$.[1, 20, 21] These historical results were encouraging because of the semiconductor's oxygen stability, with improvement over time, however the processing steps relied on batch processing with shadow masks to create the material thin film patterns, which is now extended to in-line patterning as part of this doctoral work's new science. Any differences, due to processing and testing procedures, are discussed in this section to show that the material properties are invariant and the results are reliable.

The most obvious difference is the device structure, with these results having common gates, and previous work having independently gated transistor source/drain sets. Common gates allowed for low registration requirements but have generally deleterious effects on device performance. This is predominately due to increased gate leakage from the larger gate area. In some devices for $V_G \gg V_{SD}$,this leakage is seen as a positive drain current as the large source to gate voltage (V_G) promotes charge carrier transport directly from the gate to the drain.

The common gate devices had a high off current and V_T was more negative, compared with previous results.[1, 20, 21] The laboratory and equipment used to fabricate this set of devices was different to previous published work, although the device storage was the same. In general, the current conditions were less controlled and more exposed to moisture between deposition steps and during handling and transport between facilities. This change is seen in the results, which are most similar to the devices tested in a humid atmosphere of those reported by Ziqian Ding [22], see Figure 6.5.

The more negative threshold voltage $-7.18 \pm 1.09V$ and higher threshold swing, $9.61V.dec^{-1}$, are both associated with moisture creating hole trapping states within the DNTT organic semiconductor. A larger change in V_T compared toV_{TO} suggests that these trap states occur near the interface with the dielectric layer, which is the accumulation channel in these top contact bottom gate devices. Evenly distributed trap states across the semiconductor would affect the accumulation and saturation

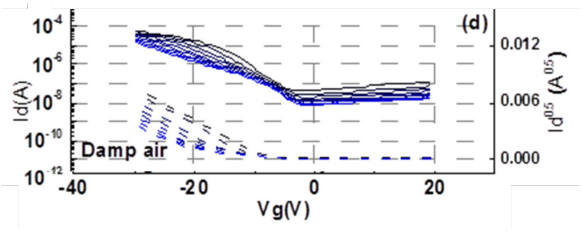


Figure 6.5: Transfer results in from previous work showing similar characteristics of transistors made here. Edited from: [22].

threshold voltage equally, which is not the case with these devices and is studied more by Ziqian Ding on the subject. [22]

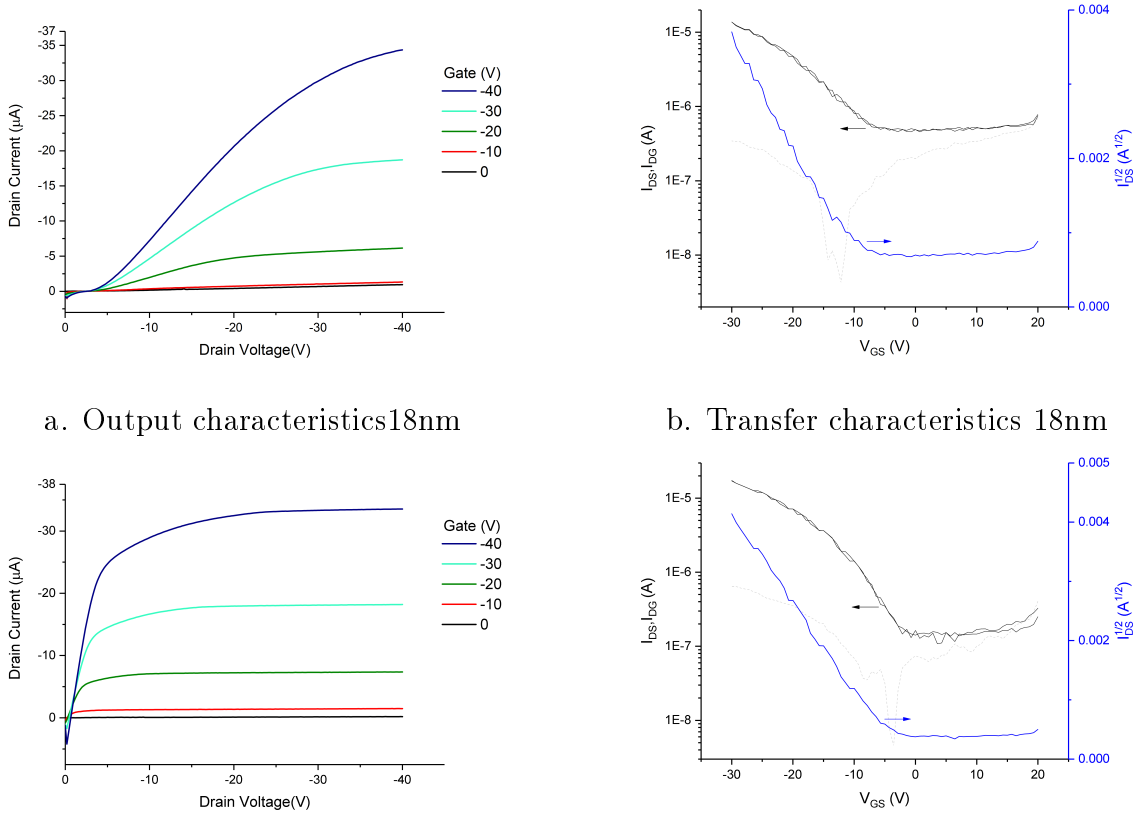
One difference with these results to those tested in damp air, is the lack of a dip in the transfer curve at around $-18V$, due to trap states existing at discrete band energies, which has analogues with pentacene organic semiconductor OTFT behaviour.[23, 24] This could be because the fabrication was within a damp environment, not the testing, creating a higher level of background trap states, with a large distribution of band energies, which mask this effect. Without this dip, the transfer gradient does not vary in steepness and so the mobilities in these devices were lower, $0.33 \pm 0.01 cm^2.V^{-1}.s^{-1}$, instead of $1.3 cm^2.V^{-1}.s^{-1}$ as found at the dip.

Another variation due to the fabrication conditions available, was the high off current leading to lower on/off ratios, here around 10^3. The moisture, particularly absorbed between deposition process, is likely creating an ion current in the dielectric, which is seen as a gate leakage in Figure 6.4. Not a single transistor had a lower leakage current than the off current. Other possible causes could be partially cured acrylate dielectric, pin hole defects, or dielectric thickness variation at the corners of the common gate thin film. However all of these were minimised with process optimisation and control before these transistors were fabricated.

These results show the importance of device structure and control of the fabrication environment, as these were the only factors to change between these results and others reported previously by the group. However for the purpose of testing the compatibility of the in-line patterning technique these control results are adequate. The mechanisms behind the behaviour is understood and the behaviour is consistent.

6.3.2 Aluminium contacts and effects of MoOx carrier injection layer

The discussion in the previous section concluded that the transistor fabrication method was reliable and the similarities and differences, with previous research, is understood



a. Output characteristics18nm

b. Transfer characteristics 18nm

c. Output characteristics - 6nm

d. Transfer characteristics - 6nm

Figure 6.6: Change in output and transfer characteristics with changing MoOx thickness for contact with aluminium contact deposited using a shadows mask. The transfer curves are obtained at $V_{DS} = -30V$.

in terms of device design (common gate leakage) and processing conditions, particularly moisture ingress. This section discusses results with aluminium thin film contacts and MoOx carrier injection layers, to test the compatibility of these materials for source drain contacts of OTFTs. The characterisation of functioning devices show that the MoOx layer introduces some contact resistance, which varies with the thin film thickness and configuration under the aluminium metal, but does provide a path of carrier injection and good yields.

6.3.2.1 MoOx effects on output characteristics and mobility

The characterisation of functioning DNTT OTFTs with aluminium contacts, with varying thickness of the MoOx charge carrier injection layer, is shown in Figure 6.6. Figure 6.6a. and c. exhibit lower output currents than measured with the gold contacts, see Figure 6.4. This difference is shared at all thicknesses of the oxide thin

film, so it must be a feature of the organic/inorganic interface.

It is known that the access resistance, that is the resistance experienced by a charge carrier as it moves through the semiconductor thickness (from/to the semiconductor channel to/from the contact), is prevalent with top contact transistors. The thermal deposition of a noble metal, like gold, onto a rough small molecule organic thin film, does not create a smooth sharp interface, see Figure 6.7. Diffusion of the metal condensate and thermal flux penetration have been suggested as mechanisms for reducing the access resistance with OTFTs.[25, 2] However with MoOx the evaporation temperature is lower (around $400°C$ compared with $1400°C$ of Au) and this increased contact area is not achieved, with a more abrupt interface. Also the insulating properties of MoOx is likely to further reduce any access resistance reduction due to contact interface enlargement. So the measured output currents in these results are more representative of the idealized OTFT thin film structure.

In this study, the saturation mobility of the transistors with Al+MoOx contact decreased with increasing MoOx thickness, from $0.15 \pm 0.04 cm^2.V^{-1}.s^{-1}$ to $0.08 \pm 0.02 cm^2.V^{-1}.s^{-1}$ for 6nm and 18nm thick films respectively, and were generally lower than the gold equivalents. This decrease in mobility is expected with the introduction of the relatively thick insulating oxide creating a contact resistance, which will decrease the injection current. This is supported by the finding that the mobility decreases with oxide thickness.

All this contributes to the conclusion that transistors with thicker MoOx thin films exhibit distinct contact resistances, seen here in the output curves as a delayed onset on the ohmic behaviour and delayed saturation. This low gate voltage effect is expected with the introduction of a more resistive contact, compared with gold. At low gate voltages the organic semiconductor resistance is large, so the contact resistance creates non-ohmic behaviour, see Equation 6.1. However, with thinner MoOx thin films, nominally 6nm, contact resistance is reduced and the linear output characteristics are comparable to gold's, but the saturation current is reduced due to access resistance changes from the reduced semiconductor interface area with the removal of contact material penetration into the semiconductor thin film.

6.3.2.2 MoOx effects on threshold voltage

The threshold voltage for Al+MoOx is more positive than for gold contacts, here $-5.83 \pm 2.14V$ and $-5.88 \pm 1.1V$ for 6nm and 18nm thin film respectively. This uniform reduction of the potential required for accumulation is possibly due to the oxide's conduction band equilibration with the organic's HOMO providing a route for

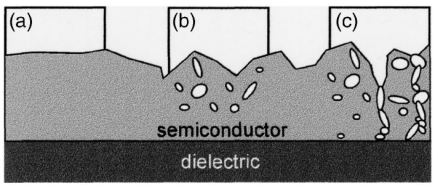
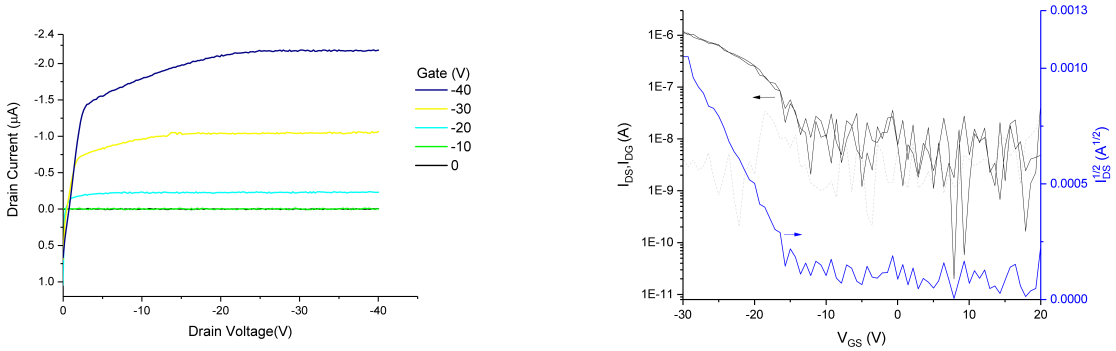


Figure 6.7: Schematic showing a. the ideal sharp interface between a metal contact and organic semiconductor, b. rough metal organic interface with metal clusters penetrated into the organic and c. with the cluster creating a conductive bridge from the contact to the dielectric layer. See original source (ref. [25]) for more details.

electron extraction from the organic, as has been seen with OLED thin film devices.[5] At equilibrium there is a more p-type energy state in the organic near the materials' interface due to band bending. In order to minimise the chemical potential of the material at the interface, an internal electric field is created leading to the band bending effect, which has similarly been attributed to improved performance with OPV.[5] This internal electric field is compensating for the required potential to inject charge carriers into the organic from the source contact, reducing V_T. However it it typically only a few tenths of eV so will not account entirely for the V_T shift.

Another explanation for the less negative threshold voltage is p-type doping of the organic with Mo_nO_{3n} clusters of varying sizes has been observed by ultraviolet photo-electron spectroscopy (UPS) and (STM). [26] In this work a significantly large shift in onset voltage for positive bias of the STM tip current-voltage measurements for doped pentacene with additional MoO_3 monolayer implies the additional clusters lead to electron trapping, which is expected with p-type doping. The hole mobility is similarly reduced but the MoO_3 dopant's electron structure leads to efficient electron transfer to the organic, increasing the hole density, leading to a slight positive shift in threshold voltage and, in theory, an increased mobility. However the efficiency of this process has been measured to be only 2%, with kelvin probe measurements of MoO_3 doped with 4,4´-Bis(carbazol-9-yl)-biphenyl (a.k.a. CBP).[27] So p-type doping is probably not entirely responsible for the increase in threshold voltage with MoOx carrier injection layers.

A final explanation for V_T being less negative, with a carrier injection layer than transfer with bare gold contacts, is the movement of charge carriers through the oxygen deficiency trap states. Air-exposed MoO_3, as was the case in this trial, has been shown to form non-stoichiometric MoOx (x<3), with oxygen vacancies leading to the reduction of the partially filled molybdenum d-band.[19] These deep trap states, filled with electrons, create a n-type semiconductor-like band structure, lowering the



a. Output characteristics - Co-evaporated Al+MoOx 18nm

b. Transfer characteristics - Co-evaporated Al+MoOx 18nm

Figure 6.8: Output and transfer characteristics of transistors with both aluminium and 18nm MoOx deposited within a single pump down, transfer obtained at $V_{DS} = -30V$.

oxide's work function.[28, 18] However MoOx has such a wide work function that even with the 1eV vacuum level shift, the work function (-5.7eV) is still larger than DNTT's ionization energy (-6.7eV), but is lower than gold (-5.1eV). The better band matching of air-exposed MoOx with DNTT, compared with gold, is seen as a less negative threshold voltage for these p-type contacts.

To demonstrate the importance of these trap states devices were made with MoOx and aluminium deposited sequentially within a single vacuum cycle. The results, see Figure 6.8, show a much higher threshold voltage, as oxide is protected from ambient exposure due to the aluminium contact. Although charge transfer at the interface has been shown before, for N,N´-di(naphthalene-1-yl)-N,N´-diphenyl-benzidine MoO_3 interfaces, to create similar defect states, these will be constrained to the oxide/organic interface and of low density.[29] The more negative V_t is most likely due to the lack of d-obital defects at the MoOx/aluminium interface, leading to an insulating oxide/-metal interface, which would inhibit electron injection into the MoOx layer. This is supported by the the high turn on voltage with these co-evaporated contacts.

6.3.2.3 MoOx effects on drain current, gate leakage & yield

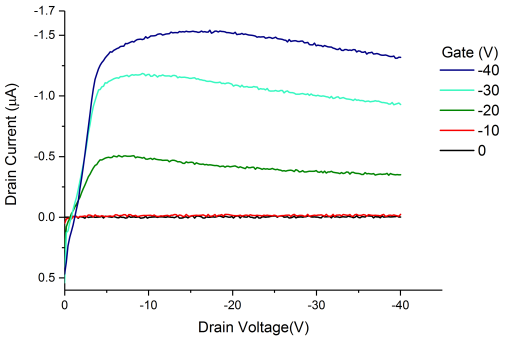
Another notable result of Figure 6.8 is the much lower output currents and lower I_{off} (gate leakage current), than the devices created by depositing a coating of MoOx followed by a separate vacuum deposition of aluminium through a shadow mask. The co-evaporated Al+MoOx contacts have almost and order of magnitude lower output current, suggesting a lower current collection at the contacts. One difference which

may have caused this result is that with the co-evaporation devices the shadow mask was fixed for both the aluminium and MoOx deposition. So, this MoOx thin film patterning, instead of coating, was further investigated to include oxide thickness variation and separate vacuum cycle depositions, see Figure 6.9.

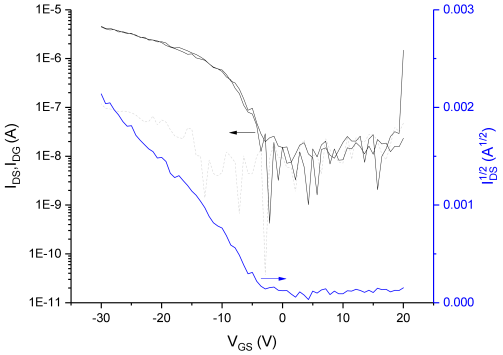
The output current, in the patterned MoOx case, is likely limited by the contact resistance reducing the current collection, to the extent that OTFTs with 18nm thick MoOx could not be characterised at the voltages concerned. The total resistance of the 6nm MoOx devices changes from $0.22M\Omega$ with a coating, to $0.55M\Omega$ with a patterned MoOx layer, at $V_g = -30V$, $V_{SD} = -2V$. The physical mechanism of this reduced current collection, due to increased resistance with MoOx lateral configuration, is the trimmed contact length due to the in-register patterning of the Al and MoOx. The contact length is the lateral distance beneath the contact from which charge carriers are collected. Transmission line measurements (TLM) can be used to ascertain this contact length and also the contact resistance. This is performed using the optimised in-patterning of lines with varying spacings, as is discussed in the following section.

In the transfer curves of OTFTs with a MoOx coating, Figure 6.6, the logarithm of the absolute gate leakage, is reflexive which suggests that there is gate leakage to both contacts, as the sign of the gate leakage gives the majority destination (source or drain) of the current. The MoOx coating might be acting as a resistive, albeit conductive bridge, between the source and drain, effectively a second semiconducting layer. This could also explain the higher off current, as the MoOx coating collects a higher proportion of the leakage and collects it to the contacts. Another possibility is aluminium deposition onto the rough MoOx surface, which could cause shadowing effects with the mask, could form metal interconnects across the channel. It was observed that the yield, due to source/drain shorting defects, increased with time, possibly due to aluminium's oxygen affinity reducing these metal shadow inter-contact interconnection's conductivity with storage time. This said, after the oxidation of the shadow mask defects, the leakage current remained constant. Overall the yield of the the aluminium devices were not above 80%, with thicker MoOx thin film coatings having higher yields.

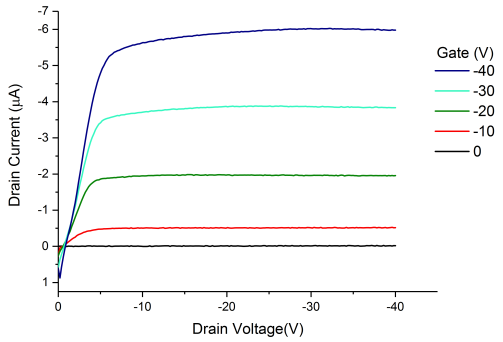
This reflexive gate leakage is not seen with the gold contact devices or with patterned MoOx, which supports the idea of lateral charge collection with a hole injection layer coating. With the gold contact devices, leakage is seen to increase with gate voltage, as discussed in the section 6.3.1. However this increasing current from the gate to the drain is removed with patterned MoOx hole injection layers, improving



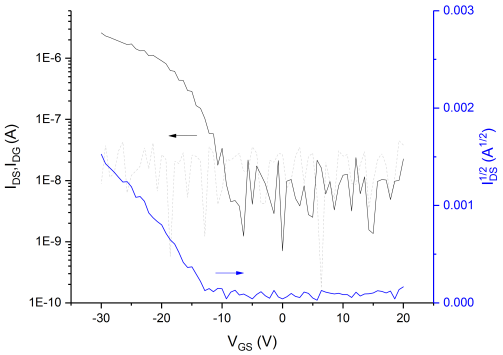
a. $12nm$ MoOx under contacts only



b.$12nm$ MoOx under contacts only



a. $6nm$ MoOx under contacts only



b. $6nm$ MoOx under contacts only

Figure 6.9: Characteristics of transistors with MoOx shadow mask patterned carrier injection layers of various thicknesses, with exposure to ambient before aluminium contact thermal evaporation, transfer obtained at $V_{DS} = -30V$.

the device performance. This is likely due to the access resistance change with gold and MoOx material depositions, see section 6.3.2.1.

6.3.2.4 Optimal compatibility of Al+MoOx OTFTs

This discussion has shown that there are several performance effects of using Al+MoOx contacts instead of gold. There is a reduced output current, particularly without an MoOx coating due to the oxide increased contact resistance, most from the access resistance changes. However there is also a reduction in the gate voltage, with air exposed samples. This is attributed to defect states creating a path for electron exchange between the organic and the MoOx.

Although the significant gate leakage can be minimised by patterning the MoOx layer this diminishes the output current below acceptable levels, when used with in-line aluminium patterning it would also require registration if the MoOx layer was

Table 6.1: Average characteristics of in-line patterned OTFTs.

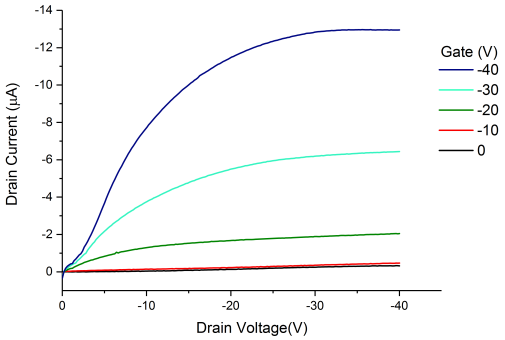
	Mask $150\mu m$	Patterned $150\mu m$	Patterned $200\mu m$	Patterned $500\mu m$
μ_{sat} $(cm^2.V^{-1}.s^{-1})$	0.09 ± 0.02	0.09 ± 0.01	0.15 ± 0.02	0.89
V_T (V)	-5.88 ± 0.67	-7.17 ± 0.55	-8.00 ± 1.62	-7.54
On/Off Ratio	10^2	10	10	10

patterned. It has been shown that the oxide thickness reduced the mobility but also increases the yield. These features of compatibility, diminished output current and mobility change with thickness, have to be balanced against the viability of manufacturing limitations and achievable yields.

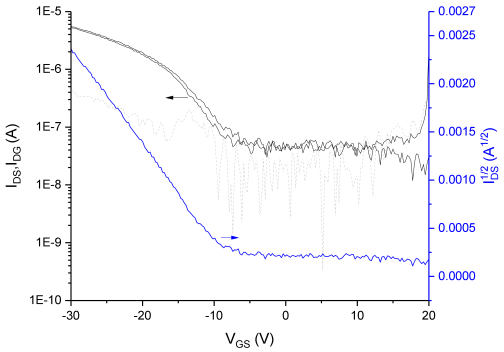
6.3.3 In-line patterned contacts

The working patterned transistors, shown in Figure 6.11, support the compatibility and viability of the in-line selective metallization with OTFTs, as fabricated in this work. The results, Figure 6.10, show functioning devices over a range of patterned contact lengths and with similar behaviour to the OTFTs with mask pattern Al contacts with some contact resistance and gate leakage, see Table 6.1. Overall a lower output current is observed, however this is attributed to the thin aluminium thin film deposited during the patterning process $(30 - 50nm)$ as opposed to $100nm$ thin film with the batch processed devices. When characterised the probe needles will make a smaller contact and damage the patterned aluminium, see Figure 6.11. Also the relative, inherent, aluminium oxide thickness $(3nm)$ will be proportionally larger.[30] The metal thickness, is limited by the system geometry as shown in Chapter 4 and with a larger industrial scale system this difference would not be observed. OTFTs with thinner MoOx were not viable as the combined yield of patterning and oxide thinness were too low.

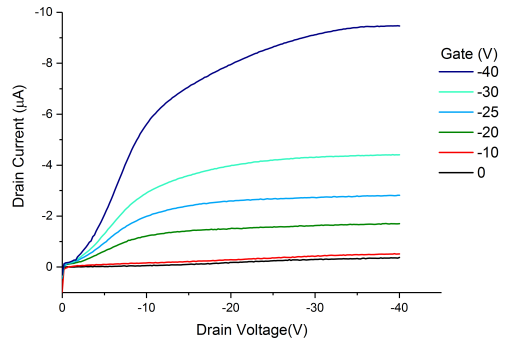
Table 6.1 also shows that the mobility increases linearly in proportion with $\frac{2L}{W}$ as predicted by the equation for output current, suggesting that the results are reliable as supported by the constant V_T of the patterned transistors within errors. This also replicates results seen in literature, with DNTT gold contact OTFTs.[31] There is a slightly higher average threshold voltage for the patterned transistors, compared to those with mask deposited contacts. Although the difference is small, almost within



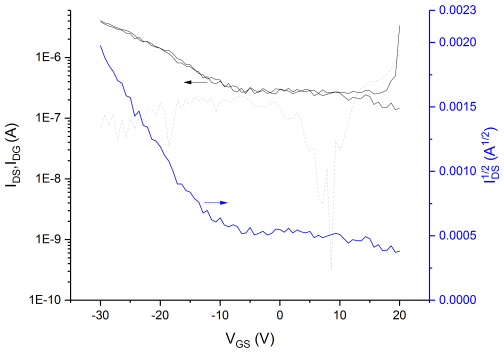
a. Output characteristics 150μm



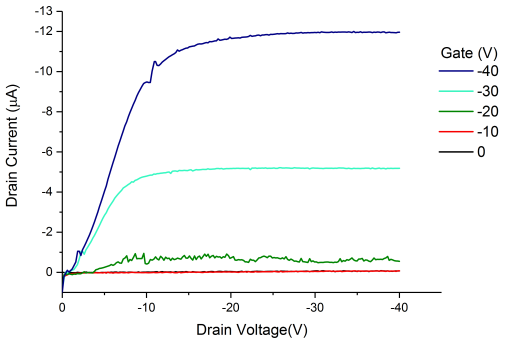
b. Transfer characteristics150μm



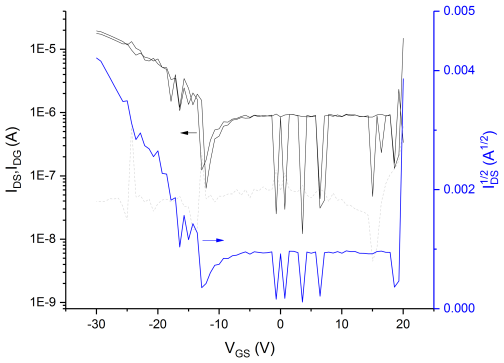
a. Output characteristics 200μm



b. Transfer characteristics 200μm



a. Output characteristics 500μm



b. Transfer characteristics 500μm

Figure 6.10: Output characteristics of patterned transistors with 18nm MoOx coating varying source drain width created using in-line patterning, and the corresponding transfer curves, obtained at $V_{DS} = -30V$.

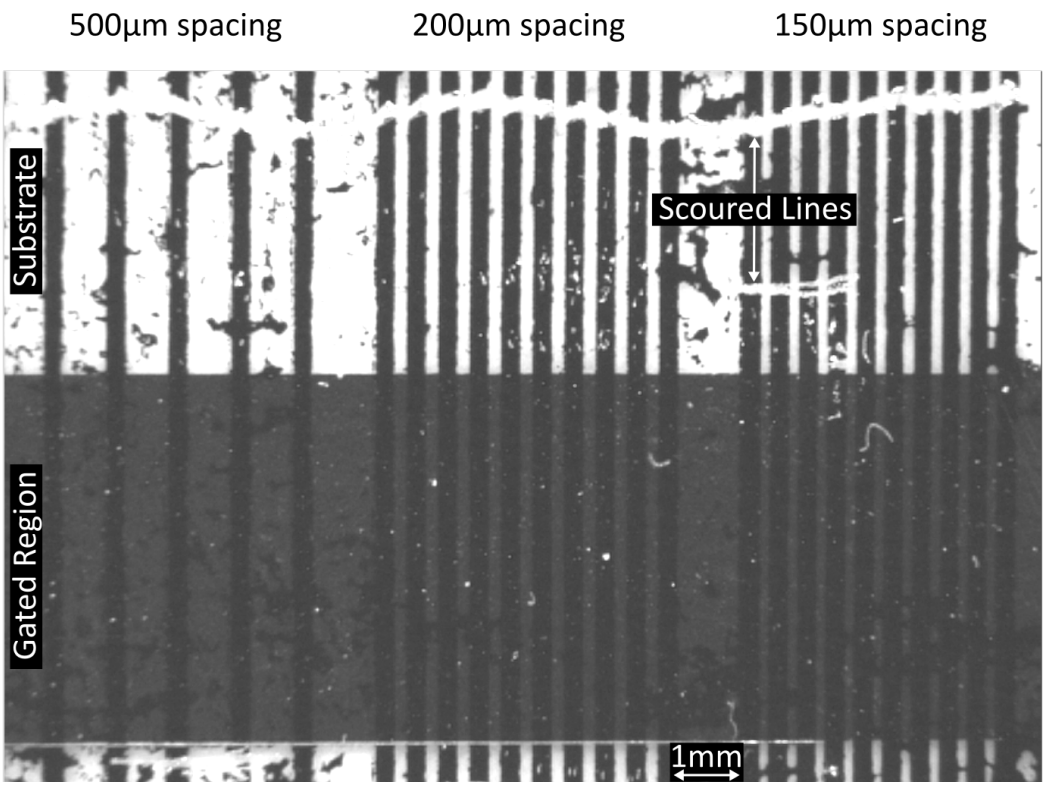


Figure 6.11: Greyscale optical microscopy image of the printed thin film transistors. Some defect are seen but each of the varying channel lengths show defect printing. White pin spots on the pattern aluminium (grey) were created by the probe needles used for characterisation.

errors, so the contact resistance is resistance of the differently fabricated devices is comparable.

From the resistance behaviour over the three source drain length a transmission line measurement can be made. The width-normalized resistance ($R_T.W$) of the transistors (inverse gradient of the linear region of the output curve) can be plotted against the varying channel length, as per reference [3], see Figure 6.1. From the y and x intercepts the transfer length of the 18nm MoOx is estimated to be: $41.5\mu m$; the contact resistance: $514K\Omega.cm$ and sheet resistance:$62M\Omega.\square^{-1}$ at $V_G = -30V$, see Figure 6.12, which leads to a contact resistivity of $1.03\Omega.cm^{-2}$.

These resistance values are quite large, compared with research but Ante et al. who found the contact resistance of DNTT with gold contacts to be $0.6K\Omega.cm$ and sheet resistance $270K\Omega.\square^{-1}$, but the contact length is of the correct order of magnitude, where previously for gold contacts it was found to be $10\mu m$.[32, 33] The vast difference in scale can be understood in terms of the different output currents due to device scale, relative gate leakage, and the difference in testing voltages. In this work the output current was an order of magnitude smaller for gold contact devices, see section 6.3.1, so the total resistance, at equivalent V_{SD}, was greater than reported by Ante. et al. Also their transfer characteristics were collected at $V_{DS} = -0.1V$ which is an order of magnitude less than used in this doctoral work, probably due to differences in the dielectric material capacitance (theirs was $800nF.cm^{-2}$, compared to $13nF.cm^{-2}$ in this work). Finally the gate voltage used for testing was an order of magnitude different, meaning these results should have an order of magnitude lower total resistance. Together, these factors mean that the resistance in this work is roughly 3 orders of magnitude greater due to different testing conditions and device materials.

Assuming this, the contact resistance would be slightly smaller for Al+MoOx contact than for gold. This confirms the results of reduced threshold voltage, as the resistance decreases due to improved band matching of MoOx with DNTT, than gold, see section 6.3.2.2. However, with the coating contact length is still larger, and so the resistivity is for Al+MoOx contact would be 4× than gold contact. The large contact length of the MoOx coating introduces a higher resistivity, leading to the reduced output currents. This is shown in the resistivity results, where work with Au contacts on DNTT found the contact resistivity to be $0.36\Omega.cm^{-2}$.[32] The triple difference is see proportionally in the output currents, Figure 6.4 and 6.6a.

Unfortunately, as the 18nm thick patterned MoOx devices did not give usable output characteristics the effect of trimming the transfer length could not be probed.

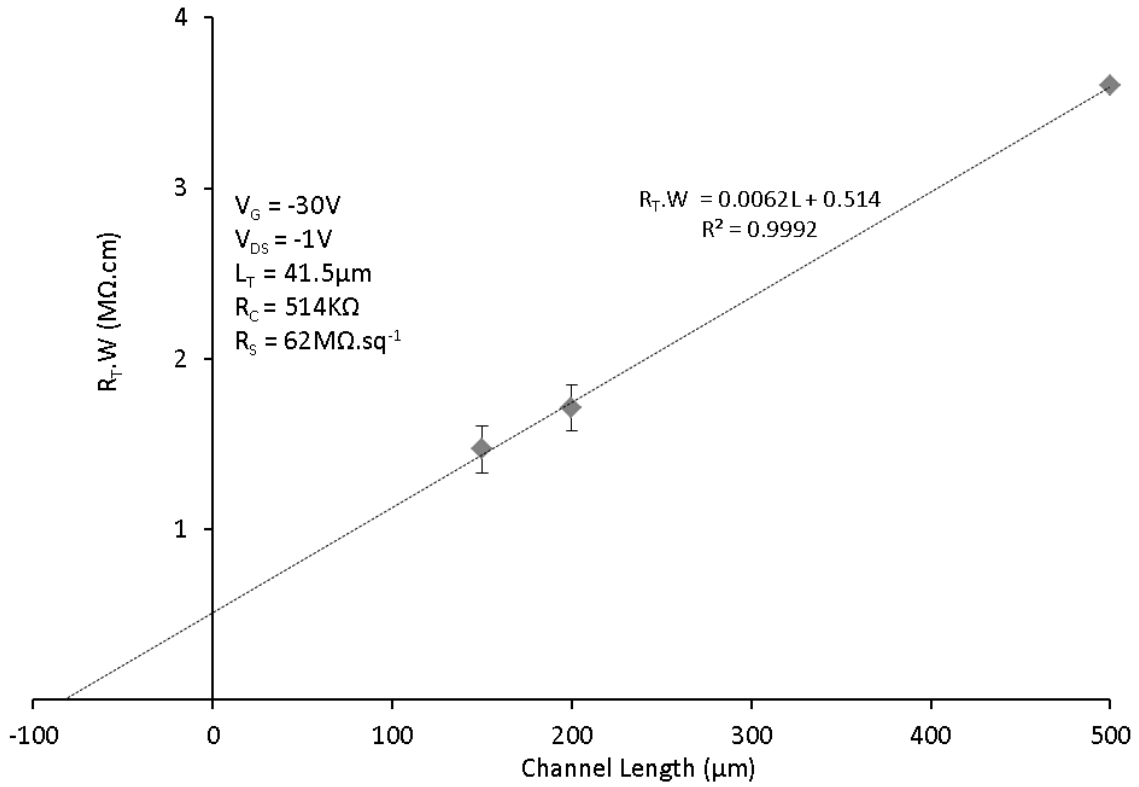


Figure 6.12: TLM analysis at $V_{DS} = -1V$ with patterned aluminium contacts and an 18nm MoOx coating, using in-line patterned aluminium contacts of varying spacings and nominal linewidth of $150\mu m$. Errors are from 4 measurements, except with $500\mu m$ channel length where on one measurement was possible.

$41.5\mu m$ is not long enough to bridge half the channel. Even though this value's error could be large, given the limited yield of the $500\mu m$ patterning and no patterning below $150\mu m$ produced to functioning devices, the sheet resistance appears to be in line with expected values, so the contact length is probably accurate. It is worth noting that with 37% ($1/e$) of charge carriers originating from beyond $41.5\mu m$, it is possible this effect accounted for the reflective behaviour of the leakage, as discussed in the section 6.3.2.3.

Understanding the performance change with time is important if the transistors are to be used in a logic circuit where device outputs need to be calibrated. Over 2 weeks, it was found that the average OTFT saturation mobility for the patterned contacts decreased by 23%. This is the same as the performance decrease of equivalent batch process Al+MoOx contact OTFTs, implying the the patterning process has little effect on the stability. It supports the modelling in the Chapter 4 which predicted the temperature change during the process is non-damaging. This empir-

ical finding also shows that the remnant oil patterning does not damage the existing device structure, or lead to longer term effects. However the decrease is higher than Au contact OTFT performance decay rates, which in this study were found to be 10% over the same time period. This decrease is likely due to moisture ingress with more humid processing and handling conditions, as discussed in section 6.3.1. One possible causes for the disparity in Au and Al+MoOx contacts OTFT stability includes oxidation of the aluminium. However output currents did not reduce, as would be expected, although the needle probes could penetrate the oxide, masking this effect.

6.4 Conclusion

The results in this chapter have combined selective metallization, using optimal printing settings, with functional organic devices as proof of the viability and compatibility of this process. Using the patterned aluminium as the source and drain contacts necessitates the introduction of a MoOx charge carrier injection layer on the DNTT semiconductor.

Although there were some differences in the control devices, with previous work in the group, this was attributed to the ambient processing and handling conditions, as well as the common gate structure which increases leakage. In general though, the devices fabricated were reliable, had yields up to 100%, an average mobility of $0.33 \pm 0.01 cm^2.V^{-1}.s^{-1}$ and a threshold voltage of $9.61 V.dec^{-1}$.

With aluminium contacts the mobility reduced to $0.15 \pm 0.04 cm^2.V^{-1}.s^{-1}$ to $0.08 \pm 0.02 cm^2.V^{-1}.s^{-1}$ for 6nm and 18nm thick films, due to increased access resistance as the lower thermal damage of MoOx deposition, compared to Au deposition, leads to a sharper interface. In contrast, with the introduction of the MoOx layer the threshold voltage increased to $-5.83 \pm 2.14 V$ and $-5.88 \pm 1.1 V$ for 6nm and 18nm thin film respectively. This was attributed partly to band bending effects, but predominantly due to conduction through the oxygen vacancy defect states in the MoOx layer. Testing devices with MoO_3 carrier injection layers, fabricated within a single vacuum for both contact layers, increased the threshold voltage, supporting this hypothesis.

The reduced output currents of device with contact that had a patterned MoOx layer instead of a coating, were considered to be a result of the trimmed transfer length of the contact. Indeed with the coating a reflexive gate leakage implied the MoOx was coating was acting as a conductive bridge across the channel. In conclusion to these observation of batch processed devices, it was suggested that a patterned MoOx layer (18nm), with a length slightly extended beyond the edge of the contact,

was optimal. Although patterning MoOx has been performed with roller techniques before,[34] for the scope of this thesis, coatings were used. This also removed the need for registration processes, exemplifying a trade-off between the viability and compatibility of the process.

The transistors made with patterned electrodes functioned as expected, although the yield of higher pattern ratio devices was low, due to printing defects. The output currents were reduced, due to limited aluminium thickness with this equipment. Otherwise the technique created reliable device performance, demonstrated by the mobilities of changing with channel length linearly and the threshold voltages were similar to batch processed devices. Making use of the patterning, TLM analysis was performed. When compared to research on Au contact resistance with DNTT [32, 33], it showed that the contact resistance of MoOx+Al device was lower, seen as the lower V_T, but the contact length was much larger, $41.5\mu m$, so the resistivity was higher, which was characterised by the lower output currents. The lower contact resistance is favourable as it means there is potential to scale the devices, along with the patterning method, but the large contact length would need to be addressed, by patterning the MoOx layer.

The measurements of mobility over 2 weeks demonstrated that the selective metallisation process did not change the stability of the devices. However there was a difference in Au and Al+MoOx contacts of 10%. Further work is required to understand the causing mechanisms.

6.5 References

[1] Ziqian Ding, Gamal Abbas, Hazel E Assender, John J Morrison, Stephen G Yeates, Eifion R Patchett, and D Martin Taylor. Effect of Oxygen, Moisture and Illumination on the Stability and Reliability of Dinaphtho[2,3-b:2',3'-f]thieno[3,2-b]thiophene (DNTT) OTFTs during Operation and Storage. *ACS applied materials & interfaces*, 6(17):15224–31, September 2014.

[2] Zhenan Bao and Jason Locklin. *Organic Field-Effect Transistors*. CRC Press, May 2007.

[3] Dieter K. Schroder. *Semiconductor Material and Device Characterization*. John Wiley & Sons, 2006. Google-Books-ID: EmozDwAAQBAJ.

[4] Sami Hamwi, Jens Meyer, Michael Kröger, Thomas Winkler, Marco Witte, Thomas Riedl, Antoine Kahn, and Wolfgang Kowalsky. The Role of Transition Metal Oxides in Charge-Generation Layers for Stacked Organic Light-Emitting Diodes. *Advanced Functional Materials*, 20(11):1762–1766, June 2010.

[5] Do Young Kim, Jegadesan Subbiah, Galileo Sarasqueta, Franky So, Huanjun Ding, Irfan, and Yongli Gao. The effect of molybdenum oxide interlayer on organic photovoltaic cells. *Appl. Phys. Lett.*, 95(9):093304, August 2009.

[6] Vishal Shrotriya, Gang Li, Yan Yao, Chih-Wei Chu, and Yang Yang. Transition metal oxides as the buffer layer for polymer photovoltaic cells. *Applied Physics Letters*, 88(7):073508, February 2006.

[7] James Bullock, Andres Cuevas, Thomas Allen, and Corsin Battaglia. Molybdenum oxide MoOx: A versatile hole contact for silicon solar cells. *Appl. Phys. Lett.*, 105(23):232109, December 2014.

[8] Yixin Zhao, Alexandre M. Nardes, and Kai Zhu. Effective hole extraction using MoOx-Al contact in perovskite CH3nh3pbi3 solar cells. *Appl. Phys. Lett.*, 104(21):213906, May 2014.

[9] Mark T. Greiner, Michael G. Helander, Wing-Man Tang, Zhi-Bin Wang, Jacky Qiu, and Zheng-Hong Lu. Universal energy-level alignment of molecules on metal oxides. *Nature Materials*, 11(1):76–81, January 2012.

[10] James Bullock, Andres Cuevas, Thomas Allen, and Corsin Battaglia. Molybdenum oxide MoOx: A versatile hole contact for silicon solar cells. *Applied Physics Letters*, 105(23):232109, December 2014.

[11] T. J. Richards and H. Sirringhaus. Analysis of the contact resistance in staggered, top-gate organic field-effect transistors. *Journal of Applied Physics*, 102(9):094510, November 2007.

[12] M. Finetti, A. Scorzoni, and G. Soncini. Lateral current crowding effects on contact resistance measurements in four terminal resistor test patterns. *IEEE Electron Device Letters*, 5(12):524–526, December 1984.

[13] S. D. Wang, Y. Yan, and K. Tsukagoshi. Understanding contact behavior in organic thin film transistors. *Appl. Phys. Lett.*, 97(6):063307, August 2010.

[14] Roel S. Sánchez-Carrera, Sule Atahan, Joshua Schrier, and Alán Aspuru-Guzik. Theoretical Characterization of the Air-Stable, High-Mobility Dinaphtho[2,3-b:2'3'-f]thieno[3,2-b]-thiophene Organic Semiconductor. *J. Phys. Chem. C*, 114(5):2334–2340, February 2010.

[15] Tatsuya Yamamoto and Kazuo Takimiya. Facile Synthesis of Highly π-Extended Heteroarenes, Dinaphtho[2,3-b:2‘,3‘-f]chalcogenopheno[3,2-b]chalcogenophenes, and Their Application to Field-Effect Transistors. *J. Am. Chem. Soc.*, 129(8):2224–2225, February 2007.

[16] Antoine Kahn. Fermi level, work function and vacuum level. *Materials Horizons*, 3(1):7–10, 2016.

[17] R M Eastment and C H B Mee. Work function measurements on (100), (110) and (111) surfaces of aluminium. *Journal of Physics F: Metal Physics*, 3(9):1738–1745, September 1973.

[18] Irfan, Huanjun Ding, Yongli Gao, Cephas Small, Do Young Kim, Jegadesan Subbiah, and Franky So. Energy level evolution of air and oxygen exposed molybdenum trioxide films. *Appl. Phys. Lett.*, 96(24):243307, June 2010.

[19] Mark T. Greiner, Michael G. Helander, Wing-Man Tang, Zhi-Bin Wang, Jacky Qiu, and Zheng-Hong Lu. Universal energy-level alignment of molecules on metal oxides. *Nat Mater*, 11(1):76–81, January 2012.

[20] Gamal a. Abbas, Ziqian Ding, Hazel E. Assender, John J. Morrison, Stephen G. Yeates, Eifion R. Patchett, and D. Martin Taylor. A high-yielding evaporation-based process for organic transistors based on the semiconductor DNTT. *Organic Electronics*, 15(9):1998–2006, September 2014.

[21] Gamal Abbas, Hazel Assender, Mervat Ibrahim, and D. Martin Taylor. Organic thin-film transistors with electron-beam cured and flash vacuum deposited polymeric gate dielectric. *Journal of Vacuum Science & Technology B*, 29(5):052401, September 2011.

[22] Ziqian Ding. *Large Area Vacuum Fabrication of Organic Thin-Film Transistors.* PhD thesis, University of Oxford, Oxford, March 2014.

[23] C. Goldmann, D. J. Gundlach, and B. Batlogg. Evidence of water-related discrete trap state formation in pentacene single-crystal field-effect transistors. *Applied Physics Letters*, 88(6):063501, February 2006.

[24] Oana D. Jurchescu, Jacob Baas, and Thomas T. M. Palstra. Electronic transport properties of pentacene single crystals upon exposure to air. *Applied Physics Letters*, 87(5):052102, July 2005.

[25] Paul V. Pesavento, Reid J. Chesterfield, Christopher R. Newman, and C. Daniel Frisbie. Gated four-probe measurements on pentacene thin-film transistors: Contact resistance as a function of gate voltage and temperature. *Journal of Applied Physics*, 96(12):7312–7324, December 2004.

[26] Sieu D. Ha, Jens Meyer, and Antoine Kahn. Molecular-scale properties of MoO 3 -doped pentacene. *Physical Review B*, 82(15), October 2010.

[27] S. Hamwi, J. Meyer, T. Winkler, T. Riedl, and W. Kowalsky. p-type doping efficiency of MoO3 in organic hole transport materials. *Appl. Phys. Lett.*, 94(25):253307, June 2009.

[28] J. Meyer, A. Shu, M. Kröger, and A. Kahn. Effect of contamination on the electronic structure and hole-injection properties of MoO3/organic semiconductor interfaces. *Appl. Phys. Lett.*, 96(13):133308, March 2010.

[29] Kaname Kanai, Kenji Koizumi, Satoru Ouchi, Yoshiaki Tsukamoto, Kei Sakanoue, Yukio Ouchi, and Kazuhiko Seki. Electronic structure of anode interface with molybdenum oxide buffer layer. *Organic Electronics*, 11(2):188–194, February 2010.

[30] D.J. McClure and N J Copeland. Evaporated aluminum on polyester: optical, electrical, and barrier properties as a function of thickness and time (Part II). In *2010*. AIMCAL.

[31] D. Martin Taylor, Eifion R. Patchett, Aled Williams, Ziqian Ding, Hazel E. Assender, John J. Morrison, and Stephen G. Yeates. Fabrication and simulation of organic transistors and functional circuits. *Chemical Physics*, 456:85–92, July 2015.

[32] Frederik Ante, Daniel Kälblein, Tarek Zaki, Ute Zschieschang, Kazuo Takimiya, Masaaki Ikeda, Tsuyoshi Sekitani, Takao Someya, Joachim N. Burghartz, Klaus Kern, and Hagen Klauk. Contact Resistance and Megahertz Operation of Aggressively Scaled Organic Transistors. *Small*, 8(1):73–79, January 2012.

[33] Frederik Ante, Daniel Kälblein, Ute Zschieschang, Tobias W. Canzler, Ansgar Werner, Kazuo Takimiya, Masaaki Ikeda, Tsuyoshi Sekitani, Takao Someya, and Hagen Klauk. Contact Doping and Ultrathin Gate Dielectrics for Nanoscale Organic Thin-Film Transistors. *Small*, 7(9):1186–1191, May 2011.

[34] Xinge Yu, Tobin J. Marks, and Antonio Facchetti. Metal oxides for optoelectronic applications. *Nature Materials*, 15(4):383–396, March 2016.

Chapter 7

Conclusion and Future Work

Sections of this chapter have been accepted for the proceedings of NanoTexnology 10th International Symposium on Flexible Organic Electronics to be published in Materials Today: Proceedings (in-print).

7.1 Conclusion of thesis findings

This thesis has considered the viability and compatibility of an in-vacuum roll-to-roll process already used in industry to print aluminium patterns: selective metallization. It relies of flexography printing and thermal mechanisms to create high resolution ($< 10\mu m$) patterns on flexible substrates, such as PET and PEN. This thesis has answered the introductory questions in Table 1.1 in the following ways:

Could the process be used for patterning functional organic devices, and what process conditions make it viable?

Is the process compatible with functional organic devices and what considerations are specific to this process?

Is the functional organic exposed to damaging temperatures during the process?

Thermal modelling of this process has been developed to predict that the deposited oil thickness, which is a function of the radiative heating from the physical vapour source, needed to be around $1.63\mu m$ for complete masking of the non-pattern areas and removal within the metallization zone. This modelling also found the process would not expose the sensitive organic functional layers to damaging temperatures ($< 100°C$).

How does selective metallization compare to alternative techniques for creating conductive patterns, in terms of throughput, use of exotic and toxic chemicals, and the properties of the printed materials?

Can the patterned aluminium thin film achieve the necessary thickness, conductivity and surface roughness? How do these parameters interact with the processing conditions?

The produced metal thin films have excellent conductivity ($1.59\Omega.\square^{-1}$) and low surface roughness ($4.5\pm0.7nm$), with a thickness of $30-50nm$, which is not seen in solution processing techniques, highlighting the advantage of in-vacuum direct deposition methods. This modelling also confirms that the patterning quality of this process is limited by the oil patterning process (flexography). Impressively early indicative results showing $sub-10\mu m$ metal thin film patterning are presented, created at a printing speed of $10m.min^{-1}$, using CNT stamps.

What are the limits on the the printing ability, in terms resolution and pattern defect concentration?

Based on this finding the selective metallization process was used as a testing method for the flexography printing, as the metal patterns represent the transferred oil form due to the printing mechanism. Although there is significant work on modelling the effects of printing force and speed on the splitting of liquid bridges and, separately, reported results of printing variable effects on print quality, the literature review showed that there is still a lack of understanding in the literature as to how the printing process can be optimised to improve the printing quality. Using a specially developed flexography printing system, with careful experimental design, combined with a specially written image analysis code to quantify the print quality, trends in the printing quality with the printing pressure, speed and pattern variation have been assessed.

The results were analysed to show that there are 3 contributions to the printed pattern quality: plate backing and conformability of the printing roller to the substrate impression drum; plate feature deformation and, finally, ink distortion and spreading. Building on existing ink transfer understanding, together with results gathered in this doctorate, a hierarchical phenomenological model was created, that fitted the data well, for pattern ratios larger than 1, with rudimentary fitting constants.

Has the process been scaled up? What were the compromises being made between careful experimental work and high volume industrial scale processes?

Overall the trends showed that there is an optimal printing force, which is shared at different pattern scales but can change with pattern design (ratio), and that as printing speed increases the variation with printing force decreases, but the print quality also decreases. Also that the line edge roughness scaled with pattern size. The lowest achievable pattern line edge roughness, is related to the ink distortion effects, which can be minimised by printing at low speeds and choosing shear thickening inks.

Can the process be optimised, by changing the printing pressure and speed, to remove printing defects which would cause critical defects?

This chapter showed that a holistic approach to understanding a process, drawing on historical, industrial and academic research, is needed to obtain the best possible results. In this work, at optimal settings, $42N.m^{-1}$ and $10m.min^{-1}$, patterns with a peak-to-peak line edge roughness below half the pattern spacing could created.

Can the pattered aluminium be used with existing OTFT organic semiconductor? What are the effects and optimal properties of a charge carrier injection layer?

This was used to create metal contacts without critical shorting defects, that were utilised as top-contacts for common gate OTFTs, as a proof of concept functional organic device. The fabricated OTFTs showed comparable behaviour to previous work [1, 2], with an average mobility of $0.33 \pm 0.01 cm^2.V^{-1}.s^{-1}$ and a threshold voltage of $9.61 V.dec^{-1}$. Differences were attributed to fabrication conditions and device structure, as well as the introduction of charge carrier injection layer (MoOx), to accommodate for the increased work function of the aluminium thin films, compared with previous gold contacts deposited using batch shadow mask processes. The effects of this MoOx were investigated, in terms of its thickness and configuration under the contacts, to show the balance between decreased contact resistance, for pattern MoOx, and increased output behaviour, for thicker coatings. A thickness of $18nm$ was chosen with a coating configuration, as this removed registration requirements for fabrication with in-line patterning of the contacts. These results showed that high-throughput patterned devices are similar to batched processed devices with mobility of 0.09 ± 0.01, for $150\mu m$ source drain gap, and threshold voltages of -7.17 ± 0.55.

Making use of the patterning ability of the contacts, with the selective metallization process, transmission line measurements (TLM) was performed to show that Al+MoOx has a lower contact resistance than the reported value for gold contact, when experimental differences are accounted for. This is seen in the lower V_T. But the contact length is $41.5\mu m$ (4×Au) so the contact resistivity is high, leading to the decreased output characteristics.

Does the process introduce damaging chemicals onto the functional organic or printing equipment? If so, what are the effects?

The selective metallization did not affect stability (over a 2 week test). More work is required to understand the mechanisms that lead to the MoOx+Al contact having a 10% greater reduction in mobility than the Au devices, for the same period of time. Ultimately, this showed that the selective metallization process is compatible with the functional organic devices and there is often a trade off to be made between the viability of a process and its compatibility with the functional device.

To conclude exploratory results of applying this process to OLEDs, and in-vacuum flexography printing to printing an organic dielectric layer, will be presented.

7.2 Future Work

7.2.1 Selective Metallization

The first discussion chapter (Chapter 4) presented results that showed that $sub{-}10\mu m$ patterning is achievable. The ability to create metallic patterns with a high throughput method like this is exciting. However the reliability and general quality needs to be increased if it is to be used for a functional device. The delicate, and sensitive to shear, carbon nanotube stamps, need to be used with a high precision control system, which is an engineering challenge. The possible applications for this would be R2R produced functional devices such as sensors and transistors where the performance depends on scaling effects. Also the application to transparent conductors, if narrow, with wide spacing, grid patterns could be formed.

The selective metallization process is not limited to aluminium and other thermally evaporated thin film materials, such as indium tin oxide, gold, and perhaps organics, could be be explored. Using the thermal modelling presented the viability of new material could be assessed given their thermal evaporation temperatures. Another aside could be to use other deposition processes such as plasma deposition and sputtering. The thermal lift-off mechanism could rely on alternate energy (than radiation

from evaporation) to be removed. Also alternate oils could be used to match different materials thermal properties, as was studied by Pagani et al. [3], although more experimental work could be done in the area.

Finally the measurement of the excess oil is a challenging problem as the volume are small and the substrates generally large and difficult to handle with control. It would be very good to test the model by measure the excess oil, exposed to different source temperatures.

7.2.2 Flexography printing

The model for flexography printing in this doctoral thesis had meaningful agreement with the experimental data, however the generality of this hierarchical model could be further probed. By using inks of varying viscosity the ink distortion contribution to total line edge roughness could be tested, and the impact of printing speed confirmed. With smaller patterns the minimum roughness associated with the ink variation with printing force could also be further confirmed. Changing the plate backing, perhaps to an industry standard, would improve the applicability of the result to current printing machines, although the lower stiffness used in this work was useful for exploring the plate backing's impact. For lower pattern ratios the edge roughness was very large, perhaps due to non bulging deformation of the plate features. The variation of plate feature deformation due to ceiling collapse with applied pressure, could be explored. This work only considered cross direction lines, the machine direction lines will have edge roughness related to lateral effects, this is assumed to be an machine effect (drum wobble) but the ink and plate distortion effects could also be explored to give the understanding more applicability to different pattern designs.

In-vacuuum flexography is generally an under researched field but the potential is large. Many different liquid materials can be directly printed simply using the flexography process. To explore this, an organic (TPGDA) which is used as the dielectric layer in the OTFTs, was deposited in-vacuum using flexography. Printing this material in its liquid monomer state mimics the existing flash evaporation process [4], which was use to create the OTFTs in this doctoral work. In the flash evaporation process, the acrylate is vaporised and injected into the vacuum chamber, where it condenses as a liquid onto the substrate, leading to the smooth surface which is important for the subsequent condensed small molecule semiconductor structure.[5] The monomer fluid is then cured with a plasma, forming a coating which can be used in devices.

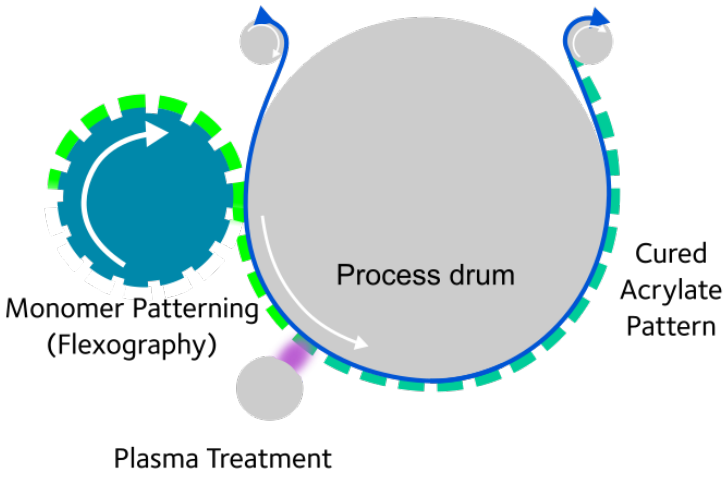


Figure 7.1: Schematic of the in-vacuum acrylate patterning process using flexography, followed by curing of the monomer liquid using an argon plasma.

With the flexography set-up used before in the doctoral thesis, TPGDA was patterned onto a polyethylene naphthalate (PEN) substrate and silicon reference chips. The plate inking was achieved as the oil had been, and the curing was achieved using a custom built plasma set-up (argon), see Figure 7.1. The TPGDA did not swell the PDMS plate with a solubility parameter of $10.52 cal^{1/2}.cm^{-3/2}$, calculated using the Fedors additive function method[6], and this was confirmed by testing with the 24 hour solubility test, as per Lee et al.[7] An image of the final print is shown in Figure 7.2 achieved with a nominal line force of $42 N.m^{-1}$ and printing speed of $10 m.min^{-1}$, which used $1mm$ and $150\mu m$ cross direction line plate patterns. The capacitance was measured to be $11 - 13 nF.cm^{-2}$ (using Tenma 72-7750 capacitance meter), however the surface was very rough: root mean square roughness: $5.88 \pm 8.43 nm$ and peak-to-peak height: $36.14 \pm 6.04 nm$.

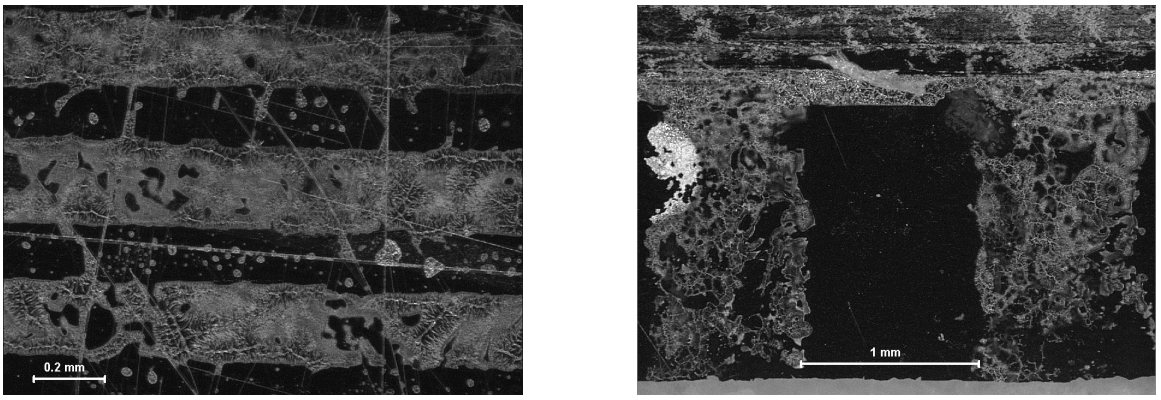
This surface roughness would cause gate shorting and leakage in OTFTs. Curing degree of the monomer could also not be ascertained due to the roughness and discontinuity of the printed thin films. This roughness could be due to the low plasma voltage (30kV used here instead of 200kV used when flash evaporating in a larger system). This has been shown to have a similar effect on the surface morphology to that seen here.[8]

Another possibility is that the surface roughness originated from the printing process, given the the low monomer liquid viscosity $0.01 mPa.s$, and string-like (filamentation) defects are seen in the results, Figure 7.2. This low viscosity also accounts for the thinness of the deposited patterns: only $40.67 \pm nm$. Flexography can typically be expected to deposit closer to micrometer thickness thin films, which would be ideal for organic dielectric layers in OTFTs. However this would require a more viscous ink (liquid monomer), and so without changing the chemistry, of this directly deposited ink, additives are needed to increase the viscosity, which may also reduce the printed roughness but introduce unwanted thin film electrical properties.

Although the surface is too rough to make devices, it is possible, with improved curing, that the surface roughness could be reduced. Most importantly though this work goes to show the wide applicability of novel in-vacuum flexography printing for functional organic devices.

7.2.3 Patterning for functional organic devices

The application of selective metallization to organic devices, showed, for the first time that this process, was viable and compatible with functional organic device fabrication. Further work could reduce the scale of the device contacts, if the line



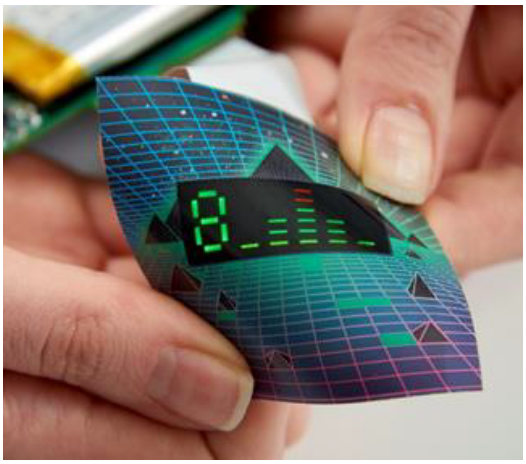
a. b.

Figure 7.2: Optical micrographs of the printed TPGDA on silicon chips 1mm line patterns at a. 1× and b. 5× magnification. The darker regions are the unpatterned silicon surface.

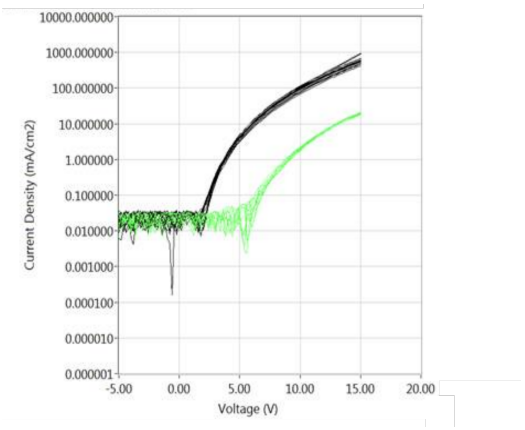
edge roughness control could be improved. First though the contact resistance due to the carrier injection layer (MoOx) needs to be reduced if these devices are to be scaled down. There are few material alternates as MoOx has the largest work function of the metal oxides.[9] However Chapter 6 showed that patterning of the MoOx layer, could improve device performance. This could be achieve with in-line thermal lift-off process, if the correct oil to match the low evaporation temperature could be found. The longer term stability of MoOx with DNTT needs to be more thoroughly investigated, to find the mechanism responsible for degradation.

As a demonstration of the wide applicability of the selective metallization process, and working with Cambride Display Technology Ltd. (CDT), organic light emitting diodes (OLED) with aluminium cathodes were created. OLEDs are a mature application of functional organics. Low resolution, cost effective light emitters are becoming more common, as they have a low density, with a large display areas and are conformable. The back cathode is a non-transparent electron transport layer for the organic (in this case polymer) emissive layer. The luminescent radiation can then pass through the hole injection and transparent conducting anode to create the desired light emission. Aluminium was chosen for the cathode layer as it is stable in air and is reflective, leading to higher front luminescence. CDT report $400cd.m^{-2}$ with $< 5V$ operating voltages, and good air stability with encapsulation, leading to lifetimes of 5 years.[10]

The in-line patterned devices worked and the IV characteristics results are shown in Figure 7.3. The device turn on voltage was slightly larger batch processed devices but this was associated with the ambient exposure during handling and transport



a.



b.

Figure 7.3: a. Sample OLED from CDT, image from reference [11]. b. Output characteristics of OLED with a cathode layer deposited using selective metallization (green line). The control (black line) were deposited with CDT's custom in-house cathode mask batch processes, which had better ambient atmosphere process control, before encapsulation.

leading to defects in the organic thin films. Also, there was low yield due to registration issues as the cathode position required mm machine direction precision. This is difficult to achieve with this custom built in-vacuum flexography set-up. The cathode pattern itself was relatively large (cm scale) and the edge roughness simply reduced to workable levels by optimising the printing force and speed. The long term stability after encapsulation was reportedly the same as the batch processed devices. This work demonstrates that this process is not just limited of OTFTs, but can be applied to a range of devices, and novel applications should be tested.

7.3 References

[1] D. Martin Taylor, Eifion R. Patchett, Aled Williams, Ziqian Ding, Hazel E. Assender, John J. Morrison, and Stephen G. Yeates. Fabrication and simulation of organic transistors and functional circuits. *Chemical Physics*, 456:85–92, July 2015.

[2] Ziqian Ding, Gamal Abbas, Hazel E Assender, John J Morrison, Stephen G Yeates, Eifion R Patchett, and D Martin Taylor. Effect of Oxygen, Moisture and Illumination on the Stability and Reliability of Dinaphtho[2,3-b:2',3'-f]thieno[3,2-b]thiophene (DNTT) OTFTs during Operation and Storage. *ACS applied materials & interfaces*, 6(17):15224–31, September 2014.

[3] A. Pagani, P. Raugei, and F. Rimediotti. Patterned Metallized Films: State-of-the-art and Growth Opportunities. In *50th Annual Technical Conference Proceedings*, pages 757–761. Society of Vacuum Coaters, 2007.

[4] John Affinito. A new method for vacuum deposition of polymer films. *Thin Solid Films*, 420–421:1–7, December 2002.

[5] Gamal Abbas, Hazel Assender, Mervat Ibrahim, and D. Martin Taylor. Organic thin-film transistors with electron-beam cured and flash vacuum deposited polymeric gate dielectric. *Journal of Vacuum Science & Technology B*, 29(5):052401, September 2011.

[6] Robert F. Fedors. A method for estimating both the solubility parameters and molar volumes of liquids. *Polym Eng Sci*, 14(2):147–154, February 1974.

[7] Jessamine Ng Lee, Cheolmin Park, and George M. Whitesides. Solvent Compatibility of Poly(dimethylsiloxane)-Based Microfluidic Devices. *Analytical Chemistry*, 75(23):6544–6554, December 2003.

[8] J. D Affinito, Stephan Eufinger, M. E Gross, G. L Graff, and P. M Martin. PML/oxide/PML barrier layer performance differences arising from use of UV or electron beam polymerization of the PML layers. *Thin Solid Films*, 308:19–25, October 1997.

[9] Mark T. Greiner, Michael G. Helander, Wing-Man Tang, Zhi-Bin Wang, Jacky Qiu, and Zheng-Hong Lu. Universal energy-level alignment of molecules on metal oxides. *Nat Mater*, 11(1):76–81, January 2012.

[10] Printed Flexible OLED Displays. Product Specifications, Cambridge Display Technology Ltd. https://www.cdtltd.co.uk/wp-content/uploads/2017/08/CDT_Flex_Displays_2017.pdf.

[11] Dr Alexander Doust. Flexible OLEDs for consumer products - cambridge display technology. https://www.cdtltd.co.uk/wp-content/uploads/2016/12/Printed-Electronics-2016_IDTechEx.pdf, 2016. IDTechEx USA.

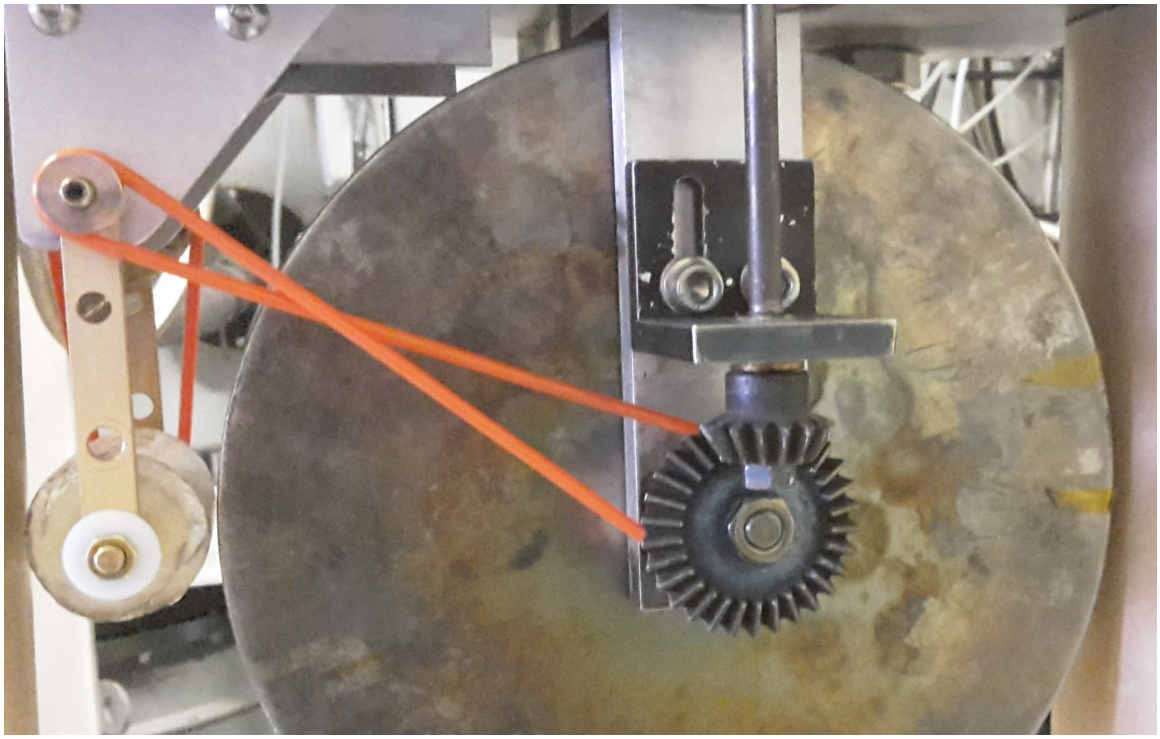
Appendix A

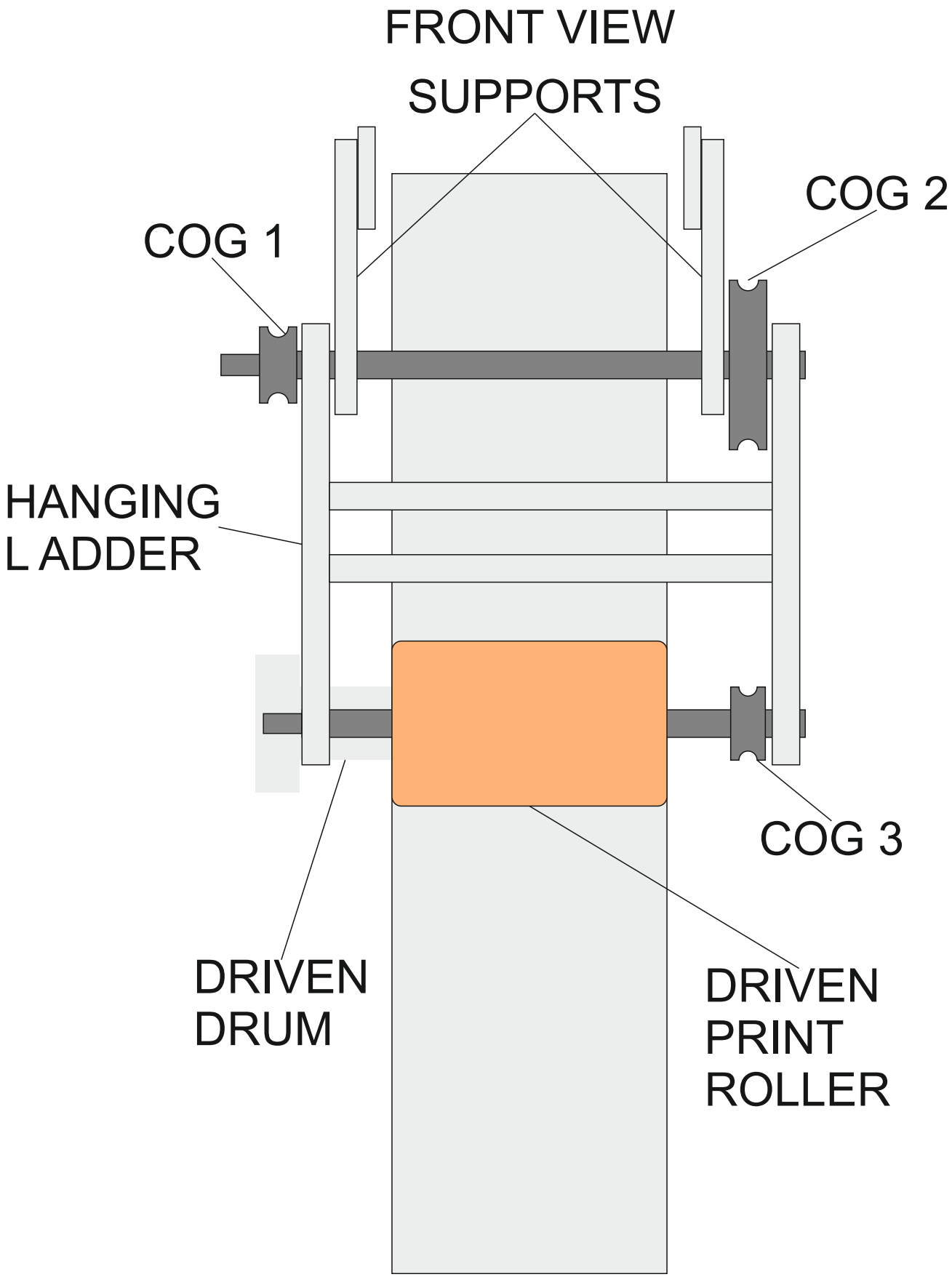
List of terms from industry used to describe flexography printing.

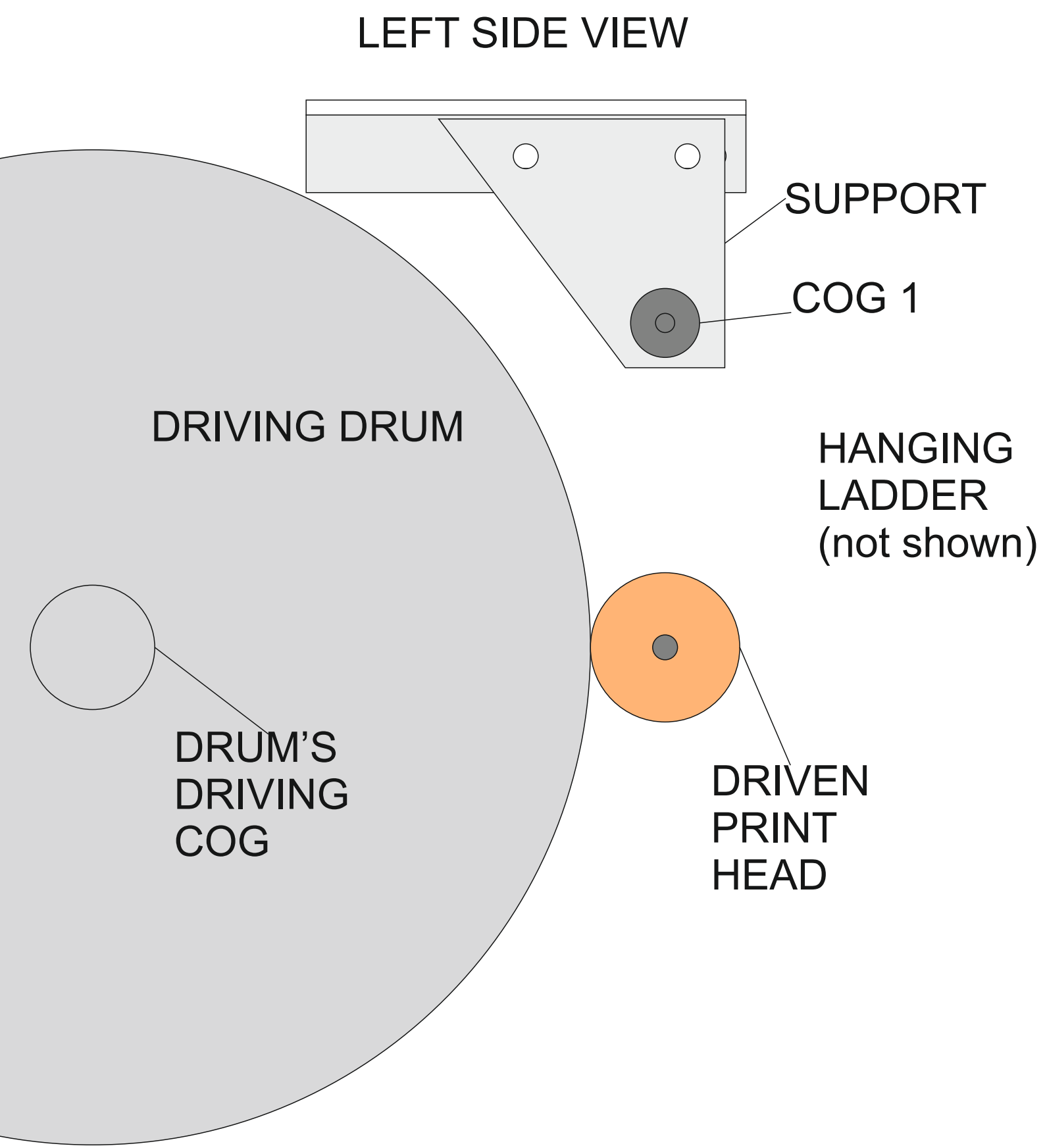
Term	Definition
Anilox	Cylinder (copper plated or ceramic) with micro pits (a.k.a. cells) used to uniformly continuously transfer ink from the ink bath or fountain roller to the printing plate.
Cell opening	The dimension of the micro pits in the anilox roll surface.
Cell volume	The volume of the micro pits in the anilox roller, $cm^3.m^{-2}$ of BCM (billion cubic microns per square inch)
Cross direction (CD)	Along the line axially parallel to the printing rollers.
Dot gain	The change in size of a halftone dot from the nominal dot size, consisting of physical and optical dot gain.
Fidelity	The degree of exactness, used in terms of the degree of exactness of the spacial mimicking of a pattern form its master.
Finish	The degree of gloss to a flat surface.
Gloss	The ability of the print surface to reflect light; antonyms: flat, matt.
Halftone	Image made of dots with consistent density, but varying size and shape, leading to apparent changes in colour and tone.
Kiss impression	The lightest impression of plate to substrate that will ensure ink transfer.
Line ruling	The number of features (half tone dots, anilox cells) per unit measurement, in^{-1} or cm^{-1}.
Machine direction (MD)	Along the line parallel to the substrate web movement.
Misting	A collection of droplets of ink at the printing contact exit, resulting from the printing inertia.
Nip	The line contact between two axially parallel rollers.
Optical Gain	The change in apparent (by optical measurement) size of the printed tone dots compared with the plate, dimensionless.
Physical Gain	The change in physical dimensions due to printing impression pressures, compared with the nominal plate feature size, dimensionless.
Solid Density	The opacity of a printed colour, numerically the logarithm of the measured reflectance.
Web	Roll-to-roll substrate; fixed width and thickness sheet of material (paper, foil or polymer film) which is unwound during R2R processing.

Appendix B

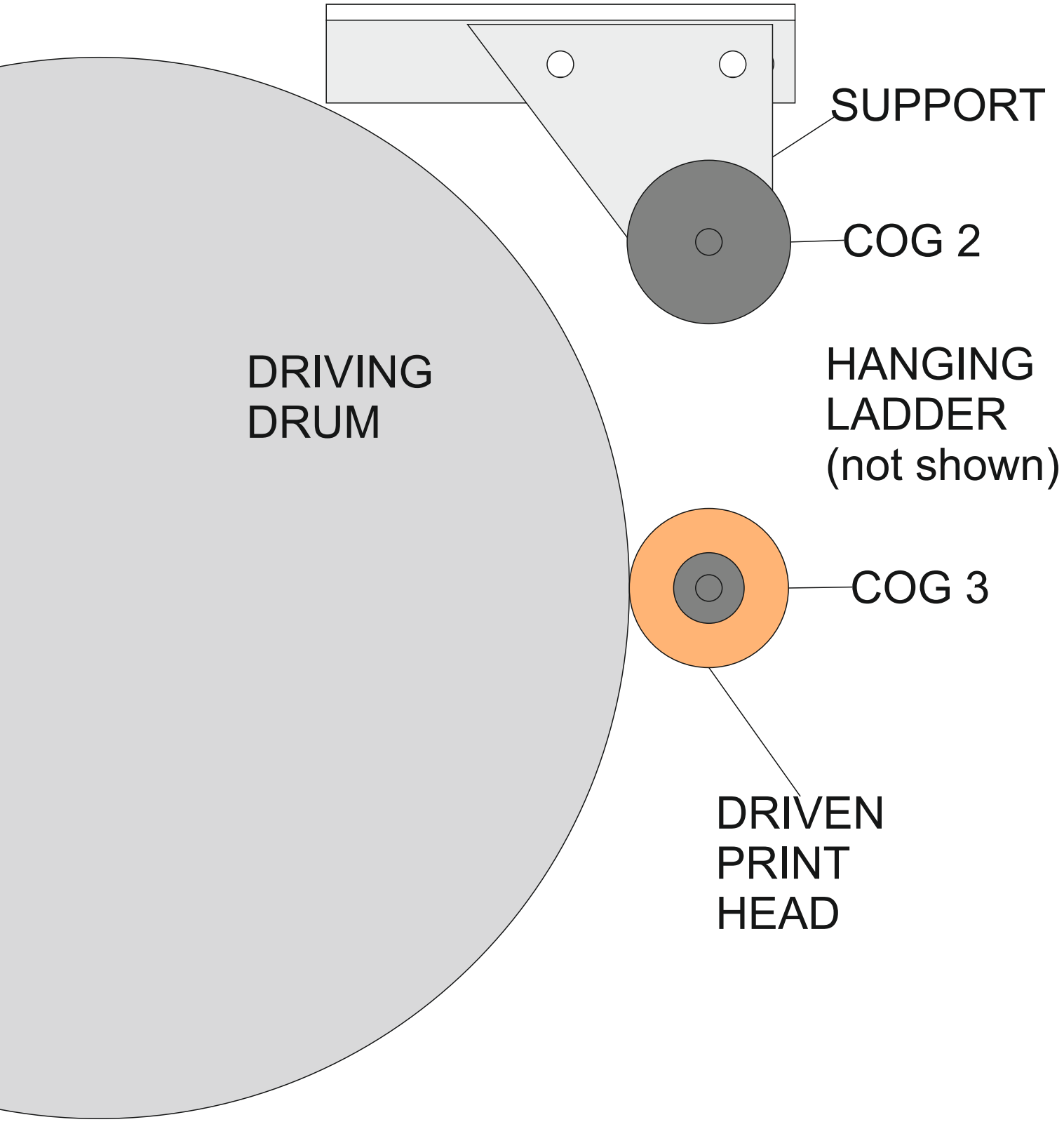
In-vacuum driven flexography system, photo and design drawings, to scale. Units: millimetres.



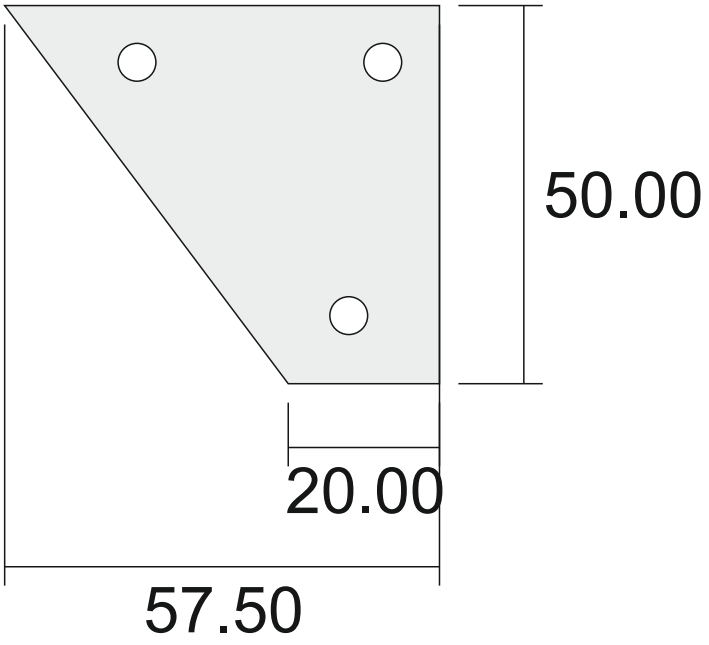

FRONT VIEW
SUPPORTS
COG 1
COG 2
HANGING
L ADDER
COG 3
DRIVEN
DRUM
DRIVEN
PRINT
ROLLER

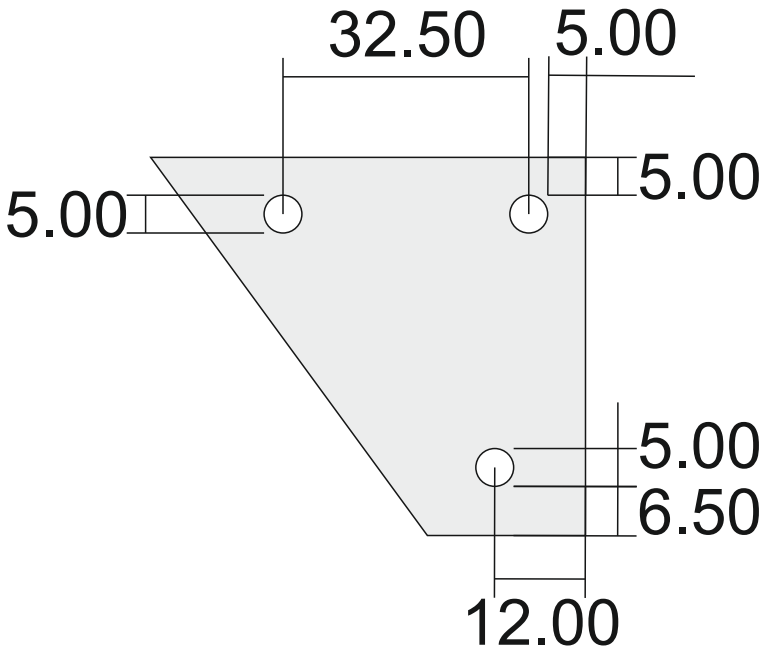

LEFT SIDE VIEW
SUPPORT
COG 1
DRIVING DRUM
HANGING
LADDER
(not shown)
DRUM'S
DRIVING
COG
DRIVEN
PRINT
HEAD

RIGHT SIDE VIEW

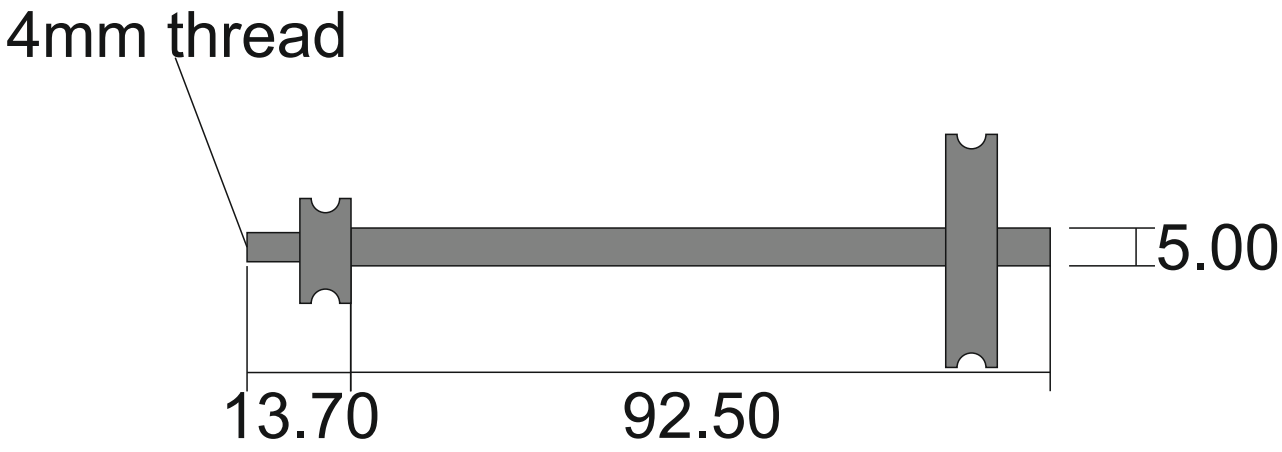


SUPPORTS X2 (4mm thick)



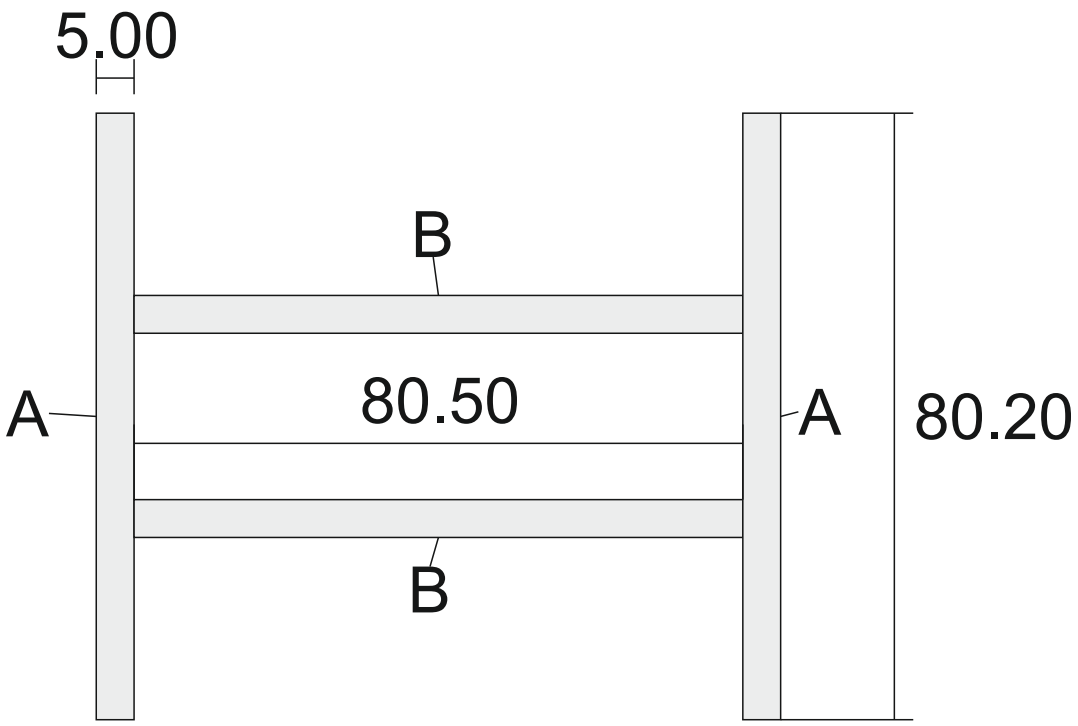


TOP WHEEL SET

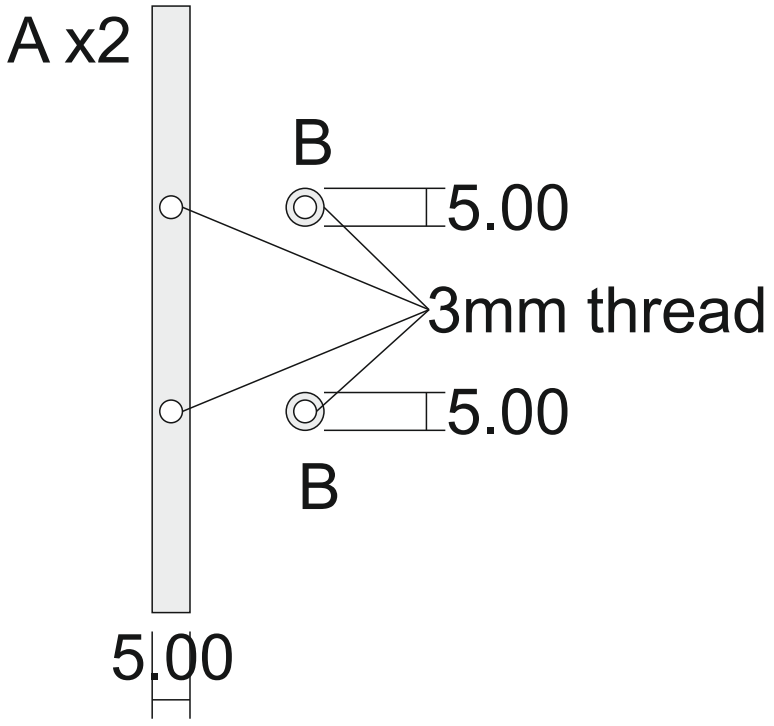


HANGING LADDER

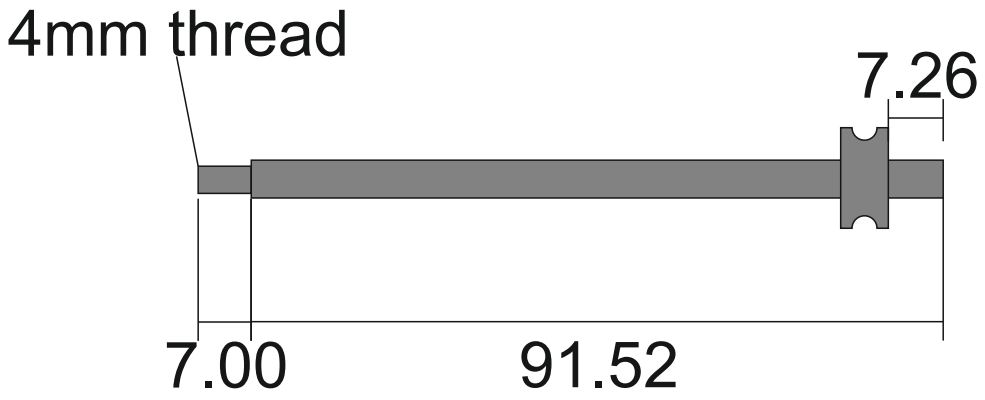
FRONT VIEW



END ON VIEW

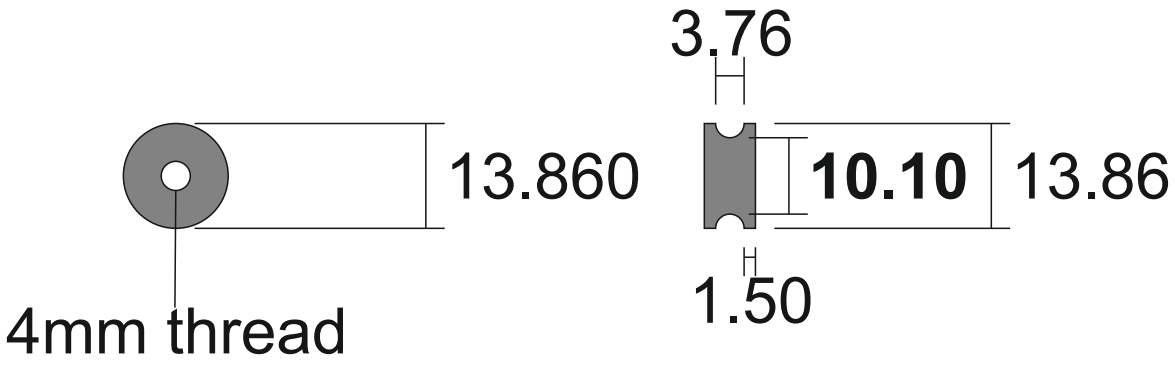


BOTTOM WHEEL SET

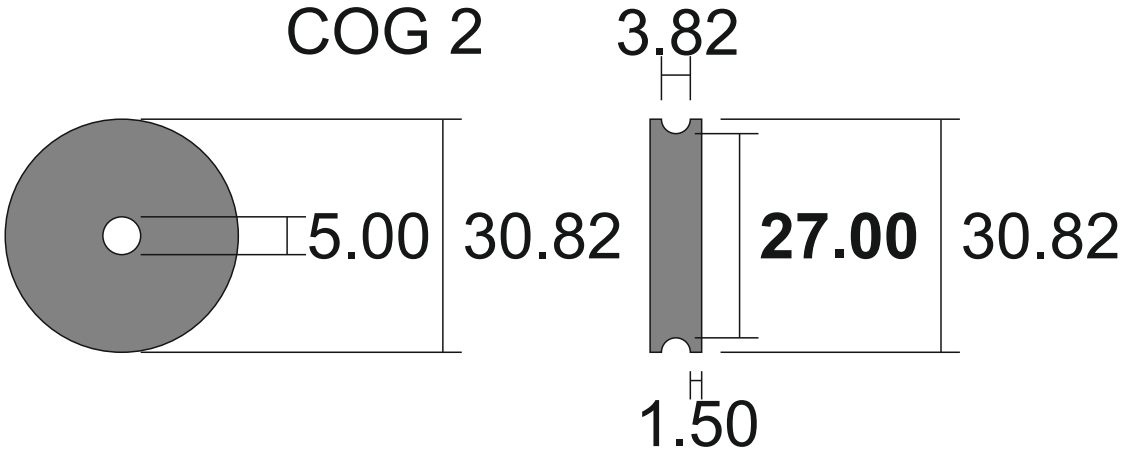


COGS

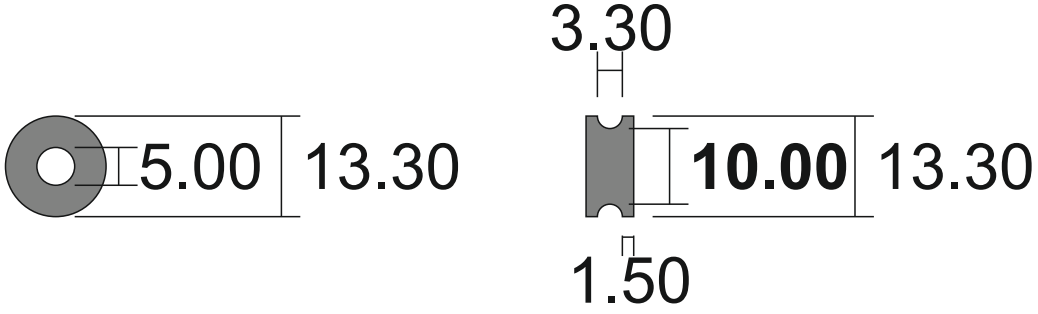
COG 1



COG 2



COG 3



Appendix C

MATLAB® image analysis code.

```
clear
PathName = 'C:\Users\XXX\Documents\Data\';
srcFiles = dir(PathName);
d=zeros(180,9);
a=1;
for i = 3 : length(srcFiles)
    filename = strcat(PathName,'\',srcFiles(i).name);
    I = imread(filename);
    if size(I,3)==3 %if the image is not greyscale, make
       it greyscale
        I=rgb2gray(I);
    end
    [BWr,BWw]=size(I); %image size used for analysis later
    %imshow(I);
    BW=edge(I,'Canny'); %find edges of stripes
    %imshow(BW);
    % BWL=bwlabel(BW);
    [L,N]=bwlabel(BW);%Number the stripes into a matrix (L
       ) of 0's and label numbers, count (N) the number of
        labels
    %imshow(L)
    %this section renumbers the labels (L) to be ordered
       from left-to-right.
    %source 07/2017: https://blogs.mathworks.com/steve
       /2008/04/14/relabeling-a-label-matrix/
    %source 07/2017: https://blogs.mathworks.com/steve
       /2008/03/25/bwlabel-search-order/
    g = regionprops(L,'BoundingBox','Extrema','
       PixelIdxList');
    boxes = cat(1, g.BoundingBox);
    left_edge = boxes(:,1);
    [sorted, sort_order] = sort(left_edge);
    s2 = g(sort_order);
    for j = 1:numel(s2)
```

```
    jth_object_idx_list = s2(j).PixelIdxList;
    L(jth_object_idx_list) = j;
end
%clean data to create 18 continuous defined stripe
   edges by 1st: connecting the found
%edges which are of the same stripe edge but not
   connected by the bwlabel
%function and 2nd: removing any small insignificant
   edges found by the canny
%edge detection.
for k=1:N
    for l=1:N %count through the numbers in L, so that
        each edge combined or removed
        if k==l
            continue
        end
        [r,c]=find(L==k); % define the two detected
           lines to be compared
        rc1=[r,c];
        [r,c]=find(L==l);
        rc2=[r,c];
        mx=max(rc2,[],1);
        mn=min(rc2,[],1);
        h= mx(:,1)-mn(:,1);
        if  h< 0.01*BWr
            L(L==l)=0;
            for m=2:(N-l) % renumber the subsequent
               edges to account for an edge being
               removed by being combined with the
               previous edge
                if or(m==l,(l-m)<1)
                    continue
                end
                L(L==l-m)=l-m+1;
            end
            %count through the numbers in L, so that
               each edge combined or removed
        else
            rows=size(rc1);
            for n=1:rows
                y=rc1(n,2);
                for b=1:18
                    if and(y>((b-1)*BWw./18), y<=(b*
                       BWw./18))
                        x=rc1(n,1);
```

```
                        L(x,y)=N+b; %re-number the
                           stripe edge while avoiding
                           combining stripes on the
                           left with the existing
                           stripe numbers (N)
                    end
                end
            end
        end
    end
end
N=numel(unique(L))-1;
maxL=max(unique(L));
o=1;
for p=1:maxL
    if any(L(:)== p)
        L(L==p)= o;
        o=o+1;
    end
end
%imshow(L);
    d1=zeros(9,9);
    for q=2:+2:N
        [r,c]=find(L==q);
        rc1=sort([r,c]);
        [r,c]=find(L==q-1);
        rc2=sort([r,c]);
        avg1=mean(rc1(:,2));
        avg2=mean(rc2(:,2));
        unitconversion=188.9764; %pixels per mm (4800
           dpi)
        w=(avg1-avg2)/unitconversion;
        maxedgeroughness_pixels= max(max(rc1(:,2))-min
           (rc1(:,2)),max(rc2(:,2))-min(rc2(:,2)));
        p2p=maxedgeroughness_pixels/unitconversion;
        rms_pixels=sqrt((std(rc1(:,2))^2+std(rc2(:,2))
           ^2)/2);
        rms=rms_pixels/unitconversion;
        %x = horzcat(w, rms, p2p);
        d1((q/2),1) = w;
        d1((q/2),2) = rms;
        d1((q/2),3) = p2p;
    end
M=nonzeros(mean(d1));
```

```
    Std=nonzeros(std(d1,1)/sqrt(9)); % calculate standard
       error of results to compare the means
    d1(1,4:6)=M;
    d1(1,7:9)=Std;
    d(a:(a+8),1:9)=d1;
    a=a+9;
end
%print data to tab delimited .txt file for export
fullFileName = fullfile(PathName, 'stripesedgeanalysis.txt
   ');
if exist(fullFileName, 'file')==2
    delete(fullFileName);
end
dlmwrite(fullFileName,d,'\t')
```